Functional design of nanocomposites and their applications in energy conversion and storage

Ruifeng Du

Tesi doctoral

Functional design of nanocomposites and their applications in energy conversion and storage

Autor:

Ruifeng Du

Director:

Prof. Andreu Cabot

Functional design of nanocomposites and their applications in energy conversion and storage

Memòria presentada per optar al grau de doctor per la

Universitat de Barcelona

Programa de doctorat en Nanociència

Autor:

Ruifeng Du

Director:

Prof. Andreu Cabot

Tutor:

Prof. Frank Güell Vilà

Lloc on s'ha dut a terme la tesi

Institut de Recerca en Energia de Catalunya (IREC)

UNIVERSITAT DE BARCELONA

Content

Acknowledgement

The writing of my doctoral thesis has come to an end, and my academic life is drawing to a close.   I am also about to leaving Barcelona and starting my new journey of life. At this moment, I have an indescribable feeling of gratitude, joy, reluctance, and excitement intertwined. The four-year study abroad life is the most beautiful scenery in my life and I will treasure this memory and keep it in my heart forever. I would like to express my heartfelt thanks to the teachers, friends, colleagues and family members who have accompanied me along the way. It is your support, help and encouragement that have made me go all the way without fear.

First of all, my heartiest thanks flow to my supervisor, Professor Andreu Cabot, for not only giving me this precious opportunity to study in Spain but also for introducing me to a new wonderful world of nanomaterials. Your humor, wisdom, tolerance, humility, and rigor have shown me what a respectable scholar should look like, and I will also take it as a model for my future research work and life. No matter how brief my group meeting presentation is, you will always say "good" and give your opinion. No matter how bad my paper is, you will seriously help me correct it and give many valuable comments. No matter how poor my performance is, you'll pass the basketball to me and tell me "do it". I may not be your best student academically, but I can proudly say that I am the one who played basketball with you the most. Andreu, you owe me a basketball Ph.D.

Secondly, I would like to express my sincere gratitude to all the members of functional nanomaterial group at IREC: Pablo Guardia, Yu Liu, Taisiia Berestok , Junfeng Liu, Xiaoting Yu, Junshan Li, Yong Zuo, Perer Zhang, Chaoqi Zhang, Mengyao Li, Congcong Xing, Dawei Yang, Xiang Wang, Ke Xiao, Bingfei Nan, Evgenii Liashenko, Alberto Ramón, Jesus Chacon, Guillem Montaña, Paulina Martinez, Linlin Yang, Gavin He, Li Gong, Guifang Zeng, Xuan Lu, Canhuang Li,

Xinqi Chang, Chaoyue Zhang, thank you for helping and sharing with me in the past five years. I wish all the friends who have left and those who are about to leave FN all the best, and hope that the friends who are still in FN can enjoy their work and life in Barcelona. I'm so proud to have been one of you.

Also, I am grateful to Prof. Jordi Arbiol, Ting Zhang and Xu Han and for checking the wonderful HRTEM of my samples. Those excellent HRTEM images really play an important role in my project and publications.

I want to thank Féix Urbain from Catalysis group of IREC for helping me design the experiment and test the performance in $CoFe_2O_4$ work.

I would like to thank Associate Professor Baoying Li from Qilu University of technology for the photocatalytic hydrogen evolution test and the TRPL test.

I also want to thank the "China Scholarship Council" for providing me the financial support that I am able to conduct my PhD research work abroad.

Finally, my appreciation beyond the word should be given to my beloved parents. Thank you for your caring, supporting and encouragement. No matter how far I am from you, you will always be my strongest backing. Specially, to my beloved wife, future Dr. Jing Liang, thank you for always being there, whether it's happiness or suffering, just like our wedding vows said. I firmly believe that with you by my side, no matter what kind of storms and waves may come in the future, we can work together to tide over.

<div align="right">

Barcelona, Spain

April, 2022

</div>

List of publications

My research results during the PhD project are listed in the following four papers that have been published in peer-reviewed journals. A full copy of each publication could be found in the Annex part at the end of the thesis.

[1] C. Zhang, **R. Du**, J.J. Biendicho, M. Yi, K. Xiao, D. Yang, T. Zhang, X. Wang, J. Arbiol, J. Llorca, Y. Zhou, J.R. Morante, A. Cabot, Tubular CoFeP@CN as a Mott–Schottky Catalyst with Multiple Adsorption Sites for Robust Lithium−Sulfur Batteries, Adv. Energy Mater. 11 (2021) 2100432. (Co-first author)

[2] F. Urbain, **R. Du**, P. Tang, V. Smirnov, T. Andreu, F. Finger, N.J. Divins, J. Llorca, J. Arbiol, A. Cabot, Upscaling high activity oxygen evolution catalysts based on $CoFe_2O_4$ nanoparticles supported on nickel foam for power-to-gas electrochemical conversion with energy efficiencies above 80%, Appl. Catal. B Environ. 259 (2019) 118055. (Corresponding author)

[3] **R. Du**, K. Xiao, B. Li, X. Han, C. Zhang, X. Wang, Y. Zuo, P. Guardia, J. Li, J. Chen, A. Cabot, Controlled oxygen doping in highly dispersed Ni-loaded g-C_3N_4 nanotubes for efficient photocatalytic H_2O_2 production, Chem. Eng. J. (2022) 135999.

[4] **R. Du**, B. Li, X. Han, K. Xiao, X. Wang, J. Arbiol, A. Cabot, 2D/2D Heterojunction of TiO_2 Nanosheets / Ultrathin g-C_3N_4 for efficient photocatalytic hydrogen evolution, Nanomaterials. (Accepted)

Authors' contribution

All the work and results presented in the thesis were carried out in the functional nanomaterials group at Catalonia Institute for Energy Research (IREC) under the supervision of Prof. Andreu Cabot. None of the publications in this thesis has been previously presented in any other thesis. Ruifeng Du, as a PhD student, contributed to the experimental work, data analysis and manuscript writing for all the publications presented in this thesis. The contributions of co-authors for each article are shown below this paragraph. The impact factor in 2022 of the journals where the manuscripts were published is provided.

Chapter 2

F. Urbain, **R. Du**, P. Tang, V. Smirnov, T. Andreu, F. Finger, N.J. Divins, J. Llorca, J. Arbiol, A. Cabot, Upscaling high activity oxygen evolution catalysts based on $CoFe_2O_4$ nanoparticles supported on nickel foam for power-to-gas electrochemical conversion with energy efficiencies above 80%, Appl. Catal. B Environ. 259 (2019)

Impact factor：19.052

In this work, F. Urbain designed the experiment, test the OER performance of the nanocomposites and wrote the first draft of the manuscript. R. Du designed the nanocomposite materials, produced the nanoparticles and Ni foam coating, conducted the characterization including XRD, FTIR, SEM, SEM-EDS, TEM and wrote the experiment part and some discussion part of the manuscript. X. Han and J. Arbiol participated in high-resolution TEM characterization, J. Llorca participated in X-ray photoelectron spectroscopy measurement. V. Smirnov, F. Finger, performed and supervised the deposition of the multijunction thin film silicon solar cells. J.R.M. T.A. and A.C. supervised the proposed and executed research program. All the authors participated in discussions and contributed to the editing of the manuscript.

Chapter 3

R. Du, B. Li, X. Han, K. Xiao, X. Wang, J. Arbiol, A. Cabot, 2D/2D Heterojunction of TiO_2 Nanosheets / Ultrathin g-C_3N_4 for efficient photocatalytic hydrogen evolution, Nanomaterials.

Impact factor：4.921

In this work, Ruifeng Du designed the experiment and the nanocomposites, prepared all the materials and conducted XRD, SEM, ZEM-EDS, TEM characterization, photoelectrochemical measurements and wrote the first draft of the manuscript. Baoying Li conducted the photocatalytic hydrogen evolution test and TRPL test. Ke Xiao, Chaoqi Zhang and Xiang Wang significantly contributed to the result discussion. X. Han and J. Arbiol participated in high-resolution TEM characterization. A. Cabot conceived and guided the project and supervised the work. The manuscript was corrected and improved by all authors.

Chapter 4

R. Du, K. Xiao, B. Li, X. Han, C. Zhang, X. Wang, Y. Zuo, P. Guardia, J. Li, J. Chen, A. Cabot, Controlled oxygen doping in highly dispersed Ni-loaded g-C3N4 nanotubes for efficient photocatalytic H_2O_2 production, Chem. Eng. J. (2022) 135999.

Impact factor: 13.273

In this work, Ruifeng Du designed the experiment and the nanocomposites, prepared all the materials and conducted XRD, SEM, ZEM-EDS characterization, photocatalytic H_2O_2 generation, photoelectrochemical measurements and write the first draft of the manuscript. Baoying Li and Jianbin Chen helped with the PL, TRPL, XPS test and DFT calculation. Ke Xiao, Chaoqi Zhang and Xiang Wang significantly contributed to the result discussion. Ke Xiao contributed to the drawing of synthetic schematics. X. Han and J. Arbiol participated in high-resolution TEM characterization.

A. Cabot conceived and guided the project and supervised the work. The manuscript was corrected and improved by all authors.

Chapter 5

C. Zhang, **R. Du**, J.J. Biendicho, M. Yi, K. Xiao, D. Yang, T. Zhang, X. Wang, J. Arbiol, J. Llorca, Y. Zhou, J.R. Morante, A. Cabot, Tubular CoFeP@CN as a Mott–Schottky Catalyst with Multiple Adsorption Sites for Robust Lithium−Sulfur Batteries, Adv. Energy Mater. 11 (2021) 2100432.

Impact factor: 29.368

Chaoqi Zhang and Ruifeng Du contributed equally to this work. Chaoqi Zhang and Ruifeng Du designed the experiment and nanocomposite materials. Chaoqi zhang test all the battery performance of the nanocomposites and wrote the first draft of the manuscript. R. Du designed the nanocomposite materials, produced the nanoparticles and nanocomposites, conducted the characterization including XRD, FTIR, Zeta potential, and TEM and wrote the experiment part of the manuscript. Ting Zhang, and J. Arbiol participated in high-resolution TEM characterization, J. Llorca participated in X-ray photoelectron spectroscopy measurement. Y. Zhou participated in DFT calculation. J.J. Biendicho, J.R. Morante and A. Cabot conceived and guided the project and supervised the work. The manuscript was corrected and improved by all authors.

Prof. Andreu Cabot

certifies that the information provided above is true.

Barcelona, April 2022

Preface

The chapters included in this PhD thesis cover the work developed by the PhD candidate Ruifeng Du at the Catalonia Institute for Energy Research (IREC) in Sant Adrià de Besòs, Barcelona, in the period 2017-2022, supported by China Scholarship Council (No. 201706400066). The thesis is particularly focused on the functional design and preparation of nanocomposites and their application in energy conversion and storage.

This thesis consists of five chapters. The first chapter mainly introduces the background, motivation and objectives of this thesis. The experiment work performed to achieve those objectives is shown in chapters 2-5. Within the general frame of optimizing functional nanocomposite design and preparation, the work presented in this thesis mainly contains the following aspects：(1) Functional design of composite nanomaterials based on specific applications; (2) According to the material design, realize the preparation of nanocomposite materials; (3) Performance testing of the prepared nanocomposites, and then using the measured results to verify our design conjectures. In chapter two, a composite based on $CoFe_2O_4$ NPs coating a Ni foam was developed for electrocatalytic oxygen evolution reaction. In chapter three, 2D/2D heterojunctions based on TiO_2 nanosheets/utrathin g-C_3N_4 were produced for photocatalytic hydrogen evolution. In chapter four, oxygen doping in highly dispersed Ni-loaded g-C_3N_4 nanotubes was prepared for photocatalytic hydrogen peroxide evolution. In chapter five, CoFeP nanorods supported on tubular g-C_3N_4 were prepared for lithium−sulfur batteries. During all the experiments, there are several difficulties throughout, including surface modification of NPs, NPs agglomeration, and uniform loading of NPs.

Summary of results

This thesis focuses on the functional design and preparation of different kind of nanocomposites and their applications in energy conversion and storage technologies, particular in OER, HER, H_2O_2ER and LSBs. For the different applications nanocomposite materials are designed, engineered and tested. First, nanocomposite materials are designed based on the requirements for various properties of the material, including conductivity, catalysis, adsorption performance, band structure, specific surface area, material stability etc. Then the composites nanocomposites are engineered using methods like NPs coating, self-assembly and in-situ growth method. Finally, as prepared functional nanocomposites are tested in specific application. Results from the tests are frequently used as feedback for the design and engineering tasks, thus optimizing the final material. An understanding of the correlation between the designed nanocomposite structure and the specific application performance allows a more rational design of functional nanocomposites.

This thesis consists of five chapters. The first chapter presents a general introduction to the synthetic strategies and applications of nanocomposites. Chapter 2 details the preparation of $CoFe_2O_4$ NPs and their incorporation on Ni foams (NFs). The coating process was optimized for large electrode areas, ensuring a proper distribution of the NPs on the NF that allowed overcoming the electrical conductivity limitations of oxide NPs. We were able to produce $CoFe_2O_4$-coated NFs having 10 cm^2 geometric surface areas with overpotentials below 300 mV for the OER at a current density of 50 mA/cm^2. The $CoFe_2O_4$-coated NFs were also tested in a photovoltaic-electrolyzer coupled system and achieved a conversion efficiency of solar to chemical up to 13%. The results in Chapter 2 were published in Appl. Catal. B Environ (2019).

In chapter 3, the preaparation of 2D/2D heterojunction of TiO_2 nanosheets/ultrathin g-C_3N_4 through the electrostatic self-assembly method is detailed. The obtained nanocomposites were applied for the photocatalytic HER under simulated solar light,

presenting high performance and good stabilities. Compared with g-C_3N_4 and pure TiO_2 nanosheets, this 2D/2D TiO_2/g-C_3N_4 heterojunction exhibited ultra-high charge separation and transport properties and obvious improvement in photocatalytic performance. The results in Chapter 3 have been accepted for publication in Nanomaterials (2022).

In chapter 4, the oxygen doping of highly dispersed Ni-loaded g-C_3N_4 nanotubes produced through an *in situ* growth method is detailed. The obtained nanocomposites were applied for photocatalytic hydrogen peroxide evolution under visible light. The hollow structure of the tubular g-C_3N_4 provides a large surface with a high density of reactive sites and efficient visible light absorption during photocatalytic reaction. Furthermore, oxygen doping and the Ni loading of the Ni/g-C_3N_4 composite catalyst displays a superior ability to separate photogenerated charge carriers and a high selectivity to the two-electron process during the ORR. The optimized composition, $Ni_{4\%}$/$O_{0.2}$tCN, displays a H_2O_2 production rate of 2464 mol g^{-1} h^{-1}, and achieves an apparent quantum yield (AQY) of 14.9% at 420 nm. The results in Chapter 4 were published in Chem. Eng. J. (2022).

Chapter 5 details the synthesis of colloidal CoFeP nanorods, tubular g-C_3N_4 and nanocomposites of CoFeP@t-CN. The as prepared CoFeP@t-CN composites were employed as sulfur hosts for LSBs. Density functional theory (DFT) calculations and experimental data confirmed that CoFeP@CN composites are characterized by a suitable electronic structure and charge rearrangement that allows them to act as a Mott-Schottky catalyst to accelerate LiPS conversion. Besides, the tubular geometry of CoFeP@CN composites facilitates the diffusion of Li ions, accommodates volume change during the reaction, and offers abundant lithiophilic/sulfiphilic sites to effectively trap soluble LiPS. As a result, S@CoFeP@CN electrodes deliver high initial capacities of 1607 mAh g^{-1} at 0.1 C, superior rate performance of 630 mAh g^{-1} at 5 C, and remarkable cycling stability with 90.44% capacity retention over 700 cycles. We further produced coin cells with high sulfur loading, 4.1 mg cm^{-2}, and

pouch cells with 0.1 Ah capacity to validate their superior cycling stability. This work was published in Adv. Energy Mater. (2021).

Finally, the results and discussion, conclusion and perspectives for future work are presented at the end of this thesis.

Resumen de Resultados

Esta tesis se centra en el diseño funcional y la preparación de diferentes tipos de nanocompuestos y sus aplicaciones en tecnologías de conversión y almacenamiento de energía, en particular en OER, HER, H_2O_2ER y LSBs. Para diferentes aplicaciones, los materiales nanocompuestos se diseñan en función de los requisitos de varias propiedades del material, incluida la conductividad, la catálisis, el rendimiento de adsorción, la estructura de la banda, el área de superficie específica, la estabilidad del material, etc. Luego, los nanocompuestos funcionales se preparan a través de diferentes métodos como recubrimiento de NPs, autoensamblaje y crecimiento in situ. Finalmente, los nanocompuestos funcionales preparados se prueban en aplicaciones específicas. La comprensión de la correlación entre la estructura del nanocompuesto diseñado y el rendimiento de la aplicación específica permite un diseño más racional de nanocompuestos funcionales.

Esta tesis consta de cinco capítulos. El primer capítulo presenta una introducción general a las estrategias sintéticas y aplicaciones de los nanocompuestos. El capítulo 2 detalla la preparación de $CoFe_2O_4$, la modificación de la superficie de las NP y el recubrimiento de soportes de Ni (NF) con las NP de $CoFe_2O_4$. El proceso de recubrimiento se optimizó para áreas de electrodos grandes, asegurando una distribución adecuada de las NP en el NF que permitió superar las limitaciones de conductividad eléctrica de las NP de óxido. Pudimos producir NFs recubiertos con $CoFe_2O_4$ con áreas superficiales geométricas de 10 cm^2 con sobrepotenciales por debajo de 300 mV para la OER a una densidad de corriente de 50 mA/cm^2. Los NF recubiertos con $CoFe_2O_4$ preparados también se probaron en un sistema acoplado de electrolizador fotovoltaico y lograron una eficiencia de conversión de energía solar a química de hasta el 13 %. Los resultados del Capítulo 2 se publicaron en Appl. Catal. B Environ (2019).

En el capítulo 3, se preparó una heterounión 2D/2D de nanoláminas de TiO_2/g-C_3N_4 ultrafinas mediante el método de autoensamblaje electrostático. Los nanocompuestos obtenidos se aplicaron para la reacción fotocatalítica de evolución de hidrógeno bajo luz solar simulada, presentando un alto rendimiento HER y buenas estabilidades. En comparación con g-C_3N_4 y nanoláminas de TiO_2 puro, esta heterounión 2D/2D TiO_2/g-C_3N_4 exhibió propiedades de transporte y separación de carga ultra altas y una mejora evidente en el rendimiento fotocatalítico. Los resultados del Capítulo 3 se publicaron en Nanomateris (2022).

En el capítulo 4, se preparó el dopaje con oxígeno en nanotubos de g-C_3N_4 cargados con Ni altamente dispersos a través de un método de crecimiento in situ. Los nanocompuestos obtenidos se aplicaron para la reacción de evolución de peróxido de hidrógeno fotocatalítico bajo luz visible. La estructura hueca del g-C_3N_4 tubular proporciona una gran superficie con una alta densidad de sitios reactivos y una absorción eficiente de la luz visible durante la reacción fotocatalítica. Además, el dopaje con oxígeno y la carga de Ni del catalizador compuesto de Ni/g-C_3N_4 muestran una capacidad superior para separar los portadores de carga fotogenerados y una alta selectividad para el proceso de dos electrones durante la reacción de reducción de oxígeno (ORR). Con la composición optimizada, $Ni_{4\%}$/$O_{0.2}$tCN, muestra una tasa de producción de H_2O_2 de 2464 mol $g^{-1} \cdot h^{-1}$ y logra un rendimiento cuántico aparente (AQY) del 14.9% a 420 nm. Los resultados del Capítulo 4 se publicaron en Chem. Eng. J. (2022).

El Capítulo 5 muestra la síntesis de nanorods de CoFeP coloidal, g-C_3N_4 tubular y nanocompuestos de CoFeP@t-CN. Los compuestos CoFeP@t-CN preparados se emplearon como materiales soporte de azufre para baterías de litio-azufre. Los cálculos DFT y los datos experimentales confirman que los compuestos CoFeP@CN se caracterizan por una estructura electrónica adecuada y un reordenamiento de carga que les permite actuar como un catalizador de Mott-Schottky para acelerar la conversión de LiPS. Además, la geometría tubular de los compuestos CoFeP@CN

facilita la difusión de los iones de litio, se adapta al cambio de volumen durante la reacción y ofrece abundantes sitios litiófilos/sulfófilos para atrapar de forma eficaz los LiPS solubles. Como resultado, los electrodos S@CoFeP@CN brindan altas capacidades iniciales de 1607 mAh•g^{-1} a 0.1 C, un rendimiento de velocidad superior de 630 mAh•g^{-1} a 5 C y una notable estabilidad cíclica con una retención de capacidad del 90.44 % durante 700 ciclos. Además, producimos celdas tipo moneda con una alta carga de azufre, 4.1 mg•cm^{-2}, y celdas tipo bolsa con una capacidad de 0.1 Ah para validar su estabilidad cíclica superior. Este trabajo fue publicado en Adv. Energy Mater. (2021).

Finalmente, la conclusión y las perspectivas de trabajo futuro se presentaron al final de esta tesis.

Abbreviation

bCN	Bulk graphitic carbonitrile C_3N_4
BE	Binding energy
BG	Band gap
CB	Conduction band
CN	Carbon nitride
CNT	Carbon nanotube
CV	Cyclic voltametry
DFT	Density functional theory
ECSA	Electrochemically active surface area
EDS	Energy dispersive X-ray spectroscopy
EELS	Electron energy loss spectroscopy
EG	Ethylene glycol
EIS	Electrochemical impedance spectroscopy
FTIR	Fourier-transform infrared spectroscopy
GC	Gas chromatography
GCE	Glassy carbon electrode
g-CN	Graphitic carbonitrile $g-C_3N_4$
HER	Hydrogen evolution reaction
HRTEM	High resolution transmission electron miroscopy
H_2O_2ER	Hydrogen peroxide evolution reaction
LIB	Lithium ion battery
LiPS	Lithium polysulfide
LSB	Lithium-sulfur battery
NC	Nanocrystal
NF	Nickel foam
NP	Nanoparticle
OAc	Oleic acid

OAm	Oleylamine
ODE	1-Octadecene
OER	Oxygen evolution reaction
ORR	Oxygen reduction reaction
PC	Photocurrent
PEI	Polyetherimide
PL	Photoluminescence
PVDF	Polyvinilidene difluride
RRDE	Roating ring-disk electrode
SEM	Scanning electron microscopy
SSA	Specific surface area
STEM	Scanning transmission electron microscopy
tCN	Tubular g-C_3N_4
TEM	Transmission electron microscopy
TGA	Theomogravimetric analysis
TOP	Tri-n-octylphosphine
TRPL	Transient photoluminescence
uCN	Ultrathin g-C_3N_4
VB	Valence band
XPS	X-ray photoelectron spectroscopy
XRD	X-ray diffraction
0D/2D	Zero-dimensional/two-dimensional
2D/2D	Two-dimensional/two-dimensional
3D	Three-dimensional

Introduction

1.1 Energy crisis and renewable energy

The protection of the environment while securing enough energy for our development is one of the greatest challenges of the 21st century.[1][2] The rapid economic growth of most of the emerging and developing countries makes the adaptation and optimization of environmentally friendly and renewable energy sources important for our societies. [3][4][5] Renewable sources of energy are those derived from resources that are renewed naturally. They include solar energy, hydro energy, wind, rain, tides, waves, and geothermal heat. Whereas non-renewable resources are natural resources that cannot be renewed quickly by natural phenomena such as carbon-based fossil fuels like coal and petroleum.[6,7]
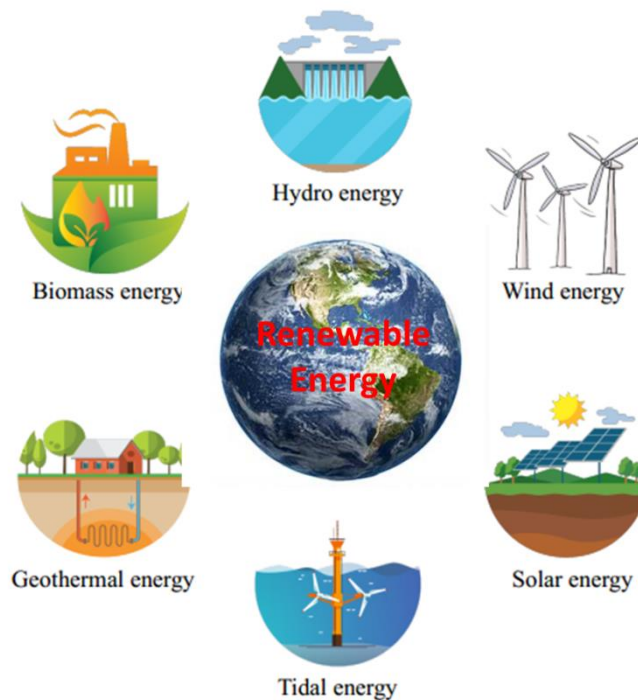
Fig 1.1. Renewable energies.[5]

In recent years, overexploitation of fossil fuels, environmental pollution, global warming, and nuclear safety issues are increasingly prominent problems. Additionally, there has been an unprecedented increase in energy demand caused by post-COVID recovery[8,9] and the tightening of world crude oil and natural gas supply caused by the Russian-Ukrainian war. [10,11]All of these make countries around the world realize the necessity and urgency of

developing and utilizing renewable energy.

Fig 1.2. (a) Renewable electricity generation increase by technology country and region, 2020-2021, (b) Share of low-carbon sources and coal in world electricity generation, 1971-2021[12].

According to a survey by IEA in Fig 1.2, renewable electricity generation in 2021 was set to expand by more than 8% to reach 8300 TWh, the fastest year-on-year growth since the 1970s. China alone should account for 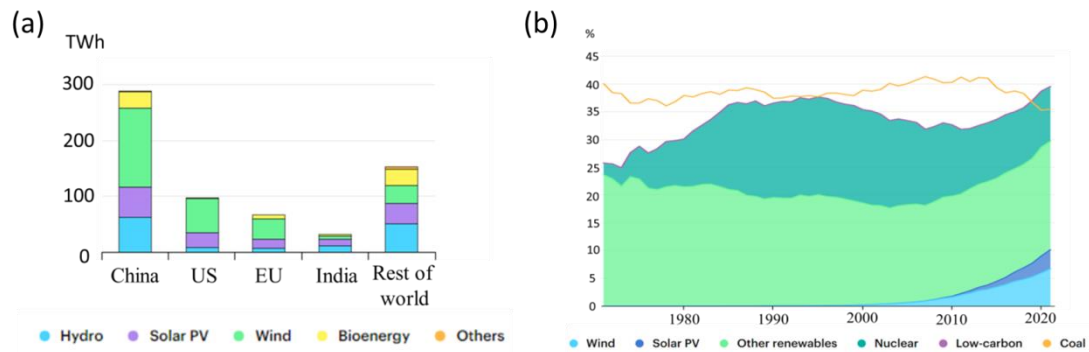almost half of the global increase in renewable electricity in 2021, followed by the United States, the European Union and India. Increases in electricity generation from all renewable sources should push the share of renewables in the electricity generation mix to an all-time high of 30% in 2021. Combined with nuclear, low-carbon sources of generation well and truly exceed output from the world's coal plants in 2021.[12] The "Revolutionary Strategy for Energy Production and Consumption" issued by China's National Development and Reform Commission and the National Energy Administration clearly states that by 2030, the country's new energy demand will be met mainly by clean energy. [13] The European Commission released a roadmap for energy independence, increasing the development and utilization of renewable energy, and striving to get rid of its dependence on Russia's energy imports by 2030. [14] Reuters also reported that the White House hopes to capitalize on growing support for a national clean energy plan that would require 80 percent of the electricity on the U.S. grid to come from emissions-free renewable energy sources by 2030. [15] According to the above, renewable energy has become an indispensable part of the energy consumption structure of various countries, and will play a very important or even dominating role in the future.

1.2 energy conversion and storage technologies

Renewable electricity generation technologies like wind and solar are promising candidates to achieve a clean and sustainable energy infrastructure. However, wind and solar power are both characterized by an intermittent availability.[16,17] Thus, a large scale energy conversion and storage solution is required in order to bridge the time gap between supply and demand. [18,19] Photo/electrochemistry energy conversion and storage technologies have been recognized as one of the most promising approaches, which can convert energy to a storable form in various mediums and then be converted back when needed.[20–22] To meet the cost-effective industry requirement of energy conversion and storage, several reaction systems are extensively studied, including:

(1) electrocatalytic oxygen evolution reaction

(2) photocatalytic hydrogen/hydrogen oxide evolution reaction

(3) electrochemical batteries, i.e. LSBs

In order to realize the efficient and stable operation of the energy conversion and storage process, numerous highly demanding requirements are placed on the structure, morphology, catalytic performance, electrical conductivity, and adsorption performance of specific reactants of our materials.[23–27]

However, it is obviously difficult to meet the requirements of all aspects of the reaction with only a single material. Therefore, the design and preparation of functional nanocomposites with high performance and good stability is a key direction of future research.[28–30]

1.3 Applications

1.3.1 Oxygen evolution reaction

Among several energy conversion systems relying on electrochemical reactions, water splitting, and metal-air batteries may be the conceptually simplest. However, the water oxidation reaction or oxygen evolution reaction (OER) is the most critical and limiting reaction for all these systems to carry out their reversible process along with oxygen reduction reaction (ORR) and/or hydrogen evaluation reaction (HER) due to its four-electron

reaction process and higher reaction potential.[31,32]

In OER, molecular oxygen is produced via two different proton/electron coupled procedures which is depending on the pH values. In acidic and neutral conditions two water molecules (H_2O) are oxidized into four protons (H^+) and an oxygen molecule (O_2), while hydroxyl groups (OH^-) are oxidized and transformed into H_2O and O_2 in basic environments. The equilibrium half-cell potentials ($E^°_a$) at 1 atm and 25 °C for OER are shown as follows:

$4\ OH^- \rightarrow 2\ H_2O\ (l) + O_2\ (g) + 4\ e^-$ $E^°_a = 0.404$ V alkaline solution

$2\ H_2O\ (l) \rightarrow 4H^+ + O_2\ (g) + 4\ e^-$ $E^°_a = 1.23$ V acidic solution
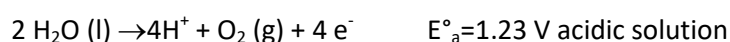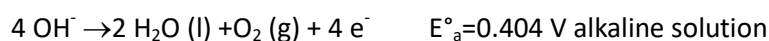
In the past several decades, various kinds of catalysts have been employed to investigate the OER performance. Up till now, noble-metal-based materials (Ru, Ir) are still placed at the top in terms of their stability in all pH values despite the fair activity towards OER.[33,34] However, the high price and scarcity of these elements become a major bottlenecks in practical applications. Considerable research efforts have been devoted to identify and optimize alternative materials with better OER activity. Currently, a large number of catalysts have been developed, including noble-metal-based, carbon-based materials (e.g. graphene and graphene oxide, CNT, nitrogen-doped carbon, g-C_3N_4, etc.),[35–37] metal alloys, oxides and oxyhydroxides of earth abundant metals (e.g. Mn, Co, Ni, and Fe, etc.) and their composite with carbon as well as complex ternary structures of spinel and perovskite systems.[38–41] To evaluate the performance of electrocatalysts towards OER, there are several other parameters that influence the reaction significantly, namely, onset/over potential, tafel slope, stability, and current density.

1.3.2 Photocatalytic H_2 generation

Solar energy conversion is one of the sustainable technologies that tackle the global warming and energy crisis. Photocatalytic hydrogen (H_2) production is a clean technology to produce an eco-friendly fuel with the help of semiconductor NPs and the abundant sunlight irradiation.[42–44] Fig 1.3.a shows a scheme of the HER by photocatalysts. The photocatalytic reaction occurring on the semiconductor photocatalysts can be divided into three parts: (1) absorving photons with energy exceeding that of the photocatalyst's band gap, generating electron and hole pairs; (2) separating carriers by migration in the semiconductor

21

photocatalyst; and (3) reaction between these carriers and H_2O.[45–47] Simultaneously, electron–hole pairs will recombine with each other, reducing the process efficiency. As shown in Figure 1.3.b, while photocatalysts are involved in hydrogen evolution, the lowest position of the conduction band (CB) should be lower than the reduction position of H_2O/H_2, while the position of the valence band (VB) should be higher than the potential of H_2O/O_2.
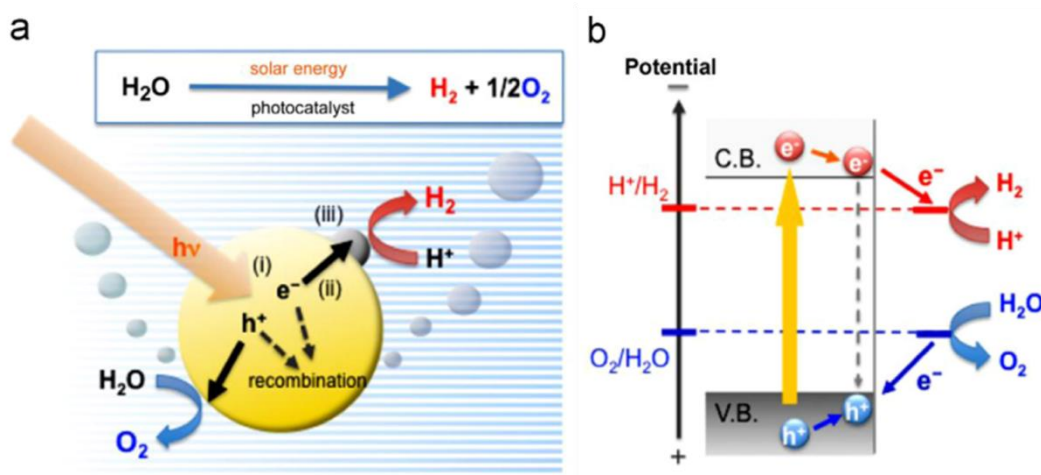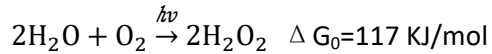

Figure 1.3. Schematic illustration of hydrogen evolution over photocatalysts.[48]

Over the last several decades, photocatalysis have been shown a promising method for H_2 production. Photocatalysts such as titanium oxide (TiO_2), graphitic-carbon nitride (g-C_3N_4) and cadmium sulfide (CdS) are the most widely explored in recent decades for water splitting.[48–50] Even though the principles controlling photocatalytic activity in the developed semiconductors were identified, several aspects remain unclear. Therefore, practical applications and the commercialization of photocatalytic H_2 production require further research.[43,50,51] In order to improve the photocatalytic HER performance, there are three basic paths we can choose from: (1) Modulation of photocatalyst morphology, band gap structure, and composition, (2) Construction of heterojunctions to facilitate charge separation, (3) Introduce a cocatalyst on the surface of the photocatalyst.

1.3.3 Photocatalytic H_2O_2

In the past few years, photochemical H_2O_2 production is attracting great interest as an alternative solar fuel. [52,53]Solar-driven H_2O_2 synthesis presents unique features of remarkable sustainability and environmental friendliness, as compared to the traditional anthraquinone

process and direct synthesis method.[54,55] As in the case of the hydrogen photogeneration, typically, reactions on photocatalysts include three main steps (Figure 1.4.a). In the first step, photons are absorbed on a semiconductor photocatalyst. If the energy of the photons is greater than the band gap of the photocatalyst, the electrons in the VB are excited to the CB, while holes are left in the VB. This step, therefore, creates the negatively charged electron (e^-) and positively charged hole (h^+) pairs. In the second step, the photoinduced e^- and h^+ separate and migrate to the photocatalyst surface. In the third step, the charge carriers react with the chemical species on the surface of the photocatalyst. Meanwhile, the photoinduced e^- and h^+ also recombine with each other without participating in any chemical reactions.[56-58]

Figure 1.4. (a) Photoexcitation and charge-decay pathway in a photocatalyst. (b) Schematic representation of the photocatalytic system for the production of H_2O_2.[58]

At present, it is accepted that H_2O_2 can be generated through either an indirect sequential two-step single-electron reduction ($O_2 \rightarrow *O_2 \rightarrow H_2O_2$) or a direct one-step two-electron reduction on the CB of photocatalyst while a water oxidation reaction takes place by injection of holes from the VB of semiconductor.[58,59] A schematic representation of a photocatalytic system for H_2O_2 production is as follow:

$2 H_2O + 4 h^+ \rightarrow O_2 + 4 H^+$ (reaction in VB)

$O_2 + * \rightarrow *O_2$

$*O_2 + 2H^+ + 2e^- \rightarrow H_2O_2$ (one-step)

$*O_2 + e^- \rightarrow *O_2^-$

$*O_2^- + H^+ \rightarrow *HOO$

$*HOO + e^- \rightarrow HOO^-$

$HOO^- + H^+ \rightarrow H_2O_2$ (two-step)

$$2H_2O + O_2 \overset{hv}{\rightarrow} 2H_2O_2 \quad \triangle G_0 = 117 \text{ KJ/mol}$$

In the past few decades, several photocatalysts have been also applied for H_2O_2 generation, including titanium dioxide[60,61], graphitic carbon nitride (g-C_3N_4) [62,63] and bismuth vanadate[64]. But to improve the conversion efficiency of solar energy to chemical energy to meet the needs of industrial production is still a major challenge. There are still some key factors in the establishment of a system for the efficient photocatalytic production of H_2O_2, including (1) the optimization of the morphology and electronic band structure of the photocatalysts (2) the minimization of the recombination of photogenerated electrons and holes (3) the selectivity of the hydrogen peroxide generation reaction.

1.3.4 Lithium-sulfur batteries (LSBs)

In the 1990s, lithium−ion batteries (LIBs) were successfully commercialized and rapidly occupied the worldwide energy market until today.[65] However, with the increasing demand for device duration especially under new applied situations such as unmanned aerial vehicles, the current LIB technology has gradually reached its limit.[66] Meanwhile, lithium−sulfur batteries (LSBs) have long been propsed as a promising high-energy-density secondary battery system since their first prototype in the 1960s. The main advantages of LSBs are an ultrahigh theoretical energy density up to 2600 Wh kg^{-1} and the benefits of cathode material including low cost, Earth abundance, and environmental friendliness.[67] The basic electrochemical process of a lithium-sulfur cell is the conversion of lithium and sulfur into lithium sulfide, 16 Li + S_8 = 8 Li_2S, via the formation of a series of intermediate polysulfides, Li_2S_x (1≤ × ≤ 8), to which is associated a voltage of about 2 V and a specific capacity of 1,675 mAh g^{-1}. The discharge process is started with the ring opening of S8, followed by the PS reduction from high-order to low-order clusters ($S_8^{2-} \rightarrow S_6^{2-} \rightarrow S_4^{2-}$), and it ends with the deposition of Li_2S_2/Li_2S. The cell charging follows a reverse LiPS evolution to that in discharge.[23,24,67,68]
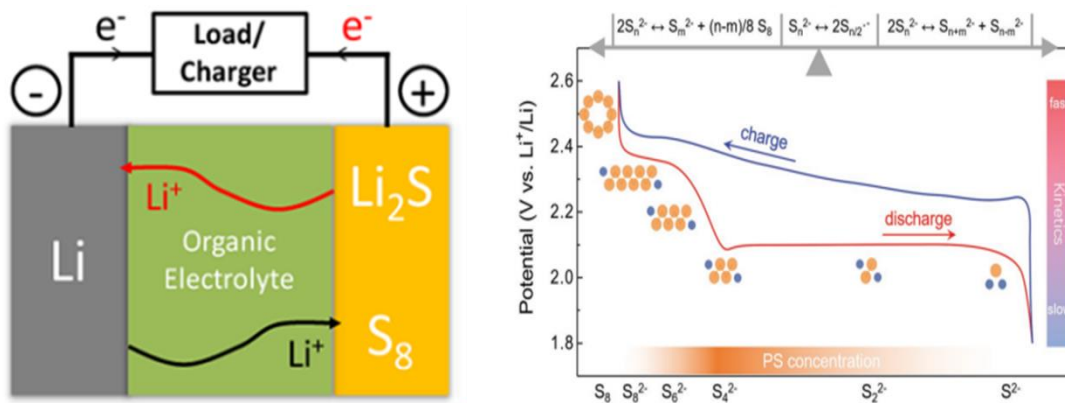
Figure 1.5. (a) Illustration of the charge (red)/discharge (black) process involved in a rechargeable Li-S cell[67], (b) The compendium of LiPS composition and evolution in Li–S batteries.[68]

In the past decade, numerous efforts have been devoted to achieving large-scale commercial application of LSBs. However, although substantial progress has been made, the road for making the sulfur-battery a practical reality is still long. Three most important issues limit its development. (1) The end products of discharging and charging are intrinsically electronic/ionic insulating to render severe kinetic difficulty. (2) Volume changes up to 80% during cycling results in heavy pressure on the cathode integrity with rapid loss of active materials. (3) The LiPS intermediates dissolve in the electrolyte and shuttle between the cathode and the anode, reducing the coulombic efficiency and cycling stability.[69–71]

1.4 The functional design of nanocomposites

Inorganic colloidal nanocrystals (NCs) are currently being employed as active components in a wide range of applications in fields such as catalysis, battery, chemical sensing and solar cells. [72–74] However, for a specific application, it is difficult to use a single nanomaterial to meet all the requirements of this application on the material's optical, electrical, magnetic, thermal, mechanical properties, catalytic properties, etc. Moreover, we also need a bridge to connect the nano-sized NPs to maximize charge transport and to ensure a proper NC dispersion. [75–77]In this context, nanocomposites have attracted wide attention during past decades because of their potential to combine desirable properties of different nanoscale building blocks to improve optical, electronic, catalytic, mechanical, and magnetic properties. For different applications, we have different requirements for the properties of various aspects of the material. Next, I will talk about the ideas of composite material design from

several specific application aspects.

(1) Electrocatalytic oxygen generation electrode materials

As an important half-reaction for electrochemical technologies such as electrolysis of water, fuel cells, etc. the OER involves a solid electrode with a high electrical conductivity, a large surface area to interact with the electrolyte and proper electrocatalytic properties, which is difficult to obtain from a single nanomaterial. Therefore, even though NCs are advantageous in catalysis due to their large specific surface area (SSA) and high exposed active sites, it is still usually needed to be combined with conductive substrate (e.g Ni foam, glass carbon, Ti plate, carbon cloth, etc.) that provide mechanical stability and contribute to the charge transport from/to the external circuit.[78–81] Moreover, in some cases NCs and substrates can interact during the reaction to further improve performance.[82,83]

(2) Photocatalytic H_2/H_2O_2 generation reaction

While photocatalytic H_2/H_2O_2 generation reactions are promising solar energy conversion pathways, their moderate conversion efficiency has always been an important factor limiting their industrialization. Several mechanisms limit the efficiency of photocatalytic reactions, including the recombination of photogenerated electrons and holes. So, large efforts have been devoted to improving the separation and transport efficiency of photogenerated electrons and holes. Construction of heterojunction nanocomposites and co-catalyst/catalyst nanocomposites are considered to be the two effective ways to solve the problem of photoelectron-hole recombination. [84,85]

Graphitic carbonitride (g-C_3N_4) with high chemical stability and low cost have received considerable attention.[86,87] Moreover, a layered structured g-C_3N_4 with polar surface is very favorable for NP loading to build heterojunction nanocomposites and co-catalyst/catalyst nanocomposites. Particular, the 2D/2D nanocomposites made of sheet-shaped particles and g-C_3N_4 offer a particularly large interface contact area that benefits charges transfer and that could highly improve photocatalytic activity.[84,88] Moreover, 0D/2D nanocomposites of metal NPs/g-C_3N_4 could also significantly increase the photocatalytic performance by transferring the photoexcited electrons to the surface of metal NPs which have the lower Fimi level.[85,89,90]

(3) Lithium-sulfur batteries

Lithium-sulfur batteries are considered to be a very promising battery technology because of their high theoretical specific capacity, abundant reserves of sulfur, low cost, and environmental friendliness. LSBs have several main problems: 1. LiPS compounds dissolve in the electrolyte, resulting in capacity loss; 2. As a non-conductive substance, sulfur has very poor conductivity, which is not conducive to the high rate performance of the battery; 3. During the charging and discharging process, the volume of sulfur expands and shrinks very greatly, which may cause damage to the battery. 4. Poor rate performance, especially at high sulfur loadings.[67,71] Due to these problems, we have to put many requirements on sulfur-host materials. (1) Good conductivity, (2) Good adsorption performance of polysulfide, (3) Spatial structure to buffer volume changes during charge and discharge, (4) Excellent catalytic performance for polysulfide conversion. Obviously this is not a problem that a single nanoparticle can solve either. Some researchers modified the NPs with high catalytic properties on structured carbon materials (carbon nanotube, graphen, etc.)[91,92] which significantly improve the capacity and rate performance. There are also some researchers who replaced the carbon material with N-doped carbon material and obtained better stability.[93,94]

1.5 The preparation of functional nanocomposites

1.5.1 Colloidal nanocrystals preparation

The solution-based synthesis of various inorganic NCs has been studied extensively. It gained much attention during the last decades and impressive progress has been made towards the synthesis of colloidal NCs with well-defined nanostructure and tailored properties.[95,96]

Figure 1.6. Colloidal synthesis Schlenk line set-up in FN group of IREC.

Colloidal synthesis routes allow producing NCs with excellent control over their properties using low amounts of energy and low capital cost equipment. Elemental, binary, ternary, quaternary and even quinary NCs can be prepared via reaction or decomposition of multiple precursors or single-molecule sources.[97,98] Reactions are usually performed under inert atmosphere in high boiling point solvents, e.g. oleylamine (OLA), octadecene (ODE), oleic acid (OA), trioctylphosphine (TOP) or ethylene glycol (EG). The typical synthesis route to produce colloidal NCs at the laboratory scale uses a Schlenk line as shown in Figure 12. Among the synthesis process, the precursors, surfactants and solvent play a crucial role in the nucleation and growth kinetics. As shown in figure 1.7, research can precisely control the size, morphology and composition of nanocrystals by adjusting the conditions of precursors, surfactants, solvents, etc.[99,100]
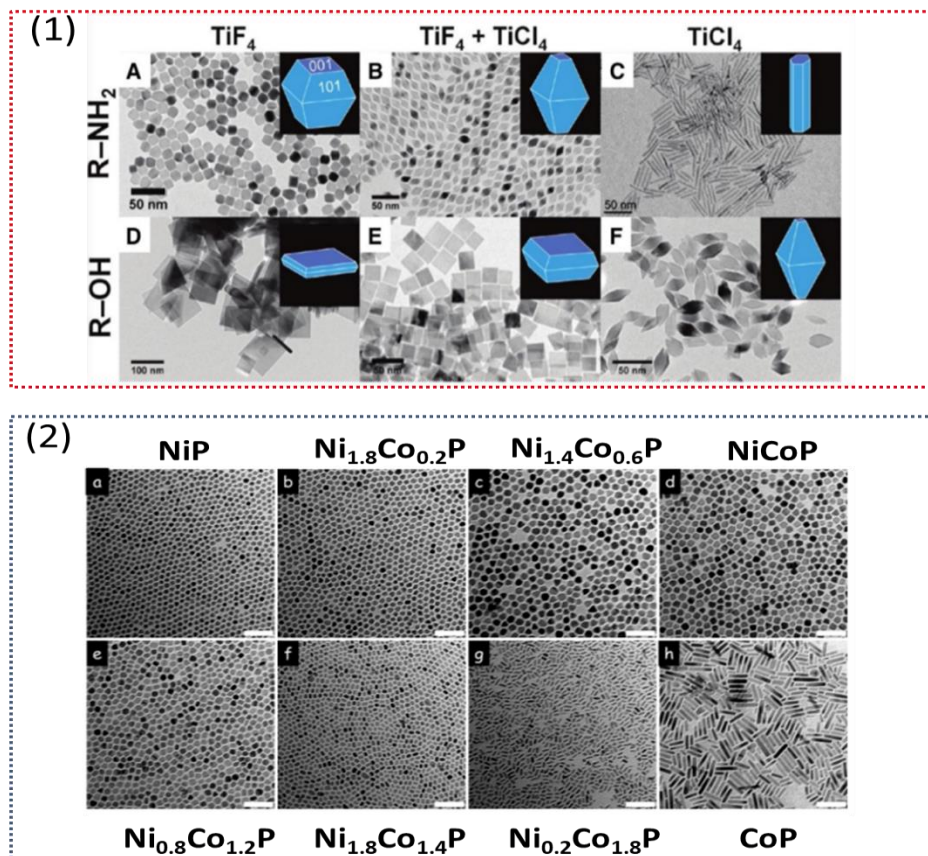

Figure 1.7. (1) TEM images of TiO$_2$ NCs synthesized using the precursor TiF$_4$ (a,d), a mixed precursor of TiF$_4$ and TiCl$_4$ (b,e), and TiCl$_4$ (c,f). Those depicted in a−c and d−f are synthesized in the presence of OLAM and 1-ODOL, respectively.[99] (2) TEM images of Ni$_{2-x}$Co$_x$P NCs with different compositions: x = 0 (a), 0.2 (b), 0.6 (c), 1 (d), 1.2 (e), 1.4 (f), 1.8 (g), and 2 (h). Scale bars = 50 nm.[100]

1.5.2 Ligands remove and exchange strategies

Surfactants, such as trioctylphosphine (TOP), oleic acid (OA), and oleylamine (OAm), are typically long hydrocarbon molecules attached to a functional headgroup and are critical components in colloidal synthesis.[101,102] These surfactants stabilize the NCs high-energy surfaces against uncontrolled growth and aggregation. Moreover, the use of surfactants may allow control of the nanocrystals shape and size by modulating the crystal growth kinetics.[103,104] Despite their essential role in the synthesis, the bulky surfactants surrounding NCs create barriers for many applications, especially for catalysis and battery, as the necessary surface active sites are blocked. Consequently, several surfactant removal methods have been reported in attempts to liberate active sites. These methods can be roughly divided into two categories:

(1) ligands removal

As shown in Figures (1-3), the ligands can be completely removed from the NCs with strong acid, strong base, oxidizing agent, reducing agent, annealing and UV-ozone/plasma treatment. The ligand removal may result in part of nanoparticle agglomeration.[105–107]

(2) ligands exchange

As shown in Fig (4-6), small carboxylate, sulfhydryl and amine ligands can be used to replace the long ligands like TOP, OAc and, OAm. This method can preserve the morphology of NPs wellbut may be inefective for strongly bound surfactants like phosphines.[108–110]
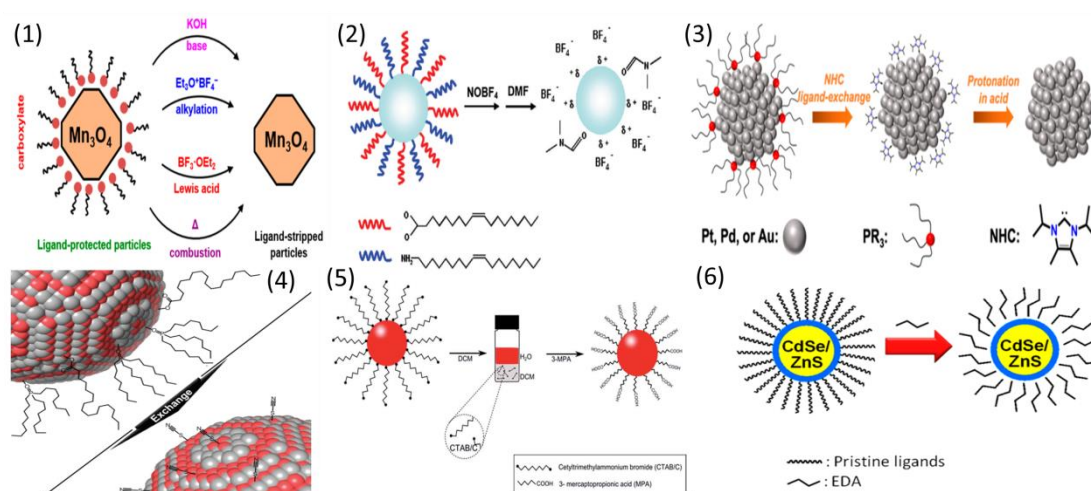

Figure 1. (a) Schematic of surface treatments to remove ligands from metal oxide surfaces for electrocatalysis. Four popular ligand removal strategies are displayed: bases (potassium hydroxide)

displace ligands, for example, with hydroxyl groups; displace carboxylate ligands by esterification; Lewis acids form dative bonds with ligands; and heating in Ar (400°C) removes ligands by combustion. [105] (b) Schematic illustration of the ligand-exchange process with NOBF$_4$.[106] (c) Schematic of NHC-mediated surfactant removal for colloidal NCs.[107] (d) Schematic of ligand exchange with ammonium thiocyanate (NH$_4$SCN).[108] (e) Schematic illustration of gold nanoparticle surface modification via a two-step ligand exchange reaction with CTAB and MPA. [109] (f) Scheme of EDA-mediated ligand exchange on an oleophilic NC surface.[110]

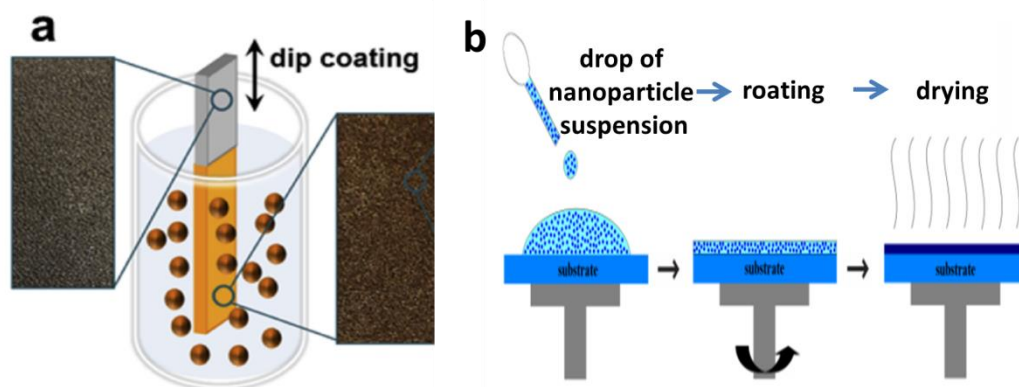## 1.5.3 Dip coating and Spin coating methods

Figure 1.7. Schematic illustration of the dip coating and spin coating

Nanocoating is an important method to realize functionalized nanodevices, which are widely used in the preparation of catalytic electrodes, battery electrodes, solar cell plates, functional ceramics, and various aspects of biomedicine and industry. In order to realize the functionalization of the substrate, we often need to modify it with different NPs.[111,112] There are two main methods of coating NPs that we commonly use, one is dip coating and the other is spin coating. For substrates with 3D structures, we usually use dip coating, and for 2D surface coatings, we usually choose spin coating. Regardless of the coating method, if you want to get a uniform coating, the coating solutions have high requirements. (1) Excellent dispersion of NPs in ink solution. Researchers often use NP surface modification methods, such as adding short-chain carboxyl, hydroxyl or amino groups on the surface of NP to achieve uniform dispersion in aqueous solutions (2) Wettability of the coating solution to the substrate. Surface modification of substrates, such as removal of oxide layer on the surface

of NF, passivation of metal and carbon material substrates, and hydroxylation of battery separators are widely used. (3) Sufficient affinity between NPs and substrate material to ensure coating stability. Using hydrogen bonding or electrostatic force to assist the coating, adding binders such as Nafion and PVDF to the ink solution, and annealing after coating are all good solutions.[112–114]

1.5.4 Electrostatic self-assembly method

Electrostatic self-assembly refers to the technology in which basic structural units (molecules, nanomaterials, micrometers or larger-scale substances) spontaneously form ordered structures under the action of electrostatic forces. Electrostatic self-assembly is an important method for constructing nanocomposites.[115,116] The basic principle of this technique is straightforward: Two oppositely charged particles, suspended in a fluid, will attract. So when our two materials meet these two conditions (1) can be uniformly dispersed in the same solvent, (2) the surface has opposite electrical properties, we can use electrostatic self-assembly to prepare nanocomposites. When two materials are electrically opposite in solution, we can assemble directly, whereas we have to surface-modify one of the materials before assembling. As shown in fig 1.9, the PEI and the HNO_3 was used to change the surface electrical properties of carbon tubes and Fe_3O_4 NPs before assembling.[117,118]
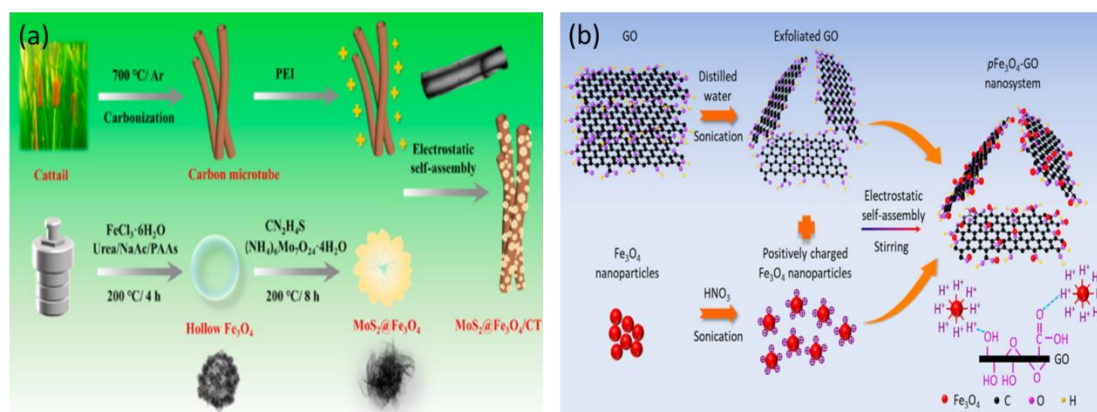

Figure 1.9. (a) Schematic illustration of the preparation of $MoS_2@Fe_3O_4/CT$,[117] (b) schematic illustration of the synthetic route of pFe_3O_4-GO nanosystem.[118]

1.5.5 In situ growth method

Whether it is NP coating, or the self-assembly, it is inevitable to carry out tedious processes

such as ligand treatment and surface modification of NPs and then assembly or coating. Moreover, due to the presence of surfactants, it will also lead to problems such as increased contact resistance and masked active sites.[119,120] Compared with coating method and self-assembly method, the in situ growth of NPs on conductive substrate or other materials to form functional nanocomposites are more desirable due to the following several advantages：(1) In situ synthesis process avoids the posterior surface modification and deposition process which simplified the production process and decrease the cost. (2) Expose more active sites on the surface of nanocomposites due to the less use of surfactants and binders. (3) The contact between two materials is firmer and closer which result in less contact resistance and make the nanocomposites more stable. [121–123]

Common in situ growth methods include the hydrothermal method and electrodeposition method, which were widely used in the preparation of conductive electrodes.[124–126] Particular, for semiconductor materials, in situ photo-oxidation or reduction can also be used to synthesize nanocomposite photocatalysts.[127,128] Moreover, for some stable materials such as carbon materials or g-C_3N_4, we can also achieve in situ synthesis in high temperature colloidal synthesis.[129,130]

1.6 Objectives

This thesis aims to design and produce the functional nanocomposites in energy conversion and storage field. The designed nanocomposites are targeted to be low cost and non-toxic, more efficient in energy conversion and storage process and more stable during the long cycle test. In the process of achieving these goals, we will encounter many difficulties including controllable synthesis of NPs, surface modification of NPs and fabrication of nanocomposites. To overcome all these challenges, several specific objectives are identified as fellow:

(1) To develop a large size of NPs coated metal substrate electrode with high electrochemical transfer efficiency and long stability for electrocatalytic OER.

(2) To explore the role of 2D/2D heterojunctions in photogenerated electron and hole separation and their impact on photocatalytic HER performance.

(3) To improve the photocatalytic H_2O_2 generation performance of g-C_3N_4 by promoting charge separation and increasing the selectivity of the reaction.

(4) To develop NP-coated hollow structured g-C_3N_4 that can effectively buffer the volume change during charge/discharge process, reduce polysulfide shuttling, accelerate the catalytic conversion of polysulfide, thus enhancing cycling stability and rate capability.

1.7 References

[1]   I. Dincer, Renewable energy and sustainable development: a crucial review, Renew. Sustain. Energy Rev. 4 (2000) 157–175.

[2]   N.L. Panwar, S.C. Kaushik, S. Kothari, Role of renewable energy sources in environmental protection: A review, Renew. Sustain. Energy Rev. 15 (2011) 1513–1524.

[3]   O. Ellabban, H. Abu-Rub, F. Blaabjerg, Renewable energy resources: Current status, future prospects and their enabling technology, Renew. Sustain. Energy Rev. 39 (2014) 748–764.

[4]   D. Gielen, F. Boshell, D. Saygin, M.D. Bazilian, N. Wagner, R. Gorini, The role of renewable energy in the global energy transformation, Energy Strateg. Rev. 24 (2019) 38–50.

[5]   Y. Ghandriz, S.M.Z. Noorbakhsh, R. Gavagsaz-Ghoachani, M. Phattanasak, Effect of wide observation of nature in renewable energy engineering education, in: 2021 Res. Invent. Innov. Congr. Innov. Electr. Electron., IEEE, 2021: pp. 193–198.

[6]   A.F. Zobaa, R.C. Bansal, Handbook of renewable energy technology, World Scientific, 2011.

[7]   R. Gross, M. Leach, A. Bauen, Progress in renewable energy, Environ. Int. 29 (2003) 105–122.

[8]   P. Jiang, Y. Van Fan, J.J. Klemeš, Impacts of COVID-19 on energy demand and consumption: Challenges, lessons and emerging opportunities, Appl. Energy. 285 (2021) 116441.

[9]   J. Tian, L. Yu, R. Xue, S. Zhuang, Y. Shan, Global low-carbon energy transition in the

post-COVID-19 era, Appl. Energy. 307 (2022) 118205.

[10]   M.E. BALBAA, M. ESHOV, N. ISMAILOVA, The Impacts of Russian-Ukrainian War on the Global Economy, (n.d.).

[11]   M.A. Ruiz Estrada, Who can Damage Severely to the World Economy? COVID-19 vs. Russian-Ukrainian War, COVID-19 vs. Russ. War (March 22, 2022). (2022).

[12]   IEA Global Energy Review 2021, https://www.iea.org/ reports/ global-energy-review-2021/renewables (Accessed April 25, 2022)

[13]   China national energy administration http://www.nea.gov.cn/2021-06/18/c_ 1310015819.htm (Accessed April 25, 2022)

[14]   Interreg Europ, REPowerEU: Joint European Action for more affordable, secure and sustainable energy   https://www.interregeurope.eu (Accessed April 25, 2022)

[15]   Reuters, EXCLUSIVE White House backs 2030 milestone on path to net zero grid, https://www.reuters.com/business/sustainable-business (Accessed April 25, 2022)

[16]   D. Anderson, M. Leach, Harvesting and redistributing renewable energy: on the role of gas and electricity grids to overcome intermittency through the generation and storage of hydrogen, Energy Policy. 32 (2004) 1603–1614.

[17]   P. Moriarty, D. Honnery, Intermittent renewable energy: The only future source of hydrogen?, Int. J. Hydrogen Energy. 32 (2007) 1616–1624.

[18]   Q. Zhang, E. Uchaker, S.L. Candelaria, G. Cao, Nanomaterials for energy conversion and storage, Chem. Soc. Rev. 42 (2013) 3127–3171.

[19]   J. Kim, S. Sengodan, S. Kim, O. Kwon, Y. Bu, G. Kim, Proton conducting oxides: A review of materials and applications for renewable energy conversion and storage, Renew. Sustain. Energy Rev. 109 (2019) 606–618.

[20]   H. Zhang, Y. Lu, W. Han, J. Zhu, Y. Zhang, W. Huang, Solar energy conversion and utilization: Towards the emerging photo-electrochemical devices based on perovskite photovoltaics, Chem. Eng. J. 393 (2020) 124766.

[21]   R. Gao, D. Yan, Recent development of Ni/Fe-based micro/nanostructures toward photo/electrochemical water oxidation, Adv. Energy Mater. 10 (2020) 1900954.

[22]   S.D. Tilley, Recent advances and emerging trends in photo-electrochemical solar energy conversion, Adv. Energy Mater. 9 (2019) 1802877.

[23] J. Kim, D. Lee, H. Jung, Y. Sun, J. Hassoun, B. Scrosati, An Advanced Lithium-Sulfur Battery, Adv. Funct. Mater. 23 (2013) 1076–1080.

[24] M. Zhao, B.-Q. Li, X.-Q. Zhang, J.-Q. Huang, Q. Zhang, A perspective toward practical lithium–sulfur batteries, ACS Cent. Sci. 6 (2020) 1095–1104.

[25] R. Shen, D. Ren, Y. Ding, Y. Guan, Y.H. Ng, P. Zhang, X. Li, Nanostructured CdS for efficient photocatalytic H2 evolution: A review, Sci. China Mater. 63 (2020) 2153–2188.

[26] D.E. Atkins, J.S. Brown, A.L. Hammond, A review of the open educational resources (OER) movement: Achievements, challenges, and new opportunities, Creative common Mountain View, 2007.

[27] M.-I. Jamesh, X. Sun, Recent progress on earth abundant electrocatalysts for oxygen evolution reaction (OER) in alkaline medium to achieve efficient water splitting–A review, J. Power Sources. 400 (2018) 31–68.

[28] H. Yuan, L. Kong, T. Li, Q. Zhang, A review of transition metal chalcogenide/graphene nanocomposites for energy storage and conversion, Chinese Chem. Lett. 28 (2017) 2180–2194.

[29] I. V Lightcap, P. V Kamat, Graphitic design: prospects of graphene-based nanocomposites for solar energy conversion, storage, and sensing, Acc. Chem. Res. 46 (2013) 2235–2243.

[30] M. Ismael, A review on graphitic carbon nitride (g-C3N4) based nanocomposites: synthesis, categories, and their application in photocatalysis, J. Alloys Compd. 846 (2020) 156446.

[31] M. Tahir, L. Pan, F. Idrees, X. Zhang, L. Wang, J.-J. Zou, Z.L. Wang, Electrocatalytic oxygen evolution reaction for energy conversion and storage: a comprehensive review, Nano Energy. 37 (2017) 136–157.

[32] T. Reier, H.N. Nong, D. Teschner, R. Schlögl, P. Strasser, Electrocatalytic oxygen evolution reaction in acidic environments–reaction mechanisms and catalysts, Adv. Energy Mater. 7 (2017) 1601275.

[33] T. Reier, M. Oezaslan, P. Strasser, Electrocatalytic oxygen evolution reaction (OER) on Ru, Ir, and Pt catalysts: a comparative study of nanoparticles and bulk materials, Acs

Catal. 2 (2012) 1765–1772.

[34] A. Zagalskaya, V. Alexandrov, Mechanistic study of IrO2 dissolution during the electrocatalytic oxygen evolution reaction, J. Phys. Chem. Lett. 11 (2020) 2695–2700.

[35] Y. Jiao, Y. Zheng, M. Jaroniec, S.Z. Qiao, Origin of the electrocatalytic oxygen reduction activity of graphene-based catalysts: a roadmap to achieve the best performance, J. Am. Chem. Soc. 136 (2014) 4394–4403.

[36] X. Liu, W. Yang, L. Chen, Z. Liu, L. Long, S. Wang, C. Liu, S. Dong, J. Jia, Graphitic carbon nitride (g-C3N4)-derived bamboo-like carbon nanotubes/Co nanoparticles hybrids for highly efficient electrocatalytic oxygen reduction, ACS Appl. Mater. Interfaces. 12 (2020) 4463–4472.

[37] J. Ban, G. Xu, L. Zhang, G. Xu, L. Yang, Z. Sun, D. Jia, Efficient Co–N/PC@ CNT bifunctional electrocatalytic materials for oxygen reduction and oxygen evolution reactions based on metal–organic frameworks, Nanoscale. 10 (2018) 9077–9086.

[38] Y. Bi, Z. Cai, D. Zhou, Y. Tian, Y. Kuang, Y. Li, X. Sun, X. Duan, Understanding the incorporating effect of Co2+/Co3+ in NiFe-layered double hydroxide for electrocatalytic oxygen evolution reaction, J. Catal. 358 (2018) 100–107.

[39] B.Y. Guan, L. Yu, X.W. Lou, General Synthesis of Multishell Mixed-Metal Oxyphosphide Particles with Enhanced Electrocatalytic Activity in the Oxygen Evolution Reaction, Angew. Chemie Int. Ed. 56 (2017) 2386–2389.

[40] L. Negahdar, F. Zeng, S. Palkovits, C. Broicher, R. Palkovits, Mechanistic aspects of the electrocatalytic oxygen evolution reaction over Ni– Co oxides, ChemElectroChem. 6 (2019) 5588–5595.

[41] H. Wang, M. Zhou, P. Choudhury, H. Luo, Perovskite oxides as bifunctional oxygen electrocatalysts for oxygen evolution/reduction reactions–A mini review, Appl. Mater. Today. 16 (2019) 56–71.

[42] J.S. Im, S.-J. Park, T. Kim, Y.-S. Lee, Hydrogen storage evaluation based on investigations of the catalytic properties of metal/metal oxides in electrospun carbon fibers, Int. J. Hydrogen Energy. 34 (2009) 3382–3388.

[43] G. Zhang, Z. Lan, X. Wang, Conjugated polymers: catalysts for photocatalytic hydrogen evolution, Angew. Chemie Int. Ed. 55 (2016) 15712–15727.

[44] J. Kosco, M. Bidwell, H. Cha, T. Martin, C.T. Howells, M. Sachs, D.H. Anjum, S. Gonzalez Lopez, L. Zou, A. Wadsworth, Enhanced photocatalytic hydrogen evolution from organic semiconductor heterojunction nanoparticles, Nat. Mater. 19 (2020) 559–565.

[45] A.A. Ismail, D.W. Bahnemann, Photochemical splitting of water for hydrogen production by photocatalysis: A review, Sol. Energy Mater. Sol. Cells. 128 (2014) 85–101.

[46] D. Ventura-Espinosa, S. Sabater, A. Carretero-Cerdán, M. Baya, J.A. Mata, High production of hydrogen on demand from silanes catalyzed by iridium complexes as a versatile hydrogen storage system, ACS Catal. 8 (2018) 2558–2566.

[47] Y. Ma, X. Dong, Y. Wang, Y. Xia, Decoupling Hydrogen and Oxygen Production in Acidic Water Electrolysis Using a Polytriphenylamine-Based Battery Electrode, Angew. Chemie Int. Ed. 57 (2018) 2904–2908.

[48] X. Chen, J. Zhang, X. Fu, M. Antonietti, X. Wang, Fe-g-C3N4-catalyzed oxidation of benzene to phenol using hydrogen peroxide and visible light, J. Am. Chem. Soc. 131 (2009) 11658–11659.

[49] L. Cheng, Q. Xiang, Y. Liao, H. Zhang, CdS-based photocatalysts, Energy Environ. Sci. 11 (2018) 1362–1391.

[50] A. Fujishima, K. Honda, Electrochemical photolysis of water at a semiconductor electrode, Nature. 238 (1972) 37–38.

[51] Y. Zhang, Y.-J. Heo, J.-W. Lee, J.-H. Lee, J. Bajgai, K.-J. Lee, S.-J. Park, Photocatalytic hydrogen evolution via water splitting: A short review, Catalysts. 8 (2018) 655.

[52] J.M. Campos-Martin, G. Blanco-Brieva, J.L.G. Fierro, Wasserstoffperoxid-Synthese: Perspektiven jenseits des Anthrachinon-Verfahrens, Angew. Chemie. 118 (2006) 7116–7139.

[53] Z. Tian, C. Han, Y. Zhao, W. Dai, X. Lian, Y. Wang, Y. Zheng, Y. Shi, X. Pan, Z. Huang, Efficient photocatalytic hydrogen peroxide generation coupled with selective benzylamine oxidation over defective ZrS3 nanobelts, Nat. Commun. 12 (2021) 1–10.

[54] T. Mahvelati-Shamsabadi, H. Fattahimoghaddam, B.-K. Lee, S. Bae, J. Ryu, Synthesis of hexagonal rosettes of g-C3N4 with boosted charge transfer for the enhanced

visible-light photocatalytic hydrogen evolution and hydrogen peroxide production, J. Colloid Interface Sci. 597 (2021) 345–360.

[55] S. Yang, A. Verdaguer-Casadevall, L. Arnarson, L. Silvioli, V. Čolić, R. Frydendal, J. Rossmeisl, I. Chorkendorff, I.E.L. Stephens, Toward the Decentralized Electrochemical Production of H2O2: A Focus on the Catalysis, ACS Catal. 8 (2018) 4064–4081.

[56] X. Zeng, Y. Liu, Y. Kang, Q. Li, Y. Xia, Y. Zhu, H. Hou, M.H. Uddin, T.R. Gengenbach, D. Xia, C. Sun, D.T. Mccarthy, A. Deletic, J. Yu, X. Zhang, Simultaneously Tuning Charge Separation and Oxygen Reduction Pathway on Graphitic Carbon Nitride by Polyethylenimine for Boosted Photocatalytic Hydrogen Peroxide Production, ACS Catal. 10 (2020) 3697–3706.

[57] Y. Shang, X. Xu, B. Gao, S. Wang, X. Duan, Single-atom catalysis in advanced oxidation processes for environmental remediation, Chem. Soc. Rev. 50 (2021) 5281–5322.

[58] H. Hou, X. Zeng, X. Zhang, Production of hydrogen peroxide by photocatalytic processes, Angew. Chemie Int. Ed. 59 (2020) 17356–17376.

[59] R. Du, K. Xiao, B. Li, X. Han, C. Zhang, X. Wang, Y. Zuo, P. Guardia, J. Li, J. Chen, Controlled oxygen doping in highly dispersed Ni-loaded g-C3N4 nanotubes for efficient photocatalytic H2O2 production, Chem. Eng. J. (2022) 135999.

[60] D. Tsukamoto, A. Shiro, Y. Shiraishi, Y. Sugano, S. Ichikawa, S. Tanaka, T. Hirai, Photocatalytic H2O2 Production from Ethanol/O2 System Using TiO2 Loaded with Au–Ag Bimetallic Alloy Nanoparticles, ACS Catal. 2 (2012) 599–603.

[61] M. Teranishi, S. Naya, H. Tada, In situ liquid phase synthesis of hydrogen peroxide from molecular oxygen using gold nanoparticle-loaded titanium (IV) dioxide photocatalyst, J. Am. Chem. Soc. 132 (2010) 7850–7851.

[62] H. Ou, C. Tang, X. Chen, M. Zhou, X. Wang, Solvated electrons for photochemistry syntheses using conjugated carbon nitride polymers, ACS Catal. 9 (2019) 2949–2955.

[63] S. Zhao, T. Guo, X. Li, T. Xu, B. Yang, X. Zhao, Carbon nanotubes covalent combined with graphitic carbon nitride for photocatalytic hydrogen peroxide production under visible light, Appl. Catal. B Environ. 224 (2018) 725–732.

[64] H. Hirakawa, S. Shiota, Y. Shiraishi, H. Sakamoto, S. Ichikawa, T. Hirai, Au nanoparticles supported on BiVO4: effective inorganic photocatalysts for H2O2

production from water and O2 under visible light, ACS Catal. 6 (2016) 4976–4982.

[65]   A. Manthiram, An Outlook on Lithium Ion Battery Technology, ACS Cent. Sci. 3 (2017) 1063–1069.

[66]   G. Zubi, R. Dufo-López, M. Carvalho, G. Pasaoglu, The lithium-ion battery: State of the art and future perspectives, Renew. Sustain. Energy Rev. 89 (2018) 292–308.

[67]   A. Manthiram, Y. Fu, Y.-S. Su, Challenges and Prospects of Lithium–Sulfur Batteries, Acc. Chem. Res. 46 (2013) 1125–1134.

[68]   G. Li, S. Wang, Y. Zhang, M. Li, Z. Chen, J. Lu, Revisiting the Role of Polysulfides in Lithium–Sulfur Batteries, Adv. Mater. 30 (2018) 1705590.

[69]   L. Chen, L.L. Shaw, Recent advances in lithium–sulfur batteries, J. Power Sources. 267 (2014) 770–783.

[70]   Y. Hu, W. Chen, T. Lei, Y. Jiao, J. Huang, A. Hu, C. Gong, C. Yan, X. Wang, J. Xiong, Strategies toward High-Loading Lithium–Sulfur Battery, Adv. Energy Mater. 10 (2020) 2000082.

[71]   J. He, A. Manthiram, A review on the status and challenges of electrocatalysts in lithium-sulfur batteries, Energy Storage Mater. 20 (2019) 55–70.

[72]   D. V Talapin, J.-S. Lee, M. V Kovalenko, E. V Shevchenko, Prospects of Colloidal Nanocrystals for Electronic and Optoelectronic Applications, Chem. Rev. 110 (2010) 389–458.

[73]   M. Nasilowski, B. Mahler, E. Lhuillier, S. Ithurria, B. Dubertret, Two-Dimensional Colloidal Nanocrystals, Chem. Rev. 116 (2016) 10934–10982.

[74]   J. van Embden, A.S.R. Chesman, J.J. Jasieniak, The Heat-Up Synthesis of Colloidal Nanocrystals, Chem. Mater. 27 (2015) 2246–2285.

[75]   I. Siró, D. Plackett, Microfibrillated cellulose and new nanocomposite materials: a review, Cellulose. 17 (2010) 459–494.

[76]   V. Viswanathan, T. Laha, K. Balani, A. Agarwal, S. Seal, Challenges and advances in nanocomposite processing techniques, Mater. Sci. Eng. R Reports. 54 (2006) 121–285.

[77]   L.L. Beecroft, C.K. Ober, Nanocomposite Materials for Optical Applications, Chem. Mater. 9 (1997) 1302–1317.

[78]   G. Ren, Q. Hao, J. Mao, L. Liang, H. Liu, C. Liu, J. Zhang, Ultrafast fabrication of nickel sulfide film on Ni foam for efficient overall water splitting, Nanoscale. 10 (2018) 17347–17353.

[79]   M. Wu, Y. Li, J. Du, C. Tao, Z. Liu, Oxygen-Evolution Activity of p–n Heterojunction NiO–SnO2 Ceramic on Ti Substrate Fabricated Using a Simple Layer-by-Layer Method, ACS Omega. 5 (2020) 22652–22660.

[80]   H. Rasouli, M.G. Hosseini, M.M. Hosseini, Ta2O5-incorporated in photoinduced electrocatalyst of TiO2-RuO2 decorated by PPy-NrGO nanocomposite for boosting overall water splitting, J. Colloid Interface Sci. 582 (2021) 254–269.

[81]   F.R. Costa, L.M. Da Silva, Fabrication and characterization of a porous gas-evolving anode constituted of lead dioxide microfibers electroformed on a carbon cloth substrate, Electrochim. Acta. 70 (2012) 365–374.

[82]   T. Reier, D. Teschner, T. Lunkenbein, A. Bergmann, S. Selve, R. Kraehnert, R. Schlögl, P. Strasser, Electrocatalytic Oxygen Evolution on Iridium Oxide: Uncovering Catalyst-Substrate Interactions and Active Iridium Oxide Species, J. Electrochem. Soc. 161 (2014) F876–F882.

[83]   L. Zhang, F. Mao, L.R. Zheng, H.F. Wang, X.H. Yang, H.G. Yang, Tuning Metal Catalyst with Metal–C3N4 Interaction for Efficient CO2 Electroreduction, ACS Catal. 8 (2018) 11035–11041.

[84]   Y. Qin, H. Li, J. Lu, Y. Feng, F. Meng, C. Ma, Y. Yan, M. Meng, Synergy between van der waals heterojunction and vacancy in ZnIn2S4/g-C3N4 2D/2D photocatalysts for enhanced photocatalytic hydrogen evolution, Appl. Catal. B Environ. 277 (2020) 119254.

[85]   J. Xu, Y. Qi, L. Wang, In situ derived Ni2P/Ni encapsulated in carbon/g-C3N4 hybrids from metal–organic frameworks/g-C3N4 for efficient photocatalytic hydrogen evolution, Appl. Catal. B Environ. 246 (2019) 72–81.

[86]   J. Fu, J. Yu, C. Jiang, B. Cheng, g-C3N4-Based heterostructured photocatalysts, Adv. Energy Mater. 8 (2018) 1701503.

[87]   J. Wen, J. Xie, X. Chen, X. Li, A review on g-C3N4-based photocatalysts, Appl. Surf. Sci. 391 (2017) 72–123.

[88] Y. Jiang, H.-Y. Chen, J.-Y. Li, J.-F. Liao, H.-H. Zhang, X.-D. Wang, D.-B. Kuang, Z-Scheme 2D/2D Heterojunction of CsPbBr3/Bi2WO6 for Improved Photocatalytic CO2 Reduction, Adv. Funct. Mater. 30 (2020) 2004293.

[89] C. Wang, K. Wang, Y. Feng, C. Li, X. Zhou, L. Gan, Y. Feng, H. Zhou, B. Zhang, X. Qu, H. Li, J. Li, A. Li, Y. Sun, S. Zhang, G. Yang, Y. Guo, S. Yang, T. Zhou, F. Dong, K. Zheng, L. Wang, J. Huang, Z. Zhang, X. Han, Co and Pt Dual-Single-Atoms with Oxygen-Coordinated Co–O–Pt Dimer Sites for Ultrahigh Photocatalytic Hydrogen Evolution Efficiency, Adv. Mater. 33 (2021) 2003327.

[90] H. Cai, B. Wang, L. Xiong, G. Yang, L. Yuan, J. Bi, X. Yu, X. Zhang, S. Yang, S. Yang, Bridging effect of Co heteroatom between g-C3N4 and Pt NPs for enhanced photocatalytic hydrogen evolution, Chem. Eng. J. 394 (2020) 124964.

[91] R. Fang, K. Chen, L. Yin, Z. Sun, F. Li, H.-M. Cheng, The Regulating Role of Carbon Nanotubes and Graphene in Lithium-Ion and Lithium–Sulfur Batteries, Adv. Mater. 31 (2019) 1800863.

[92] Z. Gao, Z. Xue, Y. Miao, B. Chen, J. Xu, H. Shi, T. Tang, X. Zhao, TiO2@Porous carbon nanotubes modified separator as polysulfide barrier for lithium-sulfur batteries, J. Alloys Compd. 906 (2022) 164249.

[93] Y. Li, G. Chen, J. Mou, Y. Liu, S. Xue, T. Tan, W. Zhong, Q. Deng, T. Li, J. Hu, C. Yang, K. Huang, M. Liu, Cobalt single atoms supported on N-doped carbon as an active and resilient sulfur host for lithium–sulfur batteries, Energy Storage Mater. 28 (2020) 196–204.

[94] Z. Li, Z. Xiao, S. Wang, Z. Cheng, P. Li, R. Wang, Engineered Interfusion of Hollow Nitrogen-Doped Carbon Nanospheres for Improving Electrochemical Behavior and Energy Density of Lithium–Sulfur Batteries, Adv. Funct. Mater. 29 (2019) 1902322.

[95] M. V Kovalenko, L. Manna, A. Cabot, Z. Hens, D. V Talapin, C.R. Kagan, V.I. Klimov, A.L. Rogach, P. Reiss, D.J. Milliron, P. Guyot-Sionnnest, G. Konstantatos, W.J. Parak, T. Hyeon, B.A. Korgel, C.B. Murray, W. Heiss, Prospects of Nanoscience with Nanocrystals, ACS Nano. 9 (2015) 1012–1057.

[96] C. Coughlan, M. Ibáñez, O. Dobrozhan, A. Singh, A. Cabot, K.M. Ryan, Compound Copper Chalcogenide Nanocrystals, Chem. Rev. 117 (2017) 5865–6109.

[97]   M. Ibáñez, D. Cadavid, R. Zamani, N. García-Castelló, V. Izquierdo-Roca, W. Li, A. Fairbrother, J.D. Prades, A. Shavel, J. Arbiol, A. Pérez-Rodríguez, J.R. Morante, A. Cabot, Composition Control and Thermoelectric Properties of Quaternary Chalcogenide Nanocrystals: The Case of Stannite Cu2CdSnSe4, Chem. Mater. 24 (2012) 562–570.

[98]   S. Ortega, M. Ibáñez, Y. Liu, Y. Zhang, M. V Kovalenko, D. Cadavid, A. Cabot, Bottom-up engineering of thermoelectric nanomaterials and devices from solution-processed nanoparticle building blocks, Chem. Soc. Rev. 46 (2017) 3510–3528.

[99]   J. Liu, Z. Wang, J. David, J. Llorca, J. Li, X. Yu, A. Shavel, J. Arbiol, M. Meyns, A. Cabot, Colloidal Ni2−xCoxP nanocrystals for the hydrogen evolution reaction, J. Mater. Chem. A. 6 (2018) 11453–11462.

[100]   T.R. Gordon, M. Cargnello, T. Paik, F. Mangolini, R.T. Weber, P. Fornasiero, C.B. Murray, Nonaqueous Synthesis of TiO2 Nanocrystals Using TiF4 to Engineer Morphology, Oxygen Vacancy Concentration, and Photocatalytic Activity, J. Am. Chem. Soc. 134 (2012) 6751–6761.

[101]   Y. Yin, A.P. Alivisatos, Colloidal nanocrystal synthesis and the organic–inorganic interface, Nature. 437 (2005) 664–670.

[102]   M.A. Boles, D. Ling, T. Hyeon, D. V Talapin, The surface science of nanocrystals, Nat. Mater. 15 (2016) 141–153.

[103]   T.-H. Yang, Y. Shi, A. Janssen, Y. Xia, Surface Capping Agents and Their Roles in Shape-Controlled Synthesis of Colloidal Metal Nanocrystals, Angew. Chemie Int. Ed. 59 (2020) 15378–15401.

[104]   D. Gao, H. Zhou, J. Wang, S. Miao, F. Yang, G. Wang, J. Wang, X. Bao, Size-Dependent Electrocatalytic Reduction of CO2 over Pd Nanoparticles, J. Am. Chem. Soc. 137 (2015) 4288–4291.

[105]   A. Nelson, Y. Zong, K.E. Fritz, J. Suntivich, R.D. Robinson, Assessment of Soft Ligand Removal Strategies: Alkylation as a Promising Alternative to High-Temperature Treatments for Colloidal Nanoparticle Surfaces, ACS Mater. Lett. 1 (2019) 177–184.

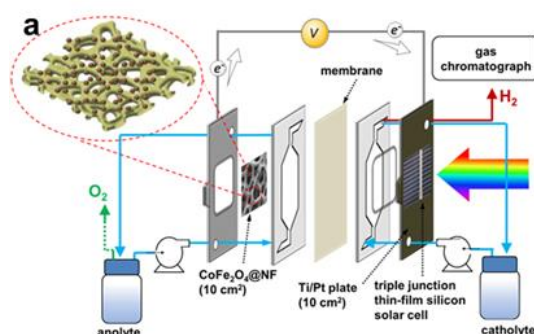[106]   A. Dong, X. Ye, J. Chen, Y. Kang, T. Gordon, J.M. Kikkawa, C.B. Murray, A Generalized

Ligand-Exchange Strategy Enabling Sequential Surface Functionalization of Colloidal Nanocrystals, J. Am. Chem. Soc. 133 (2011) 998–1006.

[107] P. Godbold, G. Johnson, A.D. Obi, R. Brown, S. Hwang, R.J. Gilliard, S. Zhang, Surfactant Removal for Colloidal Nanocrystal Catalysts Mediated by N-Heterocyclic Carbenes, J. Am. Chem. Soc. 143 (2021) 2644–2648.

[108] M.R. Dewi, G. Laufersky, T. Nann, A highly efficient ligand exchange reaction on gold nanoparticles: preserving their size, shape and colloidal stability, RSC Adv. 4 (2014) 34217–34220.

[109] M.-Q. Dai, L.-Y.L. Yung, Ethylenediamine-Assisted Ligand Exchange and Phase Transfer of Oleophilic Quantum Dots: Stripping of Original Ligands and Preservation of Photoluminescence, Chem. Mater. 25 (2013) 2193–2201.

[110] A.T. Fafarman, W. Koh, B.T. Diroll, D.K. Kim, D.-K. Ko, S.J. Oh, X. Ye, V. Doan-Nguyen, M.R. Crump, D.C. Reifsnyder, C.B. Murray, C.R. Kagan, Thiocyanate-Capped Nanocrystal Colloids: Vibrational Reporter of Surface Chemistry and Solution-Based Route to Enhanced Coupling in Nanocrystal Solids, J. Am. Chem. Soc. 133 (2011) 15753–15761.

[111] X. Zhou, A.-M. Cao, L.-J. Wan, Y.-G. Guo, Spin-coated silicon nanoparticle/graphene electrode as a binder-free anode for high-performance lithium-ion batteries, Nano Res. 5 (2012) 845–853.

[112] X. Ke, Y. Liang, L. Ou, H. Liu, Y. Chen, W. Wu, Y. Cheng, Z. Guo, Y. Lai, P. Liu, Z. Shi, Surface engineering of commercial Ni foams for stable Li metal anodes, Energy Storage Mater. 23 (2019) 547–555.

[113] Q.-C. Zhu, S.-M. Xu, M.M. Harris, C. Ma, Y.-S. Liu, X. Wei, H.-S. Xu, Y.-X. Zhou, Y.-C. Cao, K.-X. Wang, J.-S. Chen, A Composite of Carbon-Wrapped Mo2C Nanoparticle and Carbon Nanotube Formed Directly on Ni Foam as a High-Performance Binder-Free Cathode for Li-O2 Batteries, Adv. Funct. Mater. 26 (2016) 8514–8520.

[114] D. Lee, M.F. Rubner, R.E. Cohen, All-Nanoparticle Thin-Film Coatings, Nano Lett. 6 (2006) 2305–2312.

[115] Y. Matsumoto, U. Unal, Y. Kimura, S. Ohashi, K. Izawa, Synthesis and Photoluminescent Properties of Titanate Layered Oxides Intercalated with

Lanthanide Cations by Electrostatic Self-Assembly Methods, J. Phys. Chem. B. 109 (2005) 12748–12754.

[116] S. Zhang, J. Li, X. Wang, Y. Huang, M. Zeng, J. Xu, Rationally designed 1D Ag@AgVO3 nanowire/graphene/protonated g-C3N4 nanosheet heterojunctions for enhanced photocatalysis via electrostatic self-assembly and photochemical reduction methods, J. Mater. Chem. A. 3 (2015) 10119–10126.

[117] C. Wang, Y. Ma, Z. Qin, J. Wang, B. Zhong, Synthesis of hollow spherical MoS2@Fe3O4-GNs ternary composites with enhanced microwave absorption performance, Appl. Surf. Sci. 569 (2021) 150812.

[118] W. Yang, Y. Zhong, C. He, S. Peng, Y. Yang, F. Qi, P. Feng, C. Shuai, Electrostatic self-assembly of pFe3O4 nanoparticles on graphene oxide: A co-dispersed nanosystem reinforces PLLA scaffolds, J. Adv. Res. 24 (2020) 191–203.

[119] Y. Zuo, J. Li, X. Yu, R. Du, T. Zhang, X. Wang, J. Arbiol, J. Llorca, A. Cabot, A SnS2 molecular precursor for conformal nanostructured coatings, Chem. Mater. 32 (2020) 2097–2106.

[120] G.-F. Chen, T.Y. Ma, Z.-Q. Liu, N. Li, Y.-Z. Su, K. Davey, S.-Z. Qiao, Efficient and Stable Bifunctional Electrocatalysts Ni/NixMy (M = P, S) for Overall Water Splitting, Adv. Funct. Mater. 26 (2016) 3314–3323.

[121] D. Neagu, G. Tsekouras, D.N. Miller, H. Ménard, J.T.S. Irvine, In situ growth of nanoparticles through control of non-stoichiometry, Nat. Chem. 5 (2013) 916–923.

[122] H.-X. Wu, W.-M. Cao, Y. Li, G. Liu, Y. Wen, H.-F. Yang, S.-P. Yang, In situ growth of copper nanoparticles on multiwalled carbon nanotubes and their application as non-enzymatic glucose sensor materials, Electrochim. Acta. 55 (2010) 3734–3740.

[123] Z. Wen, Q. Wang, Q. Zhang, J. Li, In Situ Growth of Mesoporous SnO2 on Multiwalled Carbon Nanotubes: A Novel Composite with Porous-Tube Structure as Anode for Lithium Batteries, Adv. Funct. Mater. 17 (2007) 2772–2778.

[124] S. Peng, L. Li, X. Han, W. Sun, M. Srinivasan, S.G. Mhaisalkar, F. Cheng, Q. Yan, J. Chen, S. Ramakrishna, Cobalt Sulfide Nanosheet/Graphene/Carbon Nanotube Nanocomposites as Flexible Electrodes for Hydrogen Evolution, Angew. Chemie Int. Ed. 53 (2014) 12594–12599.

[125] C. Ernandes, L. Khalil, H. Almabrouk, D. Pierucci, B. Zheng, J. Avila, P. Dudin, J. Chaste, F. Oehler, M. Pala, F. Bisti, T. Brulé, E. Lhuillier, A. Pan, A. Ouerghi, Indirect to direct band gap crossover in two-dimensional WS2(1−x)Se2x alloys, Npj 2D Mater. Appl. 5 (2021) 7.

[126] Y. Wang, G. Zhang, W. Xu, P. Wan, Z. Lu, Y. Li, X. Sun, A 3D Nanoporous Ni–Mo Electrocatalyst with Negligible Overpotential for Alkaline Hydrogen Evolution, ChemElectroChem. 1 (2014) 1138–1144.

[127] S.-W. Cao, J. Fang, M.M. Shahjamali, Z. Wang, Z. Yin, Y. Yang, F.Y.C. Boey, J. Barber, S.C.J. Loo, C. Xue, In situ growth of Au nanoparticles on Fe2O3 nanocrystals for catalytic applications, CrystEngComm. 14 (2012) 7229–7235.

[128] H. Hu, D. Qian, P. Lin, Z. Ding, C. Cui, Oxygen vacancies mediated in-situ growth of noble-metal (Ag, Au, Pt) nanoparticles on 3D TiO2 hierarchical spheres for efficient photocatalytic hydrogen evolution from water splitting, Int. J. Hydrogen Energy. 45 (2020) 629–639.

[129] Z. Xu, B. Xu, K. Qian, Z. Li, F. Ding, M. Fan, Y. Sun, Y. Gao, In situ growth of CuS nanoparticles on g-C3N4 nanosheets for H2 production and the degradation of organic pollutant under visible-light irradiation, RSC Adv. 9 (2019) 25638–25646.

[130] X. Lu, H. Wang, Z. Wang, Y. Jiang, D. Cao, G. Yang, Room-temperature synthesis of colloidal SnO2 quantum dot solution and ex-situ deposition on carbon nanotubes as anode materials for lithium ion batteries, J. Alloys Compd. 680 (2016) 109–115.

Chapter 2

Upscaling high activity oxygen evolution catalysts based on CoFe$_2$O$_4$ nanoparticles supported on nickel foam for power-to-gas electrochemical conversion with energy efficiencies above 80%

2.1 Abstract

We investigate cobalt ferrite nanoparticles (NPs) supported on large-scale electrodes as oxygen evolution reaction (OER) catalysts. Colloidal CoFe$_2$O$_4$ NPs were loaded on low-cost and high surface area nickel foam (NF) scaffolds. The coating process was optimized for large electrode areas, ensuring a proper distribution of the NPs on the NF that allowed overcoming the electrical conductivity limitations of oxide NPs. We were able to produce CoFe$_2$O$_4$-coated NFs having 10 cm^2 geometric surface areas with overpotentials below 300 mV for the OER at a current density of 50 mA/cm^2. Such impressively low overpotentials suggested using CoFe$_2$O$_4$ NP-based electrodes within a water electrolysis device. In this prototype device, stable operating currents up to 500 mA at remarkably low cell-voltages of 1.62 and 1.53 V, at ambient and 50 ºC electrolyte temperatures, respectively, were reached during operation periods of up to 50 hours. The high electrochemical energy efficiencies reached at 50 mA/cm^2, 75 % and 81 % respectively, rendered these devices particularly appealing to be combined with low-cost photovoltaic systems for bias-free hydrogen

production. Therefore, $CoFe_2O_4$ NP-based electrolysers were coupled to low-cost thin-film silicon solar cells with 13% efficiency to complete a system that afforded solar-to-fuel efficiencies above 10%.

2.2 Introduction

The development of cost-effective large-scale electrodes for highly active and stable oxygen evolution reaction (OER) catalysis is an essential step toward reaching commercial viable solutions for electrochemical water and CO_2 reduction.[1] The OER is a complex multi-step reaction that starts with an OH coordination or H_2O dissociation step in basic or acidic electrolytes, respectively, to form OH*, where (*) represents an active site at the surface of the catalyst.[2] OH* is subsequently decomposed to O*, which reacts with another adsorbed H_2O/OH to form OOH*. In a last step OOH* is deprotonated to O_2, which is finally released. This complex reaction is kinetically less favored than the concomitant hydrogen evolution reaction (HER), mainly due to the demanding formation of oxygen double bonds and the associated multi-electron transfer step. Due to its complexity, few catalysts have demonstrated high enough OER activities for commercially relevant application. Commercial electrolysis systems currently rely on expensive and scarce elements such as iridium and ruthenium,[3] since alternative low-cost catalysts suffer from unpractical high overpotential losses to provide high enough currents (> 200 mA), what makes them not competitive with alternative H_2 production pathways.[4–6]

In recent years, potentially cost-effective catalysts based on transition metal oxides not relying on Pt-group metals have demonstrated high current water electrolysis at operation voltages below 1.6 V.[7,8] However, most of these studies have been limited to small-scale electrodes or have relied on costly and energy-intensive deposition methods. These studies consequently lack of the scalability feature, which is crucial for commercial application. Against this backdrop, the present study is dedicated toward the realization of a prototype electrolyser utilizing a potentially low-cost, scalable and high throughput process for the realization of high-performing and environmentally friendly OER catalysts on large-scale electrode scaffolds.

47

Among non-noble OER catalysts, some spinel-type binary transition metal oxides (AB_2O_4, A, B = metal) come to the fore owing to their high abundance, low toxicity, rich redox chemistry and chemical robustness. [9–11] Besides, bimetallic catalysts offer additional degrees of freedom compared to elemental compositions, enabling further optimization of active sites towards OER catalytic steps. Among these bimetallic oxide catalysts, Co-Fe spinel compounds are a particularly interesting case of a highly abundant and potentially low-cost material that shows excellent activity toward water oxidation. [12–18]

While oxides offer high electrochemical stability, they usually suffer from intrinsically inferior electrical conductivities. To circumvent this issue and at the same time maximize the density of potential catalytic sites, oxide nano-domains need to be evenly distributed through the surface of a highly conductive scaffold that facilitates the charge transfer of the conjoint OER system. However, previous studies on $CoFe_2O_4$ particles loaded on high surface area scaffolds, such as doped carbon nanofibers [15] or hematite nanorods [19], were limited to laboratory-scale applications due to the complexity and high cost of the utilized synthesis routes and the difficulties that supporting such particles onto a large area three-dimensional (3D) scaffold involve. [20]

Herein, we developed a potentially low-cost, scalable, high throughput and high yield method to produce $CoFe_2O_4$ ferrite nanoparticles (NPs). Additionally, we optimized the loading of the active NPs on large-scale Ni foams (NFs), as highly conductive, 3D and cost-effective electrode scaffold. Following the optimization of the loading process and the loaded amount of NPs, electrodes based on NFs coated with $CoFe_2O_4$ NPs were tested in a three-electrode set-up, as well as in a scaled-up two-electrode prototype electrolysis system to assess their viability for high yield H_2 production. We provide evidence that the used strategy bears great benefits regarding scalable preparation of high surface area and high activity catalysts. Additionally, we demonstrate the distribution and loading of oxide NPs to have a strong influence on the OER performance. Furthermore, we assessed the versatility of the presented system to be combined with renewable power sources by coupling the electrolyzer to a thin-film silicon solar cell for bias-free solar water splitting. Overall, the presented results set a new benchmark performance for transition metal oxides anchored on

large-scale electrode support for the OER. These results will contribute to push the frontier of the field of environmentally friendly processes and electrodes for commercially viable water electrolysis,[21]electrochemical alcohol oxidation,[22] waste water treatment,[23] or nitrate reduction systems.[24]

2.3 Experimental Section

Chemicals and Materials

Cobalt(II) acetylacetonate (Co(acac)$_2$, 97%, Sigma-Aldrich), Iron acetylacetonate (Fe(acac)$_3$, 97% Sigma-Aldrich), oleylamine (OAm, 80–90%, TCI), oleic acid (OAc, Sigma-Aldrich), Nafion (10 wt%, perfluorinated ion-exchange resin, dispersion in water), methanol (anhydrous, 99.8%, Sigma-Aldrich), carbon black (CB, VULCAN XC72), potassium hydroxide (KOH, 85%, Sigma-Aldrich), tetrafluoroboric acid (HBF$_4$, 48% Gew in H$_2$O Sigma-Aldrich) and acetonitrile (CH$_3$CN, extra dry, Fisher) were used as received without any further treatment. Chloroform, hexane, acetone, and ethanol were of analytical grade and purchased from various sources. Milli-Q water was obtained from a PURELAB flex from ELGA. An argon-filled glove box was used for storing and handling sensitive chemicals.

Synthesis of Colloidal CoFe$_2$O$_4$ Nanoparticles

All the syntheses were performed using standard airless techniques, i.e. a vacuum/dry argon gas Schlenk line. CoFe$_2$O$_4$ NPs were synthesized by loading 1.0 mmol of Fe(acac)$_3$, 1mmol of Co(acac)$_2$, 10 ml OAm and 1.0 ml OAc in a three-neck flask and degassed under vacuum at 80 ºC for 1 hour while being strongly stirred using a magnetic bar. Subsequently, the reaction flask was heated to 230 ºC and maintained for 30 min, while continuously adding nitrogen into the flask. A visible color change was observed immediately (see Figure 2.1). The obtained NPs were collected by centrifuging and washing the solid product with acetone and hexane three times. The as-prepared NPs were finally dispersed in hexane with a concentration of 10 mg/mL and stored for further use. NPs were colloidally stable in chloroform for a couple of weeks.

Ligand Removal

In a typical process, 10 mL of CoFe$_2$O$_4$ NPs dispersion in hexane (10 mg/mL) was combined

with 10 mL acetonitrile to form a two-phase mixture and then a 1 mL HBF_4 solution (48%) was added. The resulting solution was sonicated until the NPs transferred from the upper to the bottom layer. The surface modified NPs were washed with ethanol for three times and dispersed in 10 mL ethanol with a small amount of DMF for further use.

Coating of Ni Foam

Drop casting: Ni foam was sonicated in acetone, 1M HCl, Milli-Q water, and ethanol respectively. 50 µL of 10mg/mL $CoFe_2O_4$ ethanol solution was dropped on nickel foam and dried in air and subsequently annealed at 400℃ under nitrogen atmosphere.

Dip coating: Ni foam was sonicated in acetone, 1M HCl, Milli-Q water, and ethanol respectively. In a typical process, clean and dry nickel foam was immersed in 10mg/mL of $CoFe_2O_4$ ethanol solution for 2 seconds and then taken out quickly and dried in air. This process was repeated for 1, 3, 5, and 7 times and donated as 1 dip, 3 dips, 5 dips and 7 dips, respectively. The coated NFs were subsequently annealed at 400 ℃ under nitrogen atmosphere.

Characterization

Structural characterization was carried out by X-ray diffraction (XRD). The samples were scanned from 2θ = 20° to 80° at a rate of 0.02 s^{-1} in Bragg–Brentano geometry. The diffractometer was equipped with a Cu Kα (1.54051 Å) radiation source. The morphology of the as deposited foam-based electrodes was observed using a scanning electron microscope (SEM) and elemental analysis was performed by the same microscope equipped with an X-ray energy dispersive spectrometer (EDS). The samples for transmission electron microscopy (TEM) were prepared by scratching the as-prepared $CoFe_2O_4$ powders from the Ni foam substrate, followed by dispersing them in hexane and collecting them on the TEM copper grids. High resolution transmission electron microscopy (HRTEM) images and scanning transmission electron microscopy (STEM) studies were conducted by using an FEI Tecnai F20 field emission gun microscope operated at 200 kV with a point-to-point resolution of 0.19 nm, which is equipped with high angle annular dark field (HAADF) and electron energy loss spectroscopy (EELS) detectors. X-ray photoelectron spectroscopy (XPS) was done on a SPECS system equipped with an Al anode XR50 source operating at 150 mWand a Phoibos 150 MCD-9 detector. The pressure in the analysis chamber was below 10^{-7} Pa. The

area analyzed was about 2 mm × 2 mm. The pass energy of the hemispherical analyzer was set at 25 eV and the energy step was set at 0.1 eV. Data processing was performed with the CasaXPS program (Casa Software Ltd., UK). Binding energy values were centered using the C 1s peak at 284.8 eV. Fourier transform infrared (FTIR) spectra were recorded on an Alpha Bruker spectrometer

The electrochemical performance of $CoFe_2O_4$@NF electrodes towards OER reduction was assessed using a three-electrode set-up. A leak-free Ag/AgCl 3.4 M KCl reference electrode (RE) was assembled in the polytetrafluoroethylene (PTFE) frame of the cell and placed very close to the working electrode surface. The potential was transformed to the reversible hydrogen electrode (RHE) scale: E (V_{RHE}) = E ($V_{Ag/AgCl}$) + 0.0592 × pH + 0.197. The data presented for the electrochemical characterization in aqueous solutions in three-electrode configuration do not include compensation for the series resistance of the solution. For the complete electrolyzer characterization, an adapted flow cell set-up (Micro Flow Cell, Electrocell A/S) was employed, schematically depicted in Figure 2.19a. The flow rates of electrolytes within the flow cell were kept at 20 ml/min. As illustrated in Figure 2.19a, the electrolyte was directly introduced through the macroporous 3D $CoFe_2O_4$@NF electrode (geometric surface area: 10 cm^2). The electrically attached triple junction thin-film silicon device had an area of 1 cm^2, thus during the photoelectrolysis measurement an area of 1 cm^2 was illuminated. All photoelectrochemical experiments were conducted using a solar simulator equipped with a 150 W xenon lamp. The intensity of the light source was adjusted to match standard AM 1.5G sunlight at 100 mW/cm^2 intensity. The experiments for the full system assembly were carried out in a two-electrode configuration. The faradaic efficiency to H_2 was calculated using the analysis of the outlet gas by gas chromatography (GC) during potentiostatic measurements. Helium (99.999%) was used as the carrier gas. The calibration of peak area vs. gas concentration was used for the molar quantification of each gaseous effluent. The faradaic efficiency was calculated by determining the number of coulombs needed for each product and then dividing by the total charge passed during the time of the GC sampling according to the flow rate. In the photovoltaic-electrolyzer coupled system, to account for deviations in the assessment of the photovoltaic performance of the complete system, i.e. spectra variations due to diode calibration accuracy, area definition, or

temperature variation, a systematic error of 2 % was considered.[25]

2.4 Results and discussion

Synthesis and Characterization of Colloidal CoFe₂O₄ NPs

Co-Fe oxide NPs were produced in colloidal form from the reduction of cobalt and iron salts in the presence of OAm and OAc and the posterior oxidation of the reaction product in ambient conditions (Scheme 1, see Experimental Section for details). A representative TEM micrograph and the size distribution histogram of the oxidized NPs are shown in Figure 2.1. Co-Fe oxide NPs displayed a quasi-spherical geometry, with an average diameter of 7.1 ± 0.1 nm. In contrast to the product of the oxidation of iron NPs, the oxidation of Co-Fe NPs did not result in the formation of hollow structures, probably due to the relatively low diffusivity of Fe and Co through the growing Co-Fe oxide shell compared with that of Fe though FeO/Fe₂O₃. [26–28]
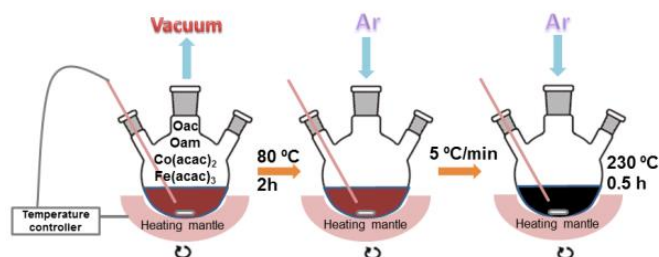
Figure 2.1. Schematic illustration of the synthesis procedure used to prepare colloidal CoFe₂O₄ NPs.

XRD analysis revealed Co-Fe oxide NPs to crystallize in the CoFe₂O₄ cubic phase (JCPDS *22-1086, Figure 2.2b).* HRTEM micrographs confirmed the crystal structure of the NPs to be compatible with the CoFe₂O₄ ferrite cubic phase ([FM3-MZ]-Space group 227) with lattice parameters a = b = c = 0.83961 nm (Figure 2.2a). HAADF-STEM and EELS analysis demonstrated the three constituent elements, Co, Fe, and O, to be present in the same ratio in all NPs and to be homogeneously distributed within each NP (Figure 2.3a).
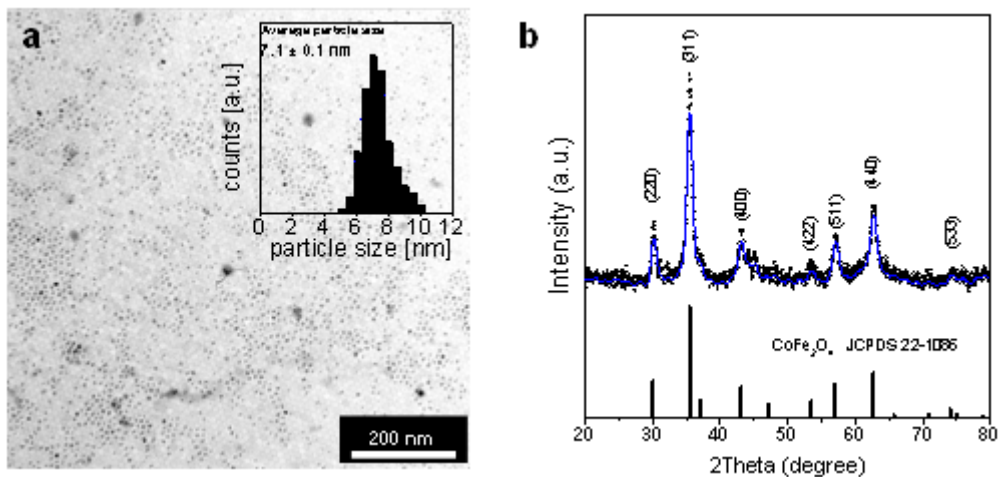
Figure 2.2. a) Representative TEM micrograph of as-prepared CoFe₂O₄ NPs. Inset displays the corresponding size distribution histogram from where an average NP diameter of 7.1 ± 0.1 nm was estimated. b) XRD pattern of the as-prepared CoFe₂O₄ NPs. Graph includes the reference pattern JCPDS 22-1086 for the cubic CoFe₂O₄ crystal phase.
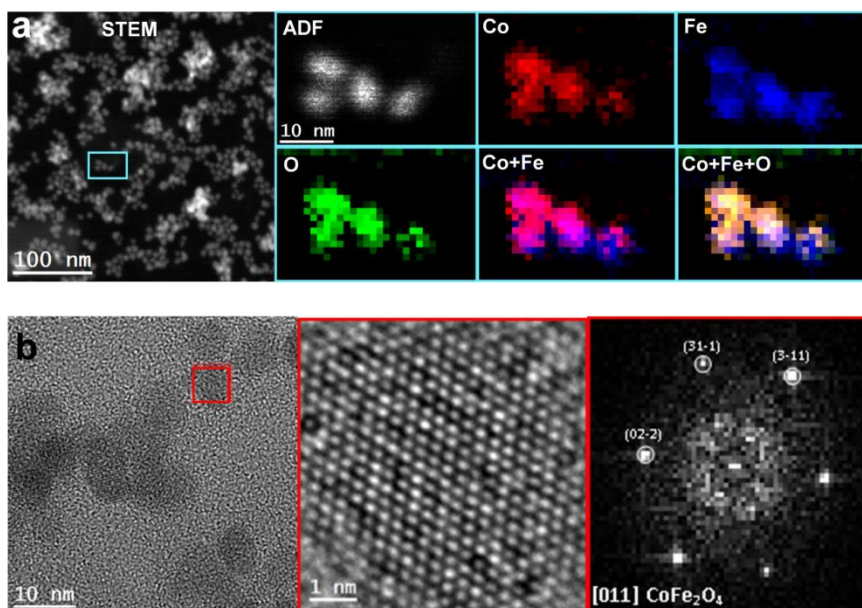

Figure 2.3. a) HAADF-STEM micrograph and EELS chemical composition maps (from cyan rectangle) for Co (red), Fe (blue), O (green) and their composites. b) HRTEM micrograph, detail of the red squared region (scale bar, 1 nm), and corresponding FFT spectrum indicating that NPs crystallized in the cubic CoFe₂O₄ phase, [FM3-MZ]-Space group 227, with lattice parameters of a = b = c = 0.83961 nm, and α = β＝γ＝90°.

N₂ adsorption–desorption isotherms of the CoFe₂O₄ NPs dried in the form of a powder displayed a type-I reversible behavior (Figure 2.4), which is generally a signature of

microporous solids. [29]CoFe$_2$O$_4$ nanopowders were characterized by a Langmuir specific surface area (SSA) of 276 m^2/g and a Brunauer–Emmett–Teller (BET) SSA of 174 m^2/g. The obtained BET SSA is among the highest reported for Co-Fe spinel NPs, slightly above that of NPs synthesized by hydrothermal[13] and micro emulsion techniques[20](~150 m^2/g), and significantly higher than materials prepared by electrospinning[15] and electrodeposition[16] (~55 m^2/g). Notice that these high SSAs were measured from the nanopowders obtained by drying the colloidal NPs in ambient conditions and with no pre-coordination of the NP into a network. Even larger SSA values would be potentially obtained through the formation of NP networks in solution, i.e. NP gelation, and the posterior drying from supercritical CO$_2$ for instance. [30,31]

Figure 2.4. N$_2$ adsorption–desorption isotherms from the CoFe$_2$O$_4$ nanopowders obtained from drying CoFe$_2$O$_4$ NPs under ambient conditions

The optimized loading of nano-sized OER catalysts onto large-scale scaffolds is an important step toward the realization of industry-viable electrodes and electrolyzers. In this direction, we first studied the deposition of NPs on small (1 cm^2) NF electrodes and subsequently optimized the deposition process for larger scaffolds (≥ 10 cm^2). Before deposition, organic ligands at the surface of as-synthesized NPs, which were used to adjust NP growth during the synthesis, were removed using a solution of tetrafluoroboric acid in acetonitrile. After successive cleaning with tetrafluoroboric acid, FTIR spectra showed the disappearance of the peaks at 2822 and 2890 cm^{-1} corresponding to C–H stretching modes, what evidenced the effective removal of hydrocarbon ligands (Figure 2.5). This ligand displacement step is key

towards producing high performance and reliable electrocatalyts since generally organic ligands strongly limit electronic transport and the ability of the NPs to interact with their surrounding media, i.e. with the scaffold and the electrolyte.[32] Furthermore, in the present case, the presence of organic ligands on the surface of the $CoFe_2O_4$ NPs impeded a homogeneous coating of the NF. Not mediating a ligand removal pretreatment, a porous two-dimensional organic film was deposited on the NF after dip coating it into a suspension of colloidal NPs (Figure 2.6).
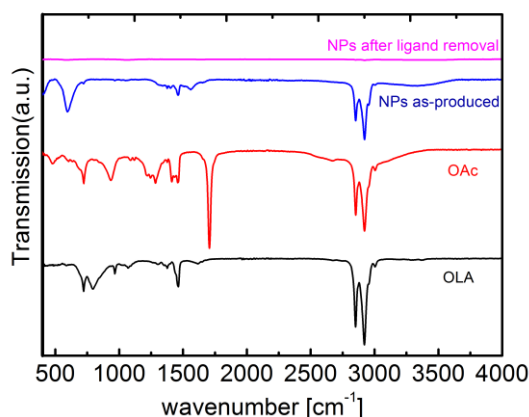
Figure 2.5. FTIR spectra of OLA, OAc, $CoFe_2O_4$ NPs as-produced and after ligand removal.
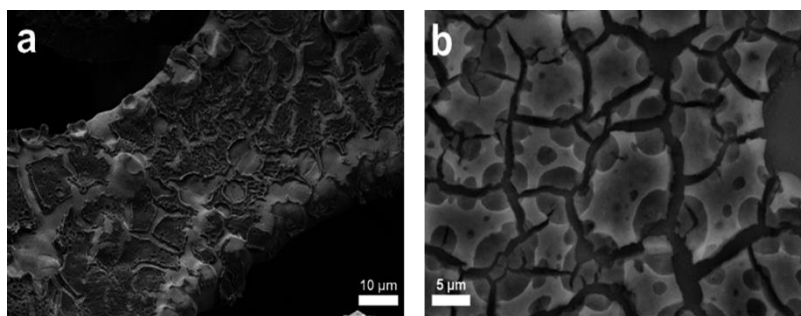
Figure 2.6. Scanning electron microscopy (SEM) images showing the Ni foam surface after immersion (1 dip) into the $CoFe_2O_4$ NP containing suspension without ligand removal. a) Scale bar: 10 µm, b) scale bar: 5 µm.

Two procedures were explored to support $CoFe_2O_4$ NPs on NFs: dip coating and drop casting. As depicted in figure 2.8a, the foam was either dipped into the dispersion of colloidal NPs and hold for 2 seconds or the suspension was dropped onto the foam (2 mg of solution) and let it dry. SEM characterization showed the dip coating process to result in a homogeneous

distribution of NPs on the NF surface. On the other hand, drop-casted NFs displayed numerous NP agglomerates.

XPS survey spectrum of the $CoFe_2O_4$ NPs supported on the NF (3 dips) demonstrated the presence of Co, Fe, O, and Ni (Figure 2.7). The Co 2p and Fe 2p spectra matched well with Co^{2+} and Fe^{3+}.[33,34] and the O 1s spectrum displayed two peaks at about 531.1 and 532.4 eV which corresponded to oxygen in the metal-oxygen bond and hydroxyl groups, respectively.[35] Quantitatively, XPS analysis showed the atomic concentration of Fe on the surface to be a threefold of that of Co: Fe/Co=3 (Table 1). Additionally XPS analysis showed a large surface Ni concentration, ca. 50 at% of the surface composition (Table 1).
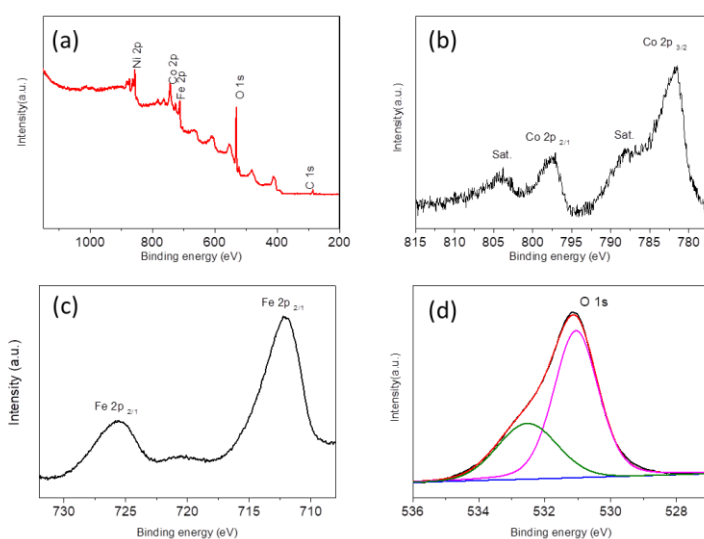
Figure 2.7. XPS spectrum for $CoFe_2O_4$ coated Ni foam before OER measurement (a) survey XPS spectra (b) XPS spectra in Co 2p, (c) Fe 2p, and (d)O 1s .

The electrochemical performance toward OER of NFs loaded with $CoFe_2O_4$ NPs (hereafter $CoFe_2O_4$@NF) is shown in Figure 2.8. In comparison with bare NF, used in industrial water splitting, $CoFe_2O_4$@NF electrodes displayed significantly enhanced OER catalytic activities. $CoFe_2O_4$@NF electrodes provided much higher current densities under the same applied potential than bare NF (Figure 2.8c). In addition, $CoFe_2O_4$@NF electrodes prepared by dip coating provided higher performance over electrodes prepared by drop casting. This result was consistent with the usual assumption that thinly dispersed oxide nanoparticles favor electrochemical performance. A significant increase in the current density for potentials > 1.5 V was measured for samples prepared by dip coating, attaining 43.8 mA/cm^2 at 1.7 V$_{RHE}$

(470 mV overpotential), which is 1.4 times higher than the current density obtained with the drop casted sample (Figure 2.8b).
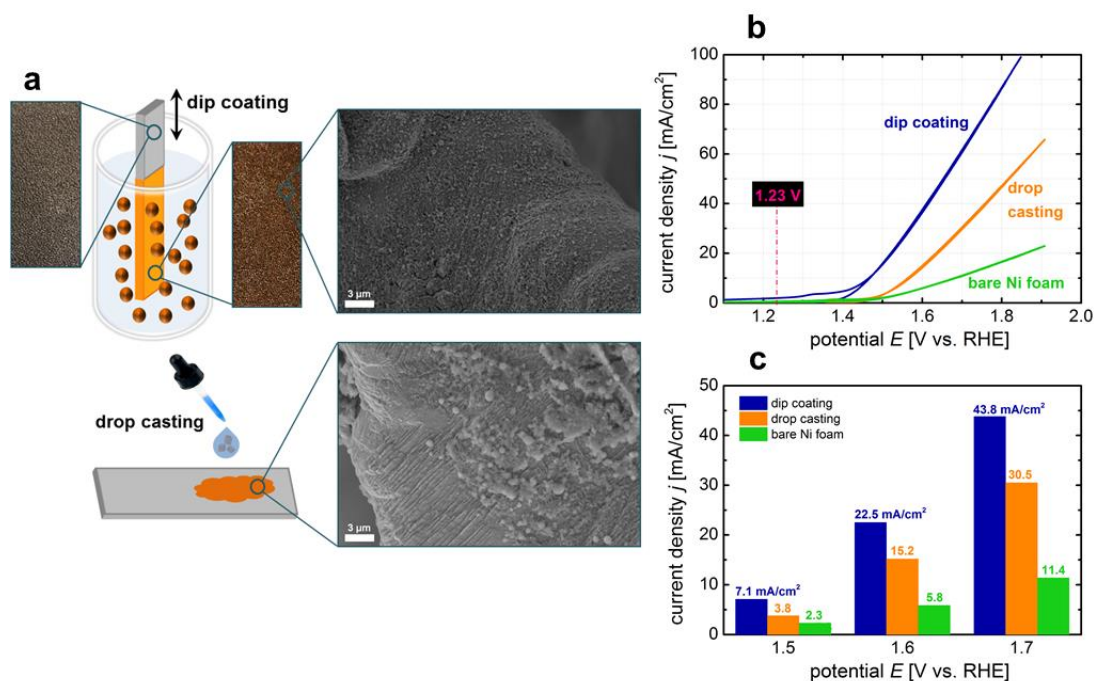

Figure 2.8. a) Schematic illustration of the two tested coating techniques for the $CoFe_2O_4$ NPs on the NF (1 cm^2 geometric area): dip coating and drop-casting, including photographs of the NF before and after the coating processes, as well as SEM images showing the distribution of the deposited NPs on the NF. b) CV curves of the NF coated with $CoFe_2O_4$ NPs by dip coating and drop casting, respectively, compared with bare NF. Measurements were conducted in 1 M KOH at a scan rate of 10 mV/s. c) Current densities achieved at different applied potentials.

The dip coating technique was further optimized for large area electrodes (10 cm^2). Figure 2.10 presents SEM images of the NF surfaces after 1, 3, 5, and 7 dips (each hold for 2 seconds) into the $CoFe_2O_4$ NP suspension. After 1 dip, major parts of the NF remained uncovered, whereas 3 dips resulted in a high coverage of the NF surface with highly dispersed NPs (Figure 2.9). Increasing the number of dips to 5 led to the formation of NP aggregates with sizes ranging from 50 to 200 nm (Figure 2.10). This effect was even more pronounced after 7 dipping times, resulting in an almost complete coverage of the NF surface by $CoFe_2O_4$ NP agglomerates.

Figure 2.9. Photograph of an uncoated (left) and a coated Ni foam (10 cm^2) with CoFe$_2$O$_4$ nanoparticles (right) after being 3 times immersed in the colloidal particle-containing solution.
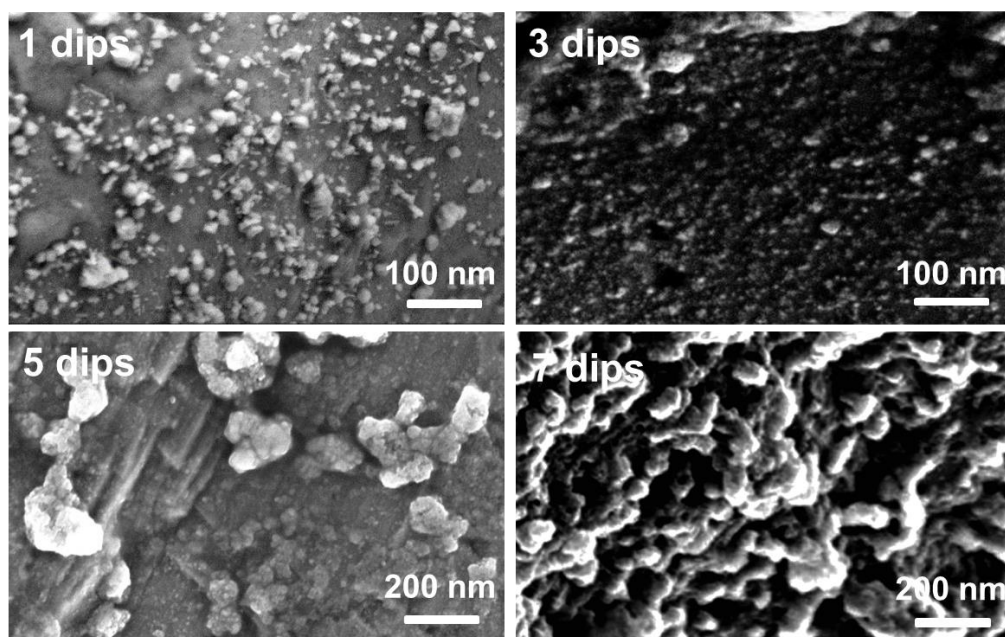

Figure 2.10. SEM micrographs of CoFe$_2$O$_4$@NF electrodes (10 cm^2) produced using different dip coating steps: 1, 3, 5, and 7 as noted in each micrograph.

The electrochemical characteristics of the large-scale CoFe$_2$O$_4$@NF electrodes were assessed in a three-electrode configuration using 1M KOH electrolyte solution (see Experimental Section). Figure 2.11a shows the CV curves of the electrode samples investigated in Figure 2.10b. The number of dip coating steps had a significant influence on the OER performance. Best performances were achieved with CoFe$_2$O$_4$@NF electrodes produced using 3 dip coating steps, in good agreement with the observed homogeneous coverage of the NF surface with

58

thinly dispersed NPs. OER overpotentials of the four tested samples for different current densities are shown in Figure 2.11b. $CoFe_2O_4$@NF electrodes produced after 3 coating steps exhibited the lowest overpotentials, with 250 mV and 460 mV for 10 mA/cm^2 and 50 mA/cm^2, respectively. Higher $CoFe_2O_4$ NP loads containing NP agglomeration provided lower OER performance. This result is understandable as oxide structures generally suffer from low electrical conductivities, which strongly limits the thickness of the oxide layer that can be practically used. The highest overpotential of 580 mV at 50 mA/cm^2 was measured for the 1 step coating $CoFe_2O_4$@NF electrode, presumably due to an insufficient coverage of the scaffold with $CoFe_2O_4$ NPs.

Commercial alkaline electrolyzers work at operating temperature between 25 and 100 ºC, which is why we tested the best performing electrode (3 dips) also under elevated electrolyte temperature. As observed in Figure 2.11a and 2.11b, the OER performance was significantly enhanced by increasing the electrolyte temperature up to 50 ºC. Extremely low overpotentials of 200 mV and 295 mV for 10 mA/cm^2 and 50 mA/cm^2, respectively, were obtained. Temperature has a strong influence on the thermodynamic and kinetic functions, including electronic, ionic and molecular diffusion. Increasing temperature can accelerate the reaction kinetics, improve diffusion, disturb the electrochemical double layer and increase the electrical conductivity of the electrolyte solution, among other, all of them having an important and beneficial influence on the OER performance. [36-38]
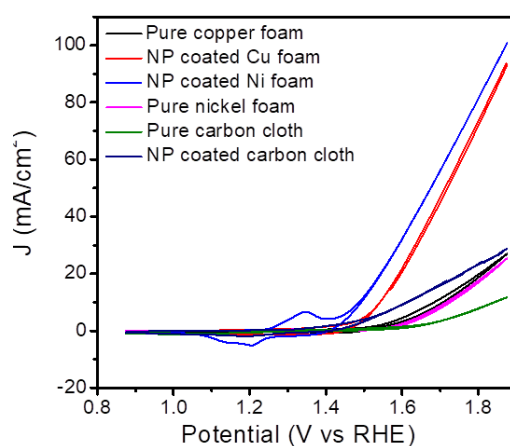

Figure 2.11. CV curves of the pure Ni foam, NP coated Ni foam, pure Cu foam, NP coated Cu foam, pure carbon cloth and NP coated carbon cloth respectively. Measurements were conducted in 1 M KOH at a scan rate of 10 mV/s.

We further compared the performance of the $CoFe_2O_4$@NF electrodes with that of other electrodes prepared from supporting the $CoFe_2O_4$ on other substrates, including Cu foam and carbon cloth (Figure 2.11). The incorporation of the $CoFe_2O_4$ NPs on any of the substrates significantly reduced their overpotential. Among the different substrates, $CoFe_2O_4$@NF electrodes achieved the best performance, with an overpotential down to 250 mV at 10 mA/cm^2. Such value is below that of most of state-of-the-art OER electrodes in literature, evidencing the high potential for commercial applications of the herein developed large-scale $CoFe_2O_4$@NF OER electrodes. State-of-the-art electrocatalytic properties toward OER of previously reported Co-Fe and NF-based electrodes are summarized in Table 2.
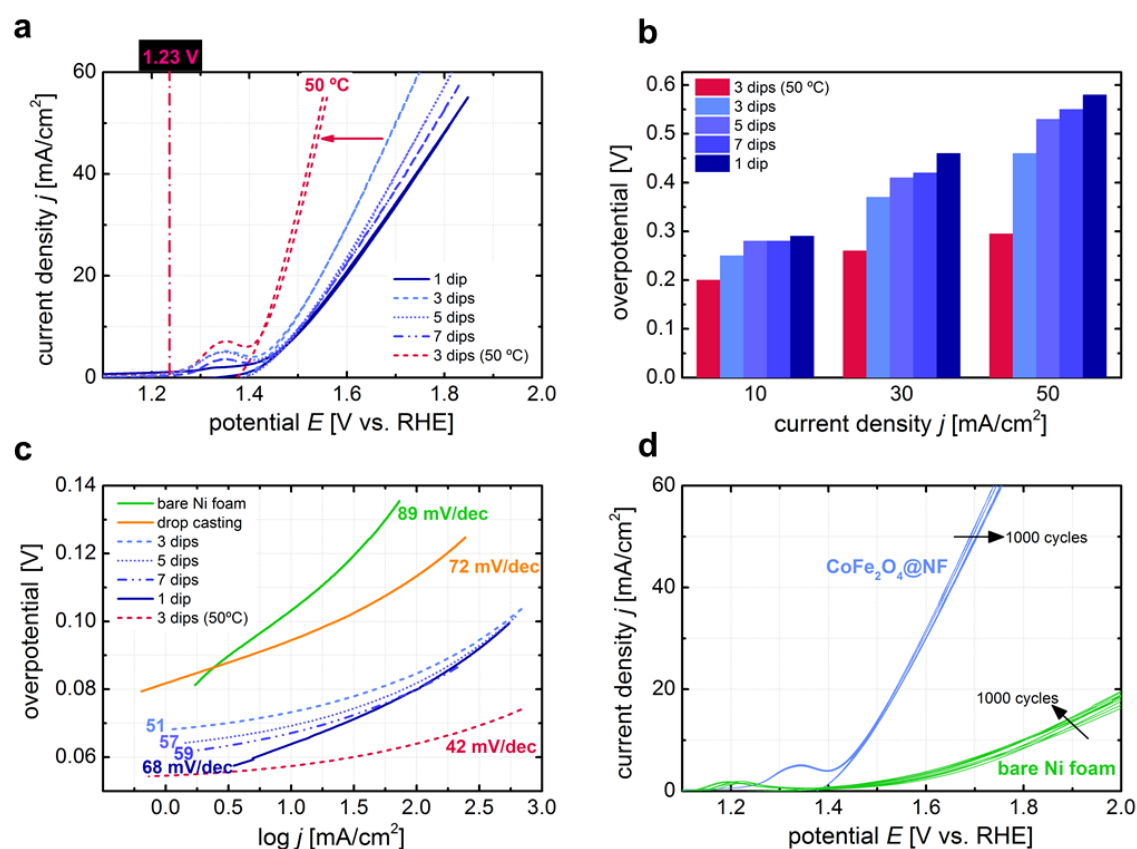

Figure 2.12. a) CV curves of NF electrodes dipped into the $CoFe_2O_4$ NP solution, for 1 (solid), 3 (dashed), 5 (dotted), and 7 (dash-dotted) times. CV curves were measured in 1M KOH at a scan rate of 10 mV/s. $CoFe_2O_4$@NF electrodes providing best OER catalytic performances (3 dips) were measured under elevated electrolyte temperature (50 ºC, pink dashed line). The H_2O/O_2 oxidation potential is indicated by the straight dash-dotted line. b) Required overpotentials derived from CV curves at

different current densities. c) Tafel plots of the tested samples. d) CV curves of the CoFe$_2$O$_4$@NF (3 dips) and bare NF electrodes, respectively, before and after 1000 cycles. Every 200th CV scan of each electrode is plotted.

The electrocatalytic kinetics for OER of the CoFe$_2$O$_4$@NF electrodes were further investigated by Tafel plots (Figure 2.12c). For comparison, the Tafel plots of the sample prepared by drop casting and the bare NF sample are also shown in Figure 2.12c. In accordance with the results shown in Figure 2.8b and 2.8c, the drop casted and the bare NF electrodes exhibited the worst kinetics among the analyzed electrodes, i.e. the highest Tafel slopes, at 89 mV/dec and 72 mV/dec, respectively. For the CoFe$_2$O$_4$@NF electrodes prepared by dip coating, Tafel slopes were impressively low and ranged from 68 mV/dec for the 1 time dipped sample to 51 mV/dec for the 3 times dipped electrode. Hence, our CoFe$_2$O$_4$@NF electrodes showed comparable and even better electrocatalytic properties toward OER than related nonprecious metal-based OER electrocatalysts reported in literature (Table 1). The CoFe$_2$O$_4$@NF electrode measured in a 50 ºC alkaline solution provided the lowest Tafel slope, 42 mV/dec, as could be expected from the corresponding CV curve in Figure 2.12a. In fact, such an outstanding kinetic behavior made it an ideal anode candidate for commercial electrolysis systems.
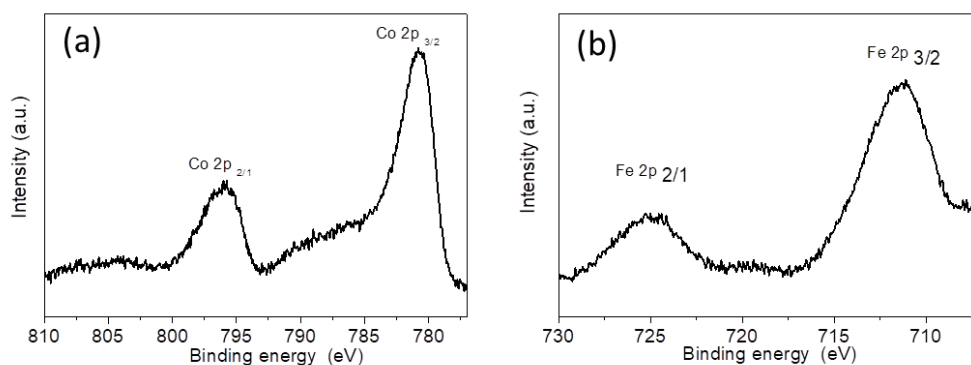

Figure 2.13. XPS spectrum for CoFe$_2$O$_4$ coated Ni foam after OER measurement (a) XPS spectra in Co 2p, and (b) Fe 2p.

XPS analysis of the electrodes after long term cycling showed no significant difference in the chemical environment of Co and Fe with respect to the results obtained from electrodes after annealing (Figure 2.13). However, quantitatively, after long term cycling the amount of Fe detected on the electrode surface was significantly lower from the initial Fe/Co=3 to the

final Fe/Co=0.5 (Table S1). In parallel, the concentration of Ni significantly increased, from 50 at% to up to an 80 at% (Table S1). On the other hand, SEM-EDX analysis showed a similar Co and Fe concentration on top of the NF. We hypothesize that during cycling a significant amount of Ni from the NF is able to diffuse within the $CoFe_2O_4$ structure and to accumulate, together with Co, on the NP surface, partially displacing Fe ions. The presence of these Ni ions on the catalyst surface may contribute to the outstanding performance obtained from $CoFe_2O_4$@NF electrodes compared with other supports and literature results (Figure2.11 and Table S2)
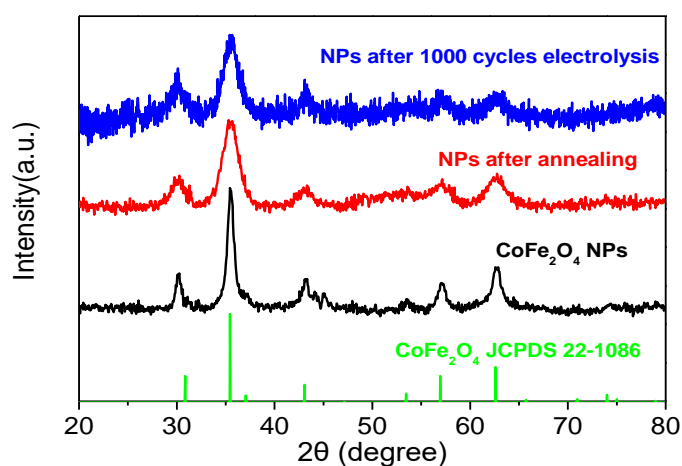

Figure 2.14. XRD pattern of the pure $CoFe_2O_4$ NPs, after annealing and NP after 1000 cycles electrolysis. Graph includes the reference pattern JCPDS 22-1086 for the cubic $CoFe_2O_4$ crystal phase.
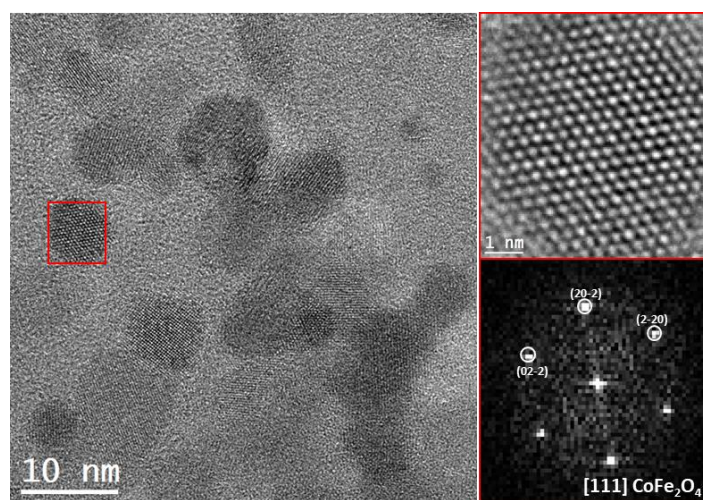

Figure 2.15. HRTEM image showing the structure of the $CoFe_2O_4$ nanoparticles (scale bar, 10 nm) after long-term operation (1000 cycles). Top right: HRTEM detail of the red squared region (scale bar, 1 nm).

Bottom right: Corresponding FFT spectrum indicating that the material crystallizes in the cubic CoFe$_2$O$_4$ phase, [FM3-MZ]-Space group 227, with lattice parameters of a = b = c = 0.83961 nm, and α = β＝γ＝90°as visualized along the [111] direction.

Besides electrochemical performance, durability is another major parameter in the realization of industry-viable electrodes for electrolyzers. In this direction, we investigated the long-term stability for CoFe$_2$O$_4$@NF electrodes (3 dips) by cycling them 1000 times in 1M KOH at ambient temperature (Figure 2.12d). Again, bare NF was utilized for comparison. CoFe$_2$O$_4$@NF electrodes showed a negligible degradation after continuous 1000 CV cycles, indicating its superior operational stability under alkaline test condition. XPS and XRD analysis of the material after long term cycling (Figures 2.14 and 2.15) also showed the chemical environment of Co and Fe and the crystal structure of the NPs to remain unmodified. The mechanical and structural stability was further confirmed by HRTEM analysis of the used catalyst, showing the CoFe$_2$O$_4$ NPs to remain thinly dispersed onto the NF and maintaining their size after the long-term experiment (Figure 2.15). No obvious NP aggregation/growth was observed, which was associated to the proper immobilization of the CoFe$_2$O$_4$ NP on the NF. Consistently with previous reports, bare NF slightly increased its activity towards OER with time (Figure 2.12d). In alkaline solution, this activity enhancement has been associated to the contribution to the catalytic activity of metallic impurities (e.g. Fe) from the electrolyte that are deposited onto the Ni surface during long-term operation.[56] Because such a behavior was not observed with CoFe$_2$O$_4$@NF electrodes, we assume that the Ni scaffold have a moderate catalytic role in this system.
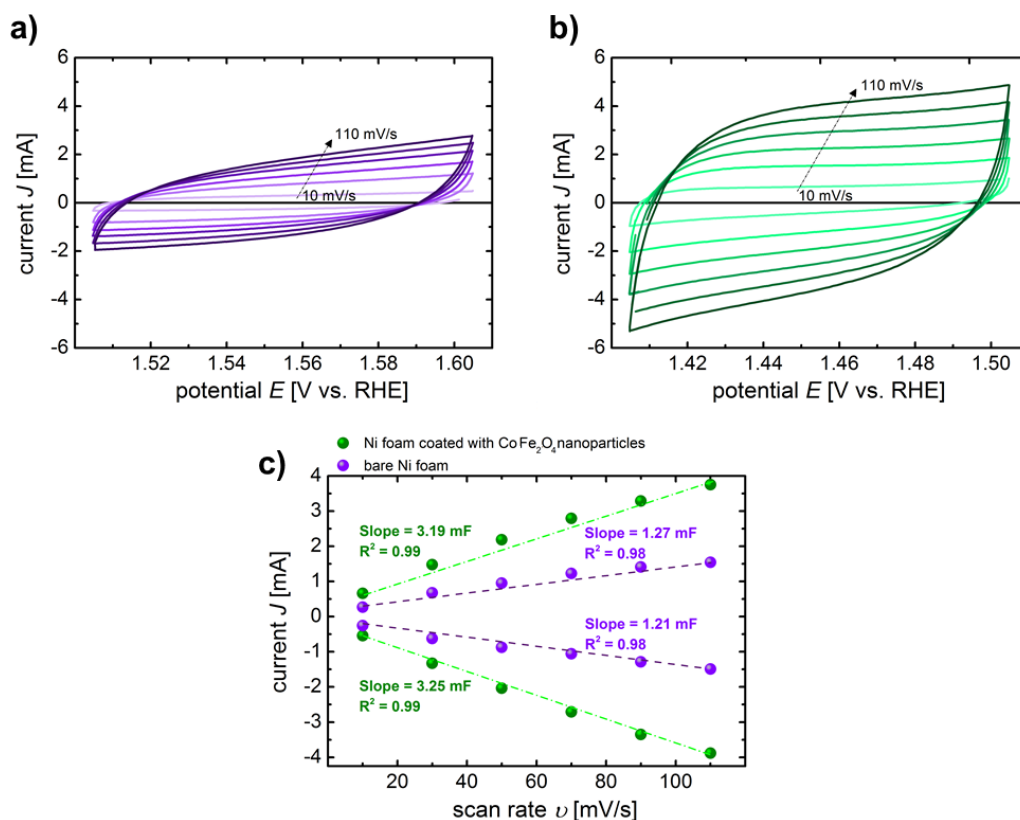
Figure 2.17. a) Cyclic voltammograms for bare Ni foam. b) Cyclic voltammograms for CoFe$_2$O$_4$ NP coated Ni foam (3 times immersion). Both cathodes were measured in 1M KOH with a geometric surface area of 1 cm2. c) Capacitive currents with a scan rate of 10, 30, 50, 70, 90, and 110 mV/s in 1M KOH. The average value of the two respective slopes was taken as Cdl value. Assuming a general specific capacitance CS = 0.040 mF/cm^2 in 1M KOH, the ECSA of the samples can be calculated to be 80.5 cm2 for the CoFe$_2$O$_4$@NF and 31.0 cm^2 for bare Ni foam.

We estimated the electrochemical active surface area (ECSA) of CoFe$_2$O$_4$@NF (3 dips) and bare NF electrodes from the electrochemical double-layer capacitance (Cdl) at the solid/liquid interface. [57]Figure 2.17a and 2.18 present the CV curves of the two electrodes recorded in a non-Faradic potential range under different scan rates. CoFe$_2$O$_4$@NF cathodes exhibited a higher Cdl than bare NF, evidencing a higher active surface area, which was estimated as 80.5 cm2 for CoFe$_2$O$_4$@NF and 31.0 cm^2 for bare NF (Figure 2.12c). This result probes the CoFe$_2$O$_4$@NF to provide a larger number of catalytically active sites and thus an improved OER activity, much higher than that of CoFe$_2$O$_4$ NPs on carbon nanofibers (20.6 cm2) and commercial RuO$_2$ catalyst (14.5 cm^2).[15]

The optimized large-scale $CoFe_2O_4$@NF electrode was subsequently integrated in a prototype electrolysis reactor. [58-60]As illustrated in Figure 2.19a, the reactor design allowed to work under flow conditions, where the anolyte and catholyte solutions are continuously recirculated through the respective compartments, i.e. a $CoFe_2O_4$@NF anode compartment performing the OER and a Ti/Pt cathode compartment performing the hydrogen evolution reaction (HER). By this design, the flow dynamics of the electrolysis set-up could be significantly enhanced, fostering higher electrochemical activity. Both compartments were separated by a membrane and a gas chromatograph was employed for gaseous product identification. The configuration can even be adapted for the additional integration of photovoltaic devices, as shown in Figure 2.19a with a thin-film silicon solar cell (see Experimental Section for details).
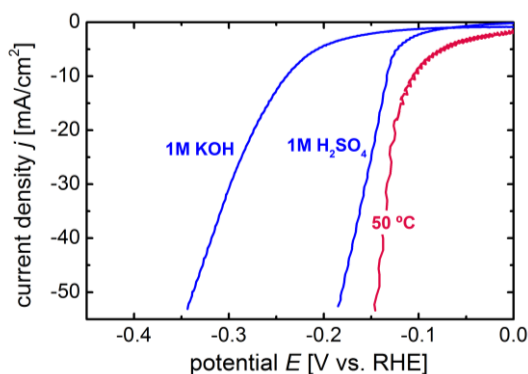

Figure 2.18. Linear sweep curves of the Ti/Pt plate in 1M KOH and 1M H_2SO_4 electrolyte solution, respectively, at a scan rate of 10 mV/s. The measurement in the 1M H_2SO_4 solution was also conducted at an electrolyte temperature of 50 ºC.

The characteristics of the complete reactor in two-electrode operation are shown in Figure 2.19b for two different configurations. The first configuration consisted in using a cation-exchange membrane (Nafion ®117) and 1M KOH electrolyte solution in both compartments. In the second configuration, we applied a bipolar membrane (BPM), enabling to operate the electrolysis reactor with two different electrolytes. In this configuration, we applied a 1M KOH (pH = 13.7) for the anolyte to perform the OER and a 1M H_2SO_4 (pH = 0) solution for the catholyte to perform the HER. As can be seen from the linear sweep voltammetry (LSV) curves in Figure 2.19b, the configuration using the BPM exhibited a better overall electrolysis behavior than the reactor configuration containing the Nafion membrane.

To provide 200 mA and 400 mA, respectively, the BPM configuration only required 1.51 V and 1.59 V, respectively, whereas in the Nafion configuration the complete electrolyser cell voltage augmented to 1.60 V and 1.76 V, respectively. The higher cell voltage was related with the reduced electrochemical performance of the Ti/Pt cathode in alkaline solution (Nafion configuration) compared to its performance in acid electrolytes (BPM configuration). In Figure 2.20, the LSV curves of Ti/Pt in 1M KOH and 1M H_2SO_4 electrolyte solution are shown. LSV curves displayed overpotentials of 340 mV and 180 mV at 50 mA/cm^2 for basic and acidic catholytes, respectively, further demonstrating the superior cathode performance in acidic medium. To simulate real electrolyser conditions, the overall polarization of the reactor device was also measured at elevated electrolyte temperatures (50 ºC) in the BPM configuration. As expected from the results shown in Figure 2.12a and Figure 2.20, the electrochemical performance increased with increasing electrolyte temperature, reaching complete electrolyzer cell voltages of 1.46 V and 1.51 V to produce 200 mA and 400 mA, respectively. From these values, electrochemical energy efficiency up to 75 % and 81 %, for ambient and elevated operation temperatures were calculated. Consequently, the herein proposed electrolyzer based on a $CoFe_2O_4$@NF electrode presents an attractive alternative to commercial systems used for surplus electric power storage, such as pumped hydroelectric storage (70–80% efficiency), power-to-gas based on alkaline and PEM electrolyzers (65–70% efficiency), or ion lithium batteries (92–95% efficiency) that have other severe limitation in terms of energy density, cost and life time.
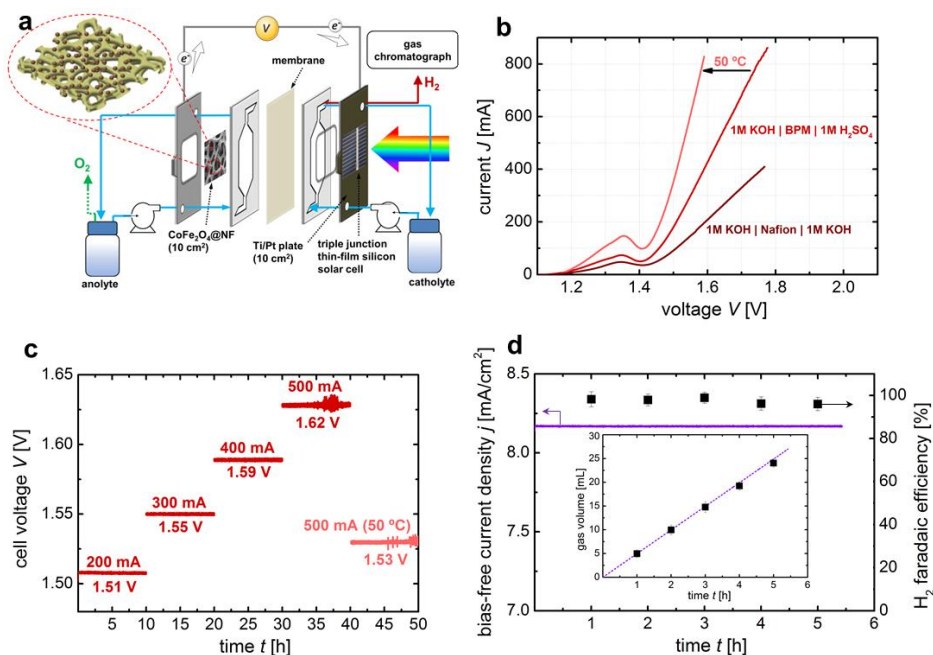
Figure 2.19. a) Sketch of the experimental prototype reactor used to assess the overall electrolysis performance. The illustration shows the different components, including a schematic illustration of the 3D NF coated with CoFe$_2$O$_4$ NPs and the coupled triple junction thin-film silicon solar cell (a-Si:H/a-Si:H/μc-Si:H) for the bias-free operation test (see Figure 2.19d). b) Linear sweep measurements of the CoFe$_2$O$_4$@NF electrodes (10 cm^2 geometric area) combined with the Ti/Pt cathode (10 cm^2 geometric area) for a configuration containing Nafion and BPM membrane, respectively. The BPM configuration (best performing) was also measured at 50 ºC electrolyte solution (1M KOH). c) Long-term behavior of the electrolysis showing the required cell voltages of the reactor as a function of the applied current (each galvanostatic testing was conducted for ~10 hours with the same electrodes and membrane). d) Bias-free solar water splitting using a triple junction a-Si:H/a-Si:H/μc-Si:H solar cell (as depicted in a)). Left y-axis shows the achieved bias-free current density over the operation time. Right y-axis represents the faradaic efficiency for H$_2$ production over the operation time. The error bars indicate standard deviations obtained from 3 experimental repeats. The inset shows the calculated gas volume obtained. The dotted purple line shows the theoretical (assuming 100% faradaic efficiency) gas evolution for the measured bias-free current density and the black squares show the experimental values.

The electrochemical durability of the prototype reactor was assessed by conducting chronoamperometry. Figure 2.19c displays the electrolyzer cell voltages at successively increasing electrolysis currents of 200, 300, 400, and 500 mA applied for 10 hours each, until

a total of 50 hours of continuous operation. The prototype electrolyzer showed no sign of decay when operated for 50 hours, even when operated at higher temperature (50 ºC).
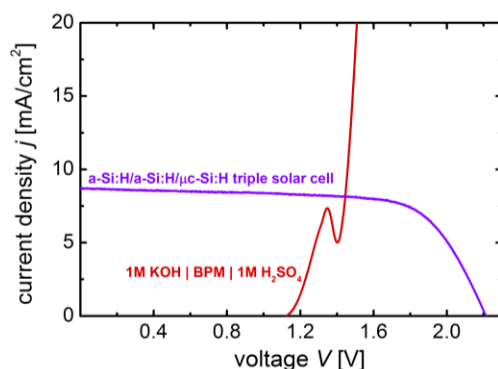

Figure 2.20. Overall polarization characteristics for the H_2O electrolysis using the $CoFe_2O_4$@NF anode and the Ti/Pt cathode in a two-electrode BPM configuration (1M KOH/BPM/1M H_2SO_4) (red curve). The measurement were conducted with a scan rate of 10 mV/s. The overlaid current density–voltage characteristics of the applied a-Si:H/a-Si:H/µc-Si:H triple junction solar cell (purple curve) was measured under simulated AM 1.5G illumination. The crossing point of both curves serves as estimation for the bias-free operation of the solar reactor device shown in Figure 2.19a and 2.19d.

Given its remarkable activity and high electrochemical energy efficiency, the prototype electrolysis reactor can be effectively powered by renewable energy sources, such as photovoltaics.[21-24] In this direction, the conversion of solar energy into chemical fuels energy is a promising route for future conversion and storage concepts. Solar-to-fuel conversion efficiencies using photovoltaics and electrolyzers depends on the efficiency of the two systems. Taking into account electrochemical conversion efficiency above 80 % as reached for $CoFe_2O_4$@NF electrodes, their combination with commercial high efficiency solar cells having 30% conversion efficiencies could result in 24 % solar-to-fuel conversion efficiencies. However, in the present work, to achieve cost-effectiveness, we aimed at reducing the system cost using amorphous silicon solar cells. Thus, we electrically connected the prototype electrolyzer to a low-cost triple junction a-Si:H/a-Si:H/µc-Si:H solar cell with a photovoltaic conversion efficiency of around 13.4% (Figure 2.19a.). [61] In figure 2.20, the system current density-voltage *(j-V)* curve is overlaid with the polarization curve of the electrolyzer device. The crossing point of both *j-V* curves, which can serve to estimate the bias-free operation current density of the solar-driven electrolyzer, lied in the plateau region

of the solar cell characteristics (near the maximum power point) at 1.45 V and 8.2 mA/cm^2. The bias-free measurement of the solar-driven electrolyzer is shown in Figure 2.19d. This result demonstrates that the prototype electrolyzer can be powered only by sunlight energy, providing current densities up to 8.2 ± 0.2 mA/cm^2. The faradaic efficiency for H_2 production, measured by gas chromatography, was found to be close to 100 % over the course of bias-free operation (> 5 hours), as depicted on the right ordinate in Figure 2.19d. The inset in Figure 2.19d shows the theoretical and experimentally determined bias-free H_2 gas production over time, proving that H_2 was the only product formed during electrolysis (besides O_2). With these values, a solar-to-hydrogen conversion efficiency of 10.0 ± 0.2 % was calculated, which is among the record bias-free water splitting efficiencies for thin-film silicon based devices. [62][63] Overall, this example demonstrates that electrolyzers based on $CoFe_2O_4$@NF electrodes can match the stringent requirements for cost-effective renewable energy conversion and storage at large scale.

The enhanced OER catalytic activity of the $CoFe_2O_4$@NF electrodes here presented can be ascribed to the combination of nano-sized active $CoFe_2O_4$ particles with the 3D macroporous structure of the supporting NF, as illustrated in Figure 2.19a. This marriage resulted in a significantly increased contact area between catalysts and electrolytes and provided a greater amount of active sites where OER could take place (see ECSA estimation in the SI, Figures S14c). The dip coating procedure eventually led to an optimum distribution of thinly dispersed $CoFe_2O_4$ NPs (Figure 2.10), which allowed to circumvent the intrinsically inferior electrical conductivity of oxide particles (see low Tafel slopes in Figure 2.12c), while ensuring an impressive stability of the $CoFe_2O_4$@NF electrode (Figure 2.12d and Figure 2.19c).

The large-scale electrode used, the high stability demonstrated and the low electrolyser cell voltages at industrial relevant currents and at ambient and elevated temperature probed the technology relevance of the present system. Values reported here are among the record performance indices for overall water splitting using inexpensive and earth-abundant catalysts. Additionally, the present study assessed their performance on large-scale electrodes in a prototype electrolyzer. While the aspect of process scalability is vital in view of a real-world application, it has neither been experimentally evidenced, nor sufficiently

discussed in previous related studies on OER materials (exemplarily see electrode areas in Table S2). These previous studies focused on laboratory scale electrodes, neglecting critical issues, which have been addressed in the present study, such as homogeneous coverage of active electrocatalyst on large-scale scaffolds, higher chemical resistivity or low-cost and high throughput and yield processing techniques.

In general, the coupling of pure academic with engineered systems is urgently needed to mature renewable fuel production processes and open the pathway towards commercial application. This aspect is successfully addressed by the herein proposed system. In addition, the scalable process of the developed $CoFe_2O_4$@NF electrode paired with the adaptability of the presented prototype reactor bears great benefits and cross-fertilization for a number of related catalytic and photovoltaic technologies. Thus, our electrolyzer concept is not limited to small active electrode areas [64][65] or expensive small-scale photovoltaic structures [66] but can be adapted to large scale designs. Nevertheless, from a scientific point of view, further attention should be devoted to investigate earth-abundant and active HER electrodes. The herein applied Ti/Pt plate served as stable and reliable proof-of-concept electrode, but could be replaced by a cathode system, which does not contain rare materials such as Pt. From a more engineering point of view, the evaluation of different approaches to upscale the photovoltaic structures up to the geometric size of the electrochemical active surface areas could be alluring if integrated photoelectrochemical cell (PEC) systems are envisaged. In this "PEC-farm" approach, multiple medium-scaled electrolyzers, i.e. electrolyzers similar to the herein presented prototype (10-100 cm^2 active photovoltaic and electrochemical electrode areas), could operate independently, while the produced fuels of all the electrolyzers would be collected together. [67] The advantageous feature of this concept is that lower photocurrent densities would be required, which would be beneficial regarding lower overpotential losses and thus, eventually higher overall solar-to-fuel efficiencies. In this regard, it is projected by techno-economic models of large scale, centralized solar H_2 production facilities that overpotential losses at high operating current densities are one of the most important factors in reducing the STH efficiency and thus, increasing the cost of H_2 [68][69]

In total, all these examples manifest the high versatility and cross-fertilization of the herein presented scalable $CoFe_2O_4$@NF electrode and electrolysis system, respectively.

Table S1. The relative atomic concentrations measured by EDS and XPS of $CoFe_2O_4$ coated nickel foam ($CoFe_2O_4$@NF) and carbon cloth ($CoFe_2O_4$@CC) before and after OER test.

Sample	Element / Technique	Co Atomic%	Fe Atomic%	O Atomic%	Ni Atomic%
$CoFe_2O_4$ powder	EDS	13.38	31.66	56.96	0
$CoFe_2O_4$@NF	EDS	1.96	4.94	36.63	56.47
$CoFe_2O_4$@NF After annealing	EDS	2.04	4.50	29.78	63.68
$CoFe_2O_4$@NF After OER	EDS	2.04	5.05	35.24	58.66
$CoFe_2O_4$@NF After annealing	XPS	10.6	33.5		55.9
$CoFe_2O_4$@NF After OER	XPS	10.1	5.6		84.3
$CoFe_2O_4$@CC After annealing	EDS	1.39	2.33	17.84	0
$CoFe_2O_4$@CC After OER	EDS	0.42	0.76	8.01	0
$CoFe_2O_4$@CC After annealing	XPS	63.8	36.2		
$CoFe_2O_4$@CC After OER	XPS	74.5	25.5		

Table S2. Overview of OER performances of Co-Fe based and other nonprecious electrocatalyst materials on Ni foam, indicating the scaffold material, the used electrolyte, the overpotential measured at 20 mA/cm^2, the Tafel slope, the active geometrical area, and the synthesis and coating method. All listed OER electrocatalysts were measured in alkaline electrolytes.

OER catalyst/scaffold	Overpotential at 10 mA/cm^2	Tafel slope	Geo. surface area	Synthesis	Ref.
CoFe$_2$O$_4$/Ni foam	**250 mV, 210 mV (at 50 ºC)**	**51 mV/dec, 42 mV/dec (at 50 ºC)**	**10 cm^2**	**Colloidal**	**This work**
CoFe$_2$O$_4$/C-fiber	378 mV	73 mV/dec	-	Hydrothermal	53
CoFe$_2$O$_4$/glassy C	450 mV	-	0.196 cm^2	Hydrothermal	54
CoFe$_2$O$_4$/NS-rGO	490 mV	70 mV/dec	0.196 cm^2	Hydrothermal	55
CoFe$_2$O$_4$/N-CNF	350 mV	80 mV/dec	0.196 cm^2	Electrospinning	56
CoFe$_2$O$_4$/C-NRA/Ni foam	240 mV	45 mV/dec	0.5 cm^2	Hydrothermal	57
CoFe$_2$O$_4$/rGO	480 mV	67 mV/dec	0.196 cm^2	Hydrothermal	58
CoFe$_2$O$_4$@Co-Fe-Bi/C-cloth	460 mV	127 mV/dec	0.25 cm^2	Hydrothermal	59
CoFe$_2$O$_4$/glassy C	410 mV	82.15 mV/dec	0.196 cm^2	Electrospinning	60
(Co$_{0.52}$Fe$_{0.48}$)$_2$P (free standing)	270 mV	30 mV/dec	0.419 cm^2	Electrochem. etching	61
Mn$_3$O$_4$/Ni foam	270 mV	86 mV/dec	0.25 cm^2	Coprecipitation	62
CO$_3$O$_4$/rm-GO/Ni foam	310 mV	67 mV/dec	1 cm^2	Hydrothermal	63
NiCo$_2$S$_4$ NW/Ni foam	260 mV	40.1 mV/dec	1 cm^2	Hydrothermal	64
Fe$_{0.33}$Co$_{0.67}$OOHPNSAs/CFC	266 mV	30 mV/dec	0.5 cm^2	Hydrothermal	65
MnO$_2$-CoP$_3$/Ti mesh	288 mv	65 mV/dec	4 cm^2	Hydrothermal	66
SnCoFe perovskite	270 mV	42.3 mV/dec	0.419 cm^2	Hydrothermal	67
Single-Atom Au/NiFe Double Hydroxide	237 mV		2 cm^2	Hydrothermal	68
Co$_3$O$_4$ Nanomeshes	307 mV	76 mV/dec	0.419 cm^2	Hydrothermal	69

2.5 Conclusion

In conclusion, we have presented a simple and scalable colloidal synthesis and coating strategy for the homogeneous anchoring of bimetallic $CoFe_2O_4$ NPs on large-scale NF. $CoFe_2O_4$@NF electrodes were demonstrated to be an efficient earth-abundant OER electrocatalysts with ultralow overpotential, large current density, small Tafel slope, and long-term durability in alkaline solution. The improved catalytic performances are believed to originate from the unique synergy between the nano-scaled active $CoFe_2O_4$ NPs and the highly conductive and high area Ni scaffold. The interdiffusion of Ni ions from the Ni scaffold to the $CoFe_2O_4$ NPs may also contribute to improve catalytic performance. Considering cost-effectiveness, facile, as well as reliable fabrication processes, and the outstanding catalytic performance of $CoFe_2O_4$@NFs may hold great potential in future energy conversion and storage devices. Moreover, the performance of the large-scale $CoFe_2O_4$@NF (10 cm^2 geometric active area) was investigated in a prototype electrolysis reactor, where currents of 500 mA were achieved with electrolyzer cell voltages of 1.62 V and 1.53 V at ambient and elevated temperatures, respectively, over prolonged operation times. Overall, the presented electrochemical results paired with the versatile synthetic and coating strategy may stimulate future lines of work, which will be needed to address efficiency improvements and techno-economical questions while assessing cost competitiveness of promising (photo)-electrochemical technologies.

2.6 References

[1]   S.B. Walker, U. Mukherjee, M. Fowler, A. Elkamel, Benchmarking and selection of Power-to-Gas utilizing electrolytic hydrogen as an energy storage alternative, Int. J. Hydrogen Energy. 41 (2016) 7717–7731.

[2]   N.-T. Suen, S.-F. Hung, Q. Quan, N. Zhang, Y.-J. Xu, H.M. Chen, Electrocatalysis for the oxygen evolution reaction: recent development and future perspectives, Chem. Soc. Rev. 46 (2017) 337–365.

[3]   C.C.L. McCrory, S. Jung, I.M. Ferrer, S.M. Chatman, J.C. Peters, T.F. Jaramillo, Benchmarking hydrogen evolving reaction and oxygen evolving reaction

electrocatalysts for solar water splitting devices, J. Am. Chem. Soc. 137 (2015) 4347–4357.

[4]   S. Ardo, D.F. Rivas, M.A. Modestino, V.S. Greiving, F.F. Abdi, E.A. Llado, V. Artero, K. Ayers, C. Battaglia, J.-P. Becker, Pathways to electrochemical solar-hydrogen technologies, Energy Environ. Sci. 11 (2018) 2768–2783.

[5]   M. Ball, M. Weeda, The hydrogen economy–vision or reality?, Int. J. Hydrogen Energy. 40 (2015) 7903–7919.

[6]   T. Rostrup-Nielsen, Manufacture of hydrogen, Catal. Today. 106 (2005) 293–296.

[7]   K. Chakrapani, G. Bendt, H. Hajiyani, I. Schwarzrock, T. Lunkenbein, S. Salamon, J. Landers, H. Wende, R. Schlögl, R. Pentcheva, Role of composition and size of cobalt ferrite nanocrystals in the oxygen evolution reaction, ChemCatChem. 9 (2017) 2988–2995.

[8]   H. Zhou, F. Yu, Q. Zhu, J. Sun, F. Qin, L. Yu, J. Bao, Y. Yu, S. Chen, Z. Ren, Water splitting by electrolysis at high current densities under 1.6 volts, Energy Environ. Sci. 11 (2018) 2858–2864.

[9]   T. Maiyalagan, K.A. Jarvis, S. Therese, P.J. Ferreira, A. Manthiram, Spinel-type lithium cobalt oxide as a bifunctional electrocatalyst for the oxygen evolution and oxygen reduction reactions, Nat. Commun. 5 (2014) 3949.

[10]   M. Tahir, L. Pan, F. Idrees, X. Zhang, L. Wang, J.-J. Zou, Z.L. Wang, Electrocatalytic oxygen evolution reaction for energy conversion and storage: a comprehensive review, Nano Energy. 37 (2017) 136–157.

[11]   M. Li, Y. Xiong, X. Liu, X. Bo, Y. Zhang, C. Han, L. Guo, Facile synthesis of electrospun MFe 2O4 (M= Co, Ni, Cu, Mn) spinel nanofibers with excellent electrocatalytic properties for oxygen evolution and hydrogen peroxide reduction, Nanoscale. 7 (2015) 8920–8930.

[12]   A. Kargar, S. Yavuz, T.K. Kim, C.-H. Liu, C. Kuru, C.S. Rustomji, S. Jin, P.R. Bandaru, Solution-processed CoFe2O4 nanoparticles on 3D carbon fiber papers for durable oxygen evolution reaction, ACS Appl. Mater. Interfaces. 7 (2015) 17851–17856.

[13]   Y. Xu, W. Bian, J. Wu, J.-H. Tian, R. Yang, Preparation and electrocatalytic activity of 3D hierarchical porous spinel CoFe2O4 hollow nanospheres as efficient catalyst for

oxygen reduction reaction and oxygen evolution reaction, Electrochim. Acta. 151 (2015) 276–283.

[14] L. Han, P. Tang, A. Reyes-Carmona, B. Rodríguez-García, M. Torréns, J.R. Morante, J. Arbiol, J.R. Galan-Mascaros, Enhanced activity and acid pH stability of prussian blue-type oxygen evolution electrocatalysts processed by chemical etching, J. Am. Chem. Soc. 138 (2016) 16037–16045.

[15] T. Li, Y. Lv, J. Su, Y. Wang, Q. Yang, Y. Zhang, J. Zhou, L. Xu, D. Sun, Y. Tang, Anchoring CoFe2O4 Nanoparticles on N‑Doped Carbon Nanofibers for High‑Performance Oxygen Evolution Reaction, Adv. Sci. 4 (2017) 1700226.

[16] X. Lu, L. Gu, J. Wang, J. Wu, P. Liao, G. Li, Bimetal‑organic framework derived CoFe2O4/C porous hybrid nanorod arrays as high‑performance electrocatalysts for oxygen evolution reaction, Adv. Mater. 29 (2017) 1604437.

[17] W. Bian, Z. Yang, P. Strasser, R. Yang, A CoFe2O4/graphene nanohybrid as an efficient bi-functional electrocatalyst for oxygen reduction and oxygen evolution, J. Power Sources. 250 (2014) 196–203.

[18] X. Ji, S. Hao, F. Qu, J. Liu, G. Du, A.M. Asiri, L. Chen, X. Sun, Core–shell CoFe 2O4@ Co–Fe–Bi nanoarray: a surface-amorphization water oxidation catalyst operating at near-neutral pH, Nanoscale. 9 (2017) 7714–7718.

[19] Y. Xu, X. Wang, H. Chen, D. Kuang, C. Su, Toward high performance photoelectrochemical water oxidation: combined effects of ultrafine cobalt iron oxide nanoparticle, Adv. Funct. Mater. 26 (2016) 4414–4421.

[20] C. Singh, A. Goyal, S. Singhal, Nickel-doped cobalt ferrite nanoparticles: efficient catalysts for the reduction of nitroaromatic compounds and photo-oxidative degradation of toxic dyes, Nanoscale. 6 (2014) 7959–7970.

[21] A.J. Martín, G.O. Larrazábal, J. Pérez-Ramírez, Towards sustainable fuels and chemicals through the electrochemical reduction of CO2: lessons from water electrolysis, Green Chem. 17 (2015) 5114–5130.

[22] P.K. Shen, C. Xu, Alcohol oxidation on nanocrystalline oxide Pd/C promoted electrocatalysts, Electrochem. Commun. 8 (2006) 184–188.

[23] G. Chen, Electrochemical technologies in wastewater treatment, Sep. Purif. Technol.

38 (2004) 11–41.

[24]   K. Bouzek, M. Paidar, A. Sadilkova, H. Bergmann, Electrochemical reduction of nitrate in weakly alkaline solutions, J. Appl. Electrochem. 31 (2001) 1185–1193.

[25]   F. Urbain, V. Smirnov, J.-P. Becker, A. Lambertz, F. Yang, J. Ziegler, B. Kaiser, W. Jaegermann, U. Rau, F. Finger, Multijunction Si photocathodes with tunable photovoltages from 2.0 V to 2.8 V for light induced water splitting, Energy Environ. Sci. 9 (2016) 145–154.

[26]   A. Lambertz, F. Finger, R.E.I. Schropp, U. Rau, V. Smirnov, Preparation and measurement of highly efficient a‐Si: H single junction solar cells and the advantages of μc‐SiOx: H n‐layers, Prog. Photovoltaics Res. Appl. 23 (2015) 939–948.

[27]   A. Cabot, V.F. Puntes, E. Shevchenko, Y. Yin, L. Balcells, M.A. Marcus, S.M. Hughes, A.P. Alivisatos, Vacancy coalescence during oxidation of iron nanoparticles, J. Am. Chem. Soc. 129 (2007) 10358–10360.

[28]   A. Cabot, M. Ibáñez, P. Guardia, A.P. Alivisatos, Reaction regimes on the synthesis of hollow particles by the Kirkendall effect, J. Am. Chem. Soc. 131 (2009) 11326–11328.

[29]   M. Ibáñez, J. Fan, W. Li, D. Cadavid, R. Nafria, A. Carrete, A. Cabot, Means and limits of control of the shell parameters in hollow nanoparticles obtained by the Kirkendall effect, Chem. Mater. 23 (2011) 3095–3104.

[30]   T. Berestok, P. Guardia, J.B. Portals, S. Estradé, J. Llorca, F. Peiró, A. Cabot, S.L. Brock, Surface Chemistry and Nano-/Microstructure Engineering on Photocatalytic In2S3 Nanocrystals, Langmuir. 34 (2018) 6470–6479. doi:10.1021/acs.langmuir.8b00406.

[31]   T. Berestok, P. Guardia, M. Ibáñez, M. Meyns, M. Colombo, M. V Kovalenko, F. Peiró, A. Cabot, Electrostatic-driven gelation of colloidal nanocrystals, Langmuir. 34 (2018) 9167–9174.

[32]   T. Berestok, P. Guardia, R. Du, J.B. Portals, M. Colombo, S. Estradé, F. Peiró, S.L. Brock, A. Cabot, Metal Oxide Aerogels with Controlled Crystallinity and Faceting from the Epoxide-Driven Cross-Linking of Colloidal Nanocrystals, ACS Appl. Mater. Interfaces. 10 (2018) 16041–16048.

[33]   Q.Q. Xiong, J.P. Tu, S.J. Shi, X.Y. Liu, X.L. Wang, C.D. Gu, Ascorbic acid-assisted

synthesis of cobalt ferrite (CoFe2O4) hierarchical flower-like microspheres with enhanced lithium storage properties, J. Power Sources. 256 (2014) 153–159.

[34] J. Liu, R. Meng, J. Li, P. Jian, L. Wang, R. Jian, Achieving high-performance for catalytic epoxidation of styrene with uniform magnetically separable CoFe2O4 nanoparticles, Appl. Catal. B Environ. 254 (2019) 214–222.

[35] M. Zhang, X. Yang, X. Kan, X. Wang, L. Ma, M. Jia, Carbon-encapsulated CoFe2O4/graphene nanocomposite as high performance anode for lithium ion batteries, Electrochim. Acta. 112 (2013) 727–734.

[36] P. Gründler, A. Kirbs, L. Dunsch, Modern thermoelectrochemistry, ChemPhysChem. 10 (2009) 1722–1746.

[37] G.G. Wildgoose, D. Giovanelli, N.S. Lawrence, R.G. Compton, High‐Temperature Electrochemistry: A Review, Electroanal. An Int. J. Devoted to Fundam. Pract. Asp. Electroanal. 16 (2004) 421–433.

[38] F. Urbain, J.-P. Becker, V. Smirnov, J. Ziegler, F. Yang, B. Kaiser, W. Jaegermann, S. Hoch, A. Maljusch, U. Rau, Influence of the operating temperature on the performance of silicon based photoelectrochemical devices for water splitting, Mater. Sci. Semicond. Process. 42 (2016) 142–146.

[39] S.H. Joo, S.J. Choi, I. Oh, J. Kwak, Z. Liu, O. Terasaki, R. Ryoo, Ordered nanoporous arrays of carbon supporting high dispersions of platinum nanoparticles, Nature. 412 (2001) 169–172.

[40] S. Klaus, Y. Cai, M.W. Louie, L. Trotochaud, A.T. Bell, Effects of Fe Electrolyte Impurities on Ni(OH)2/NiOOH Structure and Oxygen Evolution Activity, J. Phys. Chem. C. 119 (2015) 7243–7254.

[41] F. Urbain, P. Tang, N.M. Carretero, T. Andreu, J. Arbiol, J.R. Morante, Tailoring Copper Foam with Silver Dendrite Catalysts for Highly Selective Carbon Dioxide Conversion into Carbon Monoxide, ACS Appl. Mater. Interfaces. 10 (2018) 43650–43660.

[42] F. Urbain, P. Tang, N.M. Carretero, T. Andreu, L.G. Gerling, C. Voz, J. Arbiol, J.R. Morante, A prototype reactor for highly selective solar-driven CO2 reduction to synthesis gas using nanosized earth-abundant catalysts and silicon photovoltaics, Energy Environ. Sci. 10 (2017) 2256–2266.
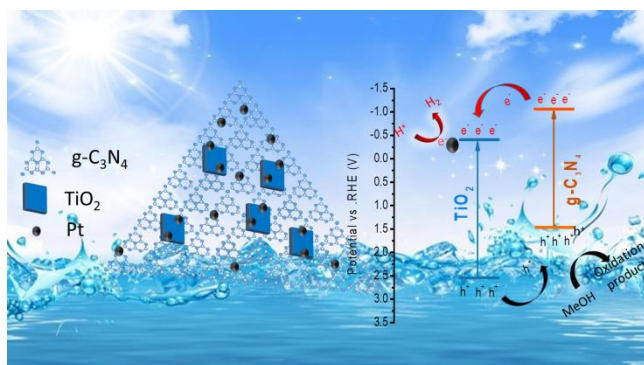
[43] E. Irtem, T. Andreu, A. Parra, M.D. Hernández-Alonso, S. García-Rodríguez, J.M. Riesco-García, G. Penelas-Pérez, J.R. Morante, Low-energy formate production from CO2 electroreduction using electrodeposited tin on GDE, J. Mater. Chem. A. 4 (2016) 13582–13588.

[44] M.D.H. ALONSO, G.P. PÉREZ, T. Andreu, E. Irtem, A. Parra, C. Fábrega, J.R. Morante, Filter-press photoelectrochemical water oxidation and CO2 reduction cell, (2018).

[45] Q. Ma, M. Li, L. Pang, X. Ren, C. Li, X. Xu, S. Liu, Solar‐to‐Hydrogen Efficiency of 9.5% by using a Thin‐Layer Platinum Catalyst and Commercial Amorphous Silicon Solar Cells, ChemCatChem. 8 (2016) 1713–1717.

[46] C. Trompoukis, A. Abass, J.-W. Schüttauf, T. Bosserez, J. Rongé, J. Lauwaert, J.A. Martens, R. Baets, Porous multi-junction thin-film silicon solar cells for scalable solar water splitting, Sol. Energy Mater. Sol. Cells. 182 (2018) 196–203.

[47] Y. Tan, H. Wang, P. Liu, Y. Shen, C. Cheng, A. Hirata, T. Fujita, Z. Tang, M. Chen, Versatile nanoporous bimetallic phosphides towards electrochemical water splitting, Energy Environ. Sci. 9 (2016) 2257–2261.

[48] N. Jiang, B. You, M. Sheng, Y. Sun, Electrodeposited cobalt‐phosphorous‐derived films as competent bifunctional catalysts for overall water splitting, Angew. Chemie Int. Ed. 54 (2015) 6251–6254.

[49] J. Jia, L.C. Seitz, J.D. Benck, Y. Huo, Y. Chen, J.W.D. Ng, T. Bilir, J.S. Harris, T.F. Jaramillo, Solar water splitting by photovoltaic-electrolysis with a solar-to-hydrogen efficiency over 30%, Nat. Commun. 7 (2016) 13237.

[50] F. Urbain, P. Tang, V. Smirnov, K. Welter, T. Andreu, F. Finger, J. Arbiol, J.R. Morante, Multilayered Hematite Nanowires with Thin‐Film Silicon Photovoltaics in an All‐Earth‐Abundant Hybrid Tandem Device for Solar Water Splitting, ChemSusChem. 12 (2019) 1428–1436.

[51] B.M. Klahr, D. Peterson, K. Randolph, E.L. Miller, Innovative Approaches to Addressing the Fundamental Materials Challenges in Advanced Water Splitting Technologies for Renewable Hydrogen Production, ECS Trans. 75 (2017) 3–11.

[52] J.H. Montoya, L.C. Seitz, P. Chakthranont, A. Vojvodic, T.F. Jaramillo, J.K. Nørskov, Materials for solar fuels and chemicals, Nat. Mater. 16 (2017) 70.

[53] A. Kargar, S. Yavuz, T.K. Kim, C.-H. Liu, C. Kuru, C.S. Rustomji, S. Jin, P.R. Bandaru, Solution-processed CoFe2O4 nanoparticles on 3D carbon fiber papers for durable oxygen evolution reaction, ACS Appl. Mater. Interfaces. 7 (2015) 17851–17856.

[54] Y. Xu, W. Bian, J. Wu, J.-H. Tian, R. Yang, Preparation and electrocatalytic activity of 3D hierarchical porous spinel CoFe2O4 hollow nanospheres as efficient catalyst for oxygen reduction reaction and oxygen evolution reaction, Electrochim. Acta. 151 (2015) 276–283.

[55] W. Yan, X. Cao, J. Tian, C. Jin, K. Ke, R. Yang, Nitrogen/sulfur dual-doped 3D reduced graphene oxide networks-supported CoFe2O4 with enhanced electrocatalytic activities for oxygen reduction and evolution reactions, Carbon N. Y. 99 (2016) 195–202.

[56] T. Li, Y. Lv, J. Su, Y. Wang, Q. Yang, Y. Zhang, J. Zhou, L. Xu, D. Sun, Y. Tang, Anchoring CoFe2O4 Nanoparticles on N‐Doped Carbon Nanofibers for High‐Performance Oxygen Evolution Reaction, Adv. Sci. 4 (2017) 1700226.

[57] X. Lu, L. Gu, J. Wang, J. Wu, P. Liao, G. Li, Bimetal‐organic framework derived CoFe2O4/C porous hybrid nanorod arrays as high‐performance electrocatalysts for oxygen evolution reaction, Adv. Mater. 29 (2017) 1604437.

[58] W. Bian, Z. Yang, P. Strasser, R. Yang, A CoFe2O4/graphene nanohybrid as an efficient bi-functional electrocatalyst for oxygen reduction and oxygen evolution, J. Power Sources. 250 (2014) 196–203.

[59] X. Ji, S. Hao, F. Qu, J. Liu, G. Du, A.M. Asiri, L. Chen, X. Sun, Core–shell CoFe 2O4@ Co–Fe–Bi nanoarray: a surface-amorphization water oxidation catalyst operating at near-neutral pH, Nanoscale. 9 (2017) 7714–7718.

[60] M. Li, Y. Xiong, X. Liu, X. Bo, Y. Zhang, C. Han, L. Guo, Facile synthesis of electrospun MFe2O4 (M= Co, Ni, Cu, Mn) spinel nanofibers with excellent electrocatalytic properties for oxygen evolution and hydrogen peroxide reduction, Nanoscale. 7 (2015) 8920–8930.

[61] Y. Tan, H. Wang, P. Liu, Y. Shen, C. Cheng, A. Hirata, T. Fujita, Z. Tang, M. Chen, Versatile nanoporous bimetallic phosphides towards electrochemical water splitting, Energy Environ. Sci. 9 (2016) 2257–2261.

[62] M.Q. Yu, Y.H. Li, S. Yang, P.F. Liu, L.F. Pan, L. Zhang, H.G. Yang, Mn3O4 nano-octahedrons on Ni foam as an efficient three-dimensional oxygen evolution electrocatalyst, J. Mater. Chem. A. 3 (2015) 14101–14104.

[63] Y. Liang, Y. Li, H. Wang, J. Zhou, J. Wang, T. Regier, H. Dai, Co3O4 nanocrystals on graphene as a synergistic catalyst for oxygen reduction reaction, Nat. Mater. 10 (2011) 780.

[64] A. Sivanantham, P. Ganesan, S. Shanmugam, Bifunctional Electrocatalysts: Hierarchical NiCo2S4 Nanowire Arrays Supported on Ni Foam: An Efficient and Durable Bifunctional Electrocatalyst for Oxygen and Hydrogen Evolution Reactions (Adv. Funct. Mater. 26/2016), Adv. Funct. Mater. 26 (2016) 4660. doi:10.1002/adfm.201670166.

[65] S.-H. Ye, Z.-X. Shi, J.-X. Feng, Y.-X. Tong, G.-R. Li, Activating CoOOH Porous Nanosheet Arrays by Partial Iron Substitution for Efficient Oxygen Evolution Reaction, Angew. Chemie Int. Ed. 57 (2018) 2672–2676. doi:10.1002/anie.201712549.

[66] J. Lian, F. Zhang, S. Lu, W. Jiang, Q. Hu, D. Li, B. Zhang, An amorphous Fe‐Co‐P‐C film supported on carbon fiber paper as an efficient electrocatalyst for the oxygen evolution reaction, ChemElectroChem. (n.d.).

[67] D. Chen, M. Qiao, Y. Lu, L. Hao, D. Liu, C. Dong, Y. Li, S. Wang, Preferential cation vacancies in perovskite hydroxide for the oxygen evolution reaction, Angew. Chemie Int. Ed. 57 (2018) 8691–8696.

[68] J. Zhang, J. Liu, L. Xi, Y. Yu, N. Chen, S. Sun, W. Wang, K.M. Lange, B. Zhang, Single-atom Au/NiFe layered double hydroxide electrocatalyst: probing the origin of activity for oxygen evolution reaction, J. Am. Chem. Soc. 140 (2018) 3876–3879.

[69] Y. Li, F.-M. Li, X.-Y. Meng, S.-N. Li, J.-H. Zeng, Y. Chen, Ultrathin Co3O4 nanomeshes for the oxygen evolution reaction, ACS Catal. 8 (2018) 1913–1920.

Chapter 3

2D/2D heterojunction of TiO$_2$ nanoparticles and ultrathin g-C$_3$N$_4$ nanosheets for efficient photocatalytic hydrogen evolution

3.1 Abstract

Photocatalytic hydrogen evolution is considered one of the promising routes to solve the energy and environmental crises. However, developing efficient and low-cost photocatalysts remains an unsolved challenge. In this work, ultrathin 2D g-C$_3$N$_4$ nanosheets are coupled with flat TiO$_2$ nanoparticles as face-to-face 2D/2D heterojunction photocatalysts through a simple electrostatic self-assembly method. Compared with g-C$_3$N$_4$ and pure TiO$_2$ nanosheets, 2D/2D TiO$_2$/g-C$_3$N$_4$ heterojunctions exhibit effective charge separation and transport properties that translate into outstanding photocatalytic performances. With the optimized heterostructure composition, stable hydrogen evolution activities threefold and fourfold higher than those of pure TiO$_2$ and g-C$_3$N$_4$ are consistently obtained. Benefiting from the favorable 2D/2D heterojunction structure, the TiO$_2$/g-C$_3$N$_4$ photocatalyst yields H$_2$ evolution rates up to 3875 μmol·g^{-1}·h^{-1} with an AQE of 7.16% at 380 nm.

Key words: hydrogen evolution, 2D/2D heterojunction, charge separation

3.2 Introduction

Owing to the abundance of low-cost solar energy, the numerous uses of hydrogen and its advantages as an energy carrier, the photocatalytic generation of hydrogen is a highly appealing process.[1,2] However, the cost-effective photogeneration of hydrogen requires high activity and stable photocatalysts, which development has been a long-standing goal. Over the past decades, numerous semiconductors have been tested as photocatalysts for hydrogen evolution. Among them, titanium dioxide (TiO_2) has received special attention owing to its stability, high abundance and low toxicity, being the earliest to be discovered and becoming the first to be industrialized.[3] Nevertheless, due to its wide bandgap and relatively fast charge recombination rate, its applicability has been strongly limited. Numerous strategies have been proposed to improve the photocatalytic performance of TiO_2, facilitating charge separation and promoting efficiency and activity,[4–7] including the control of its particle facets and morphology [8–11], its modification with co-catalysts [12–15], and its coupling with other semiconductors to form heterostructures. [16–23]

Graphite carbonitride ($g\text{-}C_3N_4$) with a layered structure similar to graphite, high chemical stability and low cost has received increasing interest in recent years.[24,25] In particular, as a polymeric semiconductor, $g\text{-}C_3N_4$ has been recently reported as a promising candidate photocatalyst due to its unique structure and electronic characteristics, with a 2.7 eV bandgap that allows absorbing part of the visible spectrum.[26,27] Besides, two-dimensional (2D) $g\text{-}C_3N_4$ nanosheets, benefiting from a huge specific surface area and a suitable band structure, have shown especially interesting properties and offer an excellent platform to produce heterojunctions with other semiconductors. [28–31]

Recently, 2D/2D heterojunctions have been demonstrated to provide great advantages to improve charge separation.[32,33] 2D/2D heterojunctions simultaneously maximize the interface and surface areas, i.e. the charge transfer between the two materials and the interaction with the media, which can potentially improve photocatalytic activities.

In the present work, we report the first synthesis of 2D/2D $TiO_2/g\text{-}C_3N_4$ heterostructures. Such composite materials are produced from the electrostatic assembly of 2D anatase TiO_2 flat nanoparticles synthesized through a simple colloidal method with 2D ultrathin $g\text{-}C_3N_4$.

The produced heterostructures are tested as photocatalysts for hydrogen evolution under simulated solar light irradiation. The excellent hydrogen evolution performance obtained after optimizing the weight contents of TiO_2 and $g-C_3N_4$ within 2D/2D heterojunction are rationalized using photoluminescence, photocurrent and impedance spectroscopy analysis.

3.4 Experiment

Synthesis of bulk $g-C_3N_4$ (bCN) and ultrathin $g-C_3N_4$ (uCN): Bulk $g-C_3N_4$ powder was synthesized by thermal polymerization of urea. Briefly, 10 g of urea (99%, Acros Organics) was placed into a ceramic crucible. The crucible was covered and heated to 550 °C at a ramp rate of 2°C min^{-1} for 4 h under air atmosphere. After cooling to room temperature, the resulting light-yellow solid was ground with the mortar to obtain the bulk $g-C_3N_4$ powder. To obtain ultrathin $g-C_3N_4$ (uCN), bulk $g-C_3N_4$ (2.0 g) was placed in a covered ceramic crucible and it was heated to 520 °C with a ramp rate of 5 °C min^{-1} for 2 h under air atmosphere to obtain a light yellow powder.

Synthesis of TiO_2 nanosheets: Titanium dioxide nanoparticles were prepared using a colloidal method. All the syntheses were performed using standard airless techniques[34,35] Typically, 10 mL of oleylamine (OAm, 80-90%, Acros Organics), 10 mL of octadecene (ODE, 90%, Sigma-Aldrich) and 1 mL of oleic acid (OAc, 90%, Sigma-Aldrich) were loaded in a three-neck flask and degassed under vacuum at 120 °C for 1 h while being strongly stirred using a magnetic bar. Then 300 mg of TiF_4 (99%, Sigma) was added in a mixed solution of 2 mL OAm, 3 mL OAc and 6 mL ODE and sonicated for 0.5 h to prepare a precursor solution. Subsequently, under nitrogen atmosphere, 10 mL of the precursor solution were slowly added to the reaction flask, which was then heated to 290 °C at a rate of 5°C min^{-1} and maintained for 1 h. The solid product by centrifuged and washed with acetone and hexane three times. The particles were finally dispersed in hexane at a concentration of 10 mg/mL.

Ligand removal from TiO_2 nanoparticles: In a typical process, 10 mL of a TiO_2 dispersion in hexane (2 mg/mL) was combined with 10 mL acetonitrile to form a two-phase mixture. Then 1 mL of a HBF_4 solution (48%, Sigma-Aldrich) was added. The resulting solution was sonicated until the particles transferred from the upper to the bottom layer. The surface-modified

particles were washed with ethanol and a 1 mol/L sodium hydroxide (85%, Sigma-Aldrich) aqueous solution three times to remove the residual fluoride ions and ligands. The particles were then washed with water to adjust the PH close to neutral. Finally, the particles were dispersed in 10 mL of water with a small amount of DMF.

Synthesis of 2D/2D TiO$_2$/ultrathin g-C$_3$N$_4$ (TiO$_2$/uCN) composite: TiO$_2$/uCN heterojunctions were produced by an electrostatic self-assembly method. Briefly, 20 mg of as prepared ultrathin g-C$_3$N$_4$ was dissolved in 10 mL of ultrapure water and sonicated for 1 h. The solution was then mixed with an ethanol solution of ligand-removed TiO$_2$ nanoparticles with a weight ratio of 1:2, 1:1 and 2:1. The mixed solution was stirred for 24 hours after 1 h of sonication. The obtained composite was collected by centrifuging, it was washed with ethanol 2 times, and it was finally dried at 60°C for 12 h. The collected materials were named T$_1$/uCN$_2$, T$_1$/uCN$_1$, T$_2$/uCN$_1$ based on the different TiO$_2$/ultrathin g-C$_3$N$_4$ weight ratios. TiO$_2$/bulk g-C$_3$N$_4$ (T/bCN) samples were prepared using the same procedure. For photocatalytic measurements, 1 wt% of Pt was loaded on the surface of the photocatalysts by a photoreduction method.

Photocatalytic hydrogen evolution procedure: Photocatalytic hydrogen evolution experiments were conducted in a Perfect Light Labsolar-Ⅲ (AG) photoreactor (Pyrex glass) connected with a closed-cycle gas circulation system. In a typical experiment, 20 mg photocatalyst was dispersed in 100 ml solution containing 10 ml methanol and 1 wt% Pt cocatalyst (40 uL 25.625 mmol/L H$_2$PtCl$_6$ aqueous solution). The mixed solution was bubbled with N2 for 30 min to ensure anaerobic state and illuminated 30 min with UV light before simulated solar light irradiation to ensure the completely loading of Pt. The incident light wavelength was provided by a 300 W Xe lamp with a AM 1.5 filter, and the reaction condition was kept at room temperature. The generated gas was analyzed by Labsolar-III (AG) gas chromatography furnished with thermal conductivity detector, and the high-purity argon was carrier gas.

Characterization: The particle size and shape of the samples were characterized by scanning electron microscopy (SEM) using in a Zeiss Auriga microscope (Carl Zeiss, Jena, Germany) with an energy-dispersive X-ray spectroscopy (EDS) detector at 20 kV to study the composition and transmission electron microscopy (TEM) using a ZEISS LIBRA 120, operating

at 120 kV. High-resolution TEM (HRTEM) studies were conducted using a field emission gun FEI Tecnai F20 microscope at 200 kV with a pointto-point resolution of 0.19 nm. Powder X-ray diffraction (XRD) patterns were collected directly from the as-synthesized nanoparticles dropped on Si(501) substrates on a Bruker AXS D8 Advance X-ray diffractometer with Nifiltered (2 μm thickness) Cu Kα radiation (λ = 1.5406 Å) operating at 40 kV and 40 mA. A LynxEye linear position-sensitive detector was used in reflection geometry. Characterization of the surface was done by X-ray photoelectron spectroscopy (XPS) on a SPECS system equipped with a XR50 source operating at 250 W and a Phoibos 150 MCD-9 detector. The pass energy of the hemispherical analyzer was set at 20 eV, and the energy step of high-resolution spectra was set at 0.05 eV. The pressure in the analysis chamber was always below 10−7 Pa. The specific surface area and analysis of the pore size distribution were obtained from nitrogen adsorption/desorption isotherms on Tristar II 3020 Micromeritics system. Fourier transform infrared (FTIR) spectra were recorded on an Alpha Bruker spectrometer. The optical properties of samples were analyzed by a UV–vis spectrophotometer (UV-2600, Shimadzu). Photoluminescence (PL) spectra of aqueous photocatalysts suspension (0.1 g/L) were collected on a fluorescence spectrophotometer (F-7000, Hitachi), and the wavelength of excitation light is 370 nm. The decay time measurements were carried out on a compact fluorescence lifetime spectrometer (Quantaurus-Tau, C11367, HAMAMATSU), and an LED lamp (365 nm) was used as an excitation source.

Electrocatalysis measurement: The photocurrent and electrochemical impedance spectroscopy (EIS) investigations were carried out on a CHI-760 electrochemical analyzer using a three-electrode cell system with indium tin oxide (ITO)/sample as the working electrode, platinum net as the counter electrode and standard calomel electrode (SCE) as the reference. A 300 W Xe lamp with a cut-off filter of 420 nm was utilized as the light source. Furthermore, the ITO/sample electrodes were fabricated as follows: first, samples (5 mg) were added into solutions containing DI water (0.5 mL), ethanol (0.5 mL) and Nafion (20uL) and ultrasonicated for 20 min. Then, the resultant sample slurry (0.1 mL) was casted onto pre-cleaned ITO glass and then dried at 60℃ for 2 h.

Apparent quantum efficiency (AQE) calculations: The apparent quantum efficiency can be

evaluated from following equation:

$$AQE = \frac{2 \times n_{H_2} \times N_A}{N}$$

n_{H_2} is the number of evolved H_2 molecules, N_A is Avogadro number (6.02×10^{23}) and N represents the number of incident photons, which can be calculated from following equation :

$$N = \frac{\text{light intensity} \, (W \, cm^{-2}) \times \text{illumination area} \, (cm^2)}{\frac{hc}{\lambda}}$$

h is plank constant (6.626×10-34 J·s = 4.136×10-15 eV·s), c is the speed of light (3.0×108 m·s^{-1}), λ is the wavelength of light (380 nm, 420 nm).

Test method for light with wavelengths of 380 and 420 nm. The photocatalytic systems with 200 mg catalyst and 100 mL solution (90 mL DI water, 10 mL methanol and 1 wt% Pt cocatalyst). The mixed solution was bubbled with N_2 for 30 min to ensure anaerobic condition and illuminated 30 min with ultraviolet light before simulated solar light irradiation to measure H_2 evolution.The test time was 1h and irradiated area is 28.26 cm^2.

The light intensity and resulting n_{H_2} are listed in the table 3.2.

3.5 Result and discussion

TiO_2/g-C_3N_4 heterostructures were obtained by the electrostatic assembly of TiO_2 nanoparticles and ultrathin g-C_3N_4 nanosheets (Figure 3.1, see Experimental section for details). Colloidal TiO_2 nanoparticles were produced in the presence of OAm and OAc using TiF_4 as the Ti precursor. Low-resolution TEM images exhibited the TiO_2 particles to have a flat square morphology with a side length of 30-50 nm and a thickness of about 5-10 nm. g-C_3N_4 nanosheets were produced by the thermal etching of bulk g-C_3N_4. As observed by scanning electron microscopy (SEM, Figure 3.2) and transmission electron microscopy (TEM, Figure 3.4b) characterization, bCN and uCN displayed significantly different morphologies. The uCN showed a thin nanosheet-based structure pointing at at the occurrence of a layer etching during the thermal process. Figure 3.2c displays the nitrogen adsorption-desorption isotherms of bCN and uCN, which further proved uCN (85.7m2/g) has a large specific surface area than bCN (46.3m2/g).
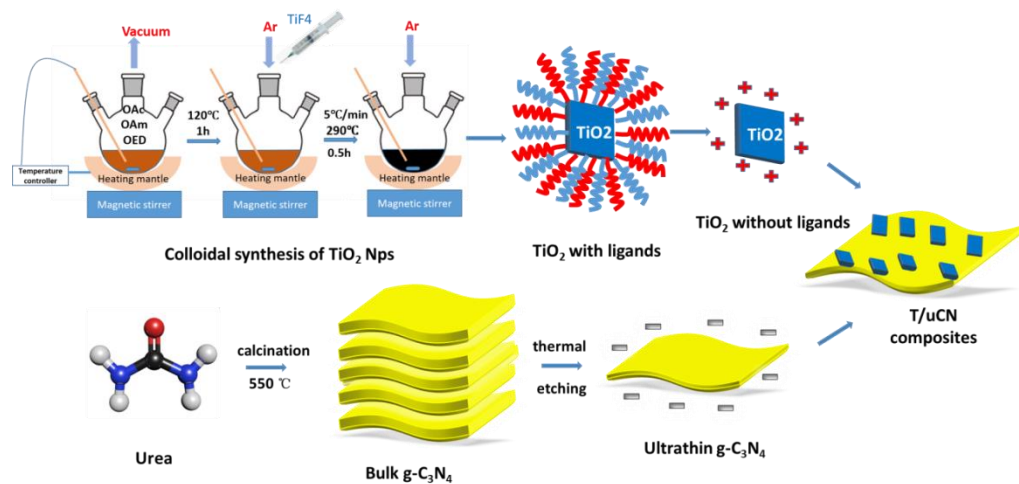
Figure 3.1. Schematic illustration of the process used to produce 2D/2D TiO$_2$/uCN composite

To positively charge the surface of the TiO$_2$ particles, enable their dispersion in an aqueous solution and promote charge transfer with the media, the organic ligands attached to the particle surface were removed using HBF$_4$ (Figure 3.3a). As observed by zeta-potential analysis, while the g-C$_3$N$_4$ nanosheets were negatively charged (V=-33.8 mV), after ligands removal the TiO$_2$ particles were positively charged (V=+18.6 mV), which enabled the electrostatic self-assembly of the two components.[36] Indeed, when combining solutions of the two types of material, a light yellow precipitate was formed. The precipitate was composed of large uCN nanosheets containing numerous TiO$_2$ particles attached to their surface. High-resolution TEM (HRTEM) analyses showed the TiO$_2$ particles to lie flat on the surface of uCN forming 2D/2D heterostructures (Figure 3.4d).
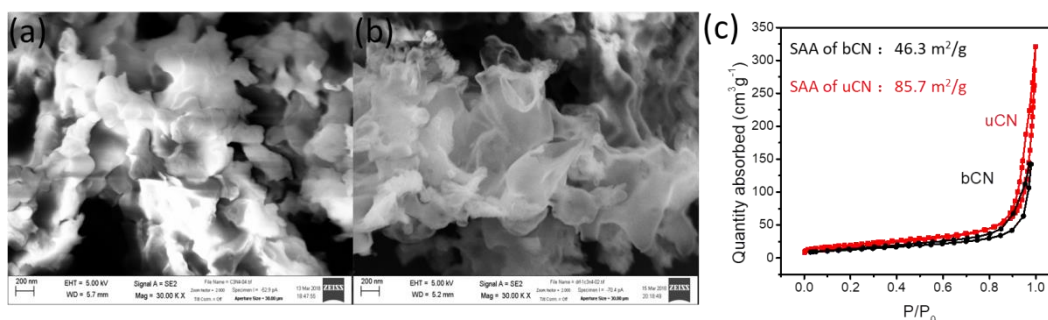
Figure 3.2. SEM image of (a)bulk g-C$_3$N$_4$ and (b)ultrathin g-C$_3$N$_4$. (c) nitrogen adsorption-desorption isotherms of bCN and uCN
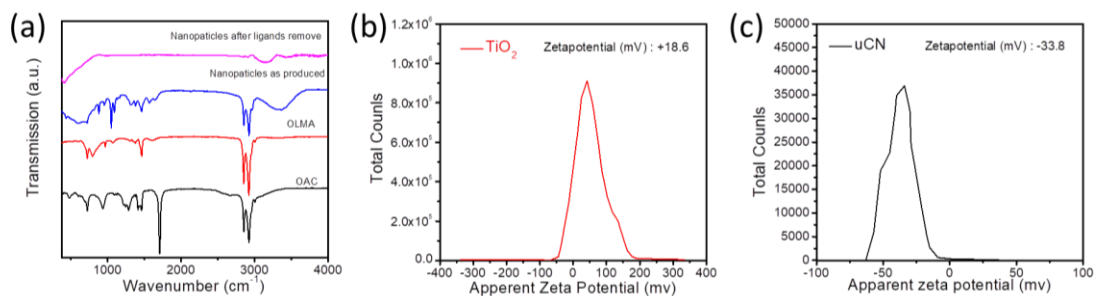
Figure 3.3. (a) FTIR spectra of OAC, OLMA and TiO_2 before and after ligands removal. (b) Zeta potential distribution spectrum of (b) TiO_2 after ligands removal and (c) uCN.
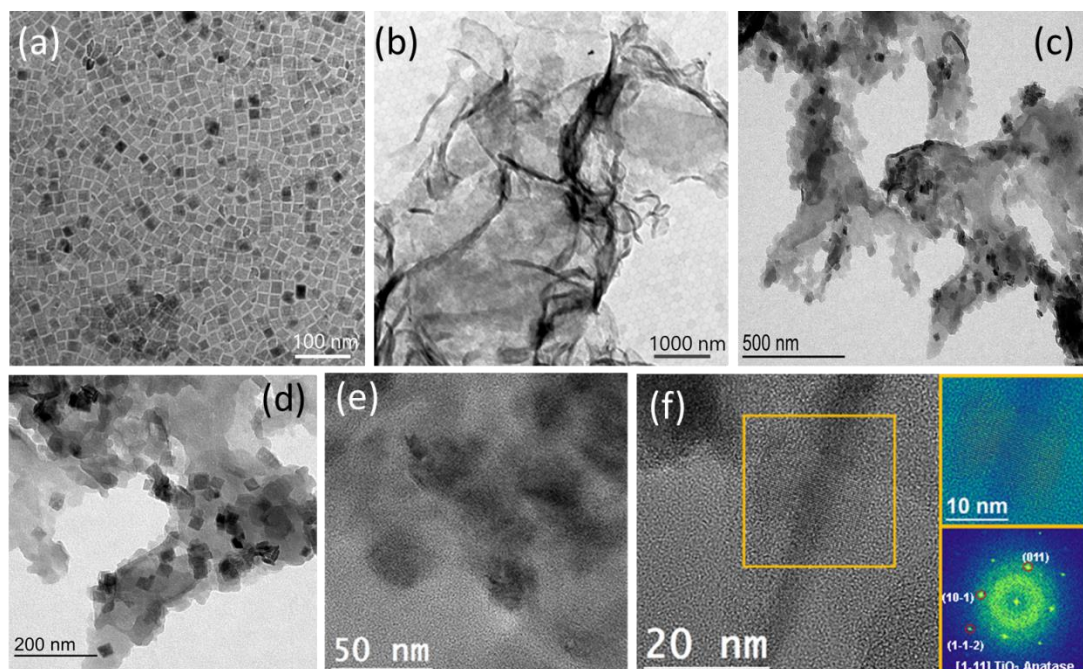
Figure 3.4. (a-c) Representative TEM images of TiO_2 nanoparticles (a); g-C_3N_4 nanosheets (b); and (c) T_1/uCN$_1$ composite. (e,f) HRTEM images of T_1/Ucn$_1$. A magnified detail (top right) of the orange squared region in the HRTEM image and its corresponding indexed power spectrum (bottom right) is shown, revealing the TiO_2 anatase phase (space group =I41/amd) with a=b=3.7840 Å, and c=9.5000 Å. TiO_2 lattice fringe distances were measured to be 0.233 nm, 0.352 nm, and 0.348 nm, at 41.30º and 139.38º which could be interpreted as the anatase TiO_2 phase, visualized along its [1-11] zone axis.

SEM-EDS elemental maps (Figure 3.5) displayed a homogeneous distribution of C, N, O, and Ti, demonstrating a uniform distribution of TiO_2 particles on the uCN surface at the

microscale. On the other hand, quantitative EDX analyses showed the TiO_2:CN weight ratio to be close to that of the nominal combination of each phase: TiO_2:CN = 0.47 for T_1/uCN; TiO_2:CN = 1.1 for T_2/uCN; and TiO_2:CN = 1.9 for T_3/uCN, obtained from mixing 1:2, 1:1 and 2:1 mass ratios of particles, respectively (Figure 3.6).
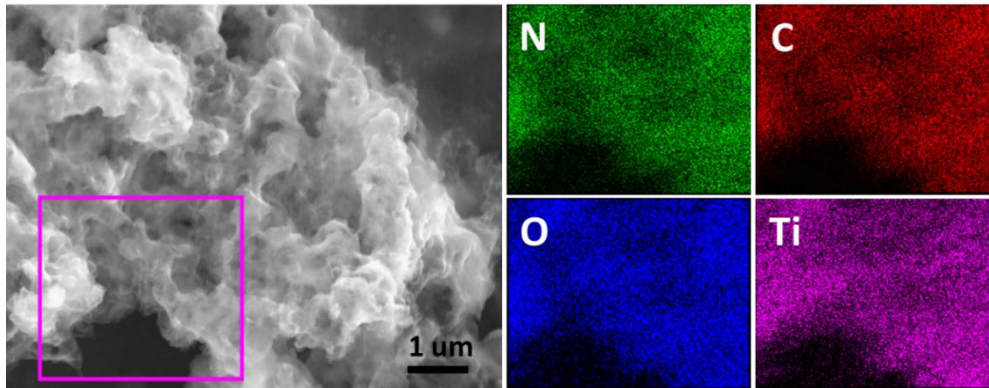
Figure 3.5. SEM image and EDS compositional maps of a T_1/uCN$_1$ composite
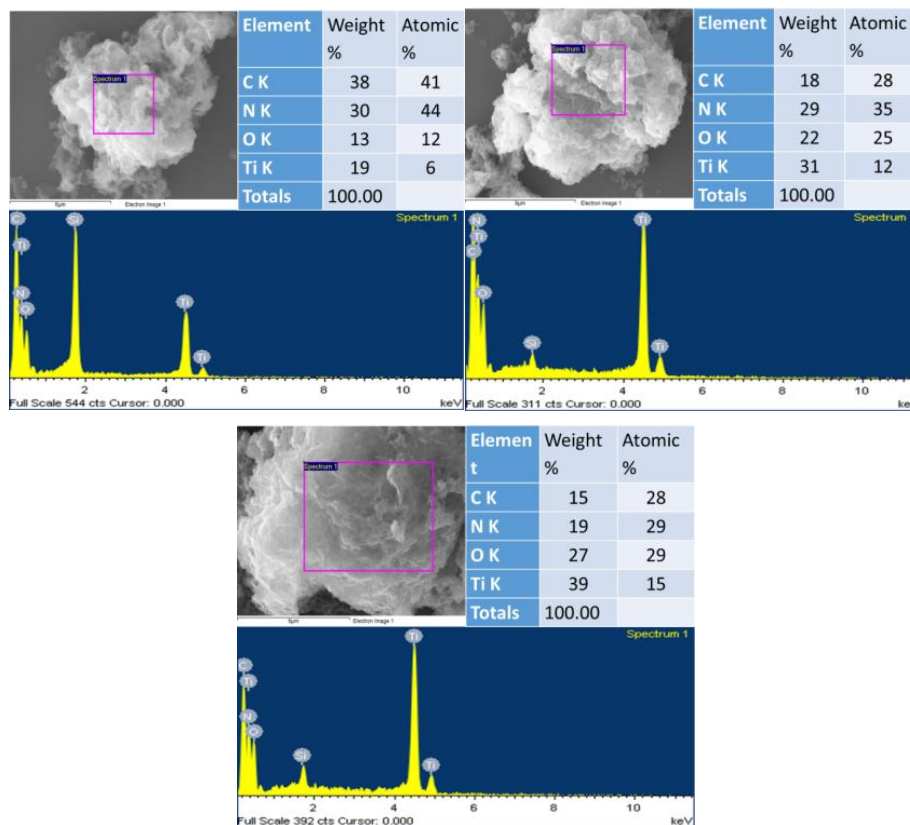
Figure 3.6. SEM image of T_1/uCN$_2$, T_1/uCN$_1$ and T_2/uCN$_1$ and corresponding EDS spectrum

Figure 3.7a displays the X-ray diffraction (XRD) patterns of bCN, uCN, TiO_2 and T/uCN samples. The XRD peaks at 25.2∘ (101), 38.0∘ (004), 47.7∘ (200) and 54.8∘ (211) are associated with the anatase TiO_2 phase (JCPDS No. 21-1272).[37] Besides, the characteristic diffraction peaks at

13.1° and 27.4° correspond to the (002) and (100) planes of g-C$_3$N$_4$ (JCPDS No. 87-1526).[38] The characteristic diffraction peaks of both TiO$_2$ and g-C$_3$N$_4$ can be observed in all the composites samples, confirming the coexistence of anatase TiO$_2$ and g-C$_3$N$_4$.

The x-ray photoelectron spectroscopy spectra of TiO$_2$, uCN and T/uCN are displayed in Figure 3.7b-f. As observed from the survey XPS spectrum, besides Ti, C, O and N, a residual amount of F from the TiF$_4$ precursor used to prepare the TiO$_2$ particles was also present in the final material (Fig. 3b). The high-resolution C 1s XPS spectrum of uCN showed two main contributions at 288.2 eV, and 284.8 eV, which were assigned to C-(N3) and C–C/C=C, respectively (Figure 3c). Compared with pure uCN, the peak for C-(N3) of the T$_1$/uCN$_1$ sample was slightly shifted to 288.2 eV. The high-resolution N 1s XPS spectra were deconvoluted using three contributions at binding energies of 398.1 eV, 499.4 eV, and 400.5 eV for uCN and 398.1 eV, 499.6 eV, and 400.7 eV for T/uCN (Figure 3d). These three contributions were assigned to N-(C$_2$), N-(C$_3$) and N-H$_x$ groups of the heptazine framework. The small shifts detected for C and some of the N components might be related to a certain degree of charge between the TiO$_2$ and the CN phases. Figure 3e displays the high-resolution Ti 2p XPS spectra of TiO$_2$ and T/uCN. Both samples show two strong peaks at approximately 458.7 and 464.5 eV which are assigned to the Ti 2p$_{3/2}$ and Ti 2p$_{1/2}$ levels of Ti within a TiO$_2$ environment. The high-resolution O 1s XPS spectra of TiO$_2$ and T/uCN were fitted with two peaks at 530.4 eV and 531.8 eV, which were associated with oxygen within the TiO$_2$ lattice and oxygen-containing surface adsorption groups such as surface hydroxyl, respectively (Figure 3f).
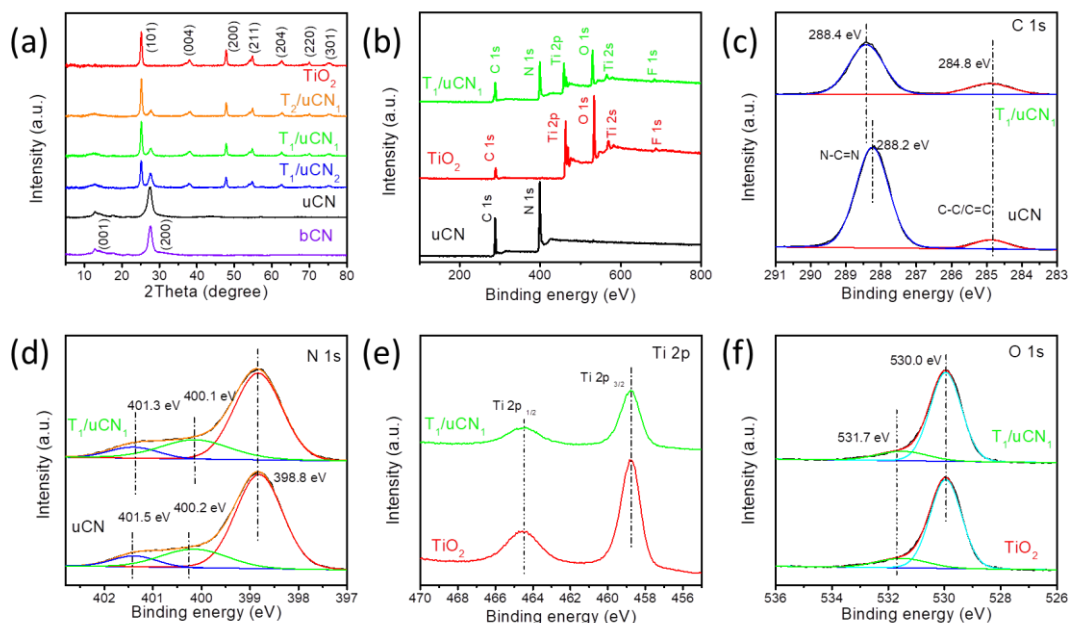
Figure 3.7. (a) XRD patterns of TiO_2, uCN and T/uCN. (b) XPS survey spectrum of TiO_2, uCN and T/uCN; High-resolution XPS spectra at the regions (c) C 1s, (d) N 1s, (e) Ti 2p, and (f) O 1s.

The UV-vis spectra showed the UV absorption edge of TiO_2 particles and uCN nanosheets at about 390 nm and 445 nm, respectively (Figure 3.8a). T/uCN composites showed a similar onset absorption edge as uCN, but an increased absorption below 400 nm related to the presence of the TiO_2 component. All TiO_2 and T/uCN samples presented a small absorption in the range 500-800 nm related to a small amount of F ion doping. According to the Kubelk-Munk function, the band gaps of TiO_2 and uCN samples were calculated at about 3.02 eV and 2.62 eV, respectively (Figure 3.8b).

According to Mott-Schottky analyses (Figures 3.8c,d), the flat band potentials of TiO_2 and uCN were -0.36 V and -0.86 V vs. the normal hydrogen electrode (NHE). The valence band (VB) XPS spectra of TiO_2 and uCN showed the valence band maximum (VBM) to be located at 2.89 eV and 2.46 eV from the Fermi level, respectively. Since the flat band potentials are approximately equal to the Fermi level,[39,40] the VBM was located at 2.53 eV and 1.60 eV with respect to the NHE for TiO_2 and uCN, respectively. Then, taking into account the calculated band gaps ($E_g = E_{vb} - E_{cb}$),[41] the conduction band minimum (CBM) was located at 0.49 and -1.02 for TiO_2 and uCN, respectively. Figure 3.8f displays the energy level diagram calculated for TiO_2 and uCN samples. According to this scheme, when combining uCN with

TiO$_2$, a type II heterojunction is formed, involving electron transfer from the uCN to the TiO$_2$ particles. Besides, it is predicted that within such heterostructure, photogenerated electrons will move towards the TiO$_2$ phase and photogenerated holes towards the uCN, respectively.
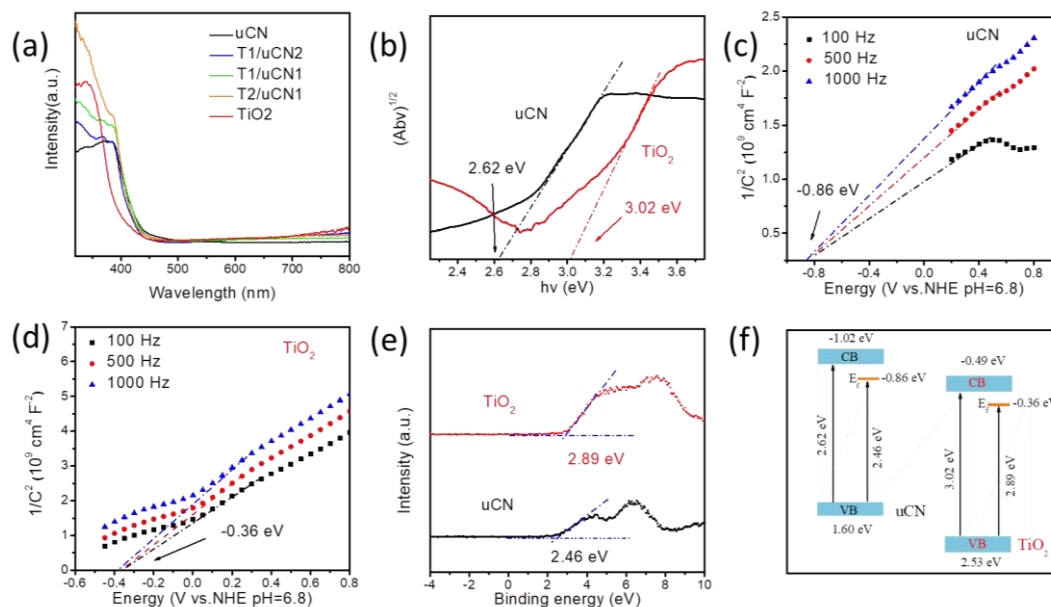

Figure 3.8. (a) UV-vis absorption spectra. (b) Kubelka-Munk transformed function of TiO$_2$ and uCN. (c,d) Mott–Schottky plots of uCN (c) and TiO$_2$ (d). (e) Valence band XPS spectrum of TiO$_2$ and uCN. (f) Diagram of the band structure of TiO$_2$ and uCN.

To analyze the photocatalytic activity towards hydrogen generation, all the samples were loaded with 1 wt% platinum as co-catalyst. Figure 3.9 displays the photocatalytic hydrogen generation from bCN, uCN, TiO$_2$, and TiO$_2$/uCN composites for 4 h under simulated solar light and using methanol as a sacrificial agent. For TiO$_2$, a high hydrogen evolution rate (HER) up to 1449 μmol·g^{-1}·h^{-1} was obtained. Besides, a notable HER was also obtained from uCN (801 μmol·g^{-1}·h^{-1}), well above that of bCN (599 μmol·g^{-1}·h^{-1}), which is consistent with the larger surface area provided by the thin layered structure of uCN. All the TiO$_2$/uCN composites displayed a significant HER improvement with respect to pure TiO$_2$ or uCN. The highest HERs were obtained with the TiO$_2$/uCN composites having a 1:1 weight ratio of the two components, reaching a HER of 3875 μmol·g^{-1}·h^{-1}, which is 2.7 and 4.8 times higher than that of TiO$_2$ and uCN, respectively. The observed synergistic effect obtained when mixing both materials is related to the transfer and thus separation of photogenerated carriers at

the 2D/2D heterojunctions, which prevents their recombination.

As a reference, we also measured the HER of TiO_2/bCN composites with the optimized weight ratio 1:1 (T_1/bCN_1). As observed in Figures 5c, the HER of T_1/bCN_1 also showed an obvious improvement with respect to that of pure TiO_2 and bCN, but the highest HER values were well below those of 2D/2D T/uCN heterojunctions having extended surface and interface areas.

The apparent quantum yield (AQY) of the process was evaluated under 380 nm (4.51 $mW \cdot cm^{-2}$) and 420 nm (12.14 $mW \cdot cm^{-2}$) irradiation (Table 3.1). For T_1/uCN_1, the AQY at 380 nm and 420 nm was estimated at 7.61 % and 2.64% respectively, which is consistent with UV-vis spectroscopy results (Figure 3.9d).
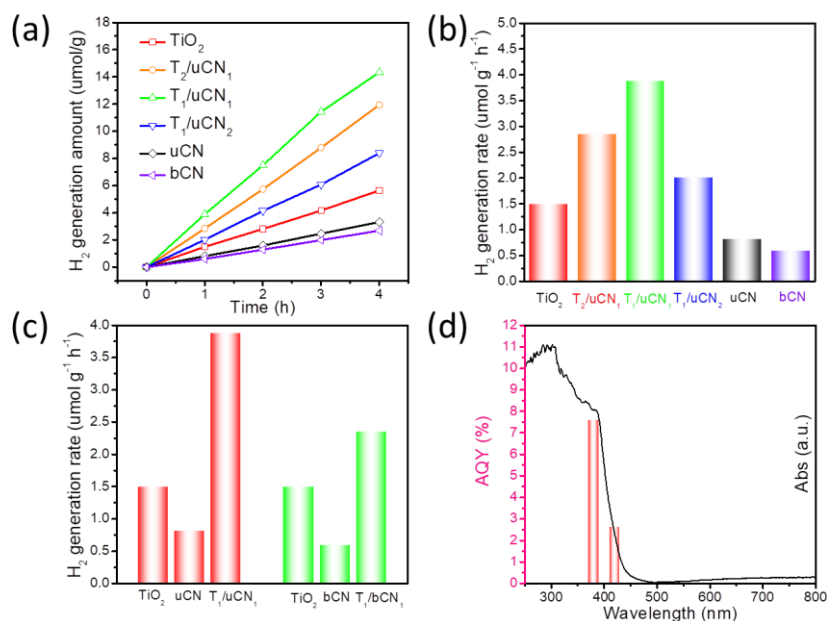
Figure 3.9. (a) Photocatalytic hydrogen generation on bCN, TiO_2 and T/uCN samples during four hours under simulated solar light illumination. (b) Photocatalytic hydrogen peroxide generation rate of bCN, TiO_2 and T/uCN samples (c) H_2 production rate contrast between T_1/uCN_1 and T_1/bCN_1. (d) Wavelength-dependent AQY of T_1/uCN_1.

Table 3.1. AQE values with different incident light wavelengths for T_1/uCN_1

Wavelength (nm)	Light intensity (mW/cm^2)	T_1/uCN_1	
		n H$_2$ (umol)	AQE (%)
380	4.51	58.3	7.16
420	12.14	55.8	2.67

Figure 3.10a displays the positive photocurrents measured from uCN, TiO$_2$ and TiO$_2$/uCN samples under simulated solar irradiation. All the composite T/uCN electrodes displayed significantly higher photocurrents than pure TiO$_2$ and uCN, especially the T_1/uCN_1 electrode that showed the highest photocurrents, fourfold higher than those of uCN and TiO$_2$. This result further confirmed an improvement of the charge separation/transport with the formation of the 2D/2D heterojunction.

Electrochemical impedance spectroscopy (EIS) was further employed to identify the charge transport dynamics. Figure 3.10b displays the Nyquist plot of the impedance spectra of TiO$_2$, uCN and T_1/uCN_1. Consistently with previous results, the T_1/uCN_1 electrode presented a much smaller arc radius than the other two samples, confirming a much lower charge transfer resistance with the formation of the 2D/2D TiO$_2$/uCN heterojunction.[42]

A strong photoluminescence (PL) peak was obtained under 370 nm light excitation from the uCN sample at about 455 nm, which is ascribed to the radiative band-to-band recombination of photogenerated charge carriers. When incorporating increasing amounts of TiO$_2$, the PL intensity of T/uCN was progressively quenched (Figure 3.10c). Additional time-resolved PL (TRPL) spectra under 365 nm light excitation (Fig 3.10d and Table 3.2) allowed calculating significantly longer PL lifetimes (4.72 ns) for T_1/uCN_1 samples than for TiO$_2$ (3.15 ns) and uCN (3.51 ns), which points at an effective separation of photogenerated charge carriers within the TiO$_2$/uCN heterostructures.[43]
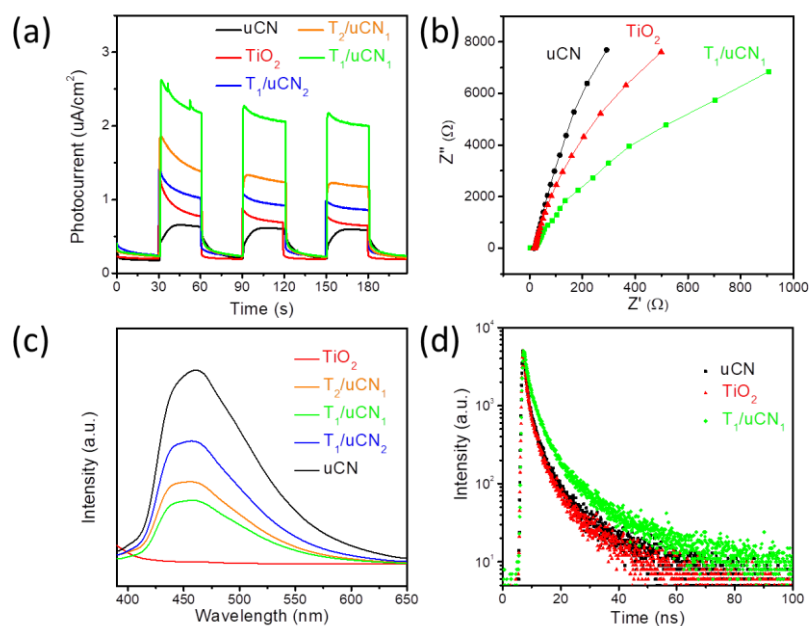
Figure 3.10. (a) Photocurrent response curves of bCN ,TiO$_2$ and T/uCN samples; (b) Electrochemical impedance spectroscopy (EIS) Nyquist plots of bCN ,TiO$_2$ and T$_1$/uCN$_1$ sample; (c,d) PL spectra and TRPL decay of bCN ,TiO$_2$ and T/uCN samples.

Table 3.2. Exponential decay-fitted parameters of fluorescence lifetime of uCN, TiO$_2$ and T$_1$/uCN$_1$

Sample	uCN	TiO$_2$	T$_1$/uCN$_1$
τ (ns)	3.51	3.15	4.72
τ_1 (ns)	1.04	0.96	1.49
τ_2 (ns)	6.03	5.47	6.93

Based on the above results, the photocatalytic mechanism displayed in Figure 3.11 is proposed for hydrogen generation in T/uCN heterojunction photocatalysts. While both TiO$_2$ and uCN can generate electrons and holes under simulated solar light irradiation, the photogenerated electron-hole pairs in pure TiO$_2$ and uCN rapidly recombine, resulting in moderate HERs. Through the formation of a 2D/2D T/uCN heterostructure, the photogenerated electrons remain or are transferred to the TiO$_2$ CB because the TiO$_2$ CBM is located 0.53 eV below that of CN. Similarly, photogenerated holes remain or are driven to the uCN VB, which is located 0.93 eV above that of TiO$_2$. Electrons at the TiO$_2$ CB migrate to the platinum, which has a larger work function, thus a lower Fermi level, from where they

are transferred to adsorbed H^+ to produce H_2. On the other hand, holes react with sacrificial methanol at the CN surface. Consequently, the photocatalytic hydrogen evolution process using sacrificial methanol can be described as follows:
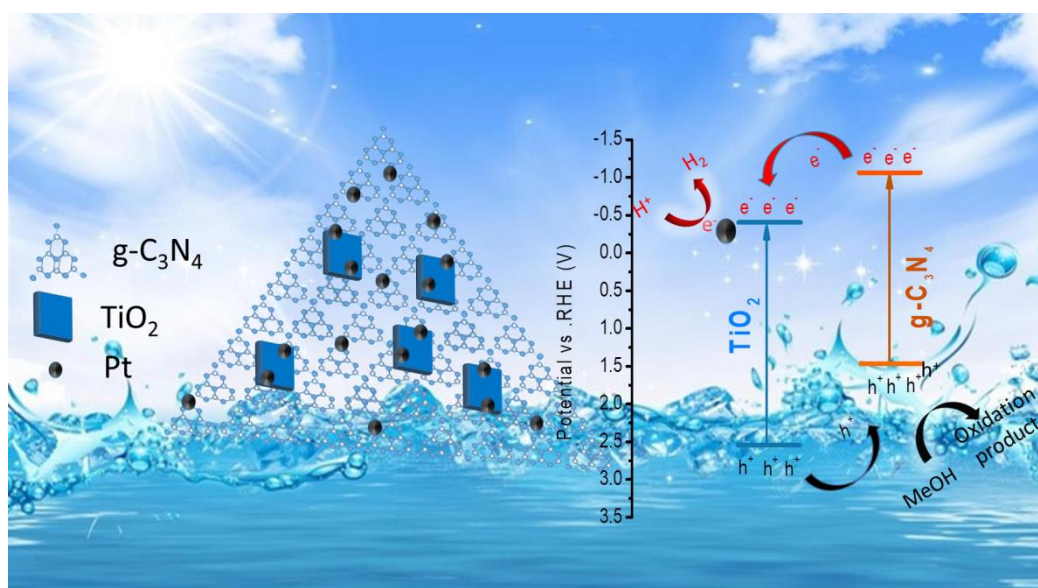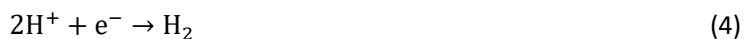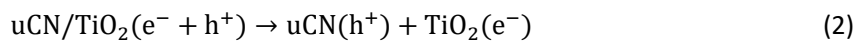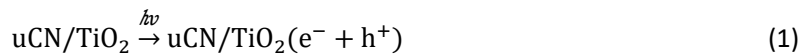
$$uCN/TiO_2 \xrightarrow{h\nu} uCN/TiO_2(e^- + h^+) \tag{1}$$

$$uCN/TiO_2(e^- + h^+) \rightarrow uCN(h^+) + TiO_2(e^-) \tag{2}$$

$$TiO_2(e^-) + Pt \rightarrow TiO_2 + Pt(e^-) \tag{3}$$

$$2H^+ + e^- \rightarrow H_2 \tag{4}$$

$$2h^+ + CH_3OH \rightarrow CH_2O + 2H^+ \tag{5}$$

Figure 3.11. Schematic diagram of photocatalytic hydrogen production over T/uCN photocatalyst

Finally, the stability of the T_1/uCN_1 photocatalyst in hydrogen evolution conditions under simulated solar light irradiation was measured through five four-hour cycles. As shown in Figure 3.12a, after this 20 h of reaction, the photocatalytic performance was hardly reduced, proving the excellent stability and reusability of the T_1/uCN_1 photocatalyst. Besides, as displayed in Figure 3.12b,c, SEM and XRD analysis of the catalyst after 20 h photocatalytic hydrogen generation reaction demonstrated the morphology and crystallographic structure of the material to be stable under photocatalytic reaction conditions.
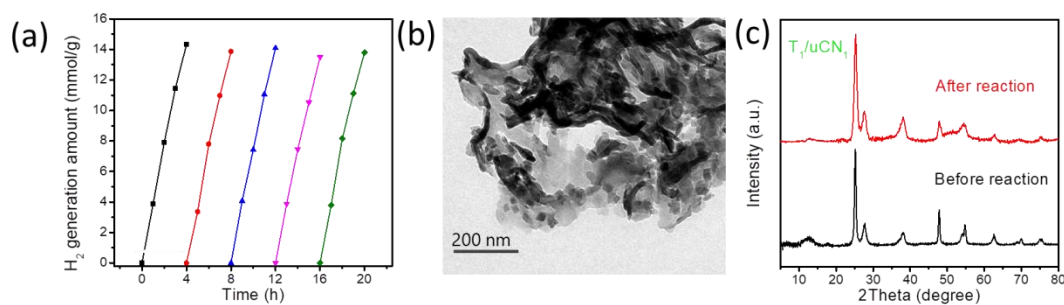
Figure 3.12. (a) Stability cycles of the T_1/uCN_1 for H_2 evolution under simulated solar light irradiation; (b) TEM image of T_1/uCN_1 after 20 h photocatalytic H_2 evolution reaction, and (c) XRD patterns of T_1/uCN_1 before and after 20 h photocatalytic hydrogen evolution reaction.

3.6 Conclusion

In summary, we detailed the synthesis of 2D/2D T/uCN heterojunctions from ultrathin g-C_3N_4 (uCN) and colloidal TiO_2 nanosheets through an electrostatic self-assembly approach. The highest hydrogen generation rate was achieved from T/uCN composites with a 1:1 mass ratio of the two components. The photocatalytic performance for H_2 production was increased in the following order: $bCN < uCN < TiO_2 < T_1/uCN_2 < T_2/uCN_1 < T_1/uCN_1$. The enhanced performance was attributed to the unique 2D/2D type II heterojunction architecture that simultaneously maximized the surface area to interact with the media and the interface between the two materials. The face-to-face interfacial contact between ultrathin layers of g-C_3N_4 and the faceted TiO_2 provided fast separation of photogenerated charges inside the composites, reducing recombination and thus increasing the apparent quantum yield.

3.7 Reference

[1]   J.M. Campos‑Martin, G. Blanco‑Brieva, J.L.G. Fierro, Hydrogen peroxide synthesis: an outlook beyond the anthraquinone process, Angew. Chemie Int. Ed. 45 (2006) 6962–6984.

[2]   Q. Xiang, B. Cheng, J. Yu, Hierarchical porous CdS nanosheet-assembled flowers with enhanced visible-light photocatalytic H2-production performance, Appl. Catal. B Environ. 138 (2013) 299–303.

[3]   A. Fujishima, K. Honda, Electrochemical photolysis of water at a semiconductor

electrode, Nature. 238 (1972) 37–38.

[4]   J. Zhang, Q. Xu, Z. Feng, M. Li, C. Li, Importance of the relationship between surface phases and photocatalytic activity of TiO2, Angew. Chemie. 120 (2008) 1790–1793.

[5]   H. Irie, Y. Watanabe, K. Hashimoto, Carbon-doped anatase TiO2 powders as a visible-light sensitive photocatalyst, Chem. Lett. 32 (2003) 772–773.

[6]   Y. Zhang, Z.-R. Tang, X. Fu, Y.-J. Xu, TiO2− graphene nanocomposites for gas-phase photocatalytic degradation of volatile aromatic pollutant: is TiO2− graphene truly different from other TiO2− carbon composite materials?, ACS Nano. 4 (2010) 7303–7314.

[7]   T.L. Thompson, J.T. Yates, Surface science studies of the photoactivation of TiO2 new photochemical processes, Chem. Rev. 106 (2006) 4428–4453.

[8]   S. Hamad, C.R.A. Catlow, S.M. Woodley, S. Lago, J.A. Mejias, Structure and stability of small TiO2 nanoparticles, J. Phys. Chem. B. 109 (2005) 15741–15748.

[9]   L. Sang, Y. Zhao, C. Burda, TiO2 nanoparticles as functional building blocks, Chem. Rev. 114 (2014) 9283–9318.

[10]   J.S. Chen, X.W. Lou, Anatase TiO2 nanosheet: an ideal host structure for fast and efficient lithium insertion/extraction, Electrochem. Commun. 11 (2009) 2332–2335.

[11]   Y.X. Zhang, G.H. Li, Y.X. Jin, Y. Zhang, J. Zhang, L.D. Zhang, Hydrothermal synthesis and photoluminescence of TiO2 nanowires, Chem. Phys. Lett. 365 (2002) 300–304.

[12]   P. Wang, J. Wang, X. Wang, H. Yu, J. Yu, M. Lei, Y. Wang, One-step synthesis of easy-recycling TiO2-rGO nanocomposite photocatalysts with enhanced photocatalytic activity, Appl. Catal. B Environ. 132 (2013) 452–459.

[13]   W. Zhou, Z. Yin, Y. Du, X. Huang, Z. Zeng, Z. Fan, H. Liu, J. Wang, H. Zhang, Synthesis of few‐layer MoS2 nanosheet‐coated TiO2 nanobelt heterostructures for enhanced photocatalytic activities, Small. 9 (2013) 140–147.

[14]   Y. Ou, J. Lin, S. Fang, D. Liao, MWNT−TiO2: Ni composite catalyst: a new class of catalyst for photocatalytic H2 evolution from water under visible light illumination, Chem. Phys. Lett. 429 (2006) 199–203.

[15]   Q. Liu, J. Huang, H. Tang, X. Yu, J. Shen, Construction 0D TiO2 nanoparticles/2D CoP nanosheets heterojunctions for enhanced photocatalytic H2 evolution activity, J.
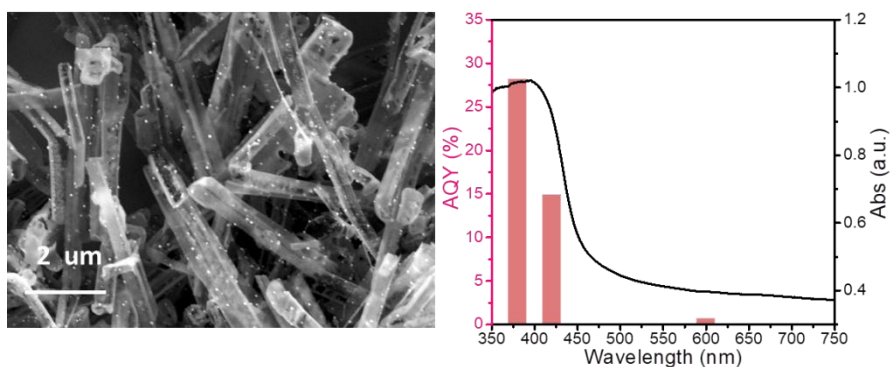
Mater. Sci. Technol. 56 (2020) 196–205.

[16] A. Meng, B. Zhu, B. Zhong, L. Zhang, B. Cheng, Direct Z-scheme TiO2/CdS hierarchical photocatalyst for enhanced photocatalytic H2-production activity, Appl. Surf. Sci. 422 (2017) 518–527.

[17] C. Cheng, A. Amini, C. Zhu, Z. Xu, H. Song, N. Wang, Enhanced photocatalytic performance of TiO2-ZnO hybrid nanostructures, Sci. Rep. 4 (2014) 1–5.

[18] J. Yan, H. Wu, H. Chen, Y. Zhang, F. Zhang, S.F. Liu, Fabrication of TiO2/C3N4 heterostructure for enhanced photocatalytic Z-scheme overall water splitting, Appl. Catal. B Environ. 191 (2016) 130–137.

[19] M. Xie, X. Fu, L. Jing, P. Luan, Y. Feng, H. Fu, Long‐lived, visible‐light‐excited charge carriers of TiO2/BiVO4 nanocomposites and their unexpected photoactivity for water splitting, Adv. Energy Mater. 4 (2014) 1300995.

[20] Y. Wang, C. Zhu, G. Zuo, Y. Guo, W. Xiao, Y. Dai, J. Kong, X. Xu, Y. Zhou, A. Xie, 0D/2D Co3O4/TiO2 Z-Scheme heterojunction for boosted photocatalytic degradation and mechanism investigation, Appl. Catal. B Environ. 278 (2020) 119298.

[21] L. Yuan, B. Weng, J.C. Colmenares, Y. Sun, Y. Xu, Multichannel charge transfer and mechanistic insight in metal decorated 2D–2D Bi2WO6–TiO2 cascade with enhanced photocatalytic performance, Small. 13 (2017) 1702253.

[22] Y. Zhang, J. Xu, J. Mei, S. Sarina, Z. Wu, T. Liao, C. Yan, Z. Sun, Strongly interfacial-coupled 2D-2D TiO2/g-C3N4 heterostructure for enhanced visible-light induced synthesis and conversion, J. Hazard. Mater. 394 (2020) 122529.

[23] Q. Liu, H. Lu, Z. Shi, F. Wu, J. Guo, K. Deng, L. Li, 2D ZnIn2S4 nanosheet/1D TiO2 nanorod heterostructure arrays for improved photoelectrochemical water splitting, ACS Appl. Mater. Interfaces. 6 (2014) 17200–17207.

[24] J. Fu, J. Yu, C. Jiang, B. Cheng, g‐C3N4‐Based heterostructured photocatalysts, Adv. Energy Mater. 8 (2018) 1701503.

[25] J. Wen, J. Xie, X. Chen, X. Li, A review on g-C3N4-based photocatalysts, Appl. Surf. Sci. 391 (2017) 72–123.

[26] Y. Ran, Y. Cui, Y. Zhang, Y. Fang, W. Zhang, X. Yu, H. Lan, X. An, Assembly-synthesis of puff pastry-like g-C3N4/CdS heterostructure as S-junctions for efficient photocatalytic

water splitting, Chem. Eng. J. 431 (2022) 133348.

[27] A. Cabot, R. Du, K. Xiao, B. Li, X. Han, C. Zhang, X. Wang, Y. Zuo, G. Pablo, J. Li, J. Chen, J. Arbiol, Controlled Oxygen Doping in Highly Dispersed Ni-Loaded G-C3n4 Nanotubes for Efficient Photocatalytic H2o2 Production, SSRN Electron. J. (2022). doi:10.2139/ssrn.4018808.

[28] X. Zhang, X. Yuan, L. Jiang, J. Zhang, H. Yu, H. Wang, G. Zeng, Powerful combination of 2D g-C3N4 and 2D nanomaterials for photocatalysis: recent advances, Chem. Eng. J. 390 (2020) 124475.

[29] Y. Zuo, X. Xu, C. Zhang, J. Li, R. Du, X. Wang, X. Han, J. Arbiol, J. Llorca, J. Liu, A. Cabot, SnS2/g-C3N4/graphite nanocomposites as durable lithium-ion battery anode with high pseudocapacitance contribution, Electrochim. Acta. 349 (2020) 136369. doi:https://doi.org/10.1016/j.electacta.2020.136369.

[30] J. Fu, Q. Xu, J. Low, C. Jiang, J. Yu, Ultrathin 2D/2D WO3/g-C3N4 step-scheme H2-production photocatalyst, Appl. Catal. B Environ. 243 (2019) 556–565.

[31] Y. Qin, H. Li, J. Lu, Y. Feng, F. Meng, C. Ma, Y. Yan, M. Meng, Synergy between van der waals heterojunction and vacancy in ZnIn2S4/g-C3N4 2D/2D photocatalysts for enhanced photocatalytic hydrogen evolution, Appl. Catal. B Environ. 277 (2020) 119254.

[32] S. Cao, B. Shen, T. Tong, J. Fu, J. Yu, 2D/2D heterojunction of ultrathin MXene/Bi2WO6 nanosheets for improved photocatalytic CO2 reduction, Adv. Funct. Mater. 28 (2018) 1800136.

[33] J. Su, G. Li, X. Li, J. Chen, 2D/2D heterojunctions for catalysis, Adv. Sci. 6 (2019) 1801702.

[34] F. Urbain, R. Du, P. Tang, V. Smirnov, T. Andreu, F. Finger, N.J. Divins, J. Llorca, J. Arbiol, A. Cabot, Upscaling high activity oxygen evolution catalysts based on CoFe2O4 nanoparticles supported on nickel foam for power-to-gas electrochemical conversion with energy efficiencies above 80%, Appl. Catal. B Environ. 259 (2019) 118055.

[35] Y. Zuo, Y. Liu, J. Li, R. Du, X. Yu, C. Xing, T. Zhang, L. Yao, J. Arbiol, J. Llorca, Solution-processed ultrathin SnS2–Pt nanoplates for photoelectrochemical water oxidation, ACS Appl. Mater. Interfaces. 11 (2019) 6918–6926.

[36] C. Zhang, R. Du, J.J. Biendicho, M. Yi, K. Xiao, D. Yang, T. Zhang, X. Wang, J. Arbiol, J. Llorca, Y. Zhou, J.R. Morante, A. Cabot, Tubular CoFeP@CN as a Mott–Schottky Catalyst with Multiple Adsorption Sites for Robust Lithium–Sulfur Batteries, Adv. Energy Mater. 11 (2021) 2100432.

[37] M. Liu, L. Piao, W. Lu, S. Ju, L. Zhao, C. Zhou, H. Li, W. Wang, Flower-like TiO 2 nanostructures with exposed {001} facets: Facile synthesis and enhanced photocatalysis, Nanoscale. 2 (2010) 1115–1117.

[38] Y. Li, K. Lv, W. Ho, F. Dong, X. Wu, Y. Xia, Hybridization of rutile TiO2 (rTiO2) with g-C3N4 quantum dots (CN QDs): an efficient visible-light-driven Z-scheme hybridized photocatalyst, Appl. Catal. B Environ. 202 (2017) 611–619.

[39] N. Tian, Y. Zhang, X. Li, K. Xiao, X. Du, F. Dong, G.I.N. Waterhouse, T. Zhang, H. Huang, Precursor-reforming protocol to 3D mesoporous g-C3N4 established by ultrathin self-doped nanosheets for superior hydrogen evolution, Nano Energy. 38 (2017) 72–81.

[40] N. Tian, H. Huang, S. Wang, T. Zhang, X. Du, Y. Zhang, Facet-charge-induced coupling dependent interfacial photocharge separation: A case of BiOI/g-C3N4 pn junction, Appl. Catal. B Environ. 267 (2020) 118697.

[41] X. Yu, R. Du, B. Li, Y. Zhang, H. Liu, J. Qu, X. An, Biomolecule-assisted self-assembly of CdS/MoS2/graphene hollow spheres as high-efficiency photocatalysts for hydrogen evolution without noble metals, Appl. Catal. B Environ. 182 (2016) 504–512.

[42] R. Du, Y. Zhang, B. Li, X. Yu, H. Liu, X. An, J. Qu, Biomolecule-assisted synthesis of defect-mediated Cd 1– x Zn x S/MoS 2/graphene hollow spheres for highly efficient hydrogen evolution, Phys. Chem. Chem. Phys. 18 (2016) 16208–16215.

[43] Y. Chen, X. Liu, L. Hou, X. Guo, R. Fu, J. Sun, Construction of covalent bonding oxygen-doped carbon nitride/graphitic carbon nitride Z-scheme heterojunction for enhanced visible-light-driven H2 evolution, Chem. Eng. J. 383 (2020) 123132.

Chapter 4

Controlled oxygen doping in highly dispersed Ni-loaded g-C$_3$N$_4$ nanotubes for efficient photocatalytic H$_2$O$_2$ production

4.1 Abstract

Hydrogen peroxide (H$_2$O$_2$) is both a key component in several industrial processes and a promising liquid fuel. The production of H$_2$O$_2$ by solar photocatalysis is a suitable strategy to convert and store solar energy into chemical energy. Here we report an oxygen-doped tubular g-C$_3$N$_4$ with uniformly dispersed nickel nanoparticles for efficient photocatalytic H$_2$O$_2$ generation. The hollow structure of the tubular g-C$_3$N$_4$ provides a large surface with a high density of reactive sites and efficient visible light absorption during the photocatalytic reaction. The oxygen doping and Ni loading enable a fast separation of photogenerated charge carriers and a high selectivity toward the two-electron process during the oxygen reduction reaction (ORR). The optimized composition, Ni$_{4\%}$/O$_{0.2}$tCN, displays an H$_2$O$_2$ production rate of 2464 mol g^{-1}·h^{-1}, which is eightfold higher than that of bulk g-C$_3$N$_4$ under visible light irradiation (λ > 420 nm), and achieves an apparent quantum yield (AQY) of 28.2% at 380 nm and 14.9% at 420 nm.

Keywords: carbon nitride; nanotubes; nickel nanoparticles; photocatalysis, H$_2$O$_2$

4.2 Introduction

Hydrogen peroxide is an important industrial raw material used among others as an eco-friendly oxidant for industrial synthesis, pulp bleaching and wastewater treatment, with a global annual demand of over 4 million tons.[1–4] Besides, H_2O_2 is also a promising liquid fuel that is safer and easier to store than compressed hydrogen.[5,6] At present, H_2O_2 is industrially produced mainly through the anthraquinone method, which is an energy-intensive process requiring large amounts of organic solvent.[7] Therefore, the development of cost-effective and environmentally friendly strategies for the large scale production of H_2O_2 is a worthwhile endeavour. In this scenario, the production of H_2O_2 using solar photocatalysis has received increased attention in recent years.[8,9]

Several photocatalysts have been applied for H_2O_2 generation, including titanium dioxide[10,11], graphitic carbon nitride (g-C_3N_4)[12,13] and bismuth vanadate[14], to cite a few. Among them, g-C_3N_4 is particularly interesting as a metal-free, non-toxic and chemically stable material that has shown excellent potential not only for H_2O_2 generation but also for hydrogen generation and wastewater treatment, among others. However, the low surface area, moderate light absorption, rapid recombination of the photogenerated electron-hole pairs and low photocatalytic reaction selectivity towards H_2O_2 generation limits the cost-effective use of g-C_3N_4 for photocatalytic H_2O_2 production. To overcome these limitations, several strategies have been developed, including tuning the g-C_3N_4 morphology, extrinsic doping, and heterojunction formation through co-catalyst loading. [15–19]

It is well known that the morphology and nanostructure of g-C_3N_4 largely affect its photocatalytic performance. To date, several g-C_3N_4 morphologies, such as nanosheets,[20] nanospheres,[21] nanorods,[22] nanofibers[23] and nanotubes[24] have been prepared. Among them, nanotubes with a one-dimensional hollow structure offer particularly large surface areas, high light absorption and fast electron transport to optimize photocatalytic performance.

Beyond controlling its morphology, the proper doping of g-C_3N_4 is critical to adjust its band structure and charge carrier concentration towards enhancing light absorption and

promoting charge injection.[25,26] Dopants such as oxygen and phosphorus can not only adjust the valence band structure of the catalyst and improve the separation efficiency of photogenerated electrons and holes, but also improve the OER selectivity toward the two-electron pathway.[27,28]

The introduction of a co-catalyst on the surface of g-C_3N_4 is an effective strategy to improve photocatalytic performance by increasing the charge separation ability. Various noble metal co-catalyst, such as Pt, Pd, and Au, have been demonstrated to promote hydrogen evolution performance.[29–33] Nevertheless, the high cost of noble metals and the moderate H_2O_2 production rates reached limit the cost-effectiveness of the process. Thus, the development of co-catalysts based on abundant and low-cost elements, such as MoS_2, Ni, NiP or CoP, [34–37] that provide an efficient and high rate photocatalytic H_2O_2 production is highly desirable.

In this study, we detail the synthesis of hollow tubular g-C_3N_4 (tCN), demonstrate its controlled oxygen doping (OtCN), and describe its surface modification with highly dispersed nickel nanoparticles (Ni/OtCN) through a photoreduction process. Nitrogen adsorption-desorption isotherms, UV–vis absorption and photoluminescence spectroscopies, and photochemical tests are used to investigate the charge separation and transfer abilities of these materials. Besides, rotating ring disk electrode analysis, active species capture experiments and DFT calculations are used to analyze the mechanism of H_2O_2 generation. Owing to its unique 1-D hollow structure, high charge separation efficiency and excellent reaction selectivity, Ni/OtCN achieved outstanding H_2O_2 photocatalytic generation performance.

4.3 Experimental

Preparation of tubular g-C_3N_4 precursor (C-M): g-C_3N_4 nanotubes were prepared by a self-assembly method using melamine (99%, Acros Organics) and cyanuric acid (99%, Acros Organics). Typically, 1 g melamine and 1 g cyanuric acid were separately added into 300 ml deionized water under stirring at 80 °C for about 10 minutes until completely dissolved. Then the melamine solution was slowly added to the cyanuric acid solution under homogeneous stirring, and let it self-assemble at 80 °C for 1.5 hours. The product was centrifuged and

washed twice with 80 °C deionized water to remove the unassembled melamine and cyanuric acid. The filtered product was re-dispersed in deionized water and then settled at room temperature for 12 hours. Then the supernatant was removed to obtain a flocculent precipitate. The precipitate was then freeze-dried for 48 hours to obtain the g-C_3N_4 precursor that we will refer to as C-M.

Preparation of O-doped tubular g-C_3N_4 (OtCN) and bulk g-C_3N_4 (bCN): The OtCN was prepared by a two-step heating process. In detail, 2 g C-M was introduced into a lidded porcelain crucible and calcined at 520 °C for 2h with a temperature increase rate of 2 °C·min^{-1} under Ar atmosphere. Then the product was mixed with the proper amount (0 g, 200 mg, 400 mg, 600 mg, or 800 mg) of ammonium persulfate (98%, Sigma) and calcined again at 520 °C for 2h with a temperature ramp of 5 °C·min^{-1}. The products were named O_xtCN, with x=0, 0.1, 0.2, 0.3, or 0.4 for the different amounts of ammonium persulfate introduced. The bulk g-C_3N_4 (bCN) was prepared through a similar method but replacing the C-M with melamine and adding no ammonium persulfate.

Preparation of Ni/OtCN, Au/OtCN and Pt/OtCN: 100 mg of OtCN was added into 100 ml deionized water containing 10 ml triethanolamine (99%, Acros Organics), 8.5 mg nickel acetate tetrahydrate (99%, Acros Organics), and 500 mg sodium hypophosphite (99%, Sigma), and the solution was sonicated for 30 min. Afterwards, argon was bubbled into the solution for 30 min to displace the oxygen. Then the solution was irradiated with UV-vis light (300 W Xe lamp) under continuous stirring and argon bubbling for 30 min. The product was centrifuged and washed 3 times with water and ethanol (90%, Acros Organics) and finally dried under vacuum for 6h. The sample was named $Ni_{2\%}$/OtCN. Samples with higher Ni concentration, Ni_x/OtCN (x=4%, 6% and 8%), were prepared using the same procedure but adding the proper higher amount of nickel acetate. Au/OtCN and Pt/OtCN samples were also prepared by this photo-deposition method using H_2PtCl_6 ·$6H_2O$ (99%, Acros Organics) and $HAuCl_4$ ·$4H_2O$ (99%, Acros Organics) precursors and irradiating the samples with UV light for 1 h.

Characterization: The size and shape of the samples were characterized by scanning electron microscopy (SEM) analysis was carried out in a Zeiss Auriga microscope (Carl Zeiss, Jena,

Germany) with an energy-dispersive X-ray spectroscopy (EDX) detector at 20 kV to study the composition and transmission electron microscopy (TEM) using a ZEISS LIBRA 120, operating at 120 kV. Scanning TEM (STEM) and high-resolution TEM (HRTEM) were carried out under the 200 keV Tecnai F20 field emission microscope. Electron energy loss spectroscopy (EELS) and high-angle annular dark-field (HAADF) STEM were carried out using a Gatan Quantum image filter embedded in the F20 (S) TEM. Powder X-ray diffraction (XRD) patterns were collected directly from the as-synthesized particles dropped on Si (501) substrates on a Bruker AXS D8 Advance X-ray diffractometer with Nifiltered (2 μm thickness) Cu Kα radiation (λ = 1.5406 Å) operating at 40 kV and 40 mA. A LynxEye linear position-sensitive detector was used in reflection geometry. Characterization of the surface was done by X-ray photoelectron spectroscopy (XPS) on a SPECS system equipped with an XR50 source operating at 250 W and a Phoibos 150 MCD-9 detector. The pass energy of the hemispherical analyzer was set at 20 eV, and the energy step of high-resolution spectra was set at 0.05 eV. The pressure in the analysis chamber was always below 10^{-7} Pa. The specific surface area and analysis of the pore size distribution were obtained from nitrogen adsorption/desorption isotherms on Tristar II 3020 Micromeritics system. UV-vis absorption spectra were identified by the PerkinElmer LAMBDA 950 UV-vis spectrophotometer. Fourier transformed infrared (FTIR) spectra were recorded on an Alpha Bruker spectrometer. The optical properties of samples were analyzed by a UV–vis spectrophotometer (UV-2600, Shimadzu). Photoluminescence (PL) spectra of aqueous photocatalysts suspension (0.1 g·L^{-1}) were collected on a fluorescence spectrophotometer (F-7000, Hitachi), and the wavelength of excitation light is 300 nm. The decay time measurements were carried out on a compact fluorescence lifetime spectrometer (Quantaurus-Tau, C11367, HAMAMATSU), and an LED lamp (365 nm) was used as an excitation source. Electron paramagnetic resonance (EPR) analysis was performed on an EPR spectrometer (Jeol FA 200) in the presence of 10 mM 5, 5-dimethyl-1-pyrrolidine N-oxide (DMPO) as the spin trapper. DMPO was dispersed in methanol for detection $^*O_2^-$. Before the test, the Xenon research lamp (300W) was used to irradiate the photocatalyst suspension for 3 minutes.

Electrocatalysis measurements: The photocurrent and electrochemical impedance

spectroscopy (EIS) investigations were carried out on a CHI-760 electrochemical analyzer using a three-electrode cell system with indium tin oxide (ITO)/sample as the working electrode, platinum net as the counter electrode and standard calomel electrode (SCE) as the reference. A 300 W Xe lamp with a cut-off filter of 420 nm was utilized as the light source. Furthermore, the ITO/sample electrodes were fabricated as follows: first, samples (5 mg) were added into solutions containing DI water (0.5 ml), ethanol (0.5 ml) and Nafion (20 ul) and ultrasonicated for 20 min. Then, the resultant sample slurry (0.1 ml) was cast onto pre-cleaned ITO glass and then dried at 60 ℃ for 2 h.

Photocatalytic reduction of oxygen to hydrogen peroxide: The photocatalytic reduction of O_2 to H_2O_2 was analyzed according to the literature with a slight modification 50 mg of photocatalyst suspended in 90 ml of water and 10 ml ethanol. The suspension solutions were first ultrasonically dispersed for 30 min in the dark and then stirred for 30 min before irradiation to reach the absorption–desorption equilibrium. The light source was provided by a Xe lamp at 300 W with 420 nm cut-off filter. The average light intensity was 100 mW·cm^{-2}. At certain time intervals, 2 ml solution was sampled and centrifuged to remove the photocatalysts. The reactions were carried out in the air atmosphere without special instructions. The amount of H_2O_2 was analyzed by iodometry. 1ml 1 M KI solution and 0.002 M $(NH_4)_6Mo_7O_{24}$ were added to the obtained solution, which was then kept for 30 min. The H_2O_2 molecules reacted with iodide anions (I$^-$) under acidic conditions (H_2O_2 + 3 I$^-$ + 2 H$^+$ → I^{3-} + 2 H_2O) to produce triiodide anions (I^{3-}) possessing a strong absorption at around 350 nm. The amount of I^{3-} was determined by means of UV–vis spectroscopy on the basis of the absorbance at 350 nm, from which the amount of H_2O_2 produced during each reaction was estimated. The standard curve line of UV-vis absorption spectrum of different H_2O_2 amounts could be found in fig 4.20.

Rotating ring-disk electrode (RRDE) test: To electrochemically determine the selectivity of the catalyst toward the production of H_2O_2 instead of H_2O, one can estimate the electron transfer number (n) of the ORR reaction. The closer the electron transfer number is to 2, the higher the H_2O_2 generation efficiency. A rotating ring-disk electrode (RRDE) was used to estimate n, and thus assess the ORR pathway and H_2O_2 generation efficiency. Within an RRDE, the peroxide species produced at the disk electrode are detected by the ring electrode. Thus,

n can be determined from the ratio of the ring current (Ir) and the disk current (Id) using the following equation:

$$n = 4\frac{I_d}{I_d + I_r/N}$$ (8)

where N is the collection efficiency of the ring electrode, which is estimated at 0.42.(Fig 4.21) Besides, the percentage of H_2O_2 produced can be determined from:

$$\%HOO^- = 200 \times \frac{I_r/N}{I_d + I_r/N}$$

(9)

When calibrating N, N_2 saturated 0.1 M KOH and 0.004 M $K_3Fe(CN)_6$ were used as the electrolyte.[38][39] The electrodes were the same as those used in the ORR measurements. The electrode was rotated at a certain angular velocity and the amperometric i-t measurements were performed. The voltage of the disk and ring was set to 0.1 V and 1.5 V, respectively. The N value is calculated by using the following equation:

$$N = \frac{I_r}{I_d}$$

Computational method: The density functional theory (DFT) calculations were performed by Vienna Ab-initio Simulation Package[40][41] (VASP), using the Projected Augmented Wave[42] (PAW) method. The revised Perdew-Burke-Ernzerhof (PBE) functional was used to describe the exchange and correlation effects.[43][44] For all the geometry optimizations, the cutoff energy was set to be 500 eV. Spin-polarization calculations were included in all cases. Reciprocally proportional to the lattice

parameters, the Monkhorst-Pack grids[45] were set to be 3×3×1 for performing the surface calculations. The g-C_3N_4 and oxygen doped g-C_3N_4 were simulated as single-layer structure; while the Ni/OCN was simulated as one single-layer OCN coated on a three-layer nickel. A vacuum layer of 20 Å was applied in the z-direction of the slab models, preventing the vertical interactions between slabs.

The $4e^-$ elementary steps of ORR were calculated via the following procedures:

$O_2 + * \rightarrow *O_2$

$*O_2 + (H^+ + e^-) \rightarrow *OOH$

*OOH + (H$^+$ + e$^-$) $\rightarrow$ *O + H$_2$O

*O + (H$^+$ + e$^-$) $\rightarrow$ *OH

*OH + (H$^+$ + e$^-$) $\rightarrow$ * + H$_2$O
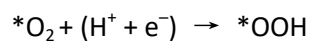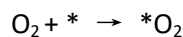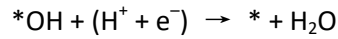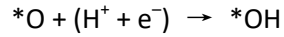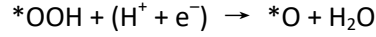
The 2e$^-$ elementary steps of ORR were calculated via the following procedures:

O$_2$ + * $\rightarrow$ *O$_2$

*O$_2$ + (H$^+$ + e$^-$) $\rightarrow$ *OOH

*OOH + (H$^+$ + e$^-$) $\rightarrow$ * + H$_2$O$_2$
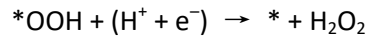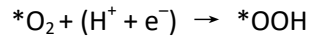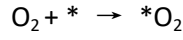
where * denotes the active sites on the catalyst surface. The computational hydrogen electrode (CHE) model [46] was used to calculate the free energies of ORR intermediates, based on which the free energy of an adsorbed species is defined as

$$\Delta G_{ads} = \Delta E_{ads} + \Delta E_{ZPE} - T\Delta S_{ads} + \Delta G_U + \Delta G_{pH}$$

where ΔE_{ads} is the electronic adsorption energy, ΔE_{ZPE} is the zero-point energy difference between adsorbed and gaseous species, $T\Delta S_{ads}$ is the corresponding entropy difference between these two states, ΔG_U is the contribution from the electrode potential (U), and ΔG_{pH} is the contribution from pH value. The electronic binding energy is referenced as ½ H$_2$ for each H atom, and (H$_2$O − H$_2$) for each O atom, plus the energy of the clean slab.

The effect of electrode potential U (ΔG_U) is defined as:

$$\Delta G_U = -neU$$

where n is the number of electrons transferred in the elementary step, and U is the electrode potential.

The effect of pH (ΔG_{pH}) is defined as:

$$\Delta G_{pH} = pH \times k_B T ln 10$$

where pH equals to 7, and k$_B$ is the Boltzmann constant.

Apparent quantum yield (AQY) calculations: The apparent quantum yield can be evaluated from the following equation:[47][48]

$$AQY = \frac{2 \times n_{H_2O_2} \times N_A}{N}$$

$n_{H_2O_2}$ is the number of evolved H$_2$O$_2$ molecules, N_A is Avogadro number (6.02×10^{23}) and N represents the number of incident photons, which can be calculated from the following equation :

$$N = \frac{\text{light intensity} \left(W \, cm^{-2} \right) \times \text{illumination area} \left(cm^2 \right)}{\frac{hc}{\lambda}}$$

h is plank constant (6.626×10^{-34} J·s = 4.136×10^{-15} eV·s), c is the speed of light (3.0×10^8 m·s^{-1}), λ is the wavelength of light (380, 420, 600 nm).

Test method for light with wavelengths of 420 and 600 nm. The photocatalytic systems with 100 mg catalyst and 100 ml O_2 saturated solution (90 ml DI water and 10 ml ethanol) were irradiated for 1 h at room temperature and atmospheric pressure. The irradiated area is 3.14 cm^2.

Test method for the 380 nm. The photocatalytic systems with 10 mg catalyst and 10 ml O_2 saturated solution (9 ml DI water and 1 ml ethanol) were irradiated for 1 h at room temperature and atmospheric pressure. The irradiated area is 1.13 cm^2. (Because the light intensity of 380nm wavelength is very low, to reduce the error, we choose a smaller test system)

The light intensity and resulting $n_{H_2O_2}$ are listed in Table 2.

4.4 Results and discussions

Structural and chemical properties of oxygen-doped tubular g-C$_3$N$_4$ and the Ni-loaded composite

Oxygen-doped tubular carbon nitride samples loaded with Ni nanocrystals (Ni/OtCN) were obtained through a 4-step process involving the synthesis of the carbon nitride precursor from the combination of melamine and cyanuric acid in water, annealing under argon at 520 °C, oxygen doping using ammonium persulfate, and photo-deposition of Ni (Figure 4.1).
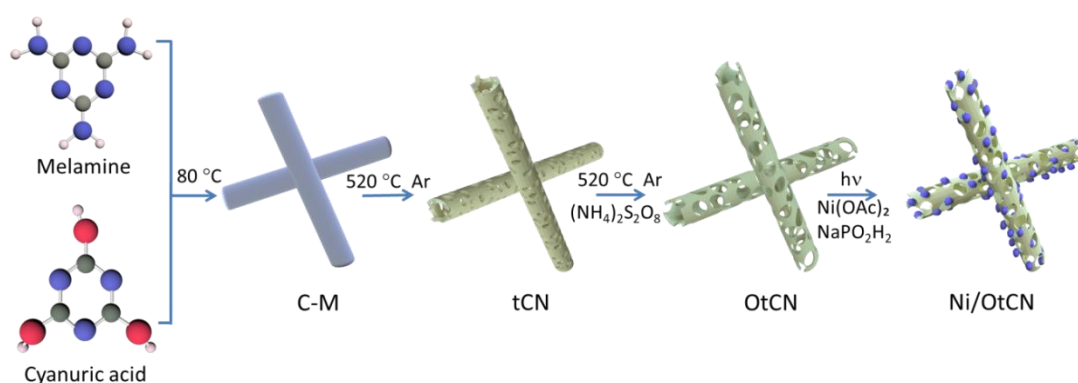

Figure 4.1. Schematic illustration on the synthesis of Ni/OtCN samples.

Because the water solubility of melamine and cyanuric acid is very low at room temperature, the two components were dissolved at 80 °C to ensure their full and uniform dispersion before self-assembly. The assembly is driven by the hydrogen bond formation between the amino group on melamine and the hydroxyl group on cyanuric acid. To determine the optimum precursor composition, materials with different melamine and cyanuric acid molar ratios (1:2, 1:1 and 2:1) were prepared for comparison. SEM analysis of the obtained precursors (Figures 4.2 and 4.4a) showed the 1:1 ratio to provide the best-defined nanorod structures, with a diameter in the range 300-600 nm and lengths of 15-30 nm. This result is consistent with the equal number of functional groups of both molecules, thus assembling at a 1:1 molar ratio. While the 1:2 and 2:1 ratios also resulted in nanorod-like structures, they showed poor uniformity and presented a large amount of unassembled precursor on their surfaces.
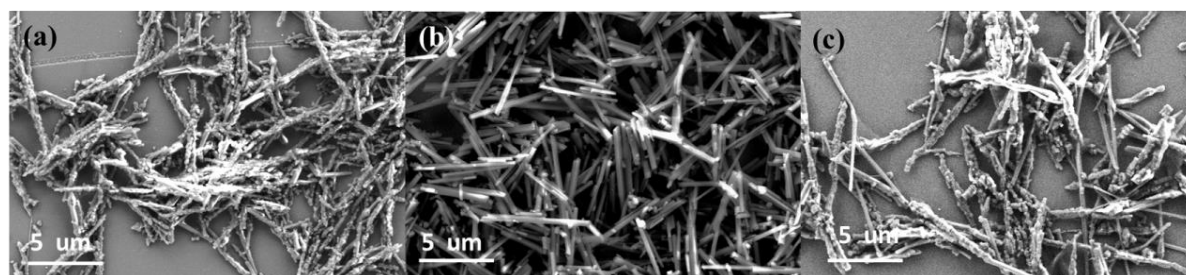
Figure 4.2. SEM image of C-M precursors with different ratio of melamine and cyanuric acid (a) 1:2; (b) 1:1; (c) 2:1.

Once the self-assembly process was completed, the material was washed with hot water to remove the residual not-assembled precursors. To prevent agglomerating during the drying process, samples were freeze-dried, which yielded dried materials with high porosity, as observed in Figure 4.3. The freeze-drying step was demonstrated as particularly important because an extensive agglomeration of the nanorods results in a high sintering and very notable loss of porosity during the posterior annealing step at 520 °C.
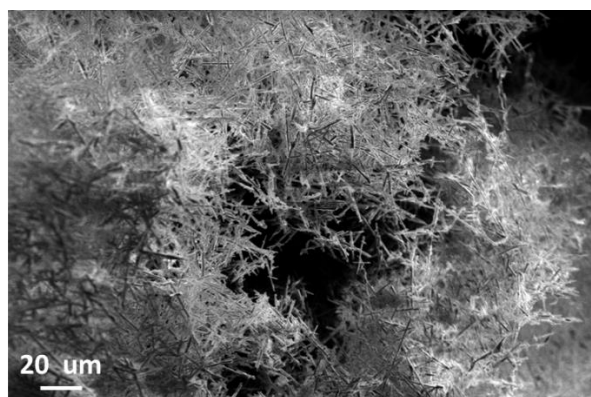
Figure 4.3. SEM image of precursors with 1:1 ratio of melamine and cyanuric acid after freeze drying.

To minimize the damage to the nanostructure during the thermal polymerization of the C-M precursor, the annealing and oxygen doping of the material was divided into two steps. The first annealing step at 520 °C used a relatively low heating rate of 2 °C·min^{-1}. After this step, samples were combined with a proper amount of ammonium persulfate and the mixture was annealed again at 520 ° C for two additional hours using a temperature ramp of 5 °C·min^{-1}. This second annealing step completed the polymerization process. Besides, during the annealing process, the ammonium persulfate releases ammonia, sulfur dioxide, and oxygen gases creating a porous fluffy structure and inhibiting the agglomeration of nanotubes. At the same time, in this oxygen-enriched atmosphere, part of the generated oxygen gas reacts with the polymerizing carbon nitride incorporating oxygen into the structure. After the two-step thermal polymerization at 520 ° C, the nanorod precursor was turned into g-C$_3$N$_4$ nanotubes that maintained approximately the same size as the precursor nanorods (Figure 4.4b).

The annealed and oxygen-doped samples, OtCN, were dispersed in a solution containing nickel acetate tetrahydrate to be loaded with nickel nanoparticles through a photodeposition process. As a result, as observed in Figure 4.4c, uniformly and highly dispersed Ni nanoparticles were grown on the surface of the OtCN. Table 5 provides results from the EDX analysis of Ni$_{4\%}$/O$_{0.2}$tCN showing the weight percentage of O and Ni to be 2.1 % and 3.2 %, respectively.

TEM analysis of OtCN samples confirmed the tubular structure of the products and further

showed the nanotube walls have a porous structure (Figure 4.4d). The tubular structure of OtCN was thus significantly different from that of bulk g-C_3N_4 (bCN) produced from the direct annealing of melamine (Figure 4.6a). TEM images of the Ni/OtCN samples also confirmed the homogeneous distribution of Ni nanoparticles and showed their size to be in the range of 20-60 nm (Figure 4.4e). HRTEM micrographs revealed that the selected nanoparticles had a crystal phase matching the Ni cubic phase (space group=FM3-M) with a=b=c=3.5241 Å (Figure 4.4f). EELS chemical composition maps obtained on the Ni/OtCN nanotubes displayed a uniform distribution of O, N and C and the presence of Ni-rich regions corresponding to the Ni nanoparticles.
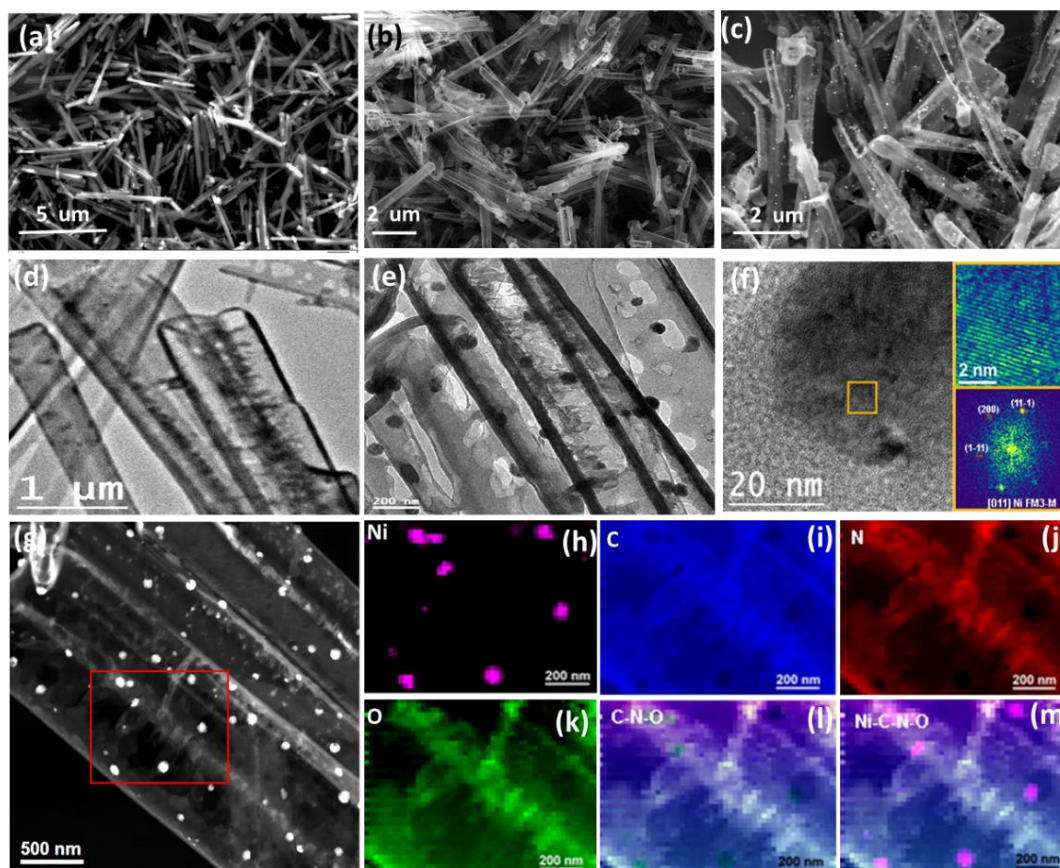
Figure 4.4. (a) SEM image of the C-M precursor. (b) SEM image of OtCN. (c) SEM image of Ni/OtCN. (d) TEM image of OtCN. (e) TEM image of Ni/OtCN. (f) HRTEM micrograph obtained on a representative region of the Ni/OtCN nanostructures. On the top right, we show a magnified detail (top right) of the orange squared region in the HRTEM image and its corresponding indexed power spectrum (bottom right) which reveals that this nanoparticle has a crystal phase in agreement with the Ni cubic phase

(space group=FM3-M) with a=b=c=3.5241 Å, visualized along its [011] zone axis. (g) HAADF STEM general detail of the Ni/OtCN catalyst, showing the presence of Ni nanoparticles as bright spots. EELS chemical composition maps were obtained on the red squared area of the STEM micrograph. Individual composition maps were obtained by using: (h) Individual Ni $L_{2,3}$-edges at 855 eV (pink), (i) C K-edges at 284 eV (blue), (j) N K-edges at 401 eV (red) and (k) O K-edges at 532 eV (green), as well as their composites for C-N-O and Ni-C-N-O.

Figure 4.7a displays the XRD patterns of $O_{0.2}$tCN, $Ni_x/O_{0.2}$tCN and a reference bCN. The main diffraction peaks at about 13.1° aand 27.4° nobserved from all the samples are assigned to the (100) and (002) family planes of g-C_3N_4, respectively. Compared with bCN, the (002) peak of OtCN samples shows a slight shift from 27.4° to 27.2° owhich is a signature of an increase of the interplanar distance associated with the presence of oxygen.[49,50] Besides, the (002) diffraction peak of OtCN is broader and weaker than that of bCN, which is attributed to the tubular structure of OtCN. The samples containing Ni show no alteration of the g-C_3N_4 diffraction peaks compared with OtCN, which indicates that the loading of Ni does not affect the OtCN structure. Meanwhile, Ni/OtCN samples display two additional XRD peaks at 44.3° 3and 51.5° that are assigned to the (111) and (200) family planes of cubic nickel. The intensity of these peaks correlates with the amount of Ni introduced, proving the successful loading of controlled amounts of nickel.

FTIR spectroscopy was used to gain further insight into the structure of the material. As shown in Figure 4.7b, all OtCN materials displayed the fingerprints of g-C_3N_4, including the absorption peak at 812 cm^{-1} that corresponds to the out-of-plane bending of the triazine units, and the range of peak at 1200–1600 cm^{-1} that are related to the stretching modes of C-N in the aromatic heterocyclic rings. Besides, OtCN samples displayed FTIR peaks at 1235 and 1075 cm^{-1}, which intensity increased with the amount of ammonium persulfate used during the synthesis. These peaks are associated with the stretching mode of C-O-C group.[27,51]

Figure 4.7c displays the UV–vis diffuse reflectance spectra of the different samples. The absorption edge of OtCN samples presented an obvious red-shift compared with that of bCN. This redshift was accentuated with the increase in the oxygen content. As shown in Figure

4.7d, the band gaps of bCN and OtCN samples, calculated according to Kubelk-Munk function, shifted from 2.73 eV for bCN, to 2.56 eV for $O_{0.4}tCN$. Besides, the presence of oxygen resulted in a notable enhancement of the Urbach tail, which is associated with the presence of defects as a result of oxygen doping.[27,50] As expected from the metallic character of the introduced Ni nanoparticles, the Ni/OtCN composites presented a strong absorption in the visible range of the spectra, which was enhanced with the increasing contents of Ni, from 2% to 8%. On the other hand, the presence of Ni did not result in a shift of the OtCN absorption edge.

Mott-Schottky analysis was used to further investigate the band structure of the samples (Figure 4.5). The flat band potentials of bCN and OtCN were obtained from the fitting of the Mott-Schottky plots and were used to estimate the position of the conduction band minimum (assuming it is ca. 0.1 eV above the flat band)[52][53] and valence band maximum (considering $E_g = E_{vb} - E_{cb}$).[43] Figure 4.7e displays the schematized band structure experimentally determined from bCN and OtCN samples.
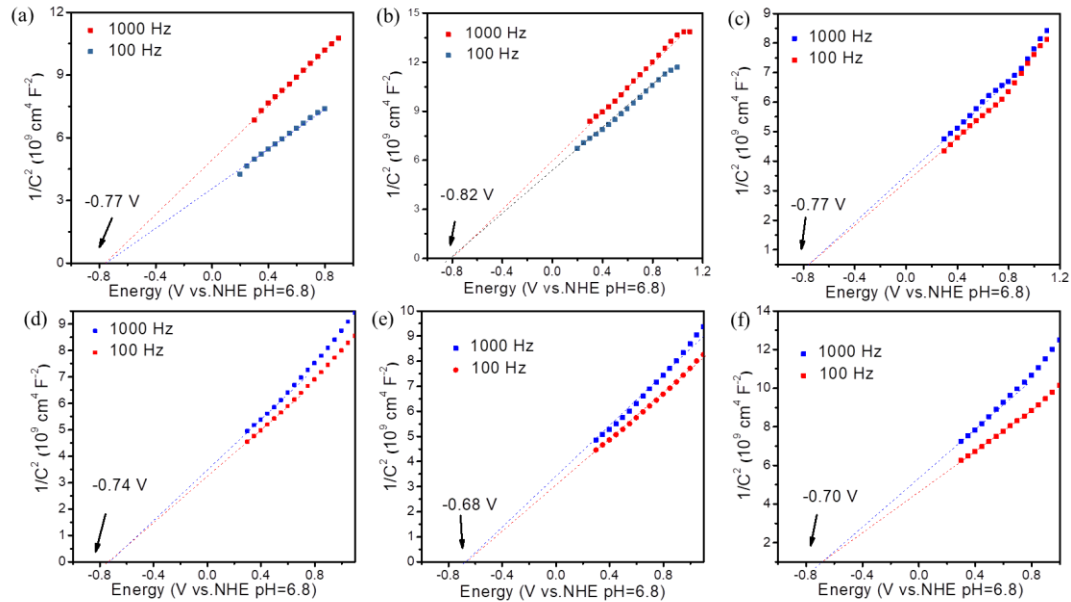

Figure 4.5. Mott–Schottky plot of (a) bCN and (b-f) O_xtCN (x=0, 0.1, 0.2, 0.3, 0.4).

Figure 4.7f displays the nitrogen adsorption-desorption isotherms of bCN and $O_{0.2}tCN$ nanotubes. Both samples exhibit type IV isotherms with H3 hysteresis loops, indicating the presence of a mesoporous structure. As shown in Table S1, the specific surface area (SSA) of $O_{0.2}tCN$ nanotubes was 124 $m^2 \cdot g^{-1}$, which is over six-fold larger than that of bCN (18.7 $m^2 \cdot g^{-1}$).

The calculated pore size distribution of the two samples is shown in Figure 4.6b. As expected from SEM images, the pore volume of OtCN, 0.97 $cm^3·g^{-1}$, was significantly larger than that of bCN, 0.19 $cm^3·g^{-1}$.
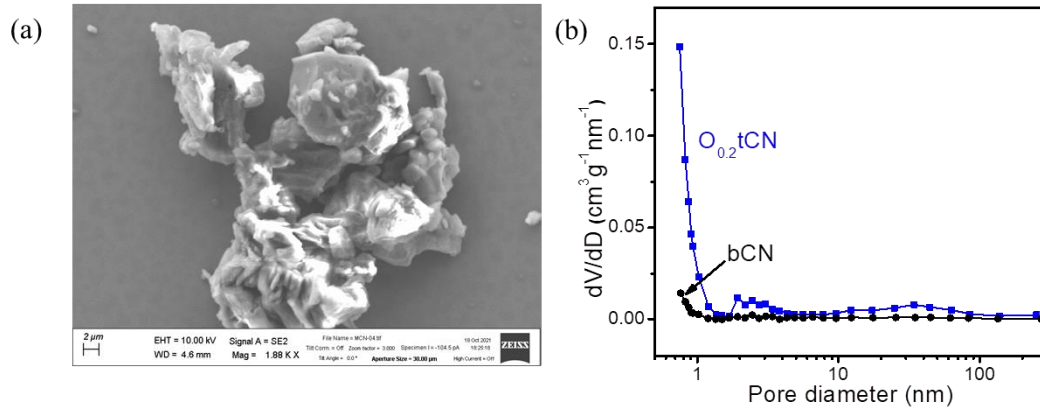

Figure 4.6. (a) SEM image of bCN; (b) pore size distribution curves of bCN and $O_{0.2}$tCN.

Table 4.1. Specific surface area (SSA) and pore volume of bCN and $O_{0.2}$tCN.

Sample	SAA ($m^2·g^{-1}$)	Pore volume ($cm^3·g^{-1}$)
BCN	18.72	0.19
$O_{0.2}$tCN	124.22	0.97
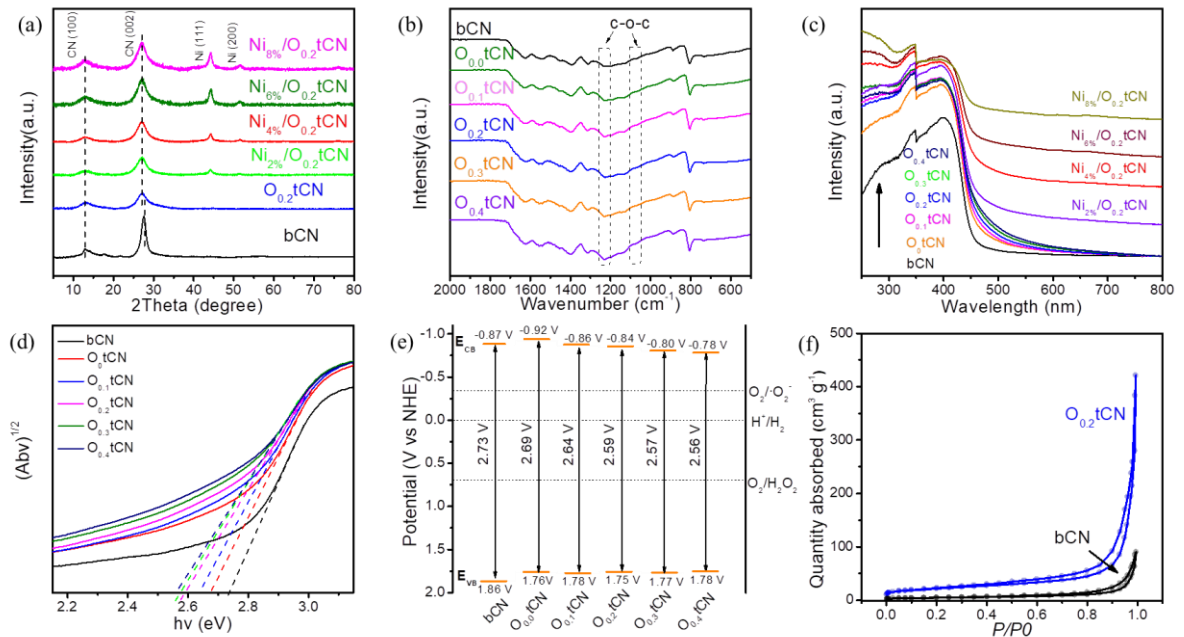
Figure 4.7. (a) XRD pattern of bCN, $O_{0.2}$tCN and Ni_x/$O_{0.2}$tCN (x=2%, 4%, 6% and 8%). (b) FTIR spectra of

bCN and O_xtCN. (c) UV–Vis absorption spectra of bCN, O_xtCN and $Ni_x/O_{0.2}$tCN. (d) plot of the band energy spectra and (e) band structure alignments for bCN and OtCN. (f) N_2 adsorption-desorption isotherms of bCN and $O_{0.2}$tCN.

Figure 4.8 displays the XPS spectra of bCN, $O_{0.2}$tCN, and $Ni_{4\%}/O_{0.2}$tCN samples. The high-resolution C 1s XPS spectra showed three main contributions at 288.2 eV, 286.5 eV, and 284.8 eV, which were assigned to C-(N_3), C–NH_x and C–C/C=C, respectively.[40] Besides, the OtCN samples displayed a fourth C 1s peak 288.5 eV corresponding to C-O obtained from the replacement of N atoms by O in the CN heterocycles. All samples displayed the presence of oxygen at their surface, including the bCN. The high-resolution O 1s XPS spectrum of bCN was fitted with two peaks at 531.7 eV and 533.1 eV, which were associated with adsorbed oxygen-containing species such as water, O_2, OH^- groups and even CO_2.[49] Besides, samples OtCN and Ni/OtCN displayed an additional contribution at 530.7 eV which is assigned to the C-O bond. Additionally, a peak at 529.7 eV was identified in the XPS spectrum of Ni/OtCN, and it was assigned to oxygen within a nickel oxide chemical environment created by the surface oxidation of the Ni nanoparticles. The high-resolution N 1s XPS spectra of bCN, $O_{0.2}$tCN and $Ni_{4\%}/O_{0.2}$tCN were fitted with three peaks at binding energies of 398.1 eV, 499.4 eV, and 400.5 eV, which were assigned to N-(C_2), N-(C_3) and N-H_x groups of the heptazine framework, respectively. Finally, the high-resolution Ni 2p XPS spectrum of Ni/OtCN was fitted with three doublets, corresponding to metallic Ni ($2p_{3/2}$ at 851.6 eV), Ni^{2+} ($2p_{3/2}$ at 855.8 eV) and a Ni^{2+} shake-up satellite ($2p_{3/2}$ at 860.4 eV).[44] While $(NH_4)_2S_2O_8$, added as the oxygen source, decomposes to NH_3 (g), SO_2 (g) and O_2 (g) during the second annealing step, no sulfur was detected by XPS and EDX analyses due to the low reactivity of sulfur within sulfur dioxide in the temperature range used (Figures 4.23 and 4.24).

The EPR spectra of bCN and OtCN samples are displayed in Figure 4.8f. The Lorentzian absorption line at g =2.0027 is a fingerprint of the unpaired electrons of the sp^2 hybridized C atoms in the aromatic rings.[27,49] The EPR signal of the OtCN sample is significantly less intense than that of bCN, which is consistent with the partial replacement N by O atoms, thus decreasing the number of lone pair electrons. According to XPS data (Table S5), the N/C ratio of OtCN (1.13) is significantly lower than that of bCN (1.21), and the O/C ratio of OtCN

(0.08) is higher than that of bCN (0.04), which is consistent with the hypothesis that O replaces N within the carbon nitride structure. Overall, the above experimental results confirmed the presence of O within OtCN replacing N atoms.
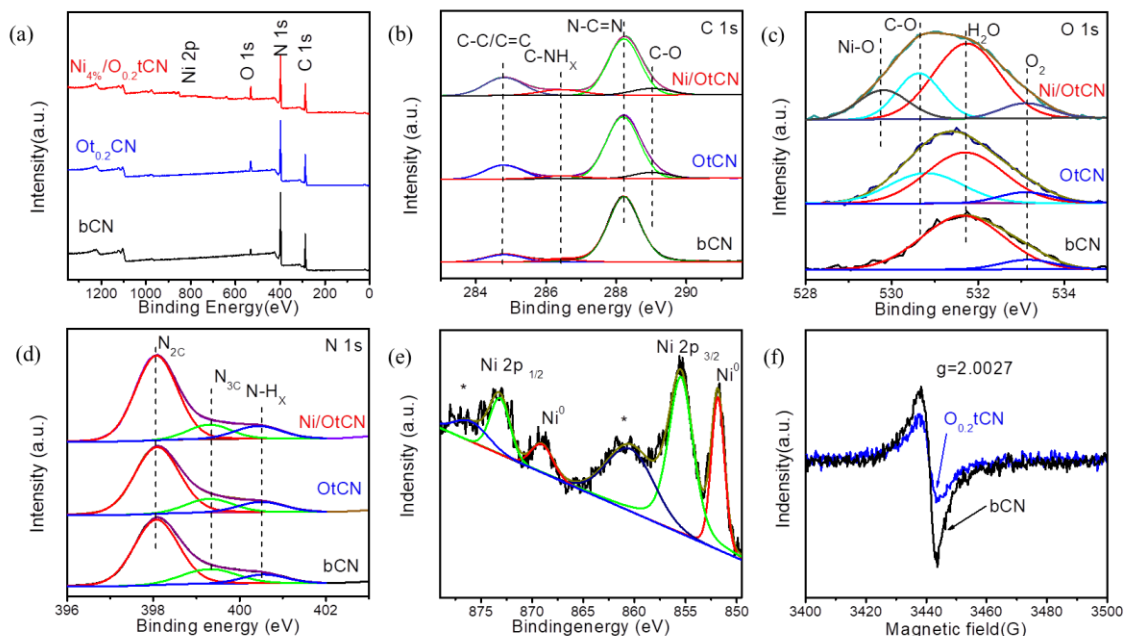

Figure 4.8. (a) XPS survey spectra. (b-d) High-resolution XPS spectra of (b) C 1s, (c) O 1s and (d) N 1s obtained from bCN, $O_{0.2}$tCN and $Ni_{4\%}/O_{0.2}$tCN. (e) Ni 2p XPS spectrum of $Ni_{4\%}/O_{0.2}$tCN. (f) EPR spectra of bCN and $O_{0.2}$tCN.

Photocatalytic H_2O_2 evolution

Figure 4.9a displays the photocatalytic H_2O_2 generation from bCN, $O_{0.2}$tCN, and $Ni_{4\%}/O_{0.2}$tCN irradiated during 2h with visible light ($\lambda > 420$ nm). The H_2O_2 production rate of $O_{0.2}$tCN was fourfold higher than that of bCN (Figure 4.9b). Besides, when loading the $O_{0.2}$tCN with Ni, the H_2O_2 evolution rate further increased to reach nearly an order of magnitude higher values than bCN. Besides the Ni/OtCN sample displayed higher H_2O_2 evolution rates than noble metal co-catalyst: Au/OtCN and Pt/OtCN. The presence of Au showed an obvious improvement over OtCN, but the presence of Pt had no positive impact on the H_2O_2 generation, which is associated with a low two-electron reaction selectivity and a high H_2O_2 decomposition rate during the oxygen reduction reaction.
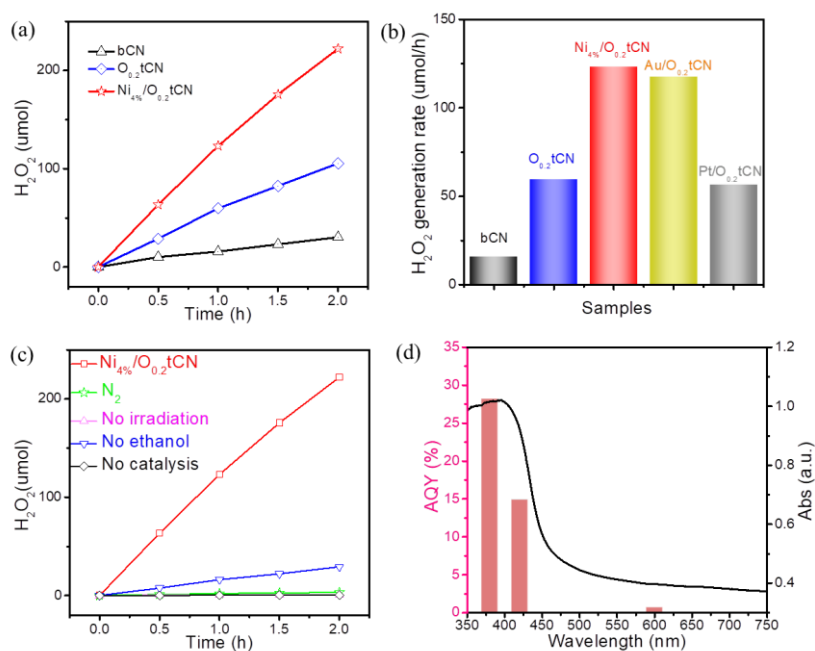
Figure 4.9. (a) Photocatalytic H_2O_2 generation on bCN, $O_{0.2}$tCN and $Ni_{4\%}/O_{0.2}$tCN during 2 h under visible light ($\lambda > 420$ nm). (b) Photocatalytic H_2O_2 generation rate of bCN, $O_{0.2}$tCN, $Ni_{4\%}/O_{0.2}$tCN, $Au_{4\%}/O_{0.2}$tCN and $Pt_{4\%}/O_{0.2}$tCN (c) H_2O_2 production on $Ni_{4\%}/O_{0.2}$tCN under different conditions: N_2 instead of O_2, no irradiation, no ethanol and no photocatalyst. (d) AQY of $Ni_{4\%}/O_{0.2}$tCN at three different wavelengths, superimposed to the UV-vis spectrum.

To find the optimal amount of oxygen doping, O_XtCN samples produced using different amounts of ammonium persulfate were tested (Figure 4.10a-b). O_XtCN samples containing relatively small amounts of oxygen ($0 < x < 0.4$) exhibited a significant enhancement of the H_2O_2 generation rate over tCN, but too high oxygen substitutions resulted in a lower H_2O_2 evolution rate. Among all the O_XtCN samples, $O_{0.2}$tCN displayed the best H_2O_2 generation performance, 58.1 $\mu mol \cdot h^{-1}$.

The amount of Ni was optimized by measuring the photocatalytic hydrogen peroxide generation on $Ni_x/O_{0.2}$tCN containing different Ni concentrations (Figure 4.10c-d). The loading of $O_{0.2}$tCN with a moderate amount of Ni nanoparticles largely enhanced the photocatalytic performance toward H_2O_2 generation. At a Ni loading of 2% and 4%, the H_2O_2 generation rate was improved to 88.2 $\mu mol \cdot h^{-1}$ and 123.2 $\mu mol \cdot h^{-1}$, which is 1.5 and 2.1 times higher than that of $O_{0.2}$tCN, respectively. When further increasing the Ni loading to 6% and 8% the H_2O_2 production rate decreased to 101 $\mu mol \cdot h^{-1}$ and 75 $\mu mol \cdot h^{-1}$, respectively.

This decrease of the H_2O_2 production rate at high Ni loads may be related to the aggregation of small Ni particles and the blocking of the visible light absorption of the C_3N_4 caused by an excess of Ni.
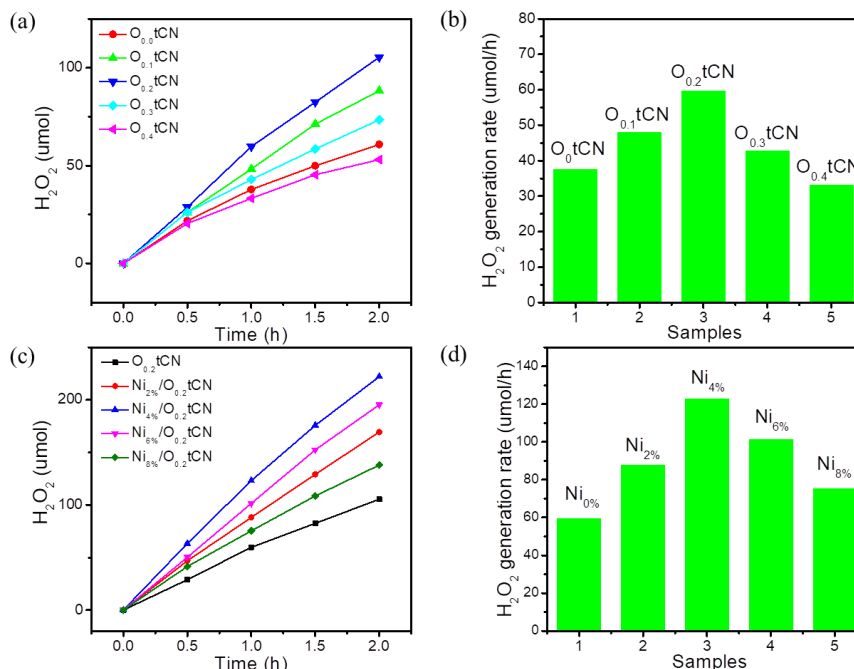

Figure 4.10. (a-b) Photocatalytic hydrogen peroxide generation amount and rate of O_xtCN (x=0.0, 0.1, 0.2, 0.3 and 0.4) and (c-d) $Ni_x/O_{0.2}$tCN (X=0, 2%, 4%, 6% and 8%).

To further evidence the advantages of OtCN over bCN, we also prepared a Ni-loaded oxygen-doped bulk g-C_3N_4 (Ni/ObCN) to be used as a reference. As observed in Figure 4.11a, the $Ni_{4\%}/O_{0.2}$bCN sample displayed a slightly improved H_2O_2 production rate over bCN, but still well below the rates obtained from OtCN samples. This moderate production rate is in part related to the small surface area of bCN and the uneven deposition of nickel nanoparticles (Figure 4.11b) caused by the insufficient active sites on the bCN surface.
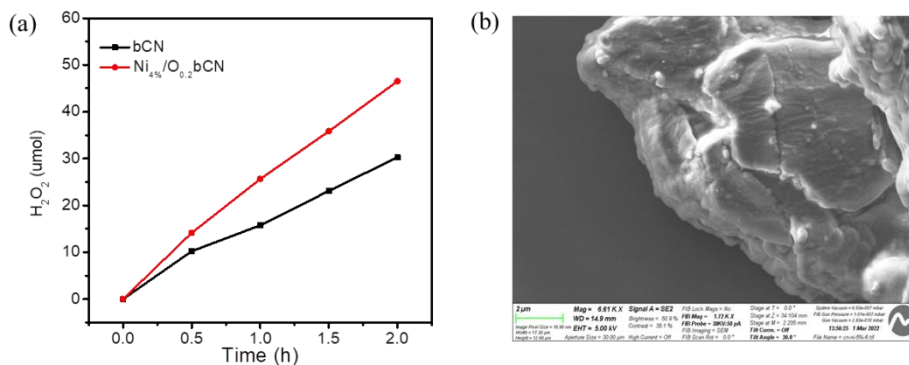
Figure 4.11. (a)The photocatalytic hydrogen peroxide generation amount of bCN and $Ni_{4\%}/O_{0.2}bCN$ and (b) SEM image of $Ni_{4\%}/O_{0.2}bCN$.
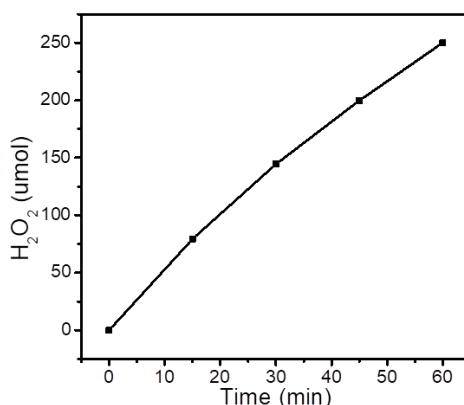

Figure 4.12. Photocatalytic hydrogen peroxide generation amount of $Ni_{4\%}/O_{0.2}tCN$ under simulate solar light.

As displayed in Figure 4.9c, control experiments demonstrated that the presence of O_2 and light irradiation were required for the H_2O_2 generation, proving the production of H_2O_2 to take place by the ORR pathway instead of the water oxidation. Besides ethanol, other sacrificial agents, such as lactic acid and triethanolamine, also enabled a high H_2O_2 generation rate (Figure 4.12). But even in the absence of ethanol or another sacrificial agent, the $Ni_{4\%}/O_{0.2}tCN$ sample was able to achieve a notable photocatalytic H_2O_2 generation (Figure 4.9c). Besides, as shown in Fig. 4.12, $Ni_{4\%}/O_{0.2}tCN$ also shows a prominent photocatalytic hydrogen peroxide generation performance of about 5012 mol $g^{-1} \cdot h^{-1}$ under simulated solar light, using an AM1.5 filter.

Table4.2. AQY under different incident light wavelengths for bCN, $O_{0.2}tCN$ and $Ni_{4\%}/O_{0.2}tCN$.

Wavelength (nm)	Light intensity (mW·cm^{-2})	$Ni_{4\%}/O_{0.2}tCN$	
		n H_2O_2 (umol·L^{-1})	AQY (%)
380	0.53	84.1	28.2
420	9.91	279	14.9
600	17.66	32.9	0.7

The apparent quantum yield (AQY) of the process was evaluated under 380 nm (0.53 mW·cm^{-2}), 420 nm (9.91 mW·cm^{-2}) and 600 nm (17.66 mW·cm^{-2}) irradiation (Table S2, see details in the experiment section). For $Ni_{4\%}/O_{0.2}tCN$, the AQY at 380 nm and 420 nm was

estimated at 28.2% and 14.9%, respectively. Even under 600 nm light irradiation, an AQY of 0.7% was achieved for $Ni_{0.4}/O_{0.2}tCN$, which is consistent with UV-vis spectroscopy results (Figure 4.9d).[56]

The electrochemical characterization of the samples allowed the further study of their charge transfer and transport properties. As observed in Figure 4.13a, bCN, $O_{0.2}tCN$ and $Ni_{4\%}/O_{0.2}tCN$ electrodes showed positive photocurrents under visible-light irradiation. Among them, $O_{0.2}tCN$ showed a slightly higher photocurrent density than bCN, but the highest photocurrents were obtained with the $Ni_{4\%}/O_{0.2}tCN$ electrode, reaching about 7.2 and 4 times higher current densities than with bCN and $O_{0.2}tCN$, respectively. These results demonstrate that $O_{0.2}tCN$ and especially the presence of Ni nanoparticles significantly increase the charge separation and transfer efficiency, which is in good agreement with the photocatalysis results. [57]

Charge transfer and transport properties were further evaluated by electrochemical impedance spectroscopy (EIS). Figure 4.13b displays the Nyquist plot of the impedance spectra for the different materials. The larger arc associated with the transfer resistance of photo-generated charges[37] has a significantly smaller diameter for $O_{0.2}tCN$ than bCN, indicating a faster charge transfer efficiency in the former. Besides, the sample containing Ni, $Ni_{4\%}/O_{0.2}tCN$, presents a much smaller arc radius than the other two samples, confirming the much lower charge transfer resistance in the presence of Ni.

Table 4.3. Exponential decay fitted parameters of fluorescence lifetime of bCN, $O_{0.2}tCN$ and $Ni_{4\%}/O_{0.2}tCN$.

Sample	bCN	$O_{0.2}tCN$	$Ni_{4\%}/O_{0.2}tCN$
τ	5.95	4.06	3.39
τ_1	1.10	1.13	0.83
τ_2	8.26	6.21	4.92

The photoluminescence (PL) spectra of the different samples under 300 nm light excitation is displayed in Figure 4.13c. The bCN sample displayed a broad and intense PL band at ca. 455 nm, which is associated with the radiative band-to-band recombination of photogenerated charge carriers within C_3N_4. With oxygen doping, the PL intensity significantly decreases

owing to the presence of oxygen-related non-radiative recombination centers. Besides, the presence of Ni introduces additional recombination sites which further quenches the C_3N_4 PL. As obtained from time-resolved PL (TRPL) spectroscopy (Figure 4.13d) and consistently with previous results, $O_{0.2}tCN$ and $Ni_{4\%}/O_{0.2}tCN$ samples exhibited much shorter average PL lifetimes (4.06 ns and 3.39 ns) than bCN (6.22 ns), demonstrating the strong electronic effect of the substitutional oxygen and nickel nanoparticles.[36][58]
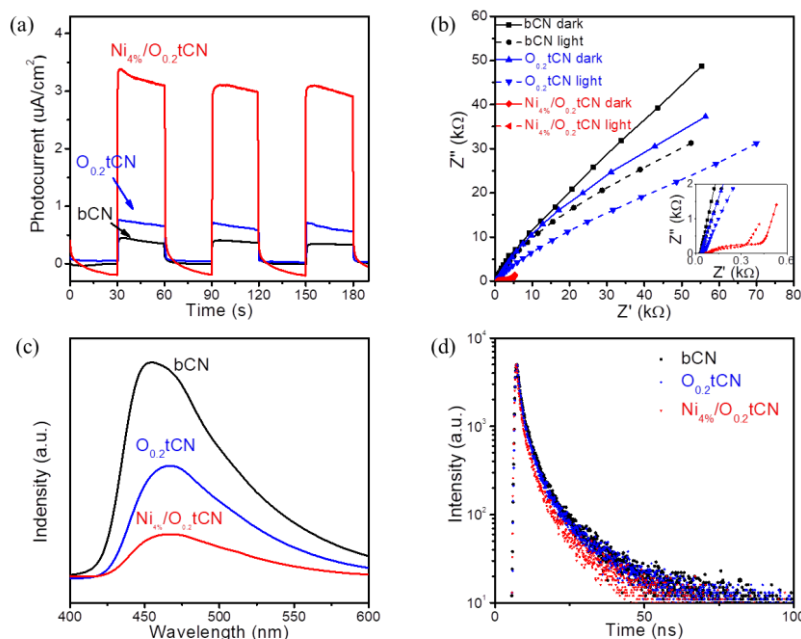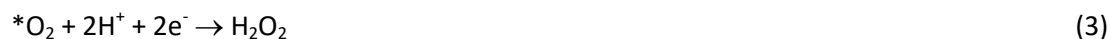

Figure 4.13. (a) Photocurrent response curves of bCN, $O_{0.2}tCN$ and $Ni_{4\%}/O_{0.2}tCN$; (b) Electrochemical impedance spectroscopy (EIS) Nyquist plots of bCN ,$O_{0.2}tCN$ and $Ni_{4\%}/O_{0.2}tCN$; (c,d) PL spectra and TRPL decay of bCN ,$O_{0.2}tCN$ and $Ni_{4\%}/O_{0.2}tCN$.
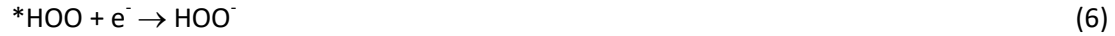
The generation of H_2O_2 from the coupling of the oxygen reduction reaction (ORR) with the oxidation of an alcohol takes place through two main pathways. Both paths share the alcohol dehydrogenation reaction and the oxygen adsorption as the initial ORR step:

$$RCH_2OH + 2h^+ \rightarrow RCHO + 2H^+ \tag{1}$$

$$O_2 + * \dashrightarrow *O_2 \tag{2}$$

In one possible path, the reduction of the adsorbed oxygen molecule ($*O_2$) can take place through a direct two-electron route:

$$*O_2 + 2H^+ + 2e^- \rightarrow H_2O_2 \tag{3}$$

The second possible ORR pathway is a two-step single-electron process, that can be broken down into the following steps:

$$*O_2 + e^- \rightarrow *O_2^- \tag{4}$$

$$*O_2^- + H^+ \rightarrow *HOO \tag{5}$$

$$*HOO + e^- \rightarrow HOO^- \tag{6}$$

$$HOO^- + H^+ \rightarrow H_2O_2 \tag{7}$$

Besides, the H_2O_2 evolution reaction competes with the oxygen reduction to H_2O, which overall involves a total of $4e^-$ (see details in the SI):

$$O_2 + 4H^+ + 4e^- \rightarrow 2H_2O \tag{8}$$

A rotating ring-disk electrode (RRDE) was used to determine the selectivity of the catalyst toward the production of H_2O_2 instead of H_2O. [59] The disk electrode was scanned cathodically at a scan rate of 10 mV·s^{-1}, while the ring potential was set at 0.5 V vs. Ag/AgCl (Figure 4.14). The linear sweep voltammetry (LSV) curves of bCN achieved I_r = 0.40 mA·cm^{-2} and I_d=-1.91 mA·cm^{-2} at -1.0 V vs. Ag/AgCl. From these values, a transfer number n =2.71 and an H_2O_2 selectivity of 60.8% was determined.[60] Similarly, a transfer number n = 2.32 and an H_2O_2 selectivity of 81.2% was obtained for $O_{0.2}$tCN, and n = 2.24 and an H_2O_2 selectivity of 88.9% for $Ni_{4\%}$/$O_{0.2}$tCN. Overall, the RRDE measurements indicated that the oxygen doping and the presence of Ni significantly promoted the two-electron pathway for oxygen reduction to H_2O_2 over the four-electron H_2O generation.

To differentiate between the one-step two-electron direct ORR ($O_2 \rightarrow H_2O_2$) and the sequential two-step single-electron indirect reduction ($O_2 \rightarrow *O_2^- \rightarrow H_2O_2$) routes,[18,19] LSV curves were analyzed in more detail (Figures 4.14 and 4.15). Notice that the bCN and $O_{0.2}$tCN samples exhibit two reduction plateaus at around −0.2 V and −0.5 V, suggesting a two-step pathway for H_2O_2 generation.[19][61] As observed in Figure 4.14b,c, no obvious H_2O_2 current is detected in the ring electrode during the first plateau, in the potential range -0.2 V to -0.4 V. Only when reaching the second plateau a ring current is measured, which indicates the successive two single-electron reduction pathway. On the other hand, after loading the

Ni nanoparticles, the first plateau almost disappears and the onset potential of the H_2O_2 current at the ring electrode approximately matches that of the disk electrode, pointing at a one-step two-electron direct reduction pathway in $Ni_{4\%}/O_{0.2}tCN$. Overall, these results indicate that the introduction of nickel transforms the reaction from a two-step single-electron process to a direct two-electron process.
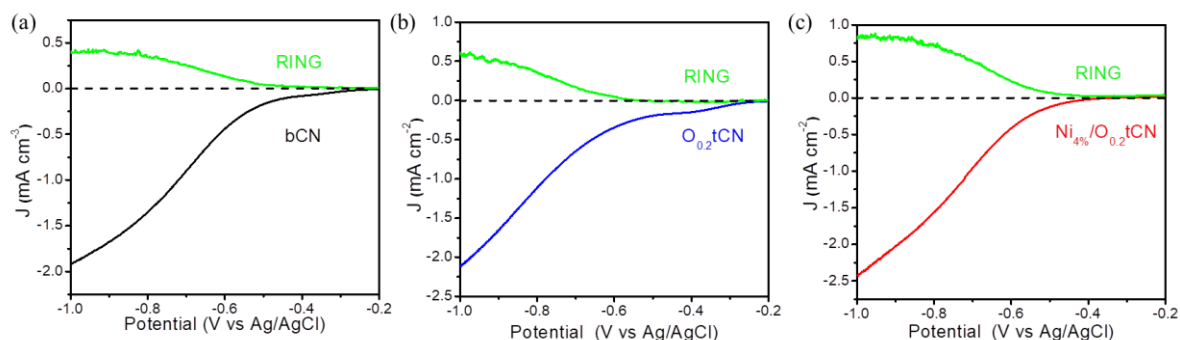

Figure 4.14. LSV curves of (a) bCN, (b) $O_{0.2}tCN$ and (c) $Ni_{4\%}/O_{0.2}tCN$ obtained using an RRDE with a rotating speed of 1600 rpm and a ring biased at 0.5 V.

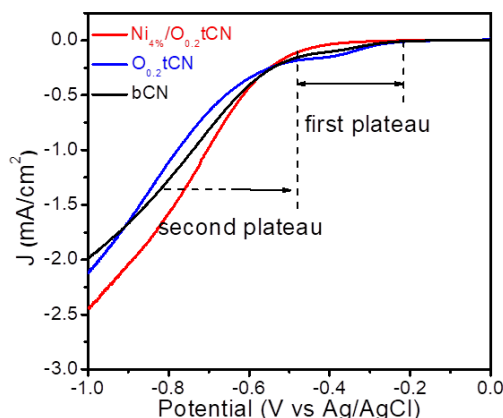**Figure 4.15.** Linear sweep voltammetry (LSV) plots of bCN, $O_{0.2}tCN$ and $Ni_{4\%}/O_{0.2}tCN$ on rotating disk electrode (RDE) with rotating speed of 1600 rpm.

DFT calculations were carried out to further understand the selectivity of the ORR process on CN, OCN and Ni/OCN. The top view of the intermediates adsorption and the free energy diagram of ORR on the three materials are shown in Figure 4.16 and Table S4. The bCN sample is characterized by the strongest adsorption strength of ORR intermediates, which may hamper the product formation. The reduction of *OOH and *OH to form the final products, H_2O_2 or H_2O, are generally considered as the limiting ORR steps determining the

reaction rate and pathway, either 2e⁻ or 4e⁻.[17] The change of Gibbs free energy (ΔG) for the reduction of *OOH and *OH on CN was calculated to be 1.42 eV and 1.35 eV, respectively (Figure 4.17d). The similar ΔG for *OOH and *OH reduction on CN points toward the simultaneous occurrence of the two-electron and four-electron pathways. With the oxygen doping, ΔG for the reduction of *OOH and *OH on OCN decreased to 0.72 eV and 0.99 eV, respectively. Besides, with the introduction of Ni, ΔG values further decreased down to 0.35 eV and 0.66 eV, respectively. The lower ΔG values obtained for OCN and particularly for Ni/OCN are consistent with experimental data obtained for OtCN and Ni/OtCN. Besides, notice that the ΔG of the reduction of *OOH is significantly lower than that of *OH reduction in OCN and Ni/OCN samples, involving a higher probability of the 2e⁻ ORR pathway than the 4e⁻. These DFT calculation results are consistent with the experimental data obtained from the RRDE test, further demonstrating that the oxygen doping and the Ni loading incline the catalyst toward two-electron reactions, which can significantly improve the H_2O_2 generation efficiency.

Table 4.4. Free energy diagram of ORR on the g-C_3N_4, O doped g-C_3N_4 (OCN) and Ni loaded O atoms doping g-C_3N_4 (Ni/OCN).

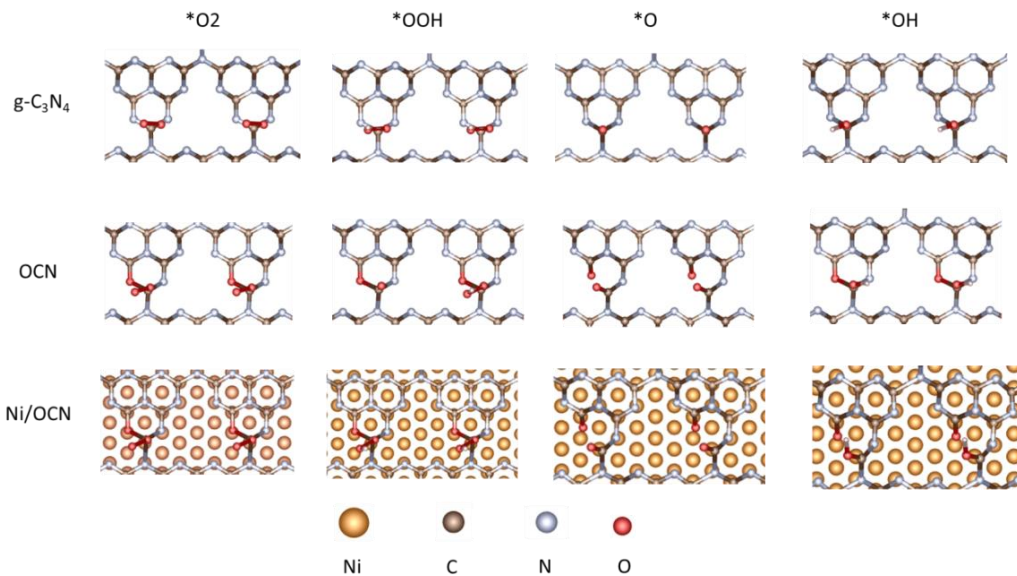|	*	*O_2	*OOH	H_2O_2	*O	*OH	OH⁻
g-C_3N_4	0	-1.92	-2.82	-1.40	-2.77	-3.98	-2.63
OCN	0	-1.82	-2.12	-1.40	-2.02	-3.62	-2.63
Ni/OCN	0	-1.06	-1.75	-1.40	-2.16	-3.29	-2.63

Figure 4.16. Top view of intermediate of *O_2, *OOH, *O and *OH for the g-C_3N_4, O doped g-C_3N_4 and Ni loaded O atoms doping g-C_3N_4.
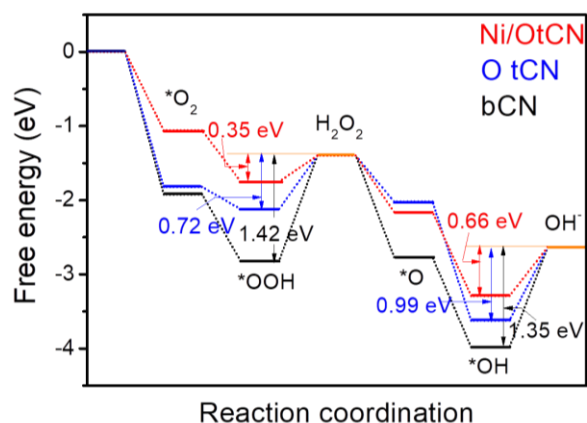

Figure 4.17. Free energy diagrams of oxygen reduction reaction steps on bCN, $O_{0.2}$tCN and $Ni_{4\%}/O_{0.2}$tCN

Additional experimentally of the ORR pathway were obtained by introducing a *O^{2-} trapping agent in the solution, PBQ (1 mM). As shown in Figure 4.18a-c, after introducing the PBQ, the H_2O_2 generation rate strongly decreased for bCN and $O_{0.2}$tCN, by an 88% and 84%, respectively, demonstrating the important role played by *O^{2-} as an intermediate during H_2O_2 generation process, i.e. pointing at the two-step single-electron process as the main pathway for H_2O_2 generation process in bCN and $O_{0.2}$tCN. On the contrary, the $Ni_{4\%}/O_{0.2}$tCN sample showed just a 35% decrease of H_2O_2 generation in the presence of PBQ, indicating the predominance of the two-electron process over the two single-electron processes.
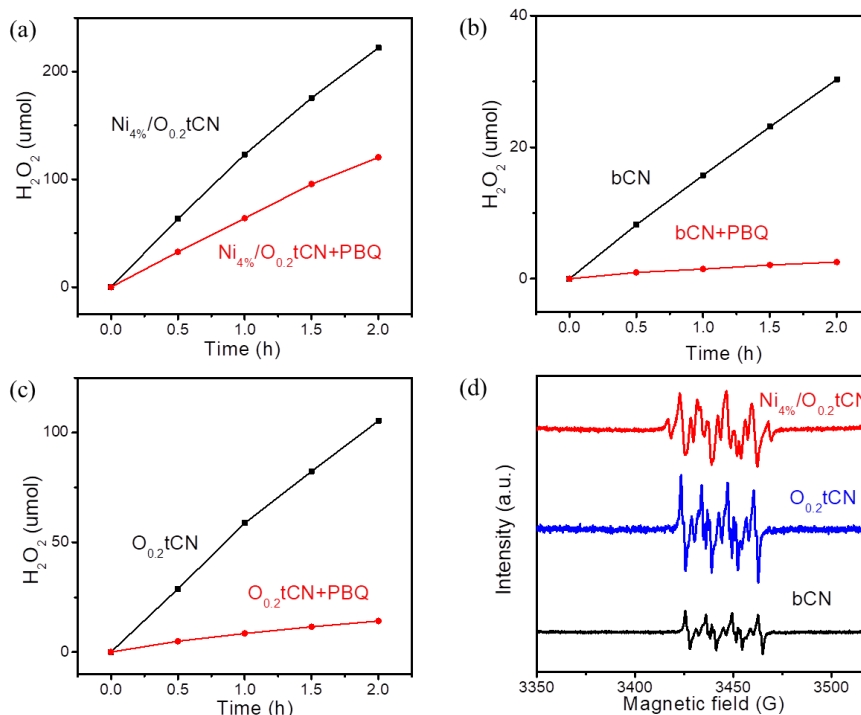
Figure 4.18. Photocatalytic H_2O_2 generation performance with and without 1MM PBQ on (a) bCN, (b) $O_{0.2}$tCN, and (c) $Ni_{4\%}/O_{0.2}$tCN. (d) EPR spectra of bCN, $O_{0.2}$tCN and $Ni_{4\%}/O_{0.2}$tCN with DMPO in methanol with the light on.

To further explore the reaction mechanism and determine the role of superoxide radicals in the reaction process, DMPO spin-trapping EPR spectroscopy was used to determine the presence of $*O_2^-$ in the surface of the photocatalyst. As shown in Figure 4.18d, after irradiating bCN with visible light for 3 min with DMPO and methanol, four characteristic EPR features were observed. These DMPO-$*O_2^-$ characteristic EPR peaks were much more intense for the $Ot_{0.2}CN$ sample under the same conditions, indicating that $O_{0.2}$tCN can generate larger amounts of $*O_2^-$ during the H_2O_2 evolution process, which is consistent with its higher H_2O_2 generation rate. On the other hand, while $Ni_{4\%}/O_{0.2}$tCN provided much higher H_2O_2 generation rates than $O_{0.2}$tCN, the $*O_2^-$ characteristic EPR signal was less intense, involving significant participation of an alternative path for H_2O_2 generation, i.e. the direct two-electron process. This result further confirms that the direct two-electron process has a fundamental role in the large H_2O_2 generation rates obtained in the presence of Ni.
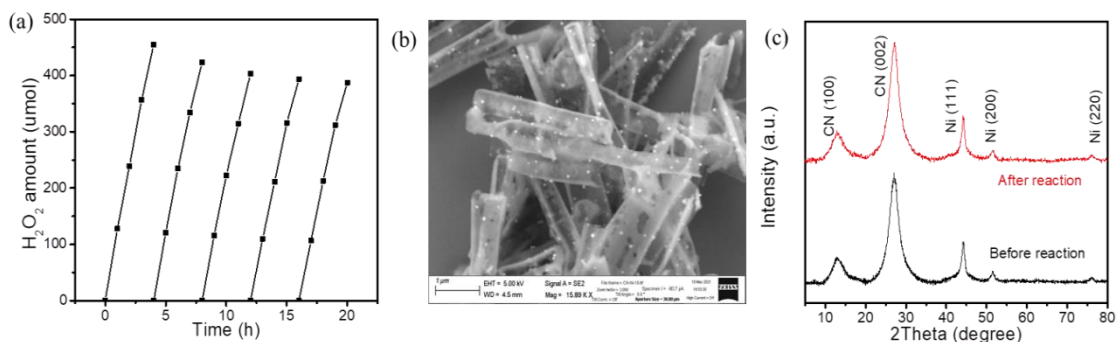
Figure 4.19. (a) Stability cycles of the $Ni_{4\%}/O_{0.2}tCN$ for H_2O_2 evolution under visible-light irradiation; (b) SEM image of $Ni_{4\%}/O_{0.2}tCN$ after 20 h photocatalytic H_2O_2 evolution reaction ; (c) XRD pattern of $Ni_{4\%}/O_{0.2}tCN$ before and after 20 h photocatalytic H_2O_2 evolution reaction.

Stability cycles of the $Ni_{4\%}/O_{0.2}tCN$ for H_2O_2 evolution under visible-light irradiation are displayed Figure 4.19a. After 20 hours of reaction, with five four-hour cycles, the catalyst maintained over 81 % photocatalytic H_2O_2 generation activities, i.e. about 99.3 mol $\cdot$ h^{-1}, demonstrating excellent stability and reusability. Besides, SEM and XRD analysis of the catalyst after 20 h photocatalytic H_2O_2 reaction demonstrated the morphology and crystallographic structure of the material to be stable under photocatalytic reaction conditions (Figure4.19b,c).
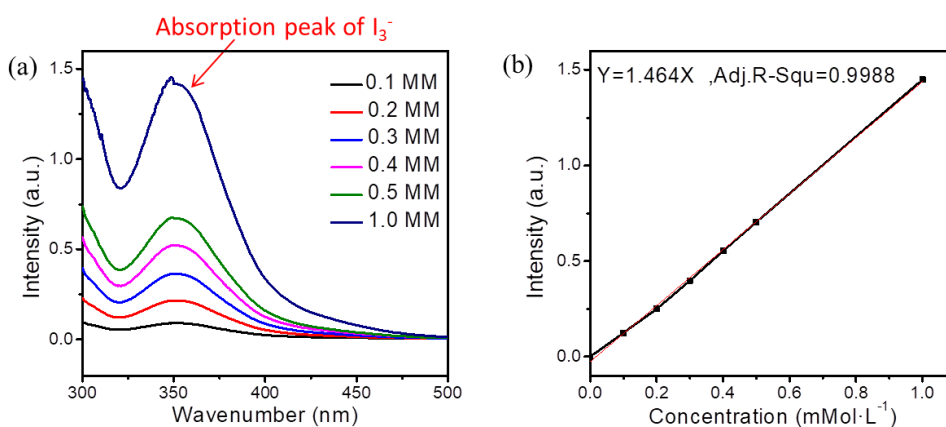

Figure 4.20. UV-vis absorption spectrum of different H_2O_2 amount in 1 M KI solution and 0.002 M $(NH_4)_6Mo_7O_{24}$.
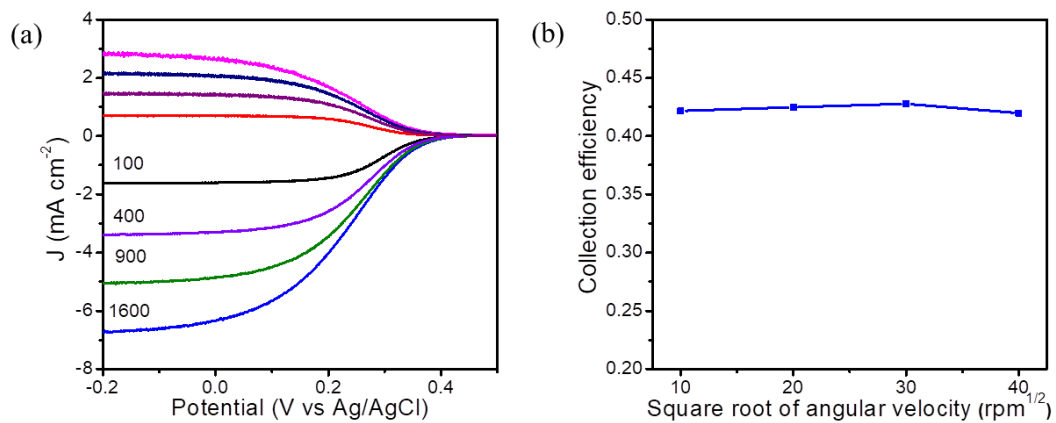
Figure 4.21. (a) LSV curves for a bare GC disk in 0.1 M KOH and 0.004 M $K_3Fe(CN)_6$. The ring is biased at 0.5 V. (b) N value of the bare RRDE under different rotating speeds.

Element	Weight%	Atomic%
C	36.21	39.78
N	58.38	57.94
O	2.13	1.90
Ni	3.24	0.78
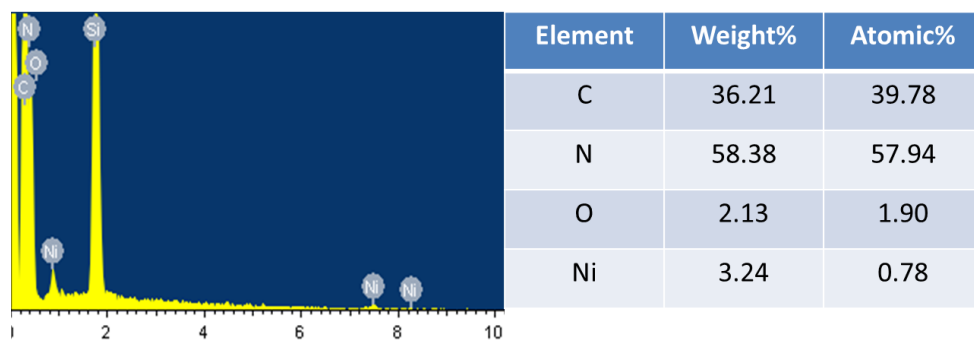
Figure 4.22. EDX spectrum of $Ni_{4\%}/O_{0.2}Tcn$ sample.

Element	Atomic %
C	42.21
N	56.10
O	1.68
S	0.00
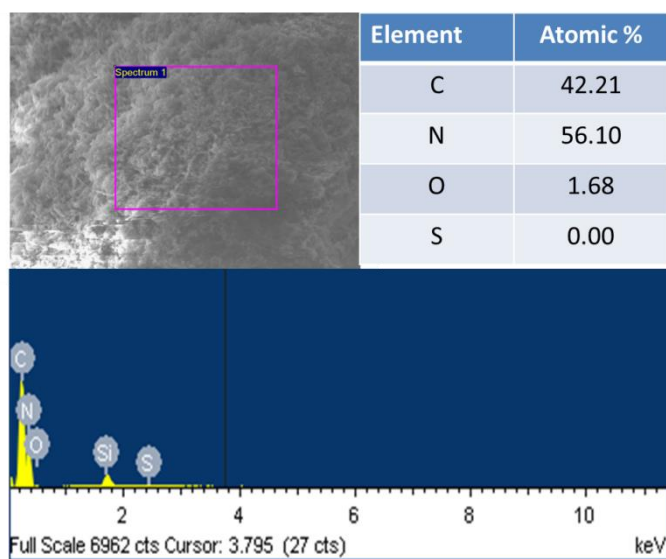
Figure 4.23. SEM images and EDX spectrum of $O_{0.2}tCN$.

Element	Atomic %
C	45.15
N	51.18
O	3.66
S	0.01

Figure 4.24. S 2p XPS spectrum and atomic ratio (measured by XPS technique) of $O_{0.2}$tCN.

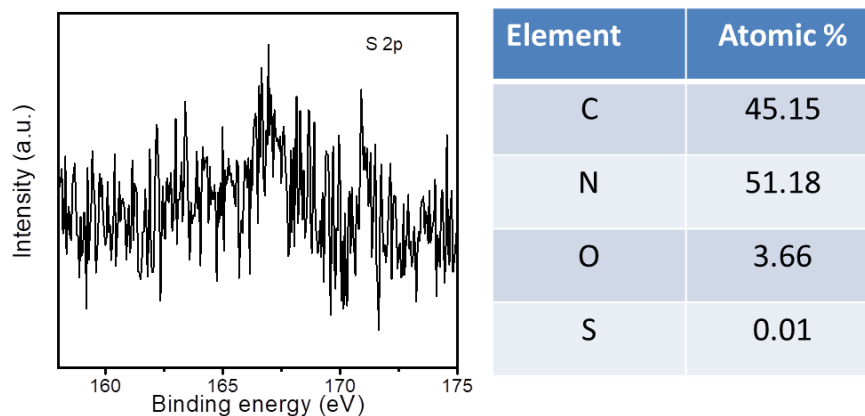**Table S5.** Relative atomic concentrations measured by EDS and XPS of bCN, $O_{0.2}$tCN and $Ni_{4\%}$/ $O_{0.2}$tCN.

Samples	Elements / Technique	C	N	O	Ni	S
bCN	XPS	44.06%	53.07%	1.88%	0	--
$O_{0.2}$tCN	XPS	45.15%	51.18%	3.66%	0	0.01%
$Ni_{4\%}$/$O_{0.2}$tCN	XPS	45.34%	48.66%	4.39%	1.61%	--
bCN	EDS	39.57%	59.29%	1.14%	0	--
$O_{0.2}$tCN	EDS	42.21%	56.10%	1.68%	0	0.00%
$Ni_{4\%}$/$O_{0.2}$tCN	EDS	39.78%	57.94%	1.90%	0.78%	--

Table S6. Comparison of photocatalytic H_2O_2 generation performance of co-catalyst/g-C_3N_4 based catalysts.

Material	Sacrificial reagent	Irradiation conditions	H_2O_2 yield ($umolh^{-1}g^{-1}$)	AQE	Ref.
CoP/g-C_3N_4	ethanol	λ>420 nm	700	--	[62]
Au/g-C_3N_4	2-propanol	UV/Vis	3735	19.5% at λ=380 nm	[63]
Cu-doped g-C_3N_4	ethanol	λ>400 nm	2263	--	[64]
g-C_3N_4 -carbon	2-propanol	UV-vis	318	10.2% at λ=420 nm	[65]
g-C_3N_4 -CNTs	formic acid	λ>420 nm	518	--	[66]
g-C_3N_4 -SiW_{11}	methanol	AM 1.5	152	6.5% at λ=420 nm	[67]
g-C_3N_4 -CoWO	electron donor	λ>420 nm	97	15.1% at λ=420 nm	[68]
Au/g-C_3N_4	C_2H_5OH	λ>420 nm	688	--	[69]
Ti_3C_2/g-C_3N_4	2-propanol	λ>420 nm	1317	--	[70]
Ni/OtCN	Ethanol	λ>420 nm	2460	14.9% at λ=420 nm	This work
		AM 1.5	5012	28.2% at λ=380 nm	

4.5 Conclusion

In summary, we detailed the synthesis of hollow tubular g-C_3N_4 (tCN), and demonstrated their controlled oxygen doping (OtCN), and their surface modification with highly dispersed nickel nanoparticles (Ni/OtCN) through a photoreduction process. OtCN samples displayed a hollow tubular structure with a large specific surface area (124 $m^2 \cdot g^{-1}$). With larger SSA and more porous structure, OtCN can provide more reactive sites, improve the light absorption by the multiple diffusion and accelerate the diffusion of reactants and products on the surface. Based on the DFT and RRDE results, the doping with oxygen and the presence of Ni nanoparticles greatly reduced the energy barrier for H_2O_2 generation, and improved the H_2O_2 selectivity from 60.8% to 88.9%, which enabled a more effective and efficient ORR towards H_2O_2 evolution. After loading the Ni nanoparticles, the electrons on the conduction band of OtCN are transferred to the surface of Ni which has a lower Femi level and then reducing the oxygen through a one-step two-electron direct reduction (O_2 are$_2O_2$) route, which is more efficient for H_2O_2 generation. Efficient charge separation and high selective formation of H_2O_2 during ORR process allow $Ni_{4\%}/O_{0.2}tCN$ to achieve an outstanding production rate up to 2464 $\mu mol\ g^{-1} \cdot h^{-1}$ under visible light and 5021 $\mu mol\ g^{-1} \cdot h^{-1}$ under simulated solar light and AQY of 28.2% at 380 nm and 14.9% at 420 nm.

4.6 References

[1]   Y. Kofuji, Y. Isobe, Y. Shiraishi, H. Sakamoto, S. Tanaka, S. Ichikawa, T. Hirai, Carbon Nitride–Aromatic Diimide–Graphene Nanohybrids: Metal-Free Photocatalysts for Solar-to-Hydrogen Peroxide Energy Conversion with 0.2% Efficiency, J. Am. Chem. Soc. 138 (2016) 10019–10025.

[2]   M. Melchionna, P. Fornasiero, M. Prato, The Rise of Hydrogen Peroxide as the Main Product by Metal-Free Catalysis in Oxygen Reductions, Adv. Mater. 31 (2019) 1802920.

[3]   S. Yang, A. Verdaguer-Casadevall, L. Arnarson, L. Silvioli, V. Čolić, R. Frydendal, J. Rossmeisl, I. Chorkendorff, I.E.L. Stephens, Toward the Decentralized Electrochemical

Production of H2O2: A Focus on the Catalysis, ACS Catal. 8 (2018) 4064–4081.

[4]   S. Kato, J. Jung, T. Suenobu, S. Fukuzumi, Production of hydrogen peroxide as a sustainable solar fuel from water and dioxygen, Energy Environ. Sci. 6 (2013) 3756–3764.

[5]   S.A. Mousavi Shaegh, N.-T. Nguyen, S.M. Mousavi Ehteshami, S.H. Chan, A membraneless hydrogen peroxide fuel cell using Prussian Blue as cathode material, Energy Environ. Sci. 5 (2012) 8225–8228.

[6]   G.H. Miley, N. Luo, J. Mather, R. Burton, G. Hawkins, L. Gu, E. Byrd, R. Gimlin, P.J. Shrestha, G. Benavides, J. Laystrom, D. Carroll, Direct NaBH4/H2O2 fuel cells, J. Power Sources. 165 (2007) 509–516.

[7]   S. Fukuzumi, Production of liquid solar fuels and their use in fuel cells, Joule. 1 (2017) 689–738.

[8]   H. Hou, X. Zeng, X. Zhang, Production of hydrogen peroxide by photocatalytic processes, Angew. Chemie Int. Ed. 59 (2020) 17356–17376.

[9]   Y. Shiraishi, T. Takii, T. Hagi, S. Mori, Y. Kofuji, Y. Kitagawa, S. Tanaka, S. Ichikawa, T. Hirai, Resorcinol–formaldehyde resins as metal-free semiconductor photocatalysts for solar-to-hydrogen peroxide energy conversion, Nat. Mater. 18 (2019) 985–993.

[10]   D. Tsukamoto, A. Shiro, Y. Shiraishi, Y. Sugano, S. Ichikawa, S. Tanaka, T. Hirai, Photocatalytic H2O2 Production from Ethanol/O2 System Using TiO2 Loaded with Au–Ag Bimetallic Alloy Nanoparticles, ACS Catal. 2 (2012) 599–603.

[11]   M. Teranishi, S. Naya, H. Tada, In situ liquid phase synthesis of hydrogen peroxide from molecular oxygen using gold nanoparticle-loaded titanium (IV) dioxide photocatalyst, J. Am. Chem. Soc. 132 (2010) 7850–7851.

[12]   H. Ou, C. Tang, X. Chen, M. Zhou, X. Wang, Solvated electrons for photochemistry syntheses using conjugated carbon nitride polymers, ACS Catal. 9 (2019) 2949–2955.

[13]   S. Zhao, T. Guo, X. Li, T. Xu, B. Yang, X. Zhao, Carbon nanotubes covalent combined with graphitic carbon nitride for photocatalytic hydrogen peroxide production under visible light, Appl. Catal. B Environ. 224 (2018) 725–732.

[14]   H. Hirakawa, S. Shiota, Y. Shiraishi, H. Sakamoto, S. Ichikawa, T. Hirai, Au nanoparticles supported on BiVO4: effective inorganic photocatalysts for H2O2

production from water and O2 under visible light, ACS Catal. 6 (2016) 4976–4982.

[15] J. Luo, Y. Liu, C. Fan, L. Tang, S. Yang, M. Liu, M. Wang, C. Feng, X. Ouyang, L. Wang, L. Xu, J. Wang, M. Yan, Direct Attack and Indirect Transfer Mechanisms Dominated by Reactive Oxygen Species for Photocatalytic H2O2 Production on g-C3N4 Possessing Nitrogen Vacancies, ACS Catal. 11 (2021) 11440–11450.

[16] Q. He, B. Viengkeo, X. Zhao, Z. Qin, J. Zhang, X. Yu, Y. Hu, W. Huang, Y. Li, Multiscale structural engineering of carbon nitride for enhanced photocatalytic H2O2 production, Nano Res. (2021).

[17] Y. Zhao, P. Zhang, Z. Yang, L. Li, J. Gao, S. Chen, T. Xie, C. Diao, S. Xi, B. Xiao, Mechanistic analysis of multiple processes controlling solar-driven H2O2 synthesis using engineered polymeric carbon nitride, Nat. Commun. 12 (2021) 1–11.

[18] L. Zhou, J. Feng, B. Qiu, Y. Zhou, J. Lei, M. Xing, L. Wang, Y. Zhou, Y. Liu, J. Zhang, Ultrathin g-C3N4 nanosheet with hierarchical pores and desirable energy band for highly efficient H2O2 production, Appl. Catal. B Environ. 267 (2020) 118396.

[19] S. Li, G. Dong, R. Hailili, L. Yang, Y. Li, F. Wang, Y. Zeng, C. Wang, Effective photocatalytic H2O2 production under visible light irradiation at g-C3N4 modulated by carbon vacancies, Appl. Catal. B Environ. 190 (2016) 26–35.

[20] Y. Zuo, X. Xu, C. Zhang, J. Li, R. Du, X. Wang, X. Han, J. Arbiol, J. Llorca, J. Liu, A. Cabot, SnS2/g-C3N4/graphite nanocomposites as durable lithium-ion battery anode with high pseudocapacitance contribution, Electrochim. Acta. 349 (2020) 136369.

[21] X. Dang, R. Yang, Z. Wang, S. Wu, H. Zhao, Efficient visible-light activation of molecular oxygen to produce hydrogen peroxide using P doped gC 3 N 4 hollow spheres, J. Mater. Chem. A. 8 (2020) 22720–22727.

[22] X. Bai, L. Wang, R. Zong, Y. Zhu, Photocatalytic Activity Enhanced via g-C3N4 Nanoplates to Nanorods, J. Phys. Chem. C. 117 (2013) 9952–9961.

[23] M. Tahir, C. Cao, N. Mahmood, F.K. Butt, A. Mahmood, F. Idrees, S. Hussain, M. Tanveer, Z. Ali, I. Aslam, Multifunctional g-C3N4 Nanofibers: A Template-Free Fabrication and Enhanced Optical, Electrochemical, and Photocatalyst Properties, ACS Appl. Mater. Interfaces. 6 (2014) 1258–1265.

[24] C. Zhang, R. Du, J.J. Biendicho, M. Yi, K. Xiao, D. Yang, T. Zhang, X. Wang, J. Arbiol, J.

Llorca, Y. Zhou, J.R. Morante, A. Cabot, Tubular CoFeP@CN as a Mott–Schottky Catalyst with Multiple Adsorption Sites for Robust Lithium–Sulfur Batteries, Adv. Energy Mater. 11 (2021) 2100432.

[25] S. Guo, Z. Deng, M. Li, B. Jiang, C. Tian, Q. Pan, H. Fu, Phosphorus‑doped carbon nitride tubes with a layered micro‑nanostructure for enhanced visible‑light photocatalytic hydrogen evolution, Angew. Chemie. 128 (2016) 1862–1866.

[26] G. Liu, P. Niu, C. Sun, S.C. Smith, Z. Chen, G.Q. Lu, H.-M. Cheng, Unique electronic structure induced high photoreactivity of sulfur-doped graphitic C3N4, J. Am. Chem. Soc. 132 (2010) 11642–11648.

[27] Z. Wei, M. Liu, Z. Zhang, W. Yao, H. Tan, Y. Zhu, Efficient visible-light-driven selective oxygen reduction to hydrogen peroxide by oxygen-enriched graphitic carbon nitride polymers, Energy Environ. Sci. 11 (2018) 2581–2589.

[28] J. Cao, H. Wang, Y. Zhao, Y. Liu, Q. Wu, H. Huang, M. Shao, Y. Liu, Z. Kang, Phosphorus-doped porous carbon nitride for efficient sole production of hydrogen peroxide via photocatalytic water splitting with a two-channel pathway, J. Mater. Chem. A. 8 (2020) 3701–3707.

[29] Y. Zhu, T. Wang, T. Xu, Y. Li, C. Wang, Size effect of Pt co-catalyst on photocatalytic efficiency of g-C3N4 for hydrogen evolution, Appl. Surf. Sci. 464 (2019) 36–42.

[30] Y. Zuo, Y. Liu, J. Li, R. Du, X. Yu, C. Xing, T. Zhang, L. Yao, J. Arbiol, J. Llorca, Solution-processed ultrathin SnS2–Pt nanoplates for photoelectrochemical water oxidation, ACS Appl. Mater. Interfaces. 11 (2019) 6918–6926.

[31] B. Li, Y. Zhang, R. Du, L. Gan, X. Yu, Synthesis of Bi2S3–Au dumbbell heteronanostructures with enhanced photocatalytic and photoresponse properties, Langmuir. 32 (2016) 11639–11645.

[32] X. Chang, J. Yang, D. Han, B. Zhang, X. Xiang, J. He, Enhancing light-driven production of hydrogen peroxide by anchoring Au onto C3N4 catalysts, Catalysts. 8 (2018) 147.

[33] G. Zuo, S. Liu, L. Wang, H. Song, P. Zong, W. Hou, B. Li, Z. Guo, X. Meng, Y. Du, Finely dispersed Au nanoparticles on graphitic carbon nitride as highly active photocatalyst for hydrogen peroxide production, Catal. Commun. 123 (2019) 69–72.

[34] H. Zhang, P. Zhang, M. Qiu, J. Dong, Y. Zhang, X.W. (David) Lou, Ultrasmall MoOx

Clusters as a Novel Cocatalyst for Photocatalytic Hydrogen Evolution, Adv. Mater. 31 (2019) 1804883.

[35] A. Indra, P.W. Menezes, K. Kailasam, D. Hollmann, M. Schröder, A. Thomas, A. Brückner, M. Driess, Nickel as a co-catalyst for photocatalytic hydrogen evolution on graphitic-carbon nitride (sg-CN): what is the nature of the active species?, Chem. Commun. 52 (2016) 104–107.

[36] X. Yu, R. Du, B. Li, Y. Zhang, H. Liu, J. Qu, X. An, Biomolecule-assisted self-assembly of CdS/MoS2/graphene hollow spheres as high-efficiency photocatalysts for hydrogen evolution without noble metals, Appl. Catal. B Environ. 182 (2016) 504–512.

[37] R. Du, Y. Zhang, B. Li, X. Yu, H. Liu, X. An, J. Qu, Biomolecule-assisted synthesis of defect-mediated Cd 1– x Zn x S/MoS 2/graphene hollow spheres for highly efficient hydrogen evolution, Phys. Chem. Chem. Phys. 18 (2016) 16208–16215.

[38] R. Zhou, Y. Zheng, M. Jaroniec, S.-Z. Qiao, Determination of the electron transfer number for the oxygen reduction reaction: from theory to experiment, ACS Catal. 6 (2016) 4720–4728.

[39] B. Lv, X. Li, K. Guo, J. Ma, Y. Wang, H. Lei, F. Wang, X. Jin, Q. Zhang, W. Zhang, Controlling Oxygen Reduction Selectivity through Steric Effects: Electrocatalytic Two‐Electron and Four‐Electron Oxygen Reduction with Cobalt Porphyrin Atropisomers, Angew. Chemie. 133 (2021) 12852–12856.

[40] G. Kresse, J. Furthmüller, Efficient iterative schemes for ab initio total-energy calculations using a plane-wave basis set, Phys. Rev. B. 54 (1996) 11169.

[41] G. Kresse, J. Hafner, Ab initio molecular-dynamics simulation of the liquid-metal–amorphous-semiconductor transition in germanium, Phys. Rev. B. 49 (1994) 14251.

[42] P.E. Blöchl, Projector augmented-wave method, Phys. Rev. B. 50 (1994) 17953.

[43] J.P. Perdew, K. Burke, M. Ernzerhof, Generalized gradient approximation made simple, Phys. Rev. Lett. 77 (1996) 3865.

[44] B. Hammer, L.B. Hansen, J.K. Nørskov, Improved adsorption energetics within density-functional theory using revised Perdew-Burke-Ernzerhof functionals, Phys. Rev. B. 59 (1999) 7413.

[45] J.D. Pack, H.J. Monkhorst, " Special points for Brillouin-zone integrations"—a reply,

Phys. Rev. B. 16 (1977) 1748.

[46] J.K. Nørskov, J. Rossmeisl, A. Logadottir, L. Lindqvist, J.R. Kitchin, T. Bligaard, H. Jonsson, Origin of the overpotential for oxygen reduction at a fuel-cell cathode, J. Phys. Chem. B. 108 (2004) 17886–17892.

[47] F. Xue, Y. Si, M. Wang, M. Liu, L. Guo, Toward efficient photocatalytic pure water splitting for simultaneous H2 and H2O2 production, Nano Energy. 62 (2019) 823–831.

[48] L. Wang, S. Cao, K. Guo, Z. Wu, Z. Ma, L. Piao, Simultaneous hydrogen and peroxide production by photocatalytic water splitting, Chinese J. Catal. 40 (2019) 470–475.

[49] Y. Jiang, Z. Sun, C. Tang, Y. Zhou, L. Zeng, L. Huang, Enhancement of photocatalytic hydrogen evolution activity of porous oxygen doped g-C3N4 with nitrogen defects induced by changing electron transition, Appl. Catal. B Environ. 240 (2019) 30–38.

[50] P. Niu, L. Zhang, G. Liu, H. Cheng, Graphene‐like carbon nitride nanosheets for improved photocatalytic activities, Adv. Funct. Mater. 22 (2012) 4763–4770.

[51] Y. Zhang, Z. Chen, J. Li, Z. Lu, X. Wang, Self-assembled synthesis of oxygen-doped g-C3N4 nanotubes in enhancement of visible-light photocatalytic hydrogen, J. Energy Chem. 54 (2021) 36–44.

[52] S. Zhao, X. Zhao, H. Zhang, J. Li, Y. Zhu, Covalent combination of polyoxometalate and graphitic carbon nitride for light-driven hydrogen peroxide production, Nano Energy. 35 (2017) 405–414.

[53] A. Ishikawa, T. Takata, J.N. Kondo, M. Hara, H. Kobayashi, K. Domen, Oxysulfide Sm2Ti2S2O5 as a stable photocatalyst for water oxidation and reduction under visible light irradiation ($\lambda \leqslant$ 650 nm), J. Am. Chem. Soc. 124 (2002) 13547–13553.

[54] C. Xing, Y. Liu, Y. Zhang, J. Liu, T. Zhang, P. Tang, J. Arbiol, L. Soler, K. Sivula, N. Guijarro, Porous NiTiO 3/TiO 2 nanostructures for photocatatalytic hydrogen evolution, J. Mater. Chem. A. 7 (2019) 17053–17059.

[55] X. Xie, L. Shang, R. Shi, G.I.N. Waterhouse, J. Zhao, T. Zhang, Tubular assemblies of N-doped carbon nanotubes loaded with NiFe alloy nanoparticles as efficient bifunctional catalysts for rechargeable zinc-air batteries, Nanoscale. 12 (2020) 13129–13136.

[56] Y. Zhao, Y. Liu, J. Cao, H. Wang, M. Shao, H. Huang, Y. Liu, Z. Kang, Efficient

production of H2O2 via two-channel pathway over ZIF-8/C3N4 composite photocatalyst without any sacrificial agent, Appl. Catal. B Environ. 278 (2020) 119289.

[57] Y. Fu, J. Zhao, H. Wang, H. Huang, Y. Liu, Y. Dou, M. Shao, Z. Kang, All-solid-state Z-scheme system of NiO/CDs/BiVO4 for visible light-driven efficient overall water splitting, Chem. Eng. J. 358 (2019) 134–142.

[58] Y. Li, H. Xu, S. Ouyang, D. Lu, X. Wang, D. Wang, J. Ye, In situ surface alkalinized gC 3 N 4 toward enhancement of photocatalytic H 2 evolution under visible-light irradiation, J. Mater. Chem. A. 4 (2016) 2943–2950.

[59] R. Liu, H. Liu, Y. Li, Y. Yi, X. Shang, S. Zhang, X. Yu, S. Zhang, H. Cao, G. Zhang, Nitrogen-doped graphdiyne as a metal-free catalyst for high-performance oxygen reduction reactions, Nanoscale. 6 (2014) 11336–11343.

[60] L. Hao, S. Zhang, R. Liu, J. Ning, G. Zhang, L. Zhi, Bottom-Up Construction of Triazine-Based Frameworks as Metal-Free Electrocatalysts for Oxygen Reduction Reaction, Adv. Mater. 27 (2015) 3190–3195.

[61] H. Kim, O.S. Kwon, S. Kim, W. Choi, J.-H. Kim, Harnessing low energy photons (635 nm) for the production of H 2 O 2 using upconversion nanohybrid photocatalysts, Energy Environ. Sci. 9 (2016) 1063–1073.

[62] Y. Peng, L. Wang, Y. Liu, H. Chen, J. Lei, J. Zhang, Visible‐light‐driven photocatalytic H2O2 production on g‐C3N4 loaded with CoP as a noble metal free cocatalyst, Eur. J. Inorg. Chem. 2017 (2017) 4797–4802.

[63] X. Chang, J. Yang, D. Han, B. Zhang, X. Xiang, J. He, Enhancing light-driven production of hydrogen peroxide by anchoring Au onto C3N4 catalysts, Catalysts. 8 (2018) 147.

[64] S. Hu, X. Qu, P. Li, F. Wang, Q. Li, L. Song, Y. Zhao, X. Kang, Photocatalytic oxygen reduction to hydrogen peroxide over copper doped graphitic carbon nitride hollow microsphere: the effect of Cu (I)-N active sites, Chem. Eng. J. 334 (2018) 410–418.

[65] R. Wang, X. Zhang, F. Li, D. Cao, M. Pu, D. Han, J. Yang, X. Xiang, Energy-level dependent H2O2 production on metal-free, carbon-content tunable carbon nitride photocatalysts, J. Energy Chem. 27 (2018) 343–350.

[66] S. Zhao, T. Guo, X. Li, T. Xu, B. Yang, X. Zhao, Carbon nanotubes covalent combined with graphitic carbon nitride for photocatalytic hydrogen peroxide production under

visible light, Appl. Catal. B Environ. 224 (2018) 725–732.

[67] S. Zhao, X. Zhao, S. Ouyang, Y. Zhu, Polyoxometalates covalently combined with graphitic carbon nitride for photocatalytic hydrogen peroxide production, Catal. Sci. Technol. 8 (2018) 1686–1695.

[68] S. Zhao, X. Zhao, Insights into the role of singlet oxygen in the photocatalytic hydrogen peroxide production over polyoxometalates-derived metal oxides incorporated into graphitic carbon nitride framework, Appl. Catal. B Environ. 250 (2019) 408–418.

[69] G. Zuo, S. Liu, L. Wang, H. Song, P. Zong, W. Hou, B. Li, Z. Guo, X. Meng, Y. Du, Finely dispersed Au nanoparticles on graphitic carbon nitride as highly active photocatalyst for hydrogen peroxide production, Catal. Commun. 123 (2019) 69–72.

[70] Y. Yang, Z. Zeng, G. Zeng, D. Huang, R. Xiao, C. Zhang, C. Zhou, W. Xiong, W. Wang, M. Cheng, Ti3C2 Mxene/porous g-C3N4 interfacial Schottky junction for boosting spatial charge separation in photocatalytic H2O2 production, Appl. Catal. B Environ. 258 (2019) 117956.

Chrapter 5

Tubular CoFeP@CN as a Mott-Schottky catalyst with multiple adsorption sites for robust lithium–sulfur batteries
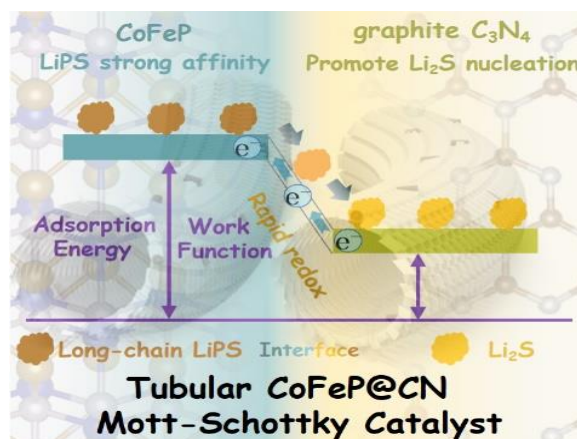
5.1 Abstract

The shuttle effect and the sluggish reaction kinetics of lithium polysulfide (LiPS) seriously compromise the performance of lithium-sulfur batteries (LSBs). To overcome these limitations and enable the fabrication of robust LSBs, here we propose the use of Mott-Schottky catalyst based on bimetallic phosphide CoFeP nanocrystals supporting on carbon nitride tubular (t-CN) nanostructures as sulfur hosts. Density functional theory calculations and experimental data confirm that CoFeP@CN composites are characterized by a suitable electronic structure and charge rearrangement that allows them to act as a Mott-Schottky catalyst to accelerate LiPS conversion. Besides, the tubular geometry of CoFeP@CN composites facilitates the diffusion of Li ions, accommodates volume change during the reaction, and offers abundant lithiophilic/sulfiphilic sites to effectively trap soluble LiPS. As a result, S@CoFeP@CN electrodes deliver high initial capacities of 1607 mAh g^{-1} at 0.1 C, superior rate performance of 630 mAh g^{-1} at 5 C, and remarkable cycling stability with 90.44% capacity retention over 700 cycles. We further produce coin cells with high sulfur loading, 4.1 mg cm^{-2}, and pouch cells with 0.1 Ah capacity to validate their superior cycling

stability. In addition, we demonstrate here that CoFeP@CN hosts greatly alleviate the often overlooked issues of low energy efficiency and serious self-discharging in LSBs.

5.2 Introduction

Lithium-sulfur batteries (LSBs) are regarded as the most promising candidate to replace lithium-ion batteries (LIBs) in next-generation energy storage systems. Compared with LIBs, LSBs are characterized by a sixfold higher theoretical energy density, 2600 W h kg^{-1}, and a potentially lower cost and environmental impact if properly selecting the cathode materials.[1–3] Despite these attractive advantages, the electrically insulating character of sulfur and the shuttle effect of intermediate lithium polysulfides (LiPS) greatly limit the practical application of LSBs.[4] Additionally, the serious volume changes and slow redox kinetics during the charging/discharging process also reduce the cycling life and power density.[5]

Several sulfur host materials have been proposed to overcome the aforementioned limitations.[2,6] Carbon-based hosts with high electrical conductivity and large specific surface area (SSA), like graphene,[7] carbon nanotubes[8] and hollow carbon spheres,[9] have been employed to disperse sulfur species and confine the volume expansion. However, the weak physical interaction between LiPS and the non-polar surfaces of these materials makes them ineffective to capture soluble LiPS, which results in a serious shuttle effect and a reduced cyclability.[10] Previous work has demonstrated that LiPS can be confined through strong chemical binding and rapid catalytic conversion at polar surfaces.[11] In this direction, the use of transition metal oxides (TMO) and sulfides (TMS) remarkably improve cycling performance. But unfortunately, polar TMO/TMS usually suffer from unsatisfying electrical conductivities that greatly limit the rate performance.

Alternatively, transition metal phosphides (TMP) with metallic character may simultaneously provide the required high electrical conductivity and polar surfaces.[12,13] Besides, TMP also show exceptional catalytic activity towards Li-S redox reactions. As an example, the Qian group showed cobalt phosphide to exhibit the best catalytic performance among several Co-based compounds and associated this experimental evidence with an appropriate p-band

position.[14] Among phosphides, bimetallic compositions provide an additional degree of freedom to tune the electronic structure and optimize electrocatalytic activity in several reactions, including hydrogen and oxygen evolution,[15, 16] and CO_2 reduction,[17] among others. To maximize the amount of LiPS adsorption sites and catalytic activity, the TMP should be nanostructured. In this direction, TMP nanocrystals (NCs) can provide relatively high SSAs and abundant unsaturated sites and defects to effectively reduce the reaction energy barrier.[18] To prevent their aggregation caused by the surface energy, and also compensate for the relatively high volumetric density of TMP, TMP NCs can be combined with lightweight support, which should be characterized by a large SSA to support a high dispersion of the TMP phase and high porosity to allow an effective diffusion of lithium ions.

As a proper support material, graphite C_3N_4 is based on abundant elements and it can be obtained with high SSA.[19] Besides, in contrast to graphene and carbon nanotubes, the presence of Lewis-base pyridine nitrogen in C_3N_4 can effectively interact with the strong Lewis-acid of terminal Li atoms in LiPS, thus contributing to prolonging the lifespan of LSBs.[20–22] In terms of geometric structure, graphite C_3N_4 nanosheets (s-CN) prepared by the traditional liquid-phase exfoliation method usually suffer from low SSA due to re-aggregation by Van der Waals forces.[23] On the other hand, template methods to produce high-SSA C_3N_4 are cumbersome and wasteful, inappropriate for a technology with a huge potential market and thus potentially requiring enormous amounts of materials.[19]

Besides, the catalytic activity of C_3N_4-based catalysts can be significantly augmented by altering their electronic structures through tuning the surface/interface atom environment.[24,25] When combining metallic TMP NCs with n-type semiconductive C_3N_4, the charge is rearranged at the created Mott-Schottky junction and a built-in electric field appears at the TMP/C_3N_4 interphase.[25–27] This electric field with altered electron cloud density potentially promotes catalytic activity, suppress the shuttle effect, and boost lithium ion diffusion, subsequently improved Li-S performance.[28,29] Despite the great promise on regulating Li-S reaction, there is little research on Mott-Schottky catalyst up to date. And to the best of our knowledge, there is no report investigating the electronic structure of TMP/C_3N_4 hetrojunction attempt to apply for LSBs.

In the present study, we first engineer and characterize a novel porous graphite C_3N_4 tubular structure (t-CN). Subsequently, we use an electrostatic self-assembly method to blend this novel t-CN with colloidal CoFeP NCs, which we selected taking into account the catalytic activity toward Li-S reaction of single-metal cobalt/iron phosphides and its proper band alignement with CN.[30,31] The obtained tubular CoFeP@CN Mott-Schottky catalysts are then analyzed both experimentally and through theoretical calculations. Afterwards, the performance of S@CoFeP@CN cathodes is thoroughly tested and their superior cycling stability and rate capability are demonstrated. Finally, lithium-sulfur pouch cells are manufactured and their potential toward practical applications is validated.

5.3 Experimental section

Preparing of CoFeP nanoparticles. In a typical synthesis, 2.4 g (10 mmol) of 1-hexadecylamine (HDA, 90%, Acros Organics) were combined with 10.0 mL of 1-octadecene (ODE, 90%, ACROS Organics) and 2.6 mL (10 mmol) of triphenyl phosphite (TPP, 99%, ACROS Organics) in a 50 mL flask. The system was degassed and heated to 150 °C and maintained at this temperature for 1 h to remove low boiling point impurities, moisture, and oxygen. After 4 mL ODE contain 384 mg (1 mmol) $Co_2(CO)_8$ (95%, ACROS Organics) and 390 mg (2 mmol) $Fe(CO)_5$ (Sigma-Aldrich) was added into the system the temperature was then increased to 290 °C in 20 min and kept there for 1 h. Afterward, the mixture was allowed to cool down to 200 °C by removing the heating mantle and then cooled rapidly down to room temperature with a water bath. The black product was isolated by precipitation with acetone. To remove as many organics as possible, two redispersion and precipitation cycles using chloroform and acetone were additionally carried out. To further remove the organic ligands, 10 mL of CoFeP NCs dispersion (10 mg mL^{-1}) in hexane (99.0%, Honeywell) was combined with 10 mL acetonitrile (99%, ACROS Organics) to form a two-phase mixture and then add 1 mL HBF_4 solution (48%) in it. The resulting solution was sonicated until the NCs transferred from the upper to the bottom layer. The surface-modified NCs were washed with ethanol three times and dispersed in 10 mL ethanol with a little amount of N,N-Dimethylformamide (DMF, 99.8%, Alfa Aesa) for further use.

Preparing tubular t-CN and s-CN. The t-CN was prepared by an annealing method using a mixture of urea and melamine as the precursor. Typically, 100 mg urea (99.5%, ACROS Organics) and 10 mg melamine (99%, ACROS Organics) was put in a mortar and grinded for 10 min. The mixture powder was loaded into a graphite die and compacted into cylinders (Ø 10 mm×10 mm) under a pressure of 10 MPa. Then cylinders were put into a crucible covered loosely with a lid and then heated at 550 °C for 4 h in static air in a muffle furnace. The ramping rate was 5 °C min^{-1}. After cooled naturally to room temperature, the resultant yellow solid was collected and grounded into powder for further use. s-CN was prepared by the same annealing method using melamine as the precursor but without any pressure treatment. After cooling naturally to room temperature, the resultant yellow solid was collected and grounded into powder, then an ultrasonic treatment was conducted for 2 hours to obtain the s-CN.

Synthesis of CoFeP@CN composites. Typically, 50 mg of t-CN powder was dispersed in 15 mL ethanol and DMF mixed solution and then sonicated for 1 h. Then 5 mL of a CoFeP ethanol dispersion (10 mg mL^{-1}) was added into the mixture solution and stirred for 24 h. The product *CoFeP@CN(also named 50%CoFeP@CN)* was washed with ethanol 3 times and dry under vacuum ov*ernight. 25%CoFeP@CN and 75%CoFeP@CN were fabricated by the same methods with different weight ratio.*

Synthesis of S@CN, S@CoFeP, S@CoFeP@CN, and S@Super P. Typically, CoFeP@CN and sulfur powder (99.98%, Sigma Aldrich) were well mixed with the weight ratio of 1:3, and then heated the mixture at 155 °C for 6 h in a sealed glass bottle under Ar protection. The redundant sulfur not incorporated into CoFeP@CN was removed by 10 mL CS$_2$ (99.9%, Alfa Aesa) and ethanol solution (1:4, volume ratio). S@CN, S@CoFeP, and S@Super P were prepared by the same method.

Materials Characterization: X-ray diffraction (XRD) patterns were detected by Bruker AXS D8 Advance X-ray diffractometer with Cu K radiation (λ = 1.5106 Å) operating at 40 kV and 40 mA. The morphology and microstructure of samples were investigated by FESEM (ZEISS Auriga) equipped with an energy-dispersive X-ray spectroscopy (EDS) detector operated at 20 kV. High-resolution TEM (HRTEM) and scanning TEM (STEM) studies were carried out

using a field emission gun FEI Tecnai F20 microscope at 200 kV with a point-to-point resolution of 0.19 nm. High angle annular dark-field (HAADF) STEM was combined with electron energy loss spectroscopy (EELS) in the Tecnai microscope by using a GATAN QUANTUM filter. X-ray photoelectron spectroscopy (XPS) measurements were carried out in normal emission using an Al anode XR50 source operating at 150 mW and a Phoibos 150 MCD-9 detector. The content of sulfur in the composites was estimated by TGA (PerkinElmer Diamond TG/DTA instrument) experiments under N_2 atmosphere. The specific surface area and analysis of the pore size distribution were obtained from nitrogen adsorption-desorption isotherms on Tristar II 3020 Micromeritics system. UV-vis absorption spectra were identified by the PerkinElmer LAMBDA 950 UV-vis spectrophotometer. Zeta potential measurements were obtained by the Malvern Zetasizer Nano ZS90 zeta instrument.

Li-S cell assembly and measurements: Li-S batteries performance was tested at room temperature in CR2032 coin-type cells. The assembly process, in which lithium foils were used as anode and Celgard 2400 membranes as separators, S@host composites electrode work as the cathode, were conducted in a glovebox filled with argon. Cathode was obtained by doctoral blade methods. Briefly, S@host composites (S@t-CN; S@CoFeP; S@CoFeP@CN and S@CoFeP@CN), conductive carbon, and PVDF binder (weight ratio = 8:1:1) were well mixed into N-methyl pyrrolidone (NMP, 99.5%, Acros Organics) to form a black slurry, and then coated it on Al foils and dried at 60 °C overnight. After drying the foil was punched into small disks with a diameter of 12.0 mm. Sulfur loading was about 1.0 mg cm^{-2}. High-loading tests were applied with sulfur-loaded of 4.1 mg cm^{-2}. The electrolyte was prepared by dissolving 1.0 M lithium bis(trifluoromethanesulfonyl)imide (LiTFSI) (99%, Acros Organics) into a solution of 1,2-dimethoxy ethane (DME, 99%, Honeywell) and 1,3-dioxolane (DOL, 99.5%, Alfa Aesar) (v/v = 1/1) and containing 0.2 M of $LiNO_3$ (99.98%, Alfa Aesar). For each coin cell, 15 µL/mg S^{-1} of electrolyte was used, high-loaded coin cells added 12 mL g^{-1}_{sulfur}, and lean electrolyte coin cells added 6.7 or 8.9 mL g^{-1}_{sulfur}. The Li-S cells were galvanostatically cycled at a voltage window of 1.7-2.8 V on a Neware BTS4008 battery tester with different C rates, low current activation was conducted before the cycling test. Cyclic voltammetry (CV) measurements were performed on a battery tester BCS-810 from Bio Logic at a scan rate of 0.1-0.4 mV s^{-1} and electrochemical impedance spectroscopy (EIS) tests were

conducted with a voltage amplitude of 10 mV in the frequency range 100 kHz to 10 mHz.

Preparation of Li$_2$S$_6$ solutions for adsorption test: Sulfur and Li$_2$S (99.9%, Alfa Aesar) were mixed with the molar ratio of 5:1, and then the powder was poured into appropriate amounts of DME/DOL (volume ratio of 1:1) solution under vigorous magnetic stirring overnight until a dark brown solution was obtained. 15 mg of Super P, t-CN, s-CN, CoFeP, and CoFeP@CN were poured into 3.0 mL 10 mM Li$_2$S$_6$ solution, respectively. All the steps were conducted under Ar atmosphere.

Symmetric cell assembly and measurements: Symmetric cells also assembled and tested under CR2032 coin cells, in which two pieces of the same electrode (average loading about 0.5 mg cm^{-2}) were used as working and counter electrodes, and 40 µL of electrolyte containing 0.5 mol L^{-1} Li$_2$S$_6$ and 1 mol L^{-1} LiTFSI dissolved in DOL/DME (v/v = 1/1) was added. Electrodes were prepared by the doctor blade method coating the host materials with conductive carbon and PVDF on Al foil. In all cases, CV measurements were performed at a scan rate of 5 mV s^{-1}.

Measurement of nucleation and dissolution of Li$_2$S: Nucleation and dissolution of Li$_2$S were conducted in CR2032 coin cells, where 1 mg host materials loaded on the carbon papers applied as work electrode, Li foil worked as the counter electrode, 20 µL catholyte was added in the positive side, in which 0.25 M Li$_2$S$_8$ dissolved in tetraglyme with 1.0 M LiTFSI added, and 20 µL of 1.0 M LiTFSI in tetraglyme solution as anolyte. The cells were first discharged at a current of 0.112 mA to 2.06 V and then hold the voltage at 2.05 V until the current decreased to 10^{-2} mA for Li$_2$S nucleation and growth. To invest the Li$_2$S dissolution, fresh cells were firstly discharged at a current of 0.10 mA to 1.80 V and subsequently discharged at 0.01 mA to 1.80 V for full transformation of S species into solid Li$_2$S, after that the cells were potentiostatically charged at 2.40 V for the dissolution of Li$_2$S into LiPS until charge current was below 10^{-5} A.

Pouch cell assembly and measurements: Both the S@CoFeP@CN cathode and lithium anode were cut into 7 × 5.5 cm pieces. The sulfur loading of the cathode in the pouch cell (7 × 5.5 cm) was 1.6 mg cm^{-2} (total sulfur loading: 61.6 mg). The E/S ratio was about 15 mL g^{-1}$_{Sulfur}$, the thickness of the lithium belt anode was 0.4 mm. Separator and electrolyte were sandwiched between the tailored S@CoFeP@CN and lithium belt. The pouch cell was

galvanostatically cycled within a voltage range of 1.5–3.0 V.

Theoretical Computation: All geometric optimizations and electronic structure calculations were performed using density functional theory (DFT), as implemented in the Vienna ab initio Simulation Package (VASP) (MedeA 3.2.1-VASP5.4.4), within the generalized gradient approximation (GGA) of Perdew–Burke–Ernzerhof (PBE) for the exchange-correlation potential. Projector augmented wave (PAW) pseudopotentials were applied with an energy cutoff of 450 eV.[1] A supercell of graphite C_3N_4 containing 4×2×1 unit cells and CoFeP containing 3×3×1 unit cells was used to model CoFeP@CN systems. For pure graphite C_3N_4, CoFeP, and CoFeP@CN, the Monkhorst–Pack k-point mesh of 5×5×1, 5×5×1, and 2×2×1 were used to perform geometry optimizations, and a 10×10×1, 10×10×1, and 4×4×1 k-point mesh were used for the electronic structure calculations, respectively. All atoms were relaxed until the Hellman–Feynman forces on individual atoms were less than 0.01 eV/Å. The vacuum thickness along the z-axis was set to 15 Å, which was large enough to prevent interaction between adjacent layers. To study the adsorption of LiPS to the surface of CoFeP and C_3N_4, we have considered constraint the lowest layer of CoFeP. The barriers for LiPS decomposition on graphite C_3N_4, CoFeP, and CoFeP@CN were calculated with the climbing-image nudged elastic band (CI-NEB) method to evaluate discharge reaction kinetics.

5.4 Results and discussions

t-CN was synthesized by annealing a mixture of urea and melamine that had been previously pressed at 10 MPa. The mixture was annealed at 550 ºC during 4 h in air and resulted in a yellow powder (see details in the Experiment Section). No post-exfoliation or etching treatment was carried out. Scanning electron microscopy (SEM) characterization of the yellow powder displayed a hollow tubular structure with 300-500 nm outer diameter and several micrometer long tubes (Figure 5.1a). Transmission electron microscopy (TEM) confirmed the tubular morphology of the product and further displayed the tube walls to be highly porous (Figure 5.1b and 5.2a). Powder X-ray diffraction (XRD) patterns revealed the obtained powder to display the graphite C_3N_4 crystal structure (Figure 5.2b). The uniform distribution of C and N in t-CN was confirmed by scanning transmission electron

microscopy-electron energy loss spectroscopy (STEM-EELS) and X-ray photoelectron spectroscopy (XPS) (Figure 5.2a,c). Meanwhile, the high-resolution XPS N1s spectrum (Figure 5.2d) proved a high 68.3% content of pyridinic nitrogen, which could be beneficial to capture LiPS by forming Li-N bonds through its extra pair of electrons.[20]
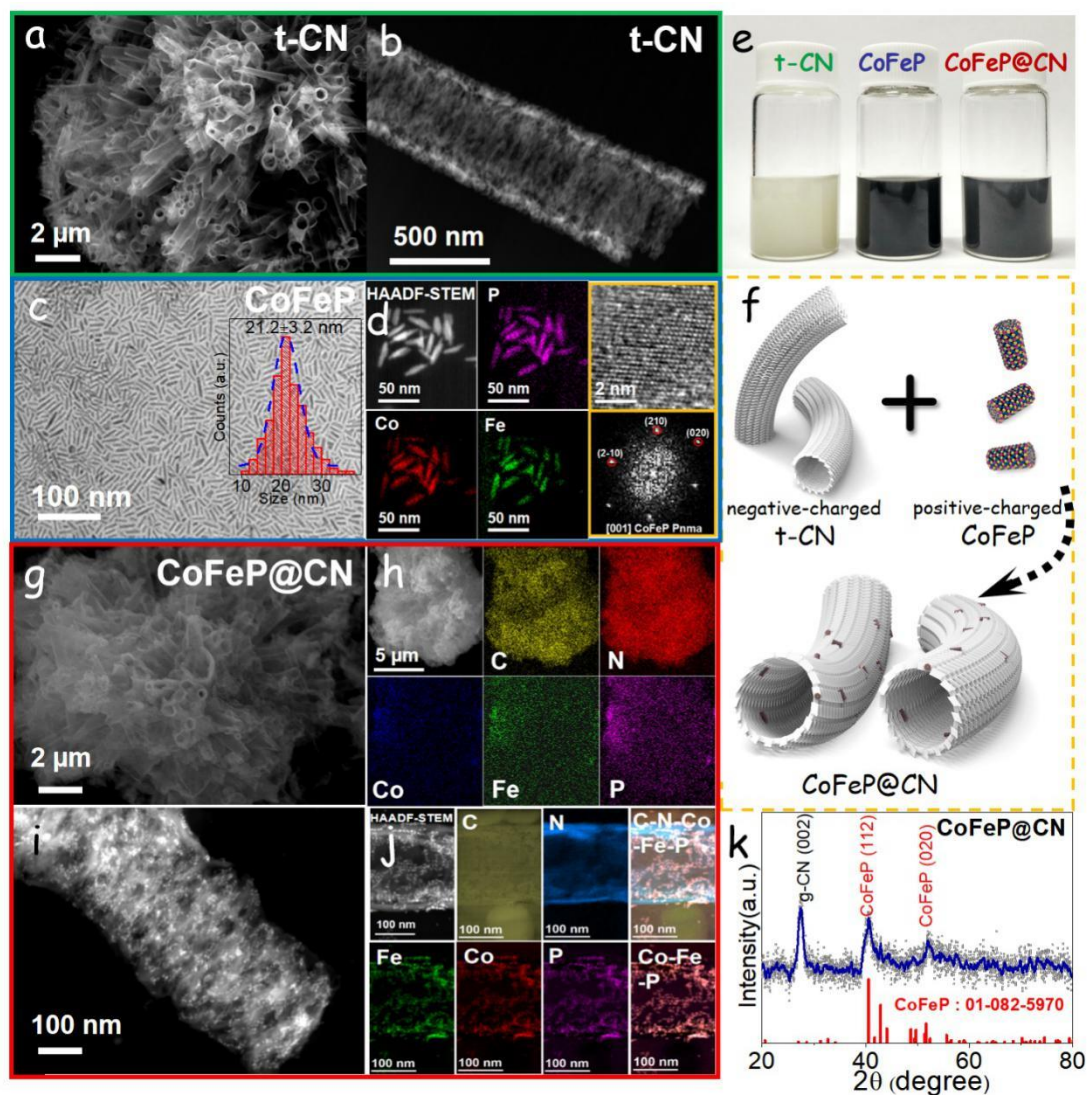

Figure 5.1. (a) FESEM and (b) TEM images of t-CN. (c) TEM image of CoFeP nanocrystals and their size distribution histogram. (d) (left and middle) HAADF STEM image and EELS chemical composition maps of CoFeP nanocrystals. (right) HRTEM image and corresponding indexed power spectrum (e) Optical image of t-CN, CoFeP, and CoFeP@CN particles dispersed in solution. (f) Schematic illustration of the process used to produce CoFeP@CN composites from the assembly of the two types of differently-charged particles. (g) FESEM image and (h) EDX compositional mapping of CoFeP@CN. (i)

TEM image of a CoFeP@CN composite. (j) HAADF STEM image and EELS chemical composition maps of CoFeP@CN. (k) XRD pattern of CoFeP@CN.
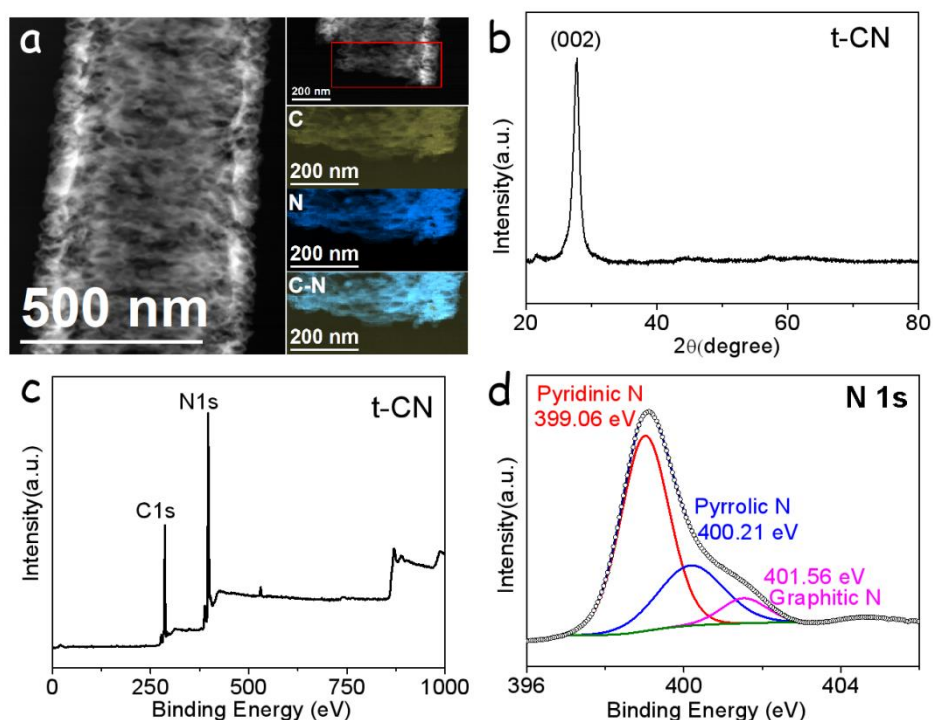

Figure 5.2. t-CN characterization: (a) HAADF STEM micrograph and EELS chemical composition maps of individual C K-edges at 284 eV (olive-drab) and N K-edges at 401 eV (lake blue) as well as composites of C-N. (b) XRD pattern. (c) XPS survey spectrum. (d) High resolution N 1s XPS spectrum

As a reference material, graphite C_3N_4 nanosheets (s-CN) were produced through the conventional liquid-phase exfoliation method. XRD and SEM analysis showed s-CN to have a similar crystallinity as t-CN, but an obviously different geometry (Figure 5.3a,b). The Barrett-Joyner-Halenda (BJH) SSA of t-CN was 186 m^2 g^{-1} and its pore volume 0.85 cm^3 g^{-1}, with a relatively narrow microporous distribution and a fraction of mesopores (Figure 5.3c, d). This contrasted with the sevenfold lower SSA and sixfold lower pore volume obtained for s-CN, related to the different geometry. s-CN suffers from strong Van der Waals' interaction that drives their re-stacking and thus results in moderate surface areas. On the contrary, the folding of C_3N_4 sheets into tubular structures can effectively avoid stacking, thus providing much larger SSAs and pore volumes. Besides a simple preparation, the t-CN reported here exhibited significant advantages in terms of SSA and pore volume compared with previously
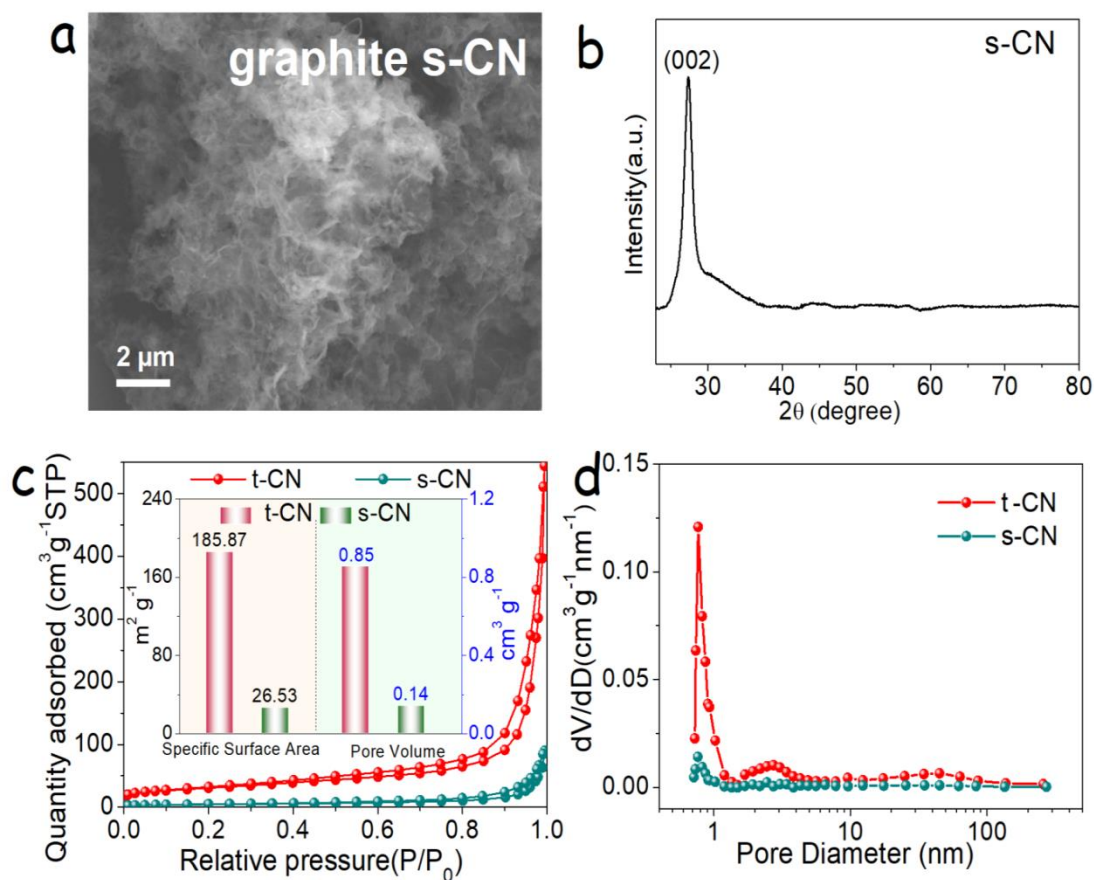
reported materials.

Figure 5.3. (a) SEM and (b) XRD pattern of s-CN nanosheets obtained from conventional liquid-phase exfoliation method. (c) N_2 adsorption-desorption isotherms of t-CN and s-CN. Inset shows the SSA and pore volume of t-CN and s-CN. (d) Pore size distribution of t-CN and s-CN samples.

CoFeP NCs with an elongated geometry and an average size of 21.2 ± 3.2 nm were produced using our previously reported colloidal synthesis method (Figure 5.1c).[32] A uniform distribution of Co, Fe, and P elements within each particle was revealed by STEM-EELS elemental composition maps (Figure 5.1d). High-resolution TEM (HRTEM) and XRD characterization proved the CoFeP NCs to have an orthorhombic crystal phase belonging to the *pnma* space group (JCPDS 01-082-5970, Figure 5.1d and 5.43). SEM-energy dispersive x-ray spectroscopy (EDX) analysis revealed the ratio of the elements of Co: Fe: P to be close to 1:1:1.2 (Figure 5.4b), with the small excess of phosphorous most probably located at the NC surface and playing a ligand role.[33]
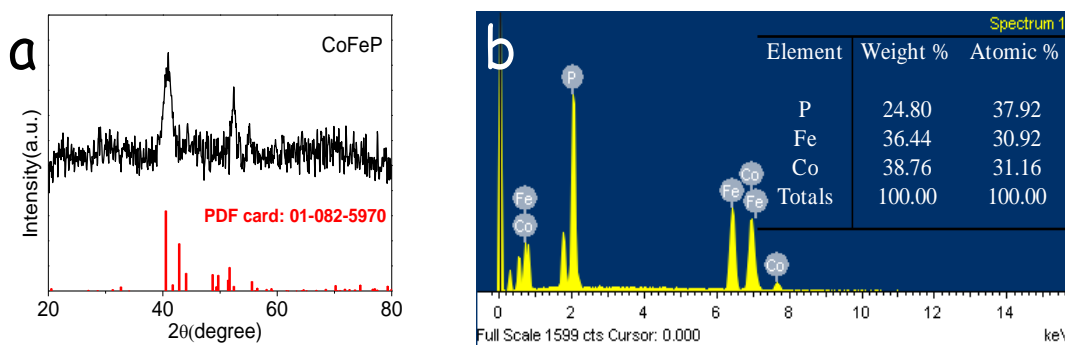
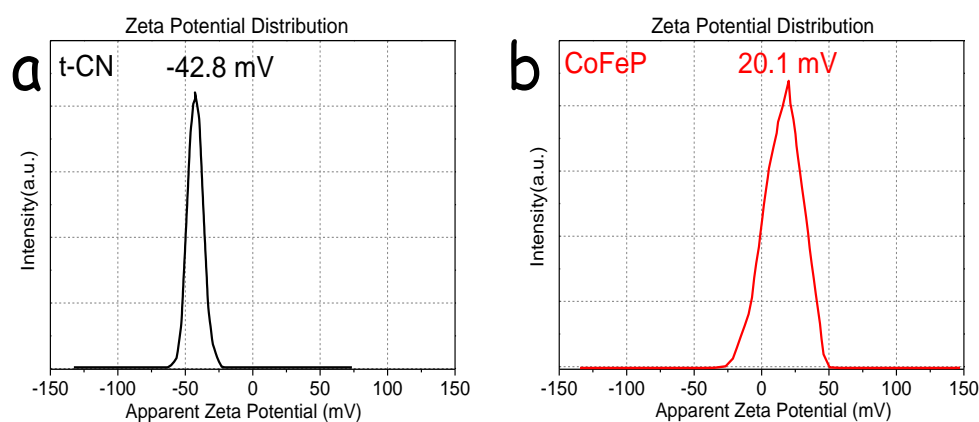**Figure 5.4.** (a) XRD pattern and (b) EDS results of CoFeP NCs.

Figure 5.5. Zeta potential plots of (a) t-CN and (b) CoFeP dispersions.

Zeta potential measurements (Figure 5.5) revealed the different signs of the charge at the surface of CoFeP NCs (positively charged) and t-CN (negatively charged). Taking advantage of this different charge, CoFeP@CN nanocomposites with a 1:1 mass ratio were prepared by a simple solution-phase electrostatic self-assembly method (Figure 5.1e,f).[34] This process maintained the tubular morphology of t-CN intact (Figure 5.1g).[35] EDX elemental maps showed a homogeneous dispersion of CoFeP NCs throughout the t-CN surface (Figure 5.1h). High-angle annular dark-field (HAADF) images further confirmed the homogeneous distribution of CoFeP NCs on t-CN (Figure 5.1i). In HAADF images, CoFeP NCs with a higher atomic number possess a stronger ability to scatter electrons than t-CN, thus appear much brighter. XRD patterns of the composites displayed diffraction peaks corresponding to both crystallographic structures: the diffraction peak at 27.4° belonging to the (002) plane of graphite C_3N_4 and the diffraction peaks at 40.5° and 51.7° corresponding to the (112) and

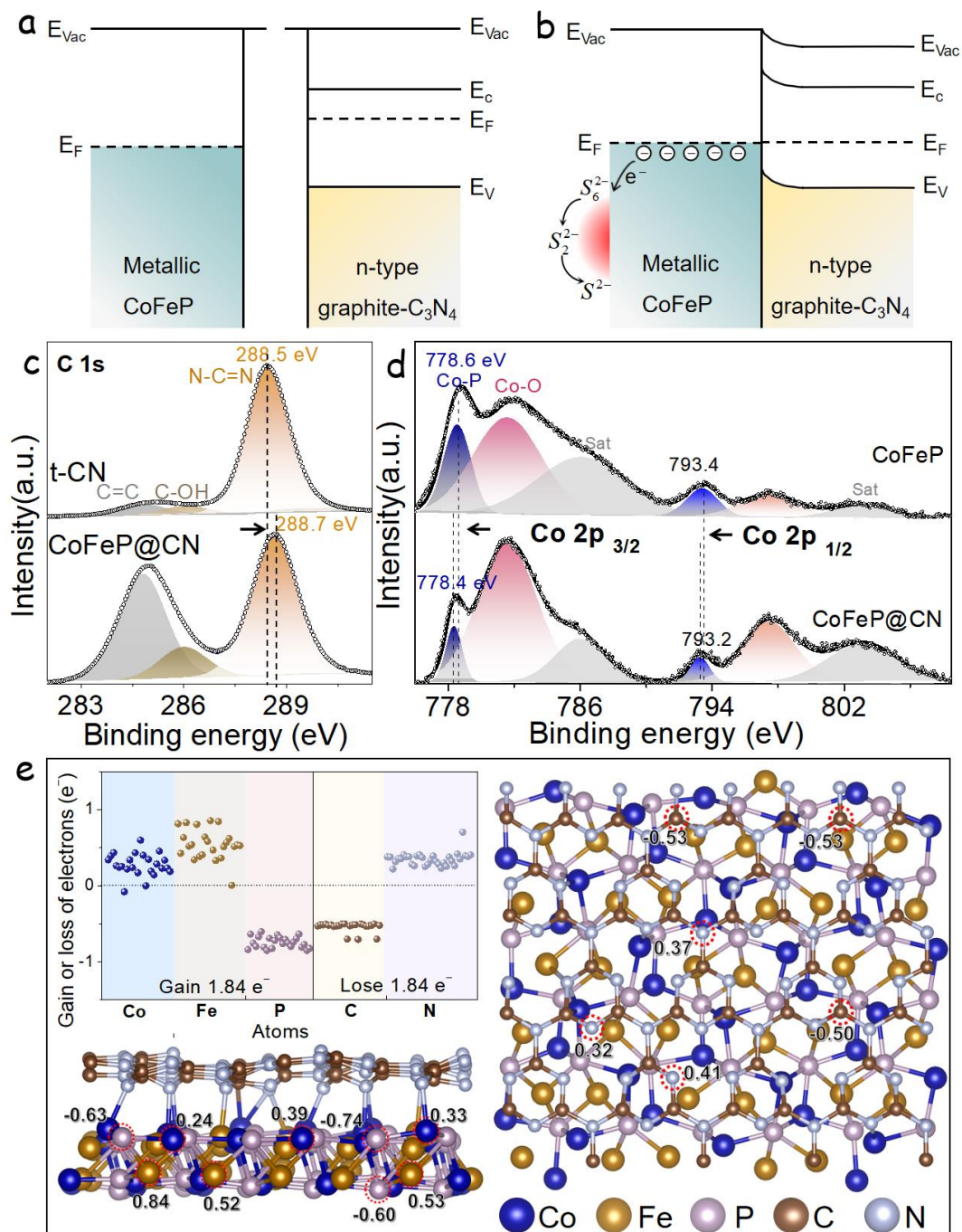(020) planes of CoFeP (Figure 5.1k).

Figure 5.6. (a,b) Energy band diagrams of metallic CoFeP and n-type semiconducting graphite-C_3N_4 before (a) and after (b) Schottky contact formation. E_{vac}=vacuum level, E_c=conduction band minimum, E_v=valence band maximum, E_F=Fermi level. (c) C 1s high-resolution XPS spectra from t-CN and CoFeP@CN. (d) Co 2p high-resolution XPS spectra from CoFeP and CoFeP@CN. (e) Gain/loss of electrons of the different atoms calculated by Bader charge analysis.

Graphite C_3N_4 is an n-type semiconductor. Its computed work function (WF) is around 4.4 eV and its band gap is ~2.6 eV.[36] On the other hand, the WF of metallic CoFeP can be estimated at around 4.8 eV (Figure 5.7).[27,37]. When placed in contact, the difference in Fermi levels drives an injection of electrons from C_3N_4 to CoFeP, until the WFs of the two materials at the interface are equilibrated. At equilibrium, an upward bending of the electron energy bands of C_3N_4 at the interface and an electric field pointing from C_3N_4 to CoFeP remain, forming a Mott-Schottky heterostructure (Figure 5.6a and b).[27,38]
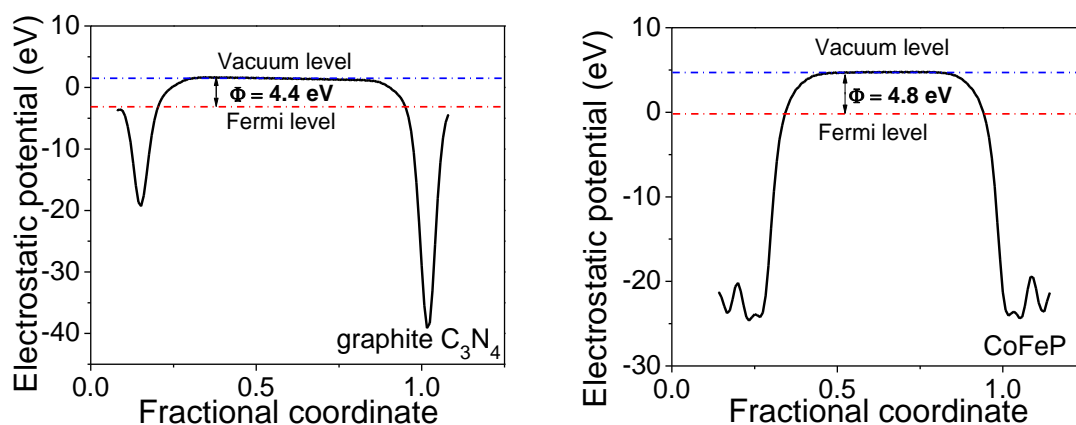

Figure 5.7. The computed work function of (a) graphite C_3N_4 and (b) CoFeP. The red and blue lines denote the Fermi level, E_F, and the vacuum energy level, E_{vaccum}, respectively.

High-resolution XPS valence band spectra confirmed the semiconducting and metallic character of t-CN and CoFeP, respectively (Figure 5.8b). The XPS valence band spectrum of CoFeP@CN composite also showed the Fermi level to lay within a band of states, as in the case of CoFeP. The C 1s spectra of t-CN and CoFeP@CN showed three bands (Figure 5.6c). The band at 284.8 eV corresponding to adventitious C-C was used as a reference. The main C 1s peak from t-CN was located at 288.5 eV and corresponded to the N−C=N chemical environment of carbon nitride.[15] In the composite material, a significant blue shift of the this N−C=N band, up to 288.7 eV, was obtained. This shift was related to the electron loss of t-CN when in contact with CoFeP NCs.[15,39]
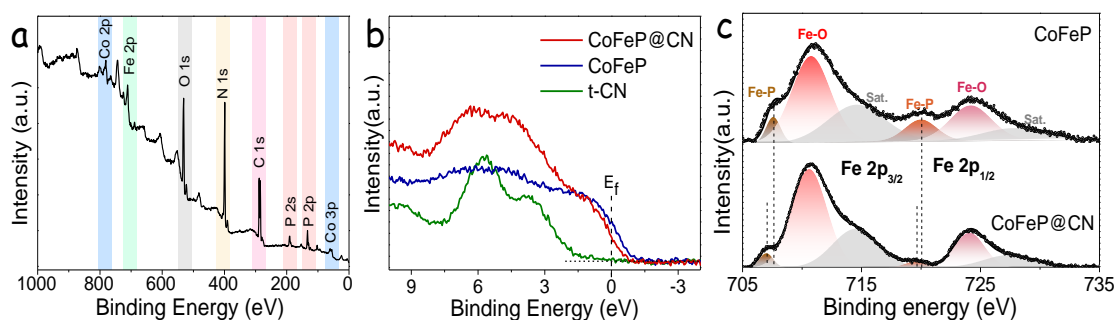
Figure 5.8. (a) XPS survey spectrum of CoFeP@CN. (b) Normalized valence band XPS spectra of t-CN, CoFeP and CoFeP@CN samples. (c) High resolution Fe 2p XPS spectra of CoFeP and CoFeP@CN samples.

The Co 2p spectrum of CoFeP displayed two bands at 778.6 eV ($2p_{3/2}$) and 793.4 eV ($2p_{1/2}$), associated with a Co-P chemical environment (Figure 5.6d). Two additional bands at 781.6 eV ($2p_{3/2}$) and 797.5 eV ($2p_{1/2}$) were assigned to oxidized cobalt species arising from the exposure of the sample to air during handling and transportation.[26,40] Additional shake-up satellite peaks located at 786.1 eV and 803.2 eV were also discerned. A slight shift of the Co 2p bands toward lower binding energies was observed when supporting the CoFeP NCs on t-CN, consistent with a charge arrangement at the interface and an increased electron density in Co atoms.[26,40]

Similar results were obtained when analyzing the Fe 2p spectra, displaying bands associated with a Fe-P environment at 707.6eV ($2p_{3/2}$) and 720.0 eV ($2p_{1/2}$), and bands associated to an oxidized environment at 710.7 eV ($2p_{3/2}$) and 724.2 eV ($2p_{1/2}$).[41] A similar band shift was observed for Fe and Co when contacting CoFeP with t-CN (Figure 5.8c).

A larger degree of surface oxidation was observed in the CoFeP NCs supported on t-CN than in the unsupported NCs. However, XRD patterns in Figure 5.1k confirmed the presence of the CoFeP phase in both samples, indicating an overall low content of $CoPO_x$ or $FePO_x$ in CoFeP@CN samples. Notice in any case that recent reports have demonstrated that TMPs with an oxidized surface can still effectively promote LiPS capture through the metal oxide and phosphate sites, which can form strong metal−S and oxide P−Li bonds, respectively.[42]

Density functional theory (DFT) calculations further demonstrated a charge redistribution at the atomic scale when placing the two materials in contact. According to XRD results of

CoFeP, we constructed a slab model based on the exposed CoFeP (112) facet and a graphite C_3N_4 monolayer to evaluate the charge transfer at the interface. Bader charge analysis calculated charge redistribution at the CoFeP/C_3N_4 interface and quantified that the bottom CoFeP unit cell gains 1.84 electrons from the CN layer. The gain/loss of electrons of the different atoms is displayed in Figure 5.6e.

Sulfur was introduced within the CoFeP@CN by a melt-diffusion process (see the Experimental Section for details). SEM characterization of the obtained S@CoFeP@CN composites revealed the tubular structure of CoFeP@CN to be conserved after S addition (Figure 5.9a). XRD patterns confirmed the presence of crystalline sulfur (JCPDS No. 08-0247) within S@CoFeP@CN composites (Figure 5.9b)[43] and a homogenous distribution of the different elements was proven by EDS mapping (Figure 5.9c). With the introduction of sulfur, the SSA value sharply decreased from 86.8 m^2 g^{-1} (CoFeP@CN) to 1.8 m^2 g^{-1} (S@CoFeP@CN), as shown in Figure 5.9d. Thermogravimetric analysis (TGA) allowed quantifying the sulfur content in the S@CoFeP@CN composite at about 70 wt%, consistent with the nominal amount introduced (Figure 5.9e). The same preparation process was employed to load equivalent amounts of sulfur into other hosts, CoFeP, t-CN, and Super P, which were used as reference materials when testing CoFeP@CN performance (Figure 5.10).
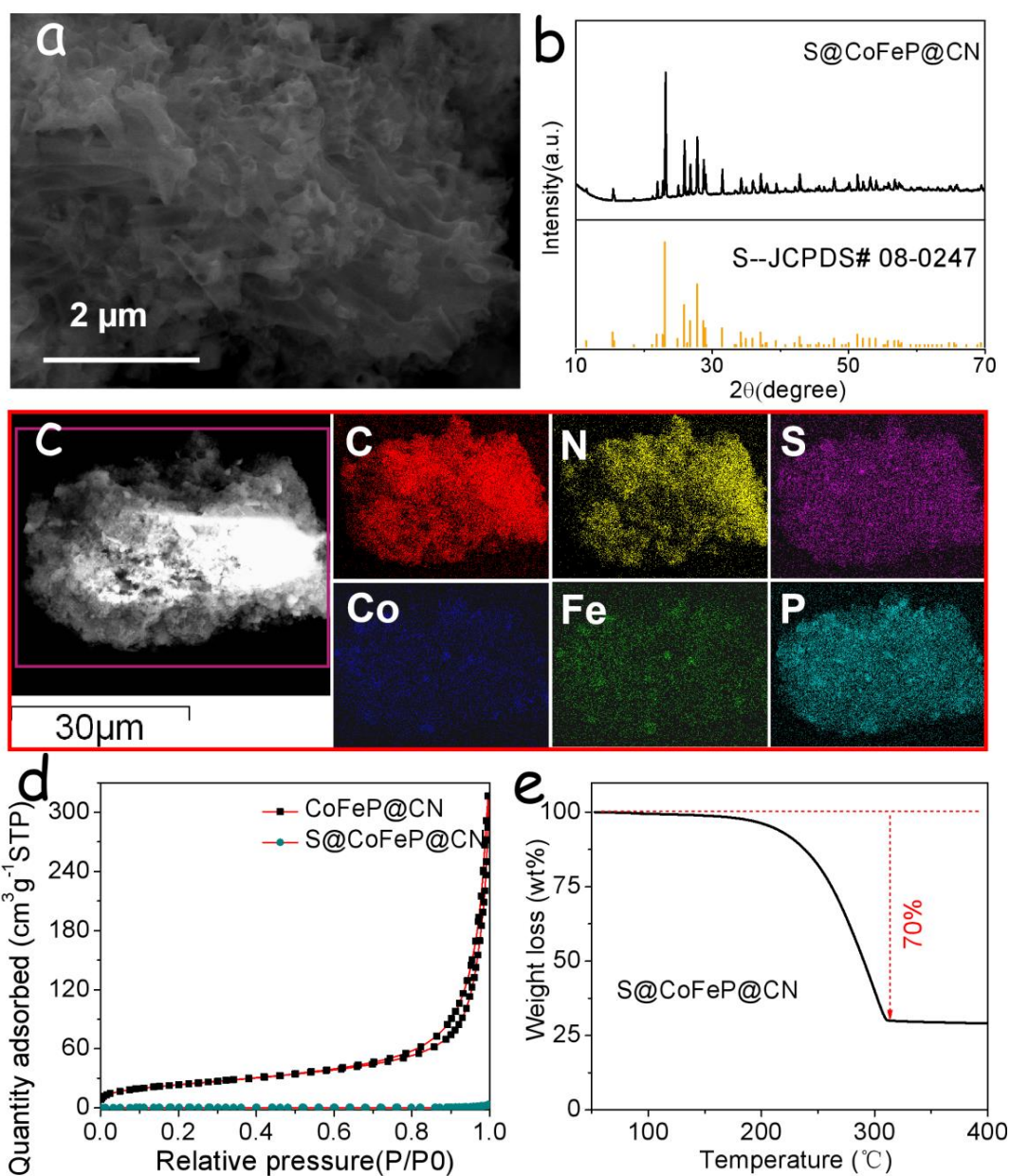
Figure 5.9. (a) SEM image, (b) XRD pattern, and (c) EDX compositional maps of S@CoFeP@CN. (d) N_2 adsorption-desorption isotherms of CoFeP@CN and S@CoFeP@CN. Calculated specific surface areas were 86.8 m^2 g^{-1} and 1.8 m^2 g^{-1} for CoFeP@CN and S@CoFeP@CN, respectively. (e) TGA curve measured in N_2 atmosphere from S@CoFeP@CN.
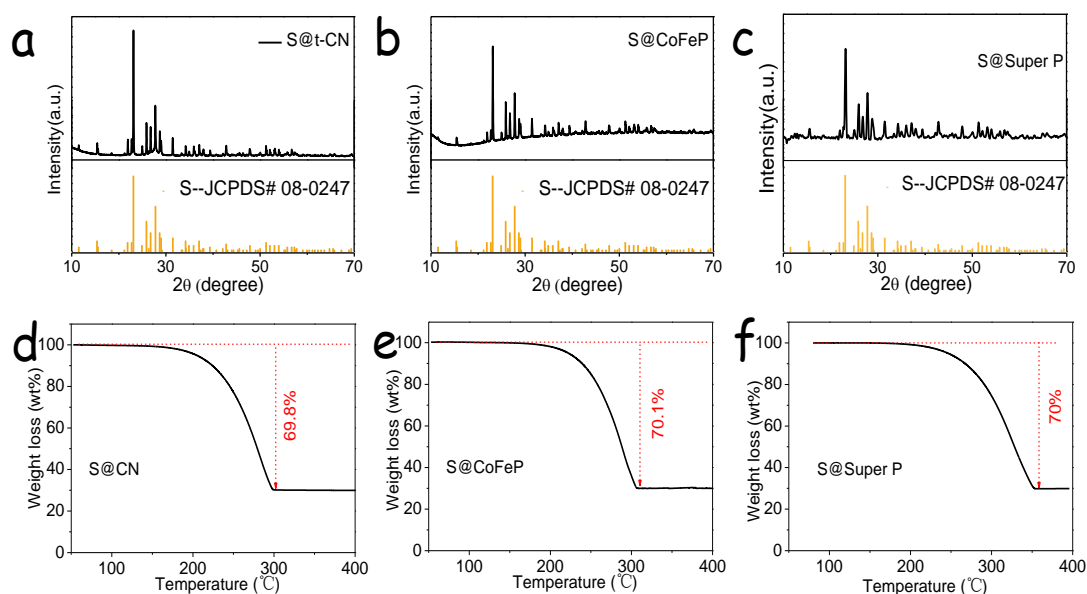
Figure 5.10. XRD patterns (a-c) and TGA curves measured in N_2 atmosphere (d-f) obtained from S@t-CN (a,d), S@CoFeP (b,e), and S@Super P (c,f).

The LiPS adsorption ability of the host material plays a key role in suppressing the shuttle effect in LSBs, thus it is the first property analyzed when screening different materials toward finding a good sulfur host. To evaluate LiPS affinity, the same amount of the different hosts was immersed into a 10 mM LiPS (~Li_2S_6) solution. After 12 h, clear differences in the color of the solution containing the different materials were observed, indicating a different degree of LiPS adsorption (Figure 5.11). Adsorption results were also confirmed by analyzing the UV–vis spectra of the solutions in the range of 400-500 cm^{-1} (Figure 5.11b).[31,44,45] We noticed that the color of the solutions containing t-CN and/or CoFeP was much lighter than that of the solution containing Super P, inferring a stronger interaction of t-CN and CoFeP with LiPS. The clearest solution was obtained with the presence of CoFeP@CN, demonstrating that the composite was characterized by an additional LiPS adsorption capability when compared with the same amount of each of the components.
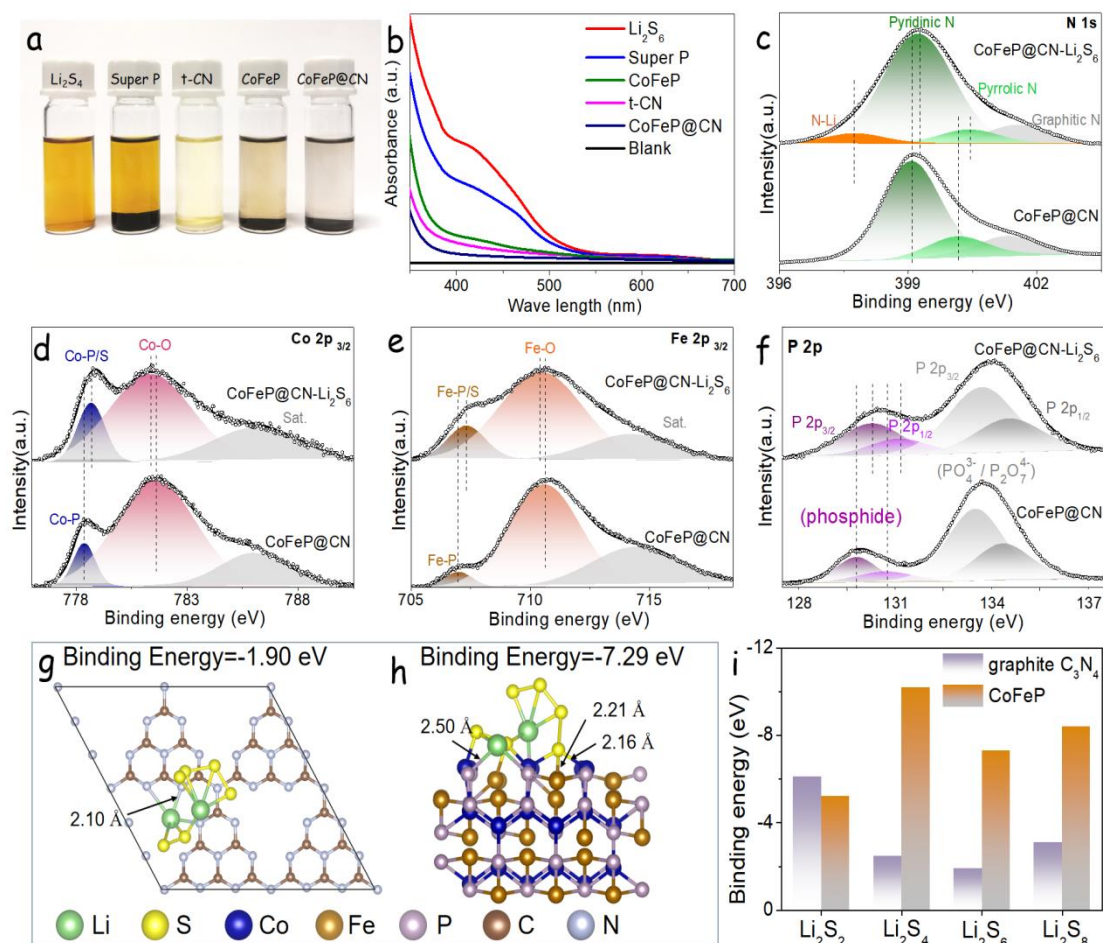
Figure 5.11. LiPS adsorption ability. (a) Optical image and (b) UV–vis spectra of the polysulfide solution containing the different adsorbers overnight. (c-f) High-resolution XPS spectrum of (c) N 1s, (d) Co 2p $_{3/2}$, (e) Fe 2p $_{3/2}$ and (f) P 2p before and after CoFeP@CN interaction with Li2S6. (g,h) Relaxed Li2S6-adsorbed structures on the surface of (g) graphite-C3N4 and (h) CoFeP calculated with DFT. (i) The calculated binding energy between LiPSs (Li_2S_2, Li_2S_4, Li_2S_6, and Li_2S_8) and graphite-C_3N_4 and CoFeP surfaces.

Additional XPS analyses were conducted to understand the chemical interaction between CoFeP@CN and LiPS during the Li_2S_6 adsorption experiment. From the comparison of the N 1s spectra of the composite before and after Li_2S_6 adsorption (Figure 5.11c), a distinct shift could be observed in the pyridinic-N band from 399.1 eV to 399.3 eV.[46] The small additional band in the CoFeP@CN-LiPS sample at 397.8 eV is attributed to N-Li bond formation during the adsorption process.[47,48] These results were consistent with previous reports demonstrating that LiPS could anchor on active nitrogen sites through dipole-dipole interactions. This Li–N chemical interaction certainly contributes to inhibiting the shuttling

effect.[49]

Meanwhile, the Co 2p$_{3/2}$ and Fe 2p$_{3/2}$ XPS spectra displayed in Figure 5.11d,e show that after interaction with Li$_2$S$_6$, bands corresponding to Co−P or Fe−P environments suffered an obvious shift to higher binding energy, indicating the formation of Co−P/S and Fe−P/S bonds.[30,44] Additionally, the relative intensity of the oxide Co and Fe bands decreased in the CoFeP@CN-LiPS sample, which was also consistent with the formation of strong Co-S and Fe-S bonds during the Li$_2$S$_6$ adsorption process which partially prevented the surface oxidation.[42,44] In Figure 5.11f, a band shift can be also found in the P 2p spectrum, which might be attributed to the accumulation of electrons at P sites related to the interaction with terminal Li atoms in Li$_2$S$_6$ species.[50,51]
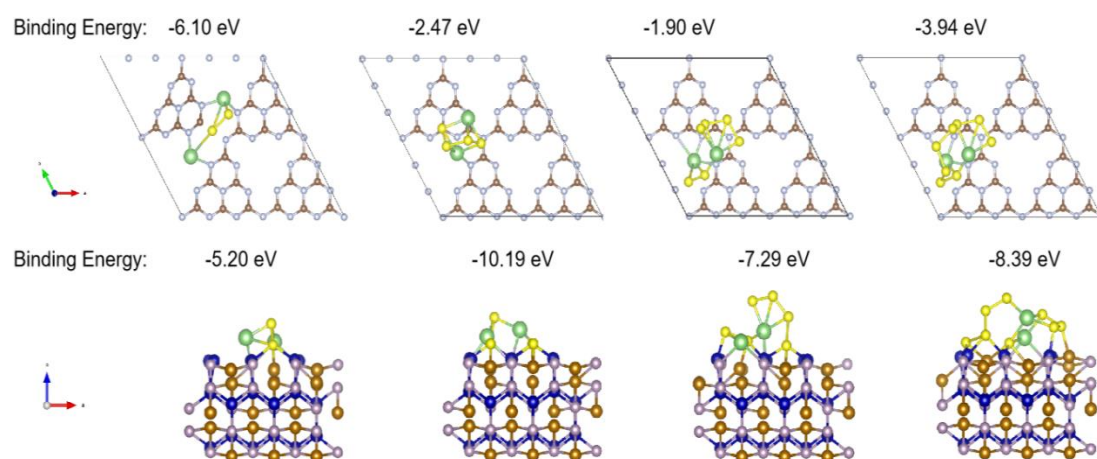

Figure 5.12. Binding energies and adsorbed structures of LiPS on the surface of g-C$_3$N$_4$ and CoFeP calculated by DFT.

DFT calculations were conducted to determine the affinity between chained LiPS species and CoFeP and t-CN. The binding energies and atomic structures between LiPS (Li$_2$S$_2$, Li$_2$S$_4$, Li$_2$S$_6$, and Li$_2$S$_8$) and CoFeP (001) and graphite C$_3$N$_4$ (001) surfaces were calculated (Figure 5.12). Compared with previous reports on graphitic carbon,[52,53] the more negative LiPS binding energies on the surface of CoFeP and graphite C$_3$N$_4$ (Figure 5.11i) indicated stronger adsorption of soluble LiPS on the latter two. The chemical adsorption of LiPS with CoFeP@CN is mainly originated from the treble interactions: i) Lewis-base pyridine N in t-CN with extra pair of electrons interact with Lewis acid of terminal Li$^{\delta+}$ atoms in LiPS; ii) chemical bonding between the terminal S$^{\delta-}$ atoms and Co$^{\delta+}$/Fe$^{\delta+}$ atoms in CoFeP NCs; and iii) chemical bonding

between $Li^{\delta+}$ atoms and $P^{\delta-}$ atoms. Taking Li_2S_6-adsorbed structures as an example (Figure 5.11g and 5.11h), Li atoms preferentially bind to N sites in C_3N_4, with a Li-N bond distance in the C_3N_4/Li_2S_6 model of only 2.10 Å. S atoms tend to bind with Co and Fe atoms into a small 2.16 Å Co-S and 2.21 Å Fe-S bond distance. Besides, the calculated Li-P bond distance was 2.50 Å. Overall, the coexistence of multiple adsorption sites to strongly capture the LiPS by Li-N, Fe/Co-S and Li-P bonds endow the great potential of CoFeP@CN composite as S host in LSBs.
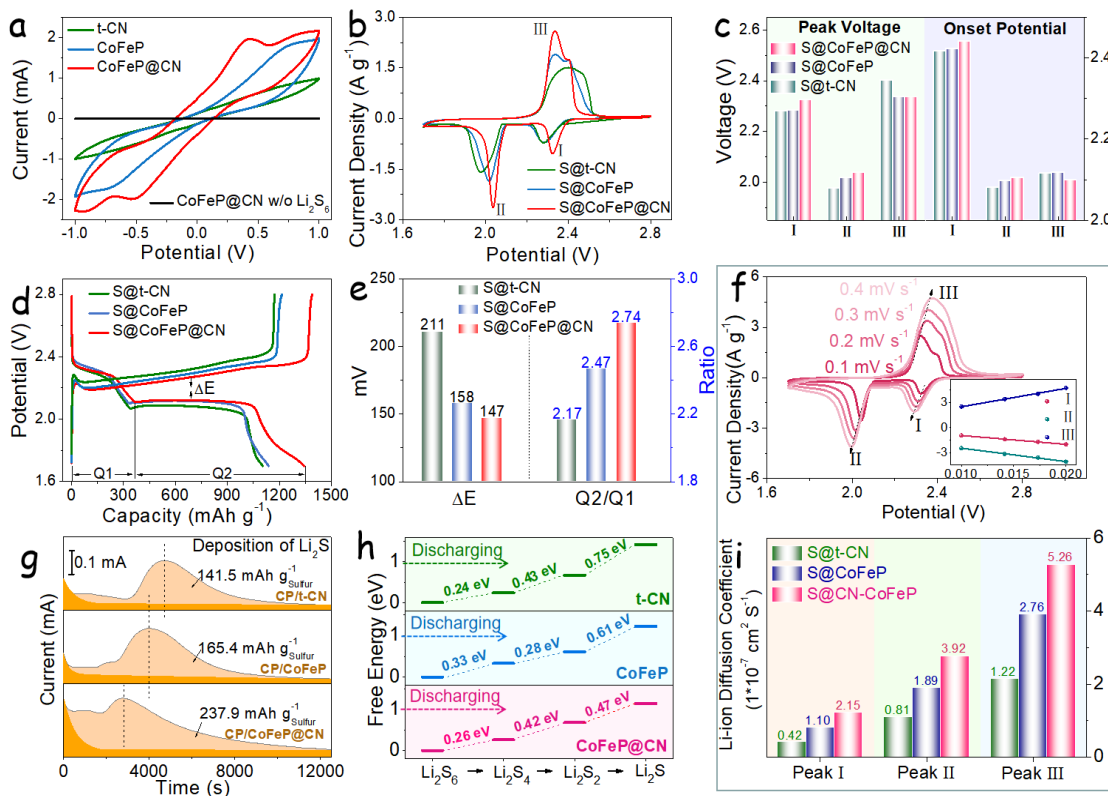

Figure 5.13. Polysulfide redox activity. (a) CV profiles of symmetrical cells with three different host materials using an electrolyte containing 0.5 mol L^{-1} Li_2S_6 and 1 mol L^{-1} LiTFSI dissolved in DOL/DME (v/v = 1/1). (b) CV profiles of lithium-sulfur coin cells. (c) Peak voltages and onset potentials obtained from CV curves with different electrodes. (d) Charging/discharging curves of different electrodes at the current rate of 0.1 C. (e) DE and Q2/Q1 values obtained from charging/discharging curves. (f) CV curves of S@CoFeP@CN electrode at various scan rates. Inset shows the CV peak current for peaks I, II, and III versus the square root of the scan rates. (g) Potentiostatic discharge profile of Li_2S nucleation at 2.05 V on different electrodes with Li_2S_8 catholyte. (h) DFT-calculated Gibbs free energy changes of reduction of LiPS (Li_2S_6, Li_2S_4, Li_2S_2, and Li_2S) in the presence of three hosts. (i) Li-ion diffusion

coefficient value at peaks I, II, and III.

To evaluate the ability of host materials to catalytically accelerate the kinetics of polysulfide conversion, cyclic voltammetry (CV) tests of Li_2S_6 symmetrical cells were conducted in the voltage window -1 to 1 V. As shown in Figure 5.13a, t-CN, CoFeP, and CoFeP@CN electrodes showed significantly different CV curves. The symmetric curves of CoFeP@CN electrodes exhibited higher peak current densities than t-CN and CoFeP electrodes, demonstrating the combination of both materials within a heterostructured composite to boost the electrochemical activity of polysulfide conversion.[54]
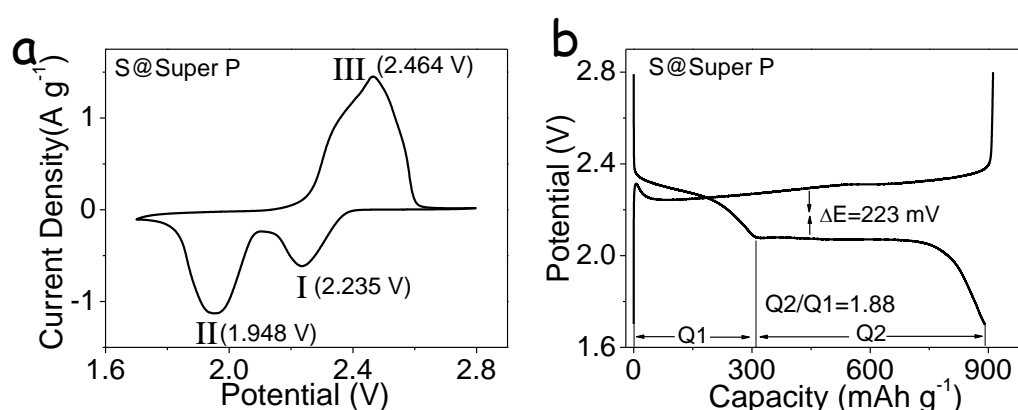

Figure 5.14. (a) CV profile at a scan rate of 0.1 mV s−1 and (b) charging/discharging curve of the S@Super P at a current rate of 0.1 C.

The electrochemical performance of the electrodes was evaluated using LSBs assembled in coin cells. Figure 5.13 and Figure 5.14a display the CV curves obtained from S@t-CN, S@CoFeP, S@CoFeP@CN and S@Super P cells, respectively. All curves showed two reduction peaks (peak I and II), which corresponded to a two-step S reduction process upon cathodic scanning: peak I was attributed to the transformation from S_8 to soluble long-chain LiPSs (Li_2S_x, 4≤x≤8), followed by a further reduction to insoluble Li_2S_2/Li_2S in peak II.[53,55] The anodic peak (peak III) was ascribed to the reverse multistep oxidation process of short-chain sulfides to LiPS and eventually to sulfur. S@CoFeP@CN electrodes exhibited the most intense peak currents and the cathodic/anodic peaks located at the most positive/negative potentials (Figure 5.13c). This result indicated that among the tested materials, CoFeP@CN was the most effective catalyst in promoting the polysulfides redox reaction kinetics. [43,53] Among the three kinds of electrode tested, the onset potentials of S@CoFeP@CN were the

highest/lowest in reduction/oxidation peaks (Figure 5.13c), demonstrating an effective decrease of the overpotential in LiPS conversion reaction.

Charging/discharging tests at different current rates were conducted for the three types of electrodes. At the current rate of 0.1 C, all electrodes showed one charging and two discharging plateaus, consistently with the measured CV peaks (Figure 5.13d). A voltage gap ΔE found between the oxidation and the second reduction plateaus introduced polarization potential in the redox reaction, which was taken as the voltage gap at 50% discharged capacity.[43,56] S@CoFeP@CN electrodes displayed a lower polarization potential (ΔE = 147 mV) than S@CoFeP (ΔE = 158 mV), S@t-CN electrodes (ΔE = 211 mV), and S@Super P electrodes (ΔE = 223 mV, Figure 5.14b), demonstrating the synergism between the two components within CoFeP@CN to accelerate the LiPS conversion kinetics. S@CoFeP electrodes exhibited a much better polarization than S@CN because of the intrinsic metallic and semiconductor nature of CoFeP and t-CN, respectively. S@CoFeP@CN electrodes also exhibited the lowest overpotentials in the phase conversion between soluble Li_2S_4 and insoluble Li_2S_2/Li_2S (Figure 5.15).[57]
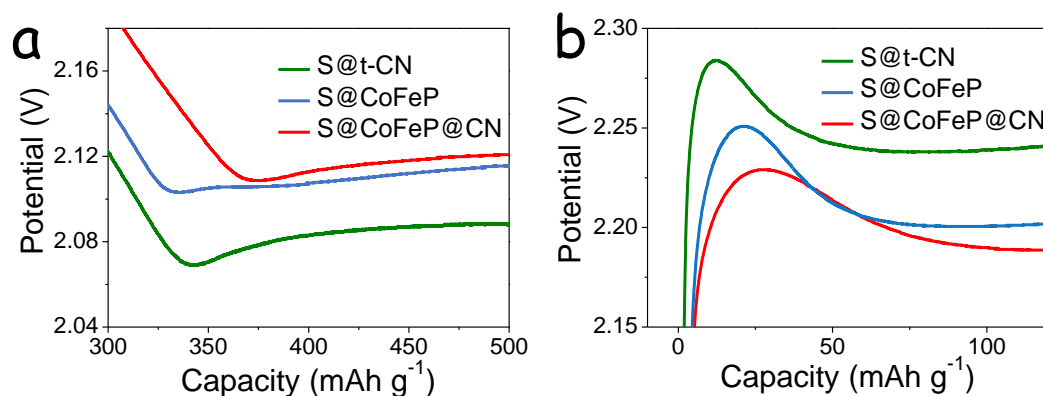

Figure 5.15. (a) Discharging and (c) charging profiles of S@t-CN, S@CoFeP, and S@CoFeP@CN electrodes showing the overpotentials for conversion between soluble LiPS and insoluble Li_2S_2/Li_2S.

The catalytic activity of the host materials toward the LiPS conversion reaction can be quantified by the ratio Q2/Q1, where Q1 and Q2 denote the capacity of the two discharge plateaus (Figure 5.13d). Q1 corresponds to the reduction of sulfur to soluble LiPS ($S_8 + 4Li^+ + 4e^- \rightarrow 2Li_2S_4$) and Q2 to the subsequent transfer to insoluble sulfide ($2Li_2S_4 + 12Li^+ + 12e^- \rightarrow$

8Li$_2$S), respectively.[43] During the second plateau (Q2), the final product Li$_2$S generally accompanied by the presence of Li$_2$S$_2$ due to sluggish reaction kinetics, which inhibits the release of capacity during the Q2 stages. Thus, while the capacity ratio should be Q2/Q1 = 3, taking into account the electrons involved in each process (4 for Q1 and 12 for Q2), generally ratios lower than 3 are obtained. Additionally, the LiPS shuttle effect is also reflected in a capacity loss. In all cases, the higher Q2/Q1, the better the catalytic ability. As displayed in Figure 5.13e, S@CoFeP@CN exhibited the highest Q2/Q1 ratio at 2.74, close to the theoretical value and well above that of S@CoFeP (2.47), S@t-CN (2.17) and S@Super P (1.88, Figure 5.14b), which further evidenced the synergistic effect towards LiPS redox reaction obtained when combining both materials in the CoFeP@CN Mott-Schottky heterostructure.

The efficiency of LSBs is limited by the high charging/discharging overpotentials that are in large part related to the sluggish kinetics of deposition/dissolution of insulating solid Li$_2$S.[58][59] Thus, we performed Li$_2$S nucleation and dissolution experiments to further assess the performance of the materials developed here. For this experiment, electrode materials were supported on carbon paper (CP, see details in the Supporting Information) which is able to soak the catholyte. From the potentiostatic discharge profiles in Figure 5.13g, CP/CoFeP@CN exhibited the sharpest nucleation peak and the fastest responsivity toward Li$_2$S nucleation, when compared with CP/t-CN and CP/CoFeP electrodes. According to Faraday's law, the conversion capacity was obtained by integrating the area below the current curves. The Li$_2$S deposition capacity of CP/CoFeP@CN (237.9 mAh g^{-1}) was larger than that of CP/t-CN and CP/CoFeP electrodes (141.5 mAh g^{-1} and 165.4 mAh g^{-1}, respectively), demonstrating that CoFeP@CN could effectively decrease the overpotential and promote the Li$_2$S nucleation reaction.[43,59] To further verify the catalytic activity of catalysts on the LiPS conversion, the Gibbs free energy changes during the LiPS reduction on t-CN, CoFeP, and CoFeP@CN were calculated (Figure 5.13h). For the liquid-to-solid (Li$_2$S$_6$ to Li$_2$S) nucleation reaction, all LiPS reduction steps were endothermic with relatively large positive Gibbs energy barriers, especially for the Li$_2$S$_2$ to Li$_2$S conversion, which was the rate-limiting step.[60] However, CoFeP@CN exhibited the lowest Gibbs free energy changes

(0.47 eV) than CoFeP and t-CN (0.61 and 0.75 eV, respectively), and this value is much lower than previously reported graphene or N-doped graphene (above 1 eV), which suggested that the composite CoFeP@CN was a relatively excellent catalyst to promote the LiPS conversion kinetics.[57,61,62] The lowest Gibbs free energy change in the reduction of Li_2S_2 measured for CoFeP@CN was consisted of Li_2S nucleation test and overall, these results demonstrated that CoFeP@CN Mott-Schottky heterostructure catalyst plays a catalytic role to accelerate the Li_2S formation.

To obtain further insight into the role of CoFeP@CN in accelerating the LiPS reaction, electrode kinetics were further analyzed by measuring CV at different scan rates, from 0.1 to 0.4 mV s^{-1} (Figure 5.13f). When increasing the scan rate, the two cathodic peaks shifted to more negative potentials and the anodic peak shifted to a positive potential, overall increasing the polarization voltage. The linear relationship between the anodic/cathodic peak current and the square root of the scanning rates pointed at a diffusion-limited reaction (insert in Figure 5.13f). Thus, the classical Randles–Sevcik equation was used to calculate the Li$^+$ diffusivity in the process:[63,64]

$$I_{\mathrm{p}} = (2.69 \cdot 10^5) n^{1.5} A D_{Li^+}{}^{0.5} C_{Li^+} v^{0.5}$$

where I_p is the peak current, n is the number of charge transfer, A is the geometric electrode area, D_{Li+} is the Li$^+$ diffusion coefficient, C_{Li+} is the concentration of Li$^+$ in the electrolyte, and v is the scan rate. At a given n, A, and C_{Li+}, sharper $Ip/v^{0.5}$ slopes denote faster Li$^+$ diffusion. As displayed in Figure 5.13f,i, S@CoFeP@CN electrodes exhibited the sharpest slopes for the 3 peaks, thus the highest Li$^+$ diffusivity during the redox reactions. In peak I, II and III, the Li$^+$ diffusion coefficients of S@CoFeP@CN were 2.15, 3.92, and 5.26×10^{-7} cm^2 S^{-1}, respectively. Li$^+$ diffusivity strongly depends on the viscosity of the electrolyte containing LiPS and the accumulation of insulating Li_2S/Li_2S_2 on the electrode.[43,64] The highest diffusivities obtained for the CoFeP@CN host reflected that the improved reaction kinetics by the Mott-Schottky catalyst was in part related to a confined shuttle effect and an improved catalytic activity towards LiPS conversion, consistently with the above results.
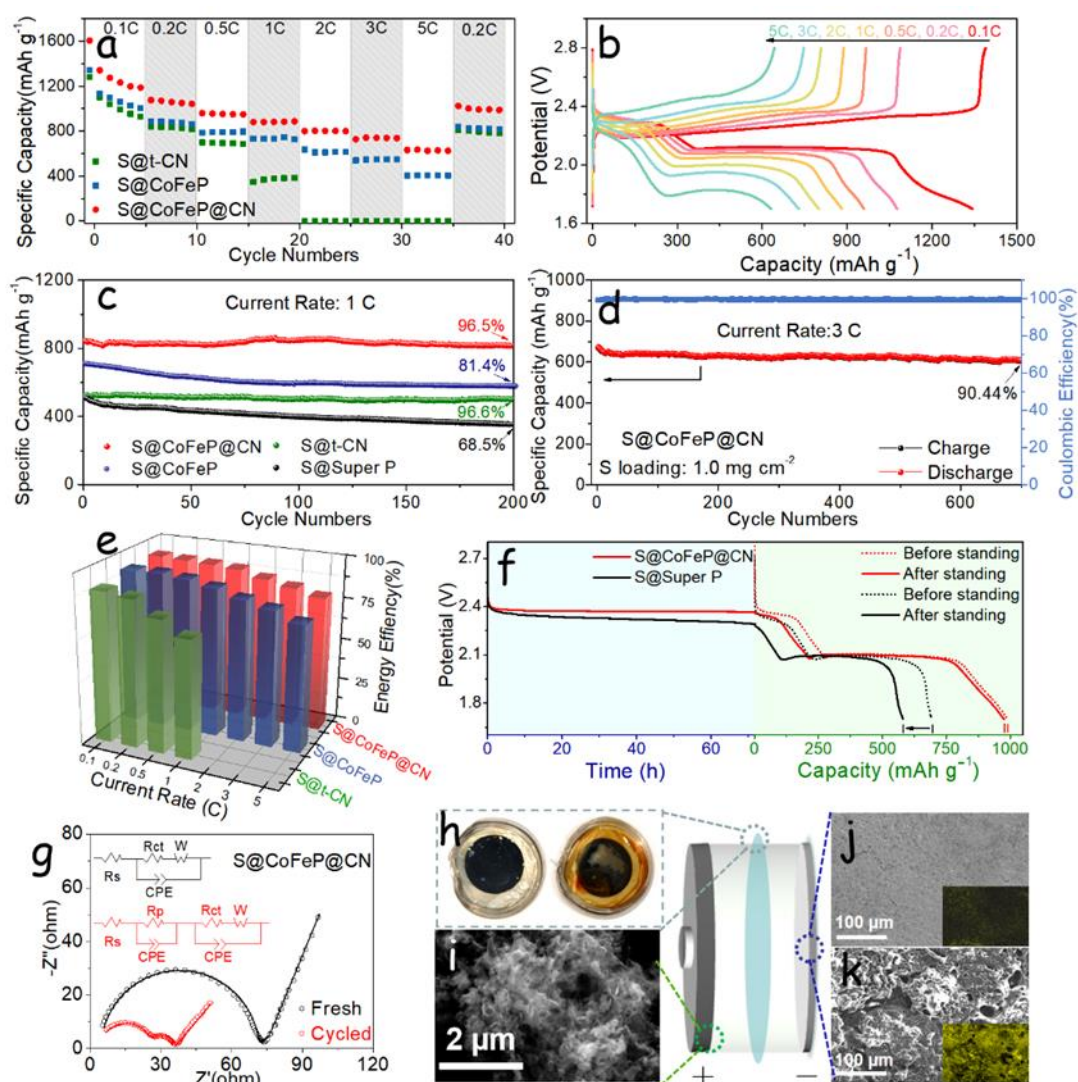
Figure 5.16. Electrochemical performance of lithium-sulfur coin cells. (a) Rate performances of S@CoFeP@CN, S@CN, and S@CoFeP electrodes. (b) Charging/discharging curves of S@CoFeP@CN electrode at current rates from 0.1 C to 5 C. (c) Capacity retention of different electrodes at 1 C over 200 cycles. (d) Cycling stability of S@CoFeP@CN electrode at 3 C over 700 cycles. (e) The energy efficiency of three different electrodes at various current rates. (f) Change of open-circuit voltage at 72 h self-discharge test and comparison of discharge curves before and after standing of S@Super P and S@CoFeP@CN electrodes. (g) EIS plot of S@CoFeP@CN electrode before and after 200 cycles at 1 C. The Nyquist curves were fitted considering the equivalent circuits shown as inset, where Rs, Rp, Rct, and W stand for the resistance of the electrolyte, insoluble Li_2S_2/Li_2S precipitation layer, interfacial charge-transportation, and semi-infinite Warburg diffusion, respectively; and CPE stands for the corresponding capacitance. (h-k) After cycling at 1 C for 200 cycles: (h) optical images of membranes recovered from coin cells based on S@CoFeP@CN electrode (left) and S@Super P electrode (right); (i)

165

SEM image of S@CoFeP@CN electrode; (j, k) SEM image of lithium foil recovered from a coin cell based on S@CoFeP@CN (j) and S@Super P (k). Inset images in (j,k) show the map of the sulfur signal detected by EDX.

Figure 5.16a shows the rate performances of the three types of electrodes tested, at current rates from 0.1 to 5 C. S@CoFeP@CN electrodes systematically exhibited the highest discharge capacity at any current rate among the different electrodes tested. A high initial discharge capacity at 1607 mAh g^{-1} was measured, demonstrating a very high sulfur activity and utilization. Even at high current rates of 5 C, the average capacity stabilized at 630 mAh g^{-1}, well above the capacity obtained for S@CoFeP and S@CN electrodes, 406 mAh g^{-1} and 0.23 mAh g^{-1}, respectively. When the current rate was returned to 0.2 C, the average capacity of the cells with S@CoFeP@CN electrodes returned to approximately 1010 mAh g^{-1}, demonstrating remarkable reversibility and stability. The galvanostatic charging/discharging profiles of S@CoFeP@CN at different current rates are displayed in Figure 5.16b. All discharge curves exhibited two well-defined discharge plateaus, even at a current density of 5.16C. In contrast, S@CoFeP electrodes displayed a similar shape but much lower capacity (Figure 5.17a), and S@CN electrodes showed a high polarization potential and no capacity response above 2 C (Figure 5.17b), due to the huge potential barrier and the limited redox kinetics of the electrode material.   And change of the Q2/Q1 ratio with the current rate can be found in Figure S20.
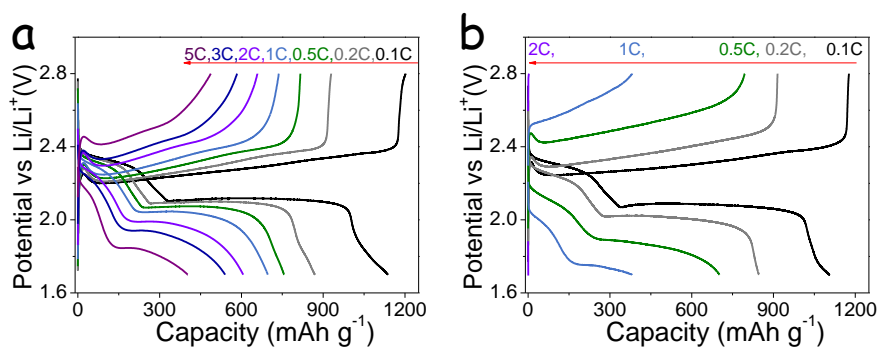

Figure 5.17. Galvanostatic charging/discharging curves of (a) S@CoFeP and (b) S@t-CN at various C rates.

To evaluate the long-term cycling stability of the different host materials, cells were continuously cycled at 1 C (Figure 5.16c). The initial discharge capacity of S@CoFeP@CN

electrodes at 1 C was about 844 mAh g^{-1}, and retained about 96.5 % capacity after 200 cycles, 814 mAh g^{-1}. Significantly lower capacity retention was obtained for S@CoFeP electrodes (81.4%), which suffered a notable capacity decay during the first 100 cycles. This result might be attributed to the relatively low SSA of the CN-free CoFeP host. The partially aggregated CoFeP NCs had insufficient active sites to anchor the initial excess of sulfur species, but as the S content decreased, its stability improved owing to its sulfiphilic surface. Capacity retention differences can be clearly observed comparing the charging/discharging profiles at various cycles (Figure 5.18a,c). Surprisingly, even though S@t-CN electrodes exhibited a relatively low initial capacity, they were characterized by remarkable stabilities, with retention of about 96.6% after 200 cycles. This superior stability can be explained by the t-CN with tubular structure here presented that provides a very high SSA to trap LiPS species by the lithiophilic sites and a high pore volume to accommodate the volume change during cycles, although a poor conductivity resulted in a large voltage gap (Figure 5.18b). Additional cycling was carried out on the S@CoFeP@CN electrodes at a higher current rate of 3 C (Figure 5d). After 700 stable cycles at 3 C, S@CoFeP@CN electrodes still provided a discharge capacity of 606 mAh g^{-1}, showing an average 0.014% decay per cycle and a stable and high coulombic efficiency above 99.6%.
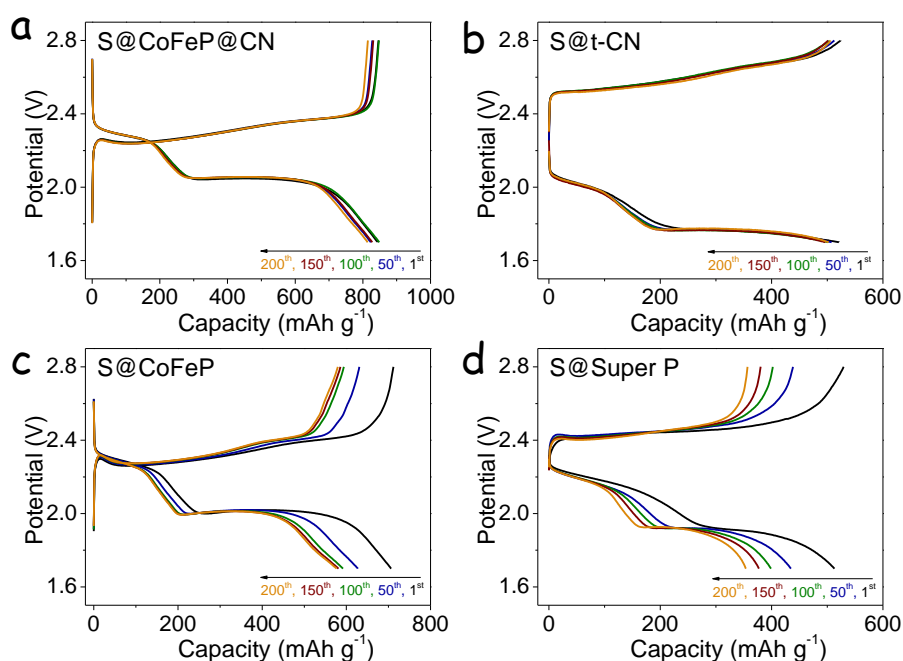

Figure 5.18. Charging/discharging profiles of four electrodes at various cycles during test at 1 C.

The compositional ratio of the host material certainly affected its catalytic performance. To determine the optimum composition, three samples with different CoFeP:t-CN weight ratio (one above and one below the 50% CoFeP:t-CN ratio analyzed in the rest of this work) were prepared and characterized. The weight ratios studied were 25%CoFeP:75%t-CN, 50%CoFeP:50%t-CN and 75%CoFeP:25%t-CN, and the samples were named as 25%CoFeP@CN, 50%CoFeP@CN, and 75%CoFeP@CN, respectively. S@50%CoFeP@CN electrodes exhibited better rate performance and higher capacity than S@25%CoFeP@CN (Figure 5.19), which can be attributed to a larger Mott-Schottky interface and catalytic sites. On the other hand, S@75%CoFeP@CN electrodes provided the worse performances, which is explained by a reduced amount of catalytic sites and thus of catalytic activity related to the aggregation of the CoFeP NCs on the surface of t-CN.
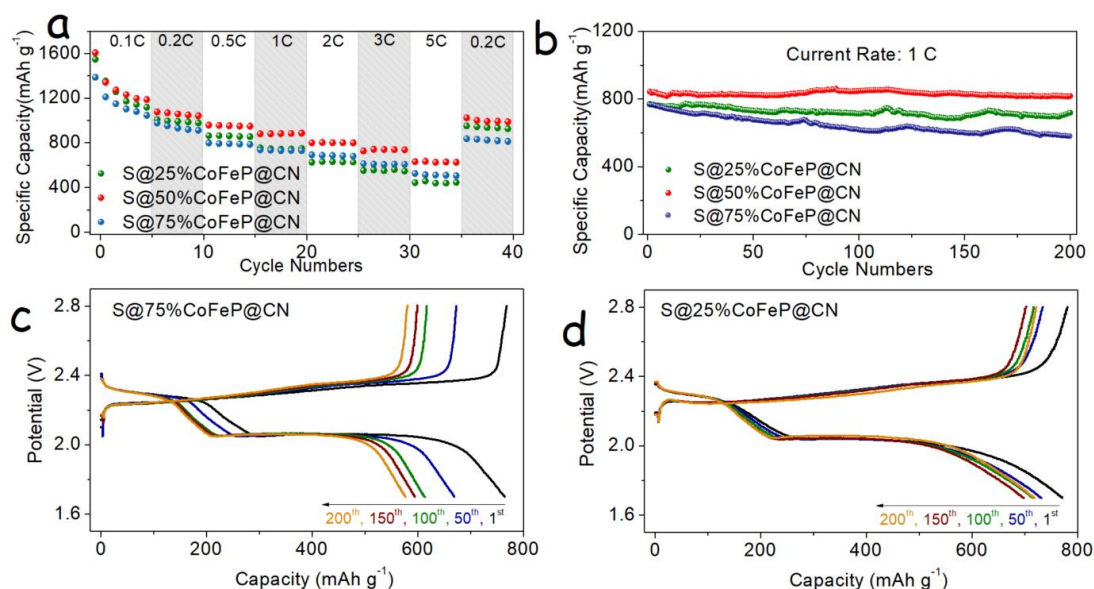

Figure 5.19. (a) Rate performances of S@25%CoFeP@CN, S@50%CoFeP@CN, and S@75%CoFeP@CN electrodes. (b) Capacity stability of different electrodes at 1 C over 200 cycles. (c,d) Charging/discharging profiles of (c) S@75%CoFeP@CN and (d) S@25%CoFeP@CN electrodes at various cycles during cycling test at 1 C.

The LSB energy conversion efficiency in the charging/discharging process, different from the above coulombic efficiency, was calculated by the ratio of energy output/input (E = ∫UIdt).[53,65] At 0.1 C current rate, the three types of electrode tested exhibited a high energy efficiency of around 90% (Figure 5.16e). When increasing the current rate, S@CoFeP@CN displayed the highest and most stable energy efficiency, retaining 89.91% efficiency at 1 C

and 79.89% at 5 C, well above the 69.37% for S@CN at 1 C and 74.61% for S@CoFeP at 5 C. We associate this higher energy efficiency to the lower polarization potential of CoFeP@CN electrodes, which was in turn related to its excellent catalytic properties, as discussed above.

Self-discharging is another main drawback of LSBs. The self-discharge profiles of S@CoFeP@CN and S@Super P electrodes are presented in Figure 5.16f. The open-circuit voltage (OCV) of the cells was measured during 72 consecutive hours after 30 stabilization cycles. During this time, S@Super P electrodes showed a significant OCV decrease to 2.288 V, denoting a notable self-discharging. On the other hand, the S@CoFeP@CN electrode maintained a much more stable OCV, with a final voltage of 2.367 V, suggesting superior stability against self-discharge. Self-discharging may be more clearly seen in the right side of Figure 5.16f, where the dash/solid curves present the discharge curves before/after 72 h of rest under a current rate of 0.2 C. After the 72 h rest period, an obvious capacity decay, from 691 to 580 mAh g^{-1}, was obtained from the S@Super P electrode, consistently with the OCV change. On the other hand, just a slight capacity loss was measured from the S@CoFeP@CN electrode, from 989.2 to 975.5 mAh g^{-1}. Under shelf storage conditions, the capacity of batteries shows exponential decay with storage time t_S, so the self-discharge behavior can be quantitatively analyzed using the following equation:[66]

$$Q_D = Q_D^0 e^{-K_S t_S}$$

Q_D^0 and Q_D are discharge capacity before and after storage for a period of time t_S, so the self-discharge constant K_S can be easily obtained from:

$$K_S = \ln \frac{Q_D^0}{Q_D} \cdot \frac{1}{t_S}$$

While S@Super P electrodes were characterized by a K_S value of 2.40×10^{-3} h^{-1}, an order of magnitude lower self-discharge constant was obtained for S@CoFeP@CN, K_S = 1.96×10^{-4} h^{-1}, S@CoFeP, K_S = 5.9×10^{-4} h^{-1}, and S@t-CN, K_S = 6.5×10^{-4} h^{-1}, electrodes in (Figure 5.20). The lower self-discharge constant of S@CoFeP@CN batteries was related to the lower loss of active material and a stronger LiPS anchoring.
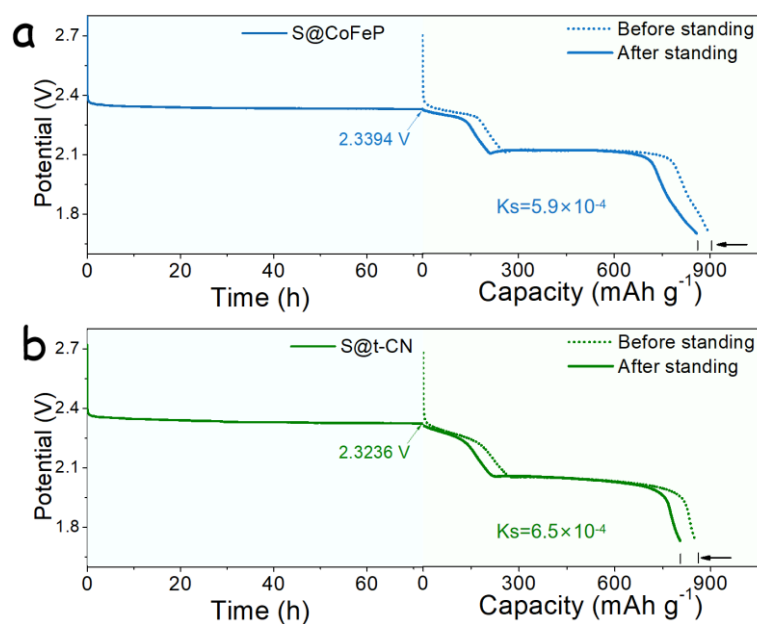
Figure 5.20. Change of open-circuit voltage during a 72 h self-discharge test and comparison of discharge curves before and after the 72 h self-standing test: (a) S@CoFeP and (b) S@t-CN electrodes.

Electrochemical impedance spectroscopy (EIS) was used to further understand the parameters behind the enhanced redox kinetics of S@CoFeP@CN electrodes. Figure 5.16g and 5.21 display the Nyquist plot obtained from S@CoFeP@CN, S@CoFeP, and S@CN coin cells before and after cycling at 1 C. The fresh electrodes displayed a semicircle in the high-frequency region associated with the charge-transfer resistance (Rct), followed by a linear dependence in the low-frequency region that is related to the diffusion of lithium ions.[43,67] Data was fitted considering the equivalent circuit displayed as an inset in Figure 5.16g. A moderate Rct was obtained for the S@CoFeP@CN electrode (62.99 Ω), when compared with that of S@CoFeP (80.36 Ω) and S@CN (125.5 Ω). This low Rct denoted an enhanced charge transferability of the CoFeP@CN composite when compared with electrodes based on each of the composite components. After charging/discharging loops, an additional semicircle in the high-frequency range was evidenced. This newly appearing loop was associated with the resistance of an insoluble Li_2S_2/Li_2S passivation layer (Rp in the equivalent circuit) grown during cycling.[60,67] After cycling, Rct notably decreased for the three types of electrode tested due to the activation process. After cycling, S@CoFeP@CN electrodes were characterized by smaller Rct (9.56 Ω) and Rp (20.14 Ω), when compared with S@CoFeP (Rct = 29.39 Ω and Rp = 23.36 Ω) and S@CN electrodes (Rct = 52.67 Ω and Rp

= 120.91 Ω). The small Rp value obtained for CoFeP and specially CoFeP@CN hosts indicated a reduction of the deposition of insulting Li_2S/Li_2S_2 on the surface, associated with an accelerated LiPS conversion.[67]
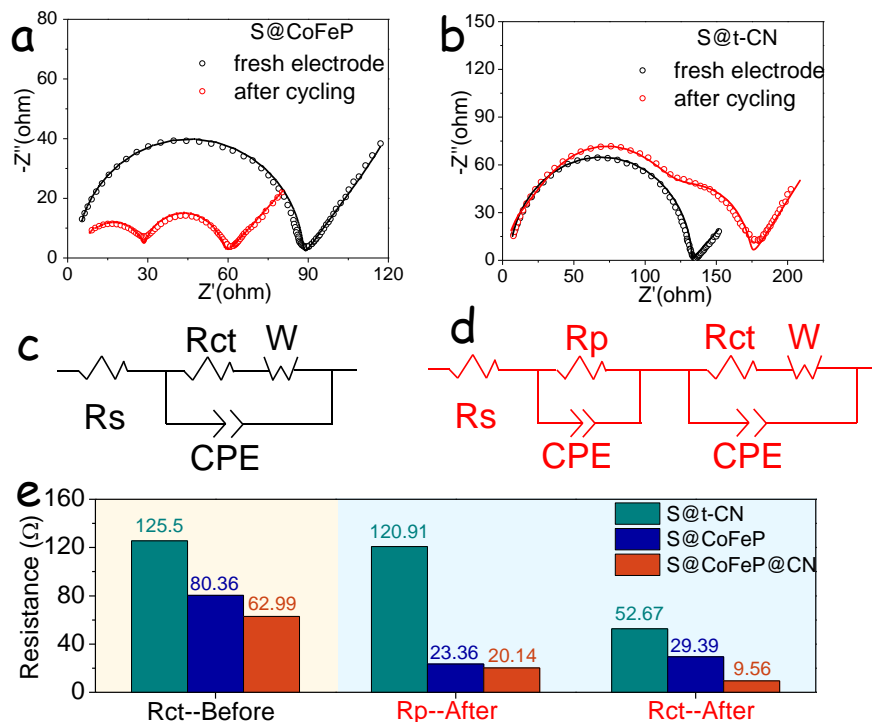

Figure 5.21. (a,b) EIS spectra of (a) S@CoFeP and (b) S@t-CN coin cells before and after 100 cycles. Black trace corresponds to fresh cell and red trace to the same cell after cycling at 1 C for 100 cycles. The solid line corresponding to the fitting result from the equivalent circuit (c) and (d), and the Rs, Rp, Rct, and W stand for the resistance of the electrolyte, insoluble Li_2S_2/Li_2S layer, interfacial charge-transportation, and semi-infinite Warburg diffusion, respectively; and CPE stands for the corresponding capacitance. (e) Different resistances of three coin cells were obtained from the equivalent circuit.

To thoroughly demonstrate that CoFeP@CN host could effectively capture soluble LiPS to confine the shuttle effect in the charging/discharging process, cycled coin cells were disassembled and analyzed after 200 cycles at 1 C. A striking contrast in the color of separators of the different cells can be observed in Figure 5.16h. The membrane disassembled from a S@CoFeP@CN cell (left one) showed a much lighter color than the dark brown membrane recovered from a S@Super P (right one). This simple visual inspection demonstrated that the CoFeP@CN host could trap polysulfide much more effectively than

Super P, and thus suppressed self-discharging and overall improved the cell efficiency and stability. Another strong evidence in support of the inhibited LiPS dissolution of CoFeP@CN was found from the surface morphology of the cycled Li anode. Different from the large cracks and severe corrosion phenomenon observed in the surface of the Li anodes recovered from S@Super P coin cells, Li foils recovered from cycled S@CoFeP@CN coin cells showed a smooth surface and lower sulfur signal at their surface, as detected by SEM and EDS analysis (Figure 5.16j,k). Finally, Figure 5.16i displays the morphology of cycled S@CoFeP@CN. Due to the inevitable grinding and shearing treatment during the slurry preparation, partial crushing happened on the S@CoFeP@CN composite, but the original tubular nanostructure was still recognizable after cycling, indicating good mechanical stability of the material towards lithiation/delithiation cycles.
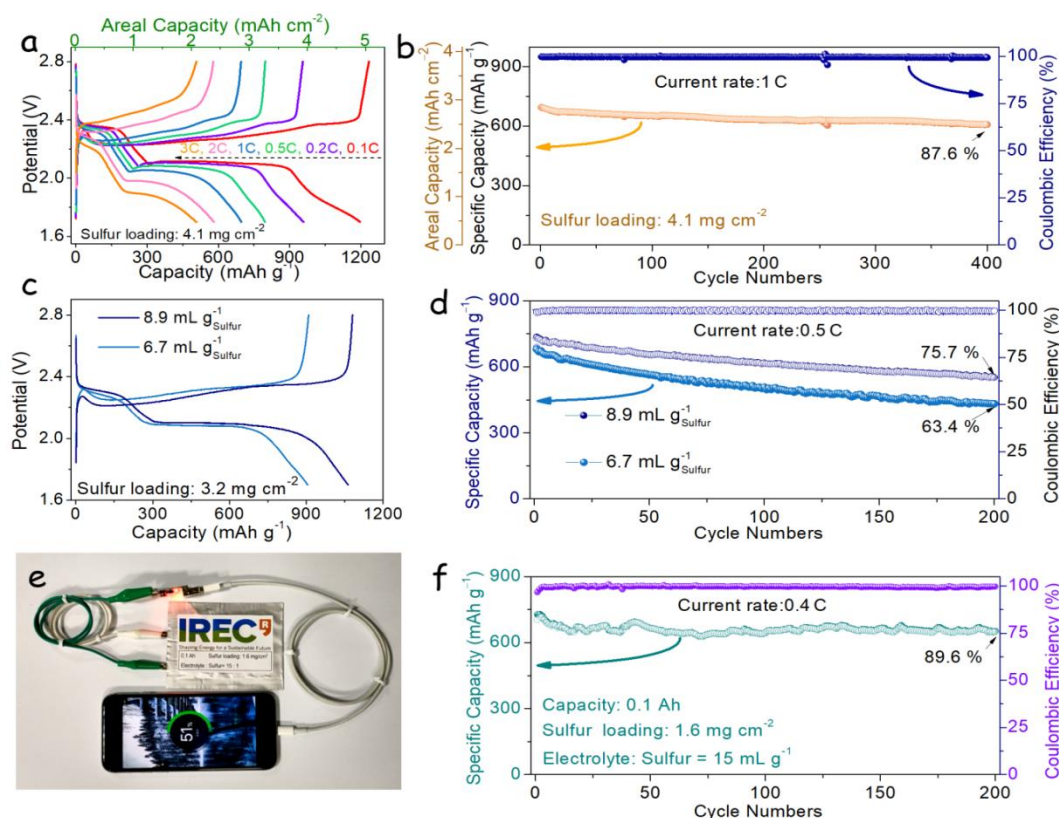
Figure 5.22. (a) Charging/discharging curves and (b) cycling performance of S@CoFeP@CN electrodes with a 4.1 mg cm^{-2} sulfur loading. (c) Charging/discharging curves of S@CoFeP@CN electrodes at 0.1 C with lean electrolyte. (d) Cycling performance of S@CoFeP@CN electrodes with lean electrolyte. (e) Optical photograph of a mobile phone being charged by a pouch cell based on a S@CoFeP@CN electrode. (f) Cycling performances at 0.4 C of a pouch cell based on a S@CoFeP@CN cathode.

Figure 5.23. Rate capability of a S@CoFeP@CN cathode loaded with 4.1 mg cm^{-2} of sulfur at various C rates.

Increasing the sulfur loading and decreasing the electrolyte addition are mandatory to achieve the high energy density LSBs required in practical applications. Hence, a series of electrochemical tests of S@CoFeP@CN electrodes were conducted with high sulfur loading and a lean electrolyte. The results of the 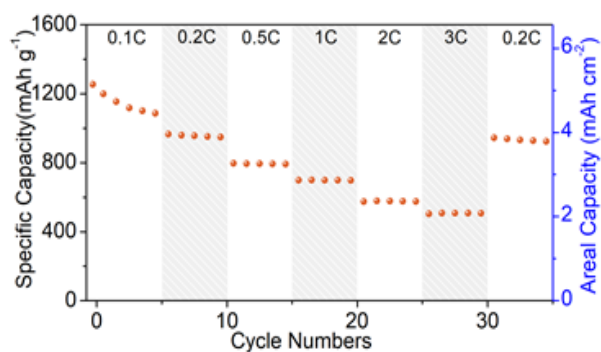rate performance of cells produced with 3.2 mg cm^{-2} high S loading can be found in Figure 5.22a. S@CoFeP@CN electrodes displayed high initial discharge capacities at 1255 mAh g^{-1}, which corresponded to an areal capacity of 5.15 mAh cm^{-2}, notably above that of commercial LIBs (4 mAh cm^{-2}). Even at high current rates of 3 C, a stable discharge capacity at 508 mAh g^{-1} was obtained. Besides, when the current rate was returned to 0.2 C, the initial capacity was recovered (Figure 5.23). All the galvanostatic charging/discharging profiles at different current rates clearly exhibited one charge plateau and two discharge plateaus, indicating that CoFeP@CN hosts could effectively reduce the polarization of LiPS conversion even under high sulfur-loading (Figure 5.22a). Figure 5.22b shows the long-term cycling performance of high sulfur loading S@CoFeP@CN electrode at 1 C. After 400 cycles, the discharge capacity was maintained at 608 mAh g^{-1}, which involved an 87.6% capacity retention, *i.e.* a 0.031% average capacity loss per cycle. Figure S30 displays the charging/discharging profiles at various cycles, exhibiting excellent stability. S@CoFeP@CN electrodes were also characterized by a high and stable coulombic efficiency at 99.3%. Lean electrolyte tests were conducted with a low electrolyte usage of 8.9 and 6.7 mL g$^{-1}_{Sulfur}$ (Figure 5.22c,d). The corresponding galvanostatic charge/discharge profiles (Figure 5.22c) clearly exhibit the enlarged voltage gap with the decreased electrolyte volume, which is attributed to deteriorative polarization caused by weakened ion transportation in

the higher viscosity electrolyte.[68] In spite of this, the S@CoFeP@CN cathode with 8.9 mL g^{-1}_{Sulfur} electrolyte still showed superior cycling stability with a capacity retention of 75.7% after 200 cycles. When the electrolyte amount decreased to 6.7 mL g^{-1}_{Sulfur}, the capacity rapidly decreased to some extent but still maintained a stable cycling performance demonstrating that the CoFeP@CN catalysts could effectively promote the Li-S reaction even under lean electrolyte conditions. Table S2 displays a comparison of several parameters of state-of-the-art TMP-based and C_3N_4-based materials as cathode hosts for LSBs. Notice that the CoFeP@CN host presented here is characterized by the highest capacities and stabilities. Besides, to illustrate the practical applicability of LSBs based on S@CoFeP@CN cathodes, pouch cells were also fabricated. S@CoFeP@CN-based pouch batteries revealed a stable operation at 0.4 C during 200 cycles, remarkable capacity retention of 89.6% was obtained and accompanied by a high coulombic efficiency at 99.5% (Figure 5.22d), and the charged mobile phone clearly demonstrate their potential (Figure 5.22c). All these results indicate that S@CoFeP@CN electrodes can definitively help LSBs to reach practical applications.

Table S2. Comparison of CoFeP@CN electrochemical performance as host cathode for LSBs with state-of-the-art TMP-based or C_3N_4-based materials.

Host material	Capacity (mAh g^{-1}) (low/high current rate)	Cycling stability(%) (cycles, current rate)	Decay rate (per cycle, %)	S content (wt%)	Ref
Co-Fe-P	1243 (0.1 C) 741 (2 C)	78.5% (500 cycles, 1 C)	0.043%	71%	11
CoP@HPCN	1058 (0.1 C) 527 (3 C)	76.9% (300 cycles, 0.2 C)	0.077%	70%	12
FeP/rGO/CNTs	1271 (0.1 C) 613 (3 C)	84% (400 cycles, 1 C)	0.04%	75%	13
CNT-MoP/GO	1301 (0.1 C) 656 (2 C)	80.3% (1156 cycles, 1 C)	0.017%	73%	14
$Ni_{12}P_5$/CNTs	1079 (0.5 C) 784 (4 C)	42.4% (1000 cycles, 0.5 C)	0.057%	65%	15

G@g-C$_3$N$_4$	1116 (0.5 C) 612 (10 C)	86% (800 cycles, 0.3 C)	0.017%	73%	16
rGO/g-C$_3$N$_4$ / CNT	1263 (0.05 C) 554 (2 C)	85% (500 cycles, 1 C)	0.03%	70.8%	17
g-C$_3$N$_4$	1170 (0.05 C) 785 (1 C)	40% (1500 cycles, 0.5 C)	0.04%	75%	18
CN-5@NSH PC	1447 (0.2 C) 387 (5 C)	72.3% (500 cycles, 1 C)	0.055%	73%	19
CoFeP@CN	**1607 (0.1 C)** **630 (5 C)**	**90.4%** **(700 cycles, 3 C)**	**0.014%**	**70%**	**Our work**

5.5 Conclusion

In summary, we reported a highly efficient sulfur host for robust LSBs, enabled by orthorhombic phased bimetallic phosphide CoFeP NCs decorated on novel nanotubular t-CN by a facile self-assembly process that took advantage of the different sign of the particles surface charge. While each of the materials provided advantages in terms of adsorption sites and available SSA, the combination of the two materials within CoFeP@CN heterostructures awoke a clear synergism between them that significantly contributed to improving LiPS adsorption and catalytic activity. Besides t-CN allowing a high distribution of CoFeP NCs, experimental results and DFT calculations displayed charge redistribution within the formed Mott-Schottky heterostructures. Additionally, experimental and theoretical work also confirmed the superior LiPS adsorbability realized by abundant sulfiphilic/lithiophilic sites in CoFeP and t-CN. Besides, the modified electron distribution within heterostructures allowed reducing the potential barriers and improved the redox kinetics during the charging/discharging processes, including LiPS phase change and Li$_2$S deposition/dissolution. Moreover, the porous CoFeP@CN host provides sufficient space to accommodate the volume change and efficient channels for Li$^+$ diffusion in reaction. As a result, S@CoFeP@CN electrodes delivered a high sulfur utilization, superior rate performance (630 mAh g^{-1} at 5 C), and remarkable cycling stability with 90.44% capacity retention over 700 cycles at 3 C. Even

with 4.1 mg cm^{-2} high-loading sulfur electrode coin cells and the 0.1 Ah capacity pouch cells test, the robust electrochemical performance results were obtained. In addition, S@CoFeP@CN electrodes exhibit high energy efficiency and low self-discharge property, which are two frequently neglected issues in material research of LSBs. This work not only demonstrated a new and highly suitable form of t-CN and further probed the suitability of metal phosphides in the field of LSBs, but also provided valuable insights into the design of heterostructural electrocatalyst to regulate LiPS.

5.6 References

[1]   P. G. Bruce, S. A. Freunberger, L. J. Hardwick, J.-M. Tarascon, *Nat. Mater.* **2012**, *11*, 19.

[2]   L. Zhou, D. L. Danilov, R. Eichel, P. H. L. Notten, *Adv. Energy Mater.* **2020**, 2001304.

[3]   Z. Liang, D. Yang, P. Tang, C. Zhang, J. J. Biendicho, Y. Zhang, J. Llorca, X. Wang, J. Li, M. Heggen, J. David, R. E. Dunin - Borkowski, Y. Zhou, J. R. Morante, A. Cabot, J. Arbiol, *Adv. Energy Mater. n/a*, 2003507.

[4]   M. Zhang, W. Chen, L. Xue, Y. Jiao, T. Lei, J. Chu, J. Huang, C. Gong, C. Yan, Y. Yan, Y. Hu, X. Wang, J. Xiong, *Adv. Energy Mater.* **2020**, *10*, 1903008.

[5]   W. Lim, S. Kim, C. Jo, J. Lee, *Angew. Chem. Int. Ed.* **2019**, *58*, 18746.

[6]   Z. Li, H. B. Wu, X. W. (David) Lou, *Energy Environ. Sci.* **2016**, *9*, 3061.

[7]   C. Zu, A. Manthiram, *Adv. Energy Mater.* **2013**, *3*, 1008.

[8]   J.-Q. Huang, Q. Zhang, S.-M. Zhang, X.-F. Liu, W. Zhu, W.-Z. Qian, F. Wei, *Carbon* **2013**, *58*, 99.

[9]   B. Zhang, X. Qin, G. R. Li, X. P. Gao, *Energy Environ. Sci.* **2010**, *3*, 1531.

[10]   H. Wang, W. Zhang, J. Xu, Z. Guo, *Adv. Funct. Mater.* **2018**, *28*, 1707520.

[11]   X. Liu, J.-Q. Huang, Q. Zhang, L. Mai, *Adv. Mater.* **2017**, *29*, 1601759.

[12]   S. Yu, W. Cai, L. Chen, L. Song, Y. Song, *J. Energy Chem.* **2020**.

[13]   H. Yuan, X. Chen, G. Zhou, W. Zhang, J. Luo, H. Huang, Y. Gan, C. Liang, Y. Xia, J. Zhang, J. Wang, X. Tao, *ACS Energy Lett.* **2017**, *2*, 1711.

[14]   J. Zhou, X. Liu, L. Zhu, J. Zhou, Y. Guan, L. Chen, S. Niu, J. Cai, D. Sun, Y. Zhu, J. Du, G. Wang, Y. Qian, *Joule* **2018**.

[15] Q. Zhu, B. Qiu, H. Duan, Y. Gong, Z. Qin, B. Shen, M. Xing, J. Zhang, *Appl. Catal. B Environ.* **2019**, *259*, 118078.

[16] Y. Tan, H. Wang, P. Liu, Y. Shen, C. Cheng, A. Hirata, T. Fujita, Z. Tang, M. Chen, *Energy Environ. Sci.* **2016**, *9*, 2257.

[17] F. Geng, Y. Bonita, V. Jain, M. Magiera, N. Rai, J. C. Hicks, *Ind. Eng. Chem. Res.* **2020**, *59*, 6931.

[18] Y. Li, Z. Dong, L. Jiao, *Adv. Energy Mater.* **2020**, *10*, 1902104.

[19] W.-J. Ong, L.-L. Tan, Y. H. Ng, S.-T. Yong, S.-P. Chai, *Chem. Rev.* **2016**, *116*, 7159.

[20] T.-Z. Hou, X. Chen, H.-J. Peng, J.-Q. Huang, B.-Q. Li, Q. Zhang, B. Li, *Small* **2016**, *12*, 3283.

[21] Q. Pang, L. F. Nazar, *ACS Nano* **2016**, *10*, 4111.

[22]   Z. Jia, H. Zhang, Y. Yu, Y. Chen, J. Yan, X. Li, H. Zhang, *J. Energy Chem.* **2020**, *43*, 71.

[23] P. Zhang, F. Wang, Y. Qin, N. Wang, *ACS Appl. Nano Mater.* **2020**.

[24] Y. Wang, R. Zhang, J. Chen, H. Wu, S. Lu, K. Wang, H. Li, C. J. Harris, K. Xi, R. V. Kumar, S. Ding, *Adv. Energy Mater.* **2019**, *9*, 1900953.

[25] X. Du, J. Huang, J. Zhang, Y. Yan, C. Wu, Y. Hu, C. Yan, T. Lei, W. Chen, C. Fan, J. Xiong, *Angew. Chem. Int. Ed.* **2019**, *58*, 4484.

[26] X. Wang, X. Tian, Y. Sun, J. Zhu, F. Li, H. Mu, J. Zhao, *Nanoscale* **2018**, *10*, 12315.

[27] Z. Zhuang, Y. Li, Z. Li, F. Lv, Z. Lang, K. Zhao, L. Zhou, L. Moskaleva, S. Guo, L. Mai, *Angew. Chem.* **2018**, *130*, 505.

[28] Y. Wang, R. Zhang, Z. Sun, H. Wu, S. Lu, J. Wang, W. Yu, J. Liu, G. Gao, S. Ding, *Adv. Mater. Interfaces* **2020**, *7*, 1902092.

[29] D. Sun, K. Liu, J. Hu, J. Zhou, *Small n/a*, 2006374.

[30] X. Chen, X. Ding, C. Wang, Z. Feng, L. Xu, X. Gao, Y. Zhai, D. Wang, *Nanoscale* **2018**, *10*, 13694.

[31] Y. Zhang, Y. Wang, R. Luo, Y. Yang, Y. Lu, Y. Guo, X. Liu, S. Cao, J.-K. Kim, Y. Luo, *Nanoscale Horiz.* **2020**, *5*, 530.

[32] J. Liu, M. Meyns, T. Zhang, J. Arbiol, A. Cabot, A. Shavel, *Chem. Mater.* **2018**, *30*, 1799.

[33] J. Liu, X. Yu, R. Du, C. Zhang, T. Zhang, J. Llorca, J. Arbiol, Y. Wang, M. Meyns, A. Cabot, *Appl. Catal. B Environ.* **2019**, *256*, 117846.

[34] T. Berestok, P. Guardia, M. Ibáñez, M. Meyns, M. Colombo, M. V. Kovalenko, F. Peiró, A. Cabot, *Langmuir* **2018**, *34*, 9167.

[35] D. Zeng, W. Xu, W.-J. Ong, J. Xu, H. Ren, Y. Chen, H. Zheng, D.-L. Peng, *Appl. Catal. B Environ.* **2018**, *221*, 47.

[36] Y.-L. Wang, Y. Tian, Z.-L. Lang, W. Guan, L.-K. Yan, *J. Mater. Chem. A* **2018**, *6*, 21056.

[37] Q. Pang, X. Liang, C. Y. Kwok, J. Kulisch, L. F. Nazar, *Adv. Energy Mater.* **2017**, *7*, 1601630.

[38] Z. Chen, Y. Yu, X. She, K. Xia, Z. Mo, H. Chen, Y. Song, J. Huang, H. Li, H. Xu, *Appl. Surf. Sci.* **2019**, *495*, 143528.

[39] J. Wu, C. Li, W. Zhang, J. Han, L. Wang, S. Wang, Y. Wang, *Energy Technol.* **2019**, *7*, 1800927.

[40] J.-X. Feng, S.-Y. Tong, Y.-X. Tong, G.-R. Li, *J. Am. Chem. Soc.* **2018**, *140*, 5118.

[41] Z. Peng, X. Qiu, G. Cai, X. Zhang, Z. Dong, *J. Alloys Compd.* **2020**, *842*, 155784.

[42] Y. Zhong, L. Yin, P. He, W. Liu, Z. Wu, H. Wang, *J. Am. Chem. Soc.* **2018**, *140*, 1455.

[43] C. Zhang, J. J. Biendicho, T. Zhang, R. Du, J. Li, X. Yang, J. Arbiol, Y. Zhou, J. R. Morante, A. Cabot, *Adv. Funct. Mater.* **2019**, *29*, 1903842.

[44] Y. Chen, W. Zhang, D. Zhou, H. Tian, D. Su, C. Wang, D. Stockdale, F. Kang, B. Li, G. Wang, *ACS Nano* **2019**, *13*, 4731.

[45] X.-F. Yu, D.-X. Tian, W.-C. Li, B. He, Y. Zhang, Z.-Y. Chen, A.-H. Lu, *Nano Res.* **2019**, *12*, 1193.

[46] J. Zhang, J.-Y. Li, W.-P. Wang, X.-H. Zhang, X.-H. Tan, W.-G. Chu, Y.-G. Guo, *Adv. Energy Mater.* **2018**, *8*, 1702839.

[47] X. Hong, J. Jin, T. Wu, Y. Lu, S. Zhang, C. Chen, Z. Wen, *J. Mater. Chem. A* **2017**, *5*, 14775.

[48] N. Pavlin, S. Hribernik, G. Kapun, S. D. Talian, C. Njel, R. Dedryvère, R. Dominko, *J. Electrochem. Soc.* **2018**, *166*, A5237.

[49] X. Chen, H.-J. Peng, R. Zhang, T.-Z. Hou, J.-Q. Huang, B. Li, Q. Zhang, *ACS Energy Lett.* **2017**, *2*, 795.

[50] Y. Luo, N. Luo, W. Kong, H. Wu, K. Wang, S. Fan, W. Duan, J. Wang, *Small* **2018**, *14*, 1702853.

[51] S. Huang, Y. V. Lim, X. Zhang, Y. Wang, Y. Zheng, D. Kong, M. Ding, S. A. Yang, H. Y. Yang, *Nano Energy* **2018**, *51*, 340.

[52] Y. Qiu, W. Li, W. Zhao, G. Li, Y. Hou, M. Liu, L. Zhou, F. Ye, H. Li, Z. Wei, S. Yang, W. Duan, Y. Ye, J. Guo, Y. Zhang, *Nano Lett.* **2014**, *14*, 4821.

[53] Z. Yuan, H.-J. Peng, T.-Z. Hou, J.-Q. Huang, C.-M. Chen, D.-W. Wang, X.-B. Cheng, F. Wei, Q. Zhang, *Nano Lett.* **2016**, *16*, 519.

[54] S. Chen, J. Luo, N. Li, X. Han, J. Wang, Q. Deng, Z. Zeng, S. Deng, *Energy Storage Mater.* **2020**, *30*, 187.

[55] Y. Li, P. Xu, G. Chen, J. Mou, S. Xue, K. Li, F. Zheng, Q. Dong, J. Hu, C. Yang, M. Liu, *Chem. Eng. J.* **2020**, *380*, 122595.

[56] W. Tian, B. Xi, Z. Feng, H. Li, J. Feng, S. Xiong, *Adv. Energy Mater.* **2019**, *9*, 1901896.

[57] Z. Du, X. Chen, W. Hu, C. Chuang, S. Xie, A. Hu, W. Yan, X. Kong, X. Wu, H. Ji, L.-J. Wan, *J. Am. Chem. Soc.* **2019**, *141*, 3977.

[58] F. Y. Fan, W. C. Carter, Y.-M. Chiang, *Adv. Mater.* **2015**, *27*, 5203.

[59] H. Yuan, H.-J. Peng, B.-Q. Li, J. Xie, L. Kong, M. Zhao, X. Chen, J.-Q. Huang, Q. Zhang, *Adv. Energy Mater.* **2018**, 1802768.

[60] Y. Pan, X. Cheng, M. Gao, Y. Fu, J. Feng, H. Ahmed, L. Gong, H. Zhang, V. S. Battaglia, *ACS Appl. Mater. Interfaces* **2020**, *12*, 32726.

[61] R. Wang, C. Luo, T. Wang, G. Zhou, Y. Deng, Y. He, Q. Zhang, F. Kang, W. Lv, Q. Yang, *Adv. Mater.* **2020**, 2000315.

[62] Y. Yan, Z. Chen, J. Yang, L. Guan, H. Hu, Q. Zhao, H. Ren, Y. Lin, Z. Li, M. Wu, *Small* **2020**, *16*, 2004631.

[63] X. Zhu, W. Zhao, Y. Song, Q. Li, F. Ding, J. Sun, L. Zhang, Z. Liu, *Adv. Energy Mater.* **2018**, *8*, 1800201.

[64] G. Zhou, H. Tian, Y. Jin, X. Tao, B. Liu, R. Zhang, Z. W. Seh, D. Zhuo, Y. Liu, J. Sun, J. Zhao, C. Zu, D. S. Wu, Q. Zhang, Y. Cui, *Proc. Natl. Acad. Sci.* **2017**, *114*, 840.

[65] A. Eftekhari, *Sustain. Energy Fuels* **2017**, *1*, 2053.

[66] Y. V. Mikhaylik, J. R. Akridge, *J. Electrochem. Soc.* **2004**, *151*, A1969.

[67] A.-H. Shao, Z. Zhang, D.-G. Xiong, J. Yu, J.-X. Cai, Z.-Y. Yang, *ACS Appl. Mater. Interfaces* **2020**, *12*, 5968.

[68]   S. Wang, S. Feng, J. Liang, Q. Su, F. Zhao, H. Song, M. Zheng, Q. Sun, Z. Song, X. Jia, J. Yang, Y. Li, J. Liao, R. Li, X. Sun, *Adv. Energy Mater.* **2021**, *11*, 2003314.

Results and discussion

Renewable energies, such as wind and solar energy, are the most promising solution to relieve the increasing energy crisis. However, wind and solar power are both characterized by intermittent availability. Hence, the photo/electrochemistry energy conversion and storage technology, such as photocatalytic H_2/H_2O_2 generation, electrocatalytic water splitting and battery, has been recognized as one of the most promising approaches, which can convert energy to a storable form in various mediums and then be converted back when needed.

To realize the conversing and storage of renewable energy into stable chemical fuel or batteries, suitable materials are needed to efficiently perform the photo/electrochemical energy conversion processes. These materials not only need to be based on abundant elements, low coat and environment friendly but also should meet the requirements of high energy conversion efficiency and long-term stability for the corresponding reaction system such as OER, HER, H_2O_2ER and LSBs.

Nanomaterials are key in the energy conversion and storage field due to their high specific performance based on a high specific surface area and a high number of exposed active sites. However, a single component is generally not enough to meet all the requirements of the applications. Hence, building functional nanocomposites which combined desired properties from each part is generally necessary. For this reason, rational nanocomposites were designed and produced here for the respective applications.

The result section started by presenting a large size of nanoparticle coated metal substrate electrode with high electrochemical transfer efficiency and long stability for electrocatalytic oxygen evolution reaction. As shown in the thesis, the $CoFe_2O_4$ NP-coated NF, which combined the outstanding catalytic properties of NPs and good conductivity and large electrochemical surface area of NF, was produced through a dip-coating method. The enhanced OER catalytic activity of the $CoFe_2O_4$@NF electrodes can be ascribed to the combination of nano-sized active $CoFe_2O_4$ particles

with the 3D macroporous structure of the supporting NF. This marriage resulted in a significantly increased contact area between catalysts and electrolytes and provided a greater amount of active sites where OER could take place. The dip-coating procedure eventually led to an optimum distribution of thinly dispersed $CoFe_2O_4$ NPs, which allowed to circumvent the intrinsically inferior electrical conductivity of oxide particles, while ensuring impressive stability of the $CoFe_2O_4$@NF electrode.

Compared with the conversion of electrical energy to chemical energy, direct photocatalytic hydrogen production may be more attractive. In chapter 3, 2D/2D heterojunction of TiO_2/g-C_3N_4 were produced through an electrostatic self-assembly method. The enhanced performance was attributed to the integrated effects of the unique 2D/2D morphology and type II heterojunction transfer mechanism. The face-to-face interfacial contact between ultrathin layers of g-C_3N_4 and the facets of TiO_2 provides fast photogenerated charges migration channels inside the composites. Also, the intimate attachment of 2D planes enables efficient charge transport through the heterojunction, which encourages charge pair separation and reduces the possibility of recombination.

H_2O_2 is a promising liquid fuel that is safer and easier to store than compressed hydrogen. Compared with photocatalytic hydrogen production, the difficulty of photocatalytic hydrogen peroxide production lies in the selectivity of the product. In chapter 4, oxygen doping Ni-loaded g-C_3N_4 nanotubes with efficient charge separation and high H_2O_2 selectivity were synthesized through an in situ photoreduction method. The hollow structure of the tubular g-C_3N_4 provides a large surface with a high density of reactive sites and efficient visible light absorption during the photocatalytic reaction. The oxygen doping and Ni loading enable a fast separation of photogenerated charge carriers and a high selectivity toward the two-electron process during the ORR. The combination of nickel nanoparticles and tubular g-C_3N_4 brings together the advantages of efficient light absorption, effective separation of charges, and high conversion efficiency of hydrogen peroxide, and finally realizes the efficient conversion of light energy to chemical energy.

Compared with the conversion and storage in the form of fuel energy, the storage and use of batteries is more convenient and faster. As shown in chapter 5, a highly efficient sulfur host for LSBs, the CoFeP NCs decorated nanotubular g-C_3N_4 was produced by a self-assembly process. The combination of the two materials within CoFeP@CN heterostructures awoke a clear synergism that significantly contributed to improving LiPS adsorption and catalytic activity. Besides, as experimental and theoretical work shown in this thesis confirmed the superior LiPS adsorbability realized by abundant sulfiphilic/lithiophilic sites in CoFeP and t-CN. Additionally, the modified electron distribution within heterostructures allowed reducing the potential barriers and improved the redox kinetics during the charging/discharging processes, including LiPS phase change and Li_2S deposition/dissolution. Moreover, the porous CoFeP@CN host provides sufficient space to accommodate the volume change and efficient channels for Li+ diffusion in reaction. Above all, the marriage of CoFeP NCs and tubular g-C_3N_4 accelerates the LiPS conversion, facilitates the diffusion of Li ions, accommodates volume change during the reaction, and offers abundant lithiophilic/sulfiphilic sites to effectively trap soluble LiPS, which result in the superior cycling stability and rate capability.

Based on all the results above, we were able to rationally construct functional nanocomposites to meet the requirements of various properties of materials according to different reactions.

Conclusion

In this thesis, four functional nanocomposite materials including $CoFe_2O_4$/Ni foam, TiO_2/g-C_3N_4, Ni/g-C_3N_4 and CoFeP/g-C_3N_4 have been developed based on different applications in energy conversion and storage filed. Moreover, the photo/ electrochemical conversion applications such as OER, H_2/H_2O_2 generation and LSBs were studied utilizing the produced nanocomposites. From the investigations we got the following conclusions:

(1) The NP coating of 3D conductive substrate is an excellent method to produce electrocatalysts with high energy conversion efficiency and outstanding stability toward OER.

(2) 2D/2D heterojunction nanocomposites with rational components and suitable band structure could promote the separation and migration of photogenerated charges, thus significantly improving the photocatalytic hydrogen evolution performance.

(3) Transition metal NPs such as Ni NPs, which worked as co-catalyst in metal/g-C_3N_4 nanocomposites, could not only accelerate the charge separation and transfer but also improve the selectivity of the hydrogen peroxide evolution process.

(4) Suitable NP-coated hollow structured g-C_3N_4 can effectively buffer the volume change during charge/discharge process, reduce polysulfide shuttling, accelerate the catalytic conversion of polysulfide, thus enhancing the cycling stability and rate capability of LSBs.

Above all, functional NP-coated nanocomposites, with rational functional design, optimized nanoparticle synthesis and successful nanocomposite construction, were shown key processes to optimize photo/ electrochemical energy conversion and storage processes.

Future work

In this thesis, we mainly focus on the design and synthesis of nanocomposites and the exploration of the energy conversion process. However, there are still some problems and challenges related to the nanocomposites preparation and energy conversion process. I will continue my research work in the following 3 main areas:

(1) Regarding the NP-coated conductive substrate electrode, further exploration of the interaction between NPs and substrates is of great significance for us to gain a deeper understanding of the reaction mechanism and improve the design of nanocomposites.

(2) Exploring the in situ colloidal syntheses on different substrates (such as g-C_3N_4, C_2N, MOF and COF) is very meaningful for us to enrich our synthetic method and broaden our material system.

(3) Improving our energy conversion efficiency testing capabilities to find the most suitable reaction conditions and improve the performance of our materials.

CURRICULUM VITAE

Personal Information

Name: Ruifeng Du

Address: Jardins de les Dones de Negre, 1, Barcelona

Tel: +34 652617448

Email: adufeng518@gmail.com

Date of Birth: May 18, 1992

Education

• 2017.9-present: PhD student

University of Barcelona, Catalonia Institute for Energy Research-IREC, Spain

Major: Nanoscience,

Key words: colloidal synthesis, photocatalysis, eletrocatalysis, LSBs

Supervisor: Prof. Andreu Cabot

• 2014.9-2017.7: Master

China University of Geoscience, China

Major: material science and engineering

Key words: transition metal sulfides, graphene, photocatalysis, eletrocatalysis

Supervisor: Prof. Yihe Zhang and Prof. Xuelian Yu

• 2010.9-2014.7: Bachelor

Major: inorganic material science and engineering

Taiyuan University of Technology, China

Research Experience

2017.10-present: functional nanomaterials group, Catalonia Institute for Energy Research, Barcelona, Spain.

  • 2019.5-present. Functional design and preparation of nanocomposites and their application in energy field.

• 2018.9-2020.12 Controlled preparation of g-C3N4 with different morphology including bulk g-C_3N_4, layered g-C_3N_4, tubular g-C_3N_4.

• 2017.10-2019.5 Colloidal synthesizing of metal alloys, metal oxides, metal phosphides nanoparticles and their surface modification.

2014.9-2017.6: Key Laboratory of ptoelectronic Physics of China University of Geoscience, school of material science and engineering.

• 2015.9-2017.6 Preparation of transition metal sulfide /graphene composites and their applications in photoelectrocatalysis.

• 2014.9-2015.7 Preparation and characterization of graphene and graphene films.

Research Interests

➣ Nanoparticle synthesizing with size, phase and morphology control

➣ NPs surface modification

➣ Functional design and preparation of nanocomposites

➣ Application: photo/electrocatalysis, OER, ORR, H_2/H_2O_2 generation, LSBs

Awards

✓ China Scholarship Council (2017)

✓ National scholarship (2016)

Conferences

2019.8.27-30, Upscaling high activity oxygen evolution catalysts based on CoFe2O4 nanoparticles supported on nickel foam for power-to-gas electrochemical conversion with energy efficiencies above 80%

Photo and ElectroCatalysis at the Atomic scale. (PECAS 2019)

Publications

[1] **R. Du**, K. Xiao, B. Li*, X. Han, C. Zhang, X. Wang, Y. Zuo, P. Guardia, J. Li, J. Chen*, A. Cabot* Controlled oxygen doping in highly dispersed Ni-loaded g-C_3N_4 nanotubes for efficient photocatalytic H_2O_2 production, Chem. Eng. J. (2022) 135999. **IF: 13.273.**

[2] C. Zhang, **R. Du**, J.J. Biendicho, M. Yi, K. Xiao, D. Yang, T. Zhang, X. Wang, J. Arbiol, J. Llorca, Y. Zhou*, J.R. Morante, A. Cabot*, Tubular CoFeP@CN as a Mott–Schottky Catalyst with Multiple Adsorption Sites for Robust Lithium–Sulfur Batteries, Adv. Energy Mater. 11 (2021) 2100432. **IF:**

29.368.

[3] F. Urbain, **R. Du***, P. Tang, V. Smirnov, T. Andreu, F. Finger, N.J. Divins, J. Llorca, J. Arbiol, A. Cabot, Upscaling high activity oxygen evolution catalysts based on $CoFe_2O_4$ nanoparticles supported on nickel foam for power-to-gas electrochemical conversion with energy efficiencies above 80%, Appl. Catal. B Environ. 259 (2019) 118055. **IF: 19.052.**

[4] **R. Du**, B. Li*, X. Han, K. Xiao, X. Wang, J. Arbiol, A. Cabot*, 2D/2D Heterojunction of TiO_2 Nanosheets / Ultrathin g-C_3N_4 for efficient photocatalytic hydrogen evolution, Nanomaterials. **IF: 4.921.**

[5] **R. Du**, Y. Zhang*, B. Li, X. Yu*, H. Liu, X. An*, J. Qu, Biomolecule-assisted synthesis of defect-mediated Cd1–xZnxS / MoS_2/ grapheme hollow spheres for highly efficient hydrogen evolution, Phys. Chem. Chem. Phys. 18 (2016) 16208–16215. **IF: 3.676.**

[6] X. Yu, **R. Du**, B. Li, Y. Zhang*, H. Liu, X. An*, Biomolecule-assisted self-assembly of CdS /MoS_2/graphene hollow spheres as high-efficiency photocatalysts for hydrogen evolution without noble metals, Appl. Catal. B Environ. 182 (2016) 504–512. **IF: 19.052.**

[7] X. Yu, **R. Du**, B. Li, L. Liu, Y. Zhang*, Cu_2ZnSnS_4–AuAg Heterodimers and Their Enhanced Catalysis for Oxygen Reduction Reaction, J. Phys. Chem. C. 121 (2017) 6712–6720. **IF: 4.126.**

[8] L. Liu, **R. Du**, Y. Zhang*, X. Yu*, A novel sandwich-type immunosensor based on three-dimensional graphene–Au aerogels and quaternary chalcogenide nanocrystals for the detection of carcino embryonic antigen, New J. Chem. 41 (2017) 9008–9013. **IF: 3.591.**

[9] T. Berestok, P. Guardia, **R. Du**, J.B. Portals, M. Colombo, S. Estradé, F. Peiró, S.L. Brock, A. Cabot*, Metal Oxide Aerogels with Controlled Crystallinity and Faceting from the Epoxide-Driven Cross-Linking of Colloidal Nanocrystals, ACS Appl. Mater. Interfaces. 10 (2018) 16041–16048. **IF: 9.229.**

[10] J. Liu, X. Yu, **R. Du**, C. Zhang, T. Zhang, J. Llorca, J. Arbiol, Y. Wang, M. Meyns, A. Cabot*, Chromium phosphide CrP as highly active and stable electrocatalysts for oxygen electroreduction in alkaline media, Appl. Catal. B Environ. 256 (2019) 117846. **IF: 19.092.**

[11] B. Li, Y. Zhang*, **R. Du**, L. Gan, X. Yu*, Synthesis of Bi_2S_3–Au dumbbell heteronanostructures with enhanced photocatalytic and photoresponse properties, Langmuir. 32 (2016) 11639–11645. **IF: 3.882.**

[12] L. Liu, Y. Zhang*, **R. Du**, J. Li, X. Yu*, An ultrasensitive electrochemical immunosensor based

on the synergistic effect of quaternary Cu_2SnZnS_4 NCs and cyclodextrin-functionalized graphene, Analyst. 142 (2017) 780–786. **IF: 4.616.**

[13] Y. Zuo, Y. Liu, J. Li, **R. Du**, X. Yu, C. Xing, T. Zhang, L. Yao, J. Arbiol, J. Llorca, A. Cabot*, Solution-processed ultrathin SnS_2–Pt nanoplates for photoelectrochemical water oxidation, ACS Appl. Mater. Interfaces. 11 (2019) 6918–6926. **IF: 9.229.**

[14] B. Li, Y. Zhang*, **R. Du**, L. Liu, X. Yu*, Controllable synthesis of Co_3O_4 nanocrystals as efficient catalysts for oxygen reduction reaction, Nanotechnology. 29 (2018) 105401. **IF: 3.874.**

[15] Y. Zuo, X. Xu, C. Zhang, J. Li, **R. Du**, X. Wang, X. Han, J. Arbiol, J. Llorca, J. Liu, A. Cabot*, SnS2/g-C3N4/graphite nanocomposites as durable lithium-ion battery anode with high pseudocapacitance contribution, Electrochim. Acta. 349 (2020) 136369. **IF: 6.901.**

[16] Y. Zuo, Y. Liu, J. Li, **R. Du**, X. Han, T. Zhang, J. Arbiol, N.J. Divins, J. Llorca, N. Guijarro, A. Cabot*, In situ electrochemical oxidation of Cu2S into CuO nanowires as a durable and efficient electrocatalyst for oxygen evolution reaction, Chem. Mater. 31 (2019) 7732–7743. **IF: 9.811.**

[17] X. Wang, L. Yang, C. Xing, X. Han, **R. Du**, R. He, P. Guardia, J. Arbiol, A. Cabot*, MOF-Derived ultrathin cobalt molybdenum phosphide nanosheets for efficient electrochemical overall water Splitting, Nanomaterials. 12 (2022) 1098. **IF: 4.921.**

[18] X. Yu, D. Wang, J. Liu, Z. Luo, **R. Du**, L. Liu, G. Zhang, Y. Zhang, A. Cabot*,Cu_2ZnSnS_4 nanocrystals as highly active and stable electrocatalysts for the oxygen reduction reaction, J. Phys. Chem. C. 120 (2016) 24265–24270. **IF: 4.126.**

[19] Y. Zuo, J. Li, X. Yu, **R. Du**, T. Zhang, X. Wang, J. Arbiol, J. Llorca, A. Cabot*, A SnS_2 molecular precursor for conformal nanostructured coatings, Chem. Mater. 32 (2020) 2097–2106. **IF: 9.811.**

[20] J. Li, Y. Zuo, J. Liu, X. Wang, X. Yu, **R. Du**, T. Zhang, M.F. Infante-Carrió, P. Tang, J. Arbiol, A. Cabot*, Superior methanol electrooxidation performance of (110)-faceted nickel polyhedral nanocrystals, J. Mater. Chem. A. 7 (2019) 22036–22043. **IF: 12.732.**

[21] B. Li, X. Yu*, X. Yu*, **R. Du**, L. Liu, Y. Zhang*, Graphene quantum dots decorated ZnO-ZnFe2O4 nanocages and their visible light photocatalytic activity, Appl. Surf. Sci. 478 (2019) 991–997. **IF: 6.707.**

[22] J. Li, Z. Luo, F. He, Y. Zuo, C. Zhang, J. Liu, X. Yu, **R. Du**, T. Zhang, M.F. Infante-Carrió, A.Cabot*, Colloidal Ni–Co–Sn nanoparticles as efficient electrocatalysts for the methanol oxidation reaction, J. Mater. Chem. A. 6 (2018) 22915–22924. **IF: 12.732.**

[23] C. Zhang, J.J. Biendicho, T. Zhang, **R. Du**, J. Li, X. Yang, J. Arbiol, Y. Zhou*, J.R. Morante, A. Cabot*, Combined high catalytic activity and efficient polar tubular nanostructure in urchin-like metallic $NiCo_2Se_4$ for high‑performance lithium–sulfur batteries, Adv. Funct. Mater. 29 (2019) 1903842. **IF: 18.808.**

[24] D. Yang, C. Zhang, J.J. Biendicho, X. Han, Z. Liang, **R. Du**, M. Li, J. Li, J. Arbiol, J. Llorca, A. Cabot*, ZnSe/N-doped carbon nanoreactor with multiple adsorption sites for stable lithium–sulfur batteries, ACS Nano. 14 (2020) 15492–15504. **IF: 15.881.**

[25] C. Xing, Y. Liu, Y. Zhang, J. Liu, T. Zhang, P. Tang, J. Arbiol, L. Soler, K. Sivula, N. Guijarro, **R. Du**, A. Cabot*, J. Llorca*, Porous $NiTiO_3/TiO_2$ nanostructures for photocatalytic hydrogen evolution, J. Mater. Chem. A. 7 (2019) 17053–17059. **IF: 12.732.**

[26] W. Tong, Y. Zhang*, H. Huang, K. Xiao, S. Yu, Y. Zhou, L. Liu, H. Li, L. Liu, T. Huang, **R. Du**, Q. An*, A highly sensitive hybridized soft piezophotocatalyst driven by gentle mechanical disturbances in water, Nano Energy. 53 (2018) 513–523. **IF: 17.881.**

Annex

Upscaling high activity oxygen evolution catalysts based on CoFe$_2$O$_4$ nanoparticles supported on nickel foam for power-to-gas electrochemical conversion with energy efficiencies above 80%

Félix Urbain[a], Ruifeng Du[a,*], Pengyi Tang[a,b], Vladimir Smirnov[c], Teresa Andreu[a,d], Friedhelm Finger[c], Nuria Jimenez Divins[e], Jordi Llorca[e], Jordi Arbiol[b,f], Andreu Cabot[a,f], Joan Ramon Morante[a,g]

[a] IREC, Catalonia Institute for Energy Research, Jardins de les Dones de Negre 1, 08930, Sant Adrià de Besòs, Barcelona, Catalonia, Spain
[b] Catalan Institute of Nanoscience and Nanotechnology (ICN2), CSIC and BIST, Campus UAB, Bellaterra, 08193, Barcelona, Catalonia, Spain
[c] IEK-5 Photovoltaik, Forschungszentrum Jülich, D-52425, Jülich, Germany
[d] Universitat Politècnica de Catalunya, Jordi Girona 1–3, 08034, Barcelona, Catalonia, Spain
[e] Institute of Energy Technologies, Department of Chemical Engineering and Barcelona Research Center in Multiscale Science and Engineering, Universitat Politècnica de Catalunya, EEBE, 08019, Barcelona, Spain
[f] ICREA, Pg. Lluís Companys 23, 08010, Barcelona, Catalonia, Spain
[g] Universitat de Barcelona, Martí i Franquès, 1, 08028, Barcelona, Catalonia, Spain

ARTICLE INFO

ABSTRACT

We investigate cobalt ferrite nanoparticles (NPs) supported on large-scale electrodes as oxygen evolution reaction (OER) catalysts. Colloidal CoFe$_2$O$_4$ NPs were loaded on low-cost and high surface area nickel foam (NF) scaffolds. The coating process was optimized for large electrode areas, ensuring a proper distribution of the NPs on the NF that allowed overcoming the electrical conductivity limitations of oxide NPs. We were able to produce CoFe$_2$O$_4$-coated NFs having 10 cm^2 geometric surface areas with overpotentials below 300 mV for the OER at a current density of 50 mA/cm^2. Such impressively low overpotentials suggested using CoFe$_2$O$_4$ NP-based electrodes within a water electrolysis device. In this prototype device, stable operating currents up to 500 mA at remarkably low cell-voltages of 1.62 and 1.53 V, at ambient and 50 °C electrolyte temperatures, respectively, were reached during operation periods of up to 50 h. The high electrochemical energy efficiencies reached at 50 mA/cm^2, 75% and 81% respectively, rendered these devices particularly appealing to be combined with low-cost photovoltaic systems for bias-free hydrogen production. Therefore, CoFe$_2$O$_4$ NP-based electrolysers were coupled to low-cost thin-film silicon solar cells with 13% efficiency to complete a system that afforded solar-to-fuel efficiencies above 10%.

1. Introduction

The development of cost-effective large-scale electrodes for highly active and stable oxygen evolution reaction (OER) catalysis is an essential step toward reaching commercial viable solutions for electrochemical water and CO$_2$ reduction [1]. The OER is a complex multi-step reaction that starts with an OH coordination or H$_2$O dissociation step in basic or acidic electrolytes, respectively, to form OH*, where (*) represents an active site at the surface of the catalyst [2]. OH* is subsequently decomposed to O*, which reacts with another adsorbed H$_2$O/OH to form OOH*. In a last step OOH* is deprotonated to O$_2$, which is finally released. This complex reaction is kinetically less favored than

the concomitant hydrogen evolution reaction (HER), mainly due to the demanding formation of oxygen double bonds and the associated multi-electron transfer step. Due to its complexity, few catalysts have demonstrated high enough OER activities for commercially relevant application. Commercial electrolysis systems currently rely on expensive and scarce elements such as iridium and ruthenium [3], since alternative low-cost catalysts suffer from unpractical high overpotential losses to provide high enough currents (> 200 mA), what makes them not competitive with alternative H$_2$ production pathways [4–6].

In recent years, potentially cost-effective catalysts based on transition metal oxides not relying on Pt-group metals have demonstrated high current water electrolysis at operation voltages below 1.6 V [7,8].

However, most of these studies have been limited to small-scale electrodes or have relied on costly and energy-intensive deposition methods. These studies consequently lack of the scalability feature, which is crucial for commercial application. Against this backdrop, the present study is dedicated toward the realization of a prototype electrolyser utilizing a potentially low-cost, scalable and high throughput process for the realization of high-performing and environmentally friendly OER catalysts on large-scale electrode scaffolds.

Among non-noble OER catalysts, some spinel-type binary transition metal oxides (AB_2O_4, A, B = metal) come to the fore owing to their high abundance, low toxicity, rich redox chemistry and chemical robustness [9–11]. Besides, bimetallic catalysts offer additional degrees of freedom compared to elemental compositions, enabling further optimization of active sites towards OER catalytic steps. Among these bimetallic oxide catalysts, Co-Fe spinel compounds are a particularly interesting case of a highly abundant and potentially low-cost material that shows excellent activity toward water oxidation [12–18].

While oxides offer high electrochemical stability, they usually suffer from intrinsically inferior electrical conductivities. To circumvent this issue and at the same time maximize the density of potential catalytic sites, oxide nano-domains need to be evenly distributed through the surface of a highly conductive scaffold that facilitates the charge transfer of the conjoint OER system. However, previous studies on $CoFe_2O_4$ particles loaded on high surface area scaffolds, such as doped carbon nanofibers [15] or hematite nanorods [19], were limited to laboratory-scale applications due to the complexity and high cost of the utilized synthesis routes and the difficulties that supporting such particles onto a large area three-dimensional (3D) scaffold involve [20].

Herein, we developed a potentially low-cost, scalable, high throughput and high yield method to produce $CoFe_2O_4$ ferrite nanoparticles (NPs). Additionally, we optimized the loading of the active NPs on large-scale Ni foams (NFs), as highly conductive, 3D and cost-effective electrode scaffold. Following the optimization of the loading process and the loaded amount of NPs, electrodes based on NFs coated with $CoFe_2O_4$ NPs were tested in a three-electrode set-up, as well as in a scaled-up two-electrode prototype electrolysis system to assess their viability for high yield H_2 production. We provide evidence that the used strategy bears great benefits regarding scalable preparation of high surface area and high activity catalysts. Additionally, we demonstrate the distribution and loading of oxide NPs to have a strong influence on the OER performance. Furthermore, we assessed the versatility of the presented system to be combined with renewable power sources by coupling the electrolyzer to a thin-film silicon solar cell for bias-free solar water splitting. Overall, the presented results set a new benchmark performance for transition metal oxides anchored on large-scale electrode support for the OER. These results will contribute to push the frontier of the field of environmentally friendly processes and

electrodes for commercially viable water electrolysis [21], electrochemical alcohol oxidation [22], waste water treatment [23], or nitrate reduction systems [24].

2. Experimental section

2.1. Chemicals and materials

Cobalt(II) acetylacetonate ($Co(acac)_2$, 97%, Sigma-Aldrich), Iron acetylacetonate ($Fe(acac)_3$, 97% Sigma-Aldrich), oleylamine (OAm, 80–90%, TCI), oleic acid (OAc, Sigma-Aldrich), Nafion (10 wt%, perfluorinated ion-exchange resin, dispersion in water), methanol (anhydrous, 99.8%, Sigma-Aldrich), carbon black (CB, VULCAN XC72), potassium hydroxide (KOH, 85%, Sigma-Aldrich), tetrafluoroboric acid (HBF_4, 48% Gew in H_2O Sigma-Aldrich) and acetonitrile (CH_3CN, extra dry, Fisher) were used as received without any further treatment. Chloroform, hexane, acetone, and ethanol were of analytical grade and purchased from various sources. Milli-Q water was obtained from a PURELAB flex from ELGA. An argon-filled glove box was used for storing and handling sensitive chemicals.

2.2. Synthesis of colloidal $CoFe_2O_4$ nanoparticles

All the syntheses were performed using standard airless techniques, i.e. a vacuum/dry argon gas Schlenk line. $CoFe_2O_4$ NPs were synthesized by loading 1.0 mmol of $Fe(acac)_3$, 1 mmol of $Co(acac)_2$, 10 ml OAm and 1.0 ml OAc in a three-neck flask and degassed under vacuum at 80 °C for 1 h while being strongly stirred using a magnetic bar. Subsequently, the reaction flask was heated to 230 °C and maintained for 30 min, while continuously adding nitrogen into the flask. A visible color change was observed immediately (see Scheme 1). The obtained NPs were collected by centrifuging and washing the solid product with acetone and hexane three times. The as-prepared NPs were finally dispersed in hexane with a concentration of 10 mg/mL and stored for further use. NPs were colloidally stable in chloroform for a couple of weeks.

2.3. Ligand removal

In a typical process, 10 mL of $CoFe_2O_4$ NPs dispersion in hexane (10 mg/mL) was combined with 10 mL acetonitrile to form a two-phase mixture and then a 1 mL HBF_4 solution (48%) was added. The resulting solution was sonicated until the NPs transferred from the upper to the bottom layer. The surface modified NPs were washed with ethanol for three times and dispersed in 10 mL ethanol with a small amount of DMF for further use.

2.4. Coating of Ni foam

2.4.1. Drop casting

Ni foam was sonicated in acetone, 1 M HCl, Milli-Q water, and ethanol respectively. 50 μL of 10 mg/mL CoFe₂O₄ ethanol solution was dropped on nickel foam and dried in air and subsequently annealed at 400°C under nitrogen atmosphere.

2.4.2. Dip coating

Ni foam was sonicated in acetone, 1 M HCl, Milli-Q water, and ethanol respectively. In a typical process, clean and dry nickel foam was immersed in 10 mg/mL of CoFe₂O₄ ethanol solution for 2 s and then taken out quickly and dried in air. This process was repeated for 1, 3, 5, and 7 times and donated as 1 dip, 3 dips, 5 dips and 7 dips, respectively. The coated NFs were subsequently annealed at 400 °C under nitrogen atmosphere. After 3 dips the CoFe₂O₄ NP loading was 3.3 mg, about 1.15 mg/cm^2. (Fig. S5).

2.5. Characterization

Structural characterization was carried out by X-ray diffraction (XRD). The samples were scanned from $2\theta = 20°$ to $80°$ at a rate of 0.02 s^{-1} in Bragg–Brentano geometry. The diffractometer was equipped with a Cu Kα (1.54051 Å) radiation source. The morphology of the as deposited foam-based electrodes was observed using a scanning electron microscope (SEM) and elemental analysis was performed by the same microscope equipped with an X-ray energy dispersive spectrometer (EDS). The samples for transmission electron microscopy (TEM) were prepared by scratching the as-prepared CoFe₂O₄ powders from the Ni foam substrate, followed by dispersing them in hexane and collecting them on the TEM copper grids. High resolution transmission electron microscopy (HRTEM) images and scanning transmission electron microscopy (STEM) studies were conducted by using an FEI Tecnai F20 field emission gun microscope operated at 200 kV with a point-to-point resolution of 0.19 nm, which is equipped with high angle annular dark field (HAADF) and electron energy loss spectroscopy (EELS) detectors. X-ray photoelectron spectroscopy (XPS) was done on a SPECS system equipped with an Al anode XR50 source operating at 150 mW and a Phoibos 150 MCD-9 detector. The pressure in the analysis chamber was below 10^{-7} Pa. The area analyzed was about 2 mm × 2 mm. The pass energy of the hemispherical analyzer was set at 25 eV and the energy step was set at 0.1 eV. Data processing was performed with the CasaXPS program (Casa Software Ltd., UK). Binding energy values were centered using the C 1s peak at 284.8 eV. Fourier transform infrared (FTIR) spectra were recorded on an Alpha Bruker spectrometer

The electrochemical performance of CoFe₂O₄@NF electrodes towards OER reduction was assessed using a three-electrode set-up. A leak-free Ag/AgCl 3.4 M KCl reference electrode (RE) was assembled in the polytetrafluoroethylene (PTFE) frame of the cell and placed very close to the working electrode surface. The potential was transformed to the reversible hydrogen electrode (RHE) scale: $E (V_{RHE}) = E (V_{Ag/AgCl}) + 0.0592 \times pH + 0.197$. The data presented for the electrochemical characterization in aqueous solutions in three-electrode configuration do not include compensation for the series resistance of the solution. For the complete electrolyzer characterization, an adapted flow cell set-up (Micro Flow Cell, Electrocell A/S) was employed, schematically depicted in Fig. 7a. The flow rates of electrolytes within the flow cell were kept at 20 ml/min. As illustrated in Fig. 7a, the electrolyte was directly introduced through the macroporous 3D CoFe₂O₄@NF electrode (geometric surface area: 10 cm^2). For details on the cyclic voltammetry (CV) and gas chromatography (GC) regarding the assessment of current-voltage behavior and the faradaic efficiency for gaseous products, respectively, the reader is referred to Ref. [41] and Ref. [42]. The electrically attached triple junction thin-film silicon device had an area of 1 cm^2, thus during the photoelectrolysis measurement an area of 1 cm^2 was illuminated. All photoelectrochemical

experiments were conducted using a solar simulator equipped with a 150 W xenon lamp. The intensity of the light source was adjusted to match standard AM 1.5 G sunlight at 100 mW/cm^2 intensity. The experiments for the full system assembly were carried out in a two-electrode configuration. The faradaic efficiency to H₂ was calculated using the analysis of the outlet gas by gas chromatography (GC) during potentiostatic measurements. Helium (99.999%) was used as the carrier gas. The calibration of peak area vs. gas concentration was used for the molar quantification of each gaseous effluent. The faradaic efficiency was calculated by determining the number of coulombs needed for each product and then dividing by the total charge passed during the time of the GC sampling according to the flow rate. In the photovoltaic-electrolyzer coupled system, to account for deviations in the assessment of the photovoltaic performance of the complete system, i.e. spectra variations due to diode calibration accuracy, area definition, or temperature variation, a systematic error of 2% was considered [25].

3. Results

3.1. Synthesis and characterization of colloidal CoFe₂O₄ NPs

Co-Fe oxide NPs were produced in colloidal form from the reduction of cobalt and iron salts in the presence of OAm and OAc and the posterior oxidation of the reaction product in ambient conditions (Scheme 1, see Experimental Section for details). A representative TEM micrograph and the size distribution histogram of the oxidized NPs are shown in Fig. 1a. Co-Fe oxide NPs displayed a quasi-spherical geometry, with an average diameter of 7.1 ± 0.1 nm. In contrast to the product of the oxidation of iron NPs, the oxidation of Co-Fe NPs did not result in the formation of hollow structures, probably due to the relatively low diffusivity of Fe and Co through the growing Co-Fe oxide shell compared with that of Fe though FeO/γ-Fe₂O₃ [26–28].

XRD analysis revealed Co-Fe oxide NPs to crystallize in the CoFe₂O₄ cubic phase (JCPDS *22-1086*, Fig. 1b). HRTEM micrographs confirmed the crystal structure of the NPs to be compatible with the CoFe₂O₄ ferrite cubic phase ([FM3-MZ]-Space group 227) with lattice parameters a = b = c = 0.83961 nm (Fig. 2b). HAADF-STEM and EELS analysis demonstrated the three constituent elements, Co, Fe, and O, to be present in the same ratio in all NPs and to be homogeneously distributed within each NP (Fig. 2a).

N₂ adsorption–desorption isotherms of the CoFe₂O₄ NPs dried in the form of a powder displayed a type-I reversible behavior (Fig. 3), which is generally a signature of microporous solids [29]. CoFe₂O₄ nanopowders were characterized by a Langmuir specific surface area (SSA) of 276 m^2/g and a Brunauer–Emmett–Teller (BET) SSA of 174 m^2/g. The obtained BET SSA is among the highest reported for Co-Fe spinel NPs, slightly above that of NPs synthesized by hydrothermal [13] and micro emulsion techniques [20] (˜150 m^2/g), and significantly higher than materials prepared by electrospinning [15] and electrodeposition [16] (˜55 m^2/g). Notice that these high SSAs were measured from the nanopowders obtained by drying the colloidal NPs in ambient conditions and with no pre-coordination of the NP into a network. Even larger SSA values would be potentially obtained through the formation
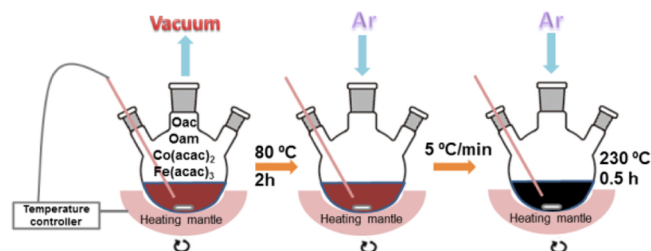
Scheme 1. Schematic illustration of the synthesis procedure used to prepare colloidal CoFe₂O₄ NPs.
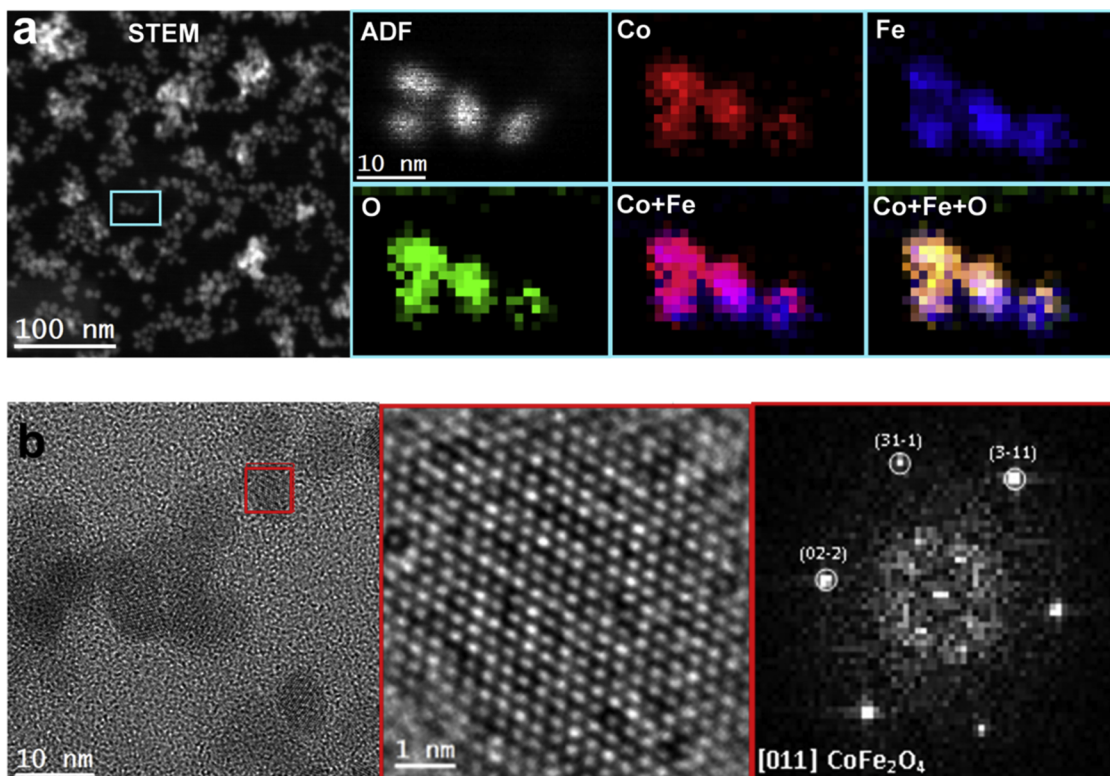
Fig. 2. a) HAADF-STEM micrograph and EELS chemical composition maps (from cyan rectangle) for Co (red), Fe (blue), O (green) and their composites. b) HRTEM micrograph, detail of the red squared region (scale bar, 1 nm), and corresponding FFT spectrum indicating that NPs crystallized in the cubic $CoFe_2O_4$ phase, [FM3-MZ]-Space group 227, with lattice parameters of a = b = c = 0.83961 nm, and $\alpha = \beta = \gamma = 90°$. (For interpretation of the references to colour in this figure legend, the reader is referred to the web version of this article).
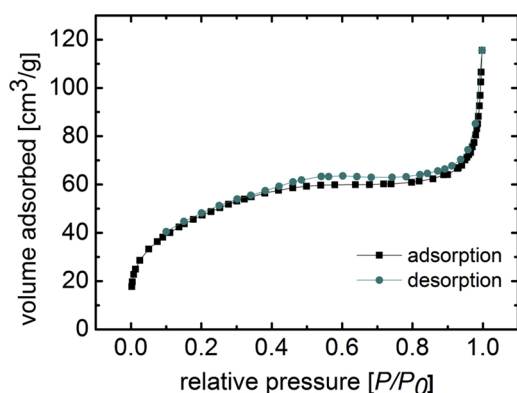

Fig. 3. N_2 adsorption–desorption isotherms from the $CoFe_2O_4$ nanopowders obtained from drying $CoFe_2O_4$ NPs under ambient conditions.

of NP networks in solution, i.e. NP gelation, and the posterior drying from supercritical CO_2 for instance [30,31].

3.2. Loading on large-scale Ni foams

The optimized loading of nano-sized OER catalysts onto large-scale scaffolds is an important step toward the realization of industry-viable electrodes and electrolyzers. In this direction, we first studied the deposition of NPs on small (1 cm^2) NF electrodes and subsequently optimized the deposition process for larger scaffolds ($\geq$ 10 cm^2). Before deposition, organic ligands at the surface of as-synthesized NPs, which were used to adjust NP growth during the synthesis, were removed using a solution of tetrafluoroboric acid in acetonitrile (see Experimental Section). After successive cleaning with tetrafluoroboric acid, FTIR spectra showed the disappearance of the peaks at 2822 and

2890 cm^{-1} corresponding to CH— stretching modes, what evidenced the effective removal of hydrocarbon ligands (Fig. S3). This ligand displacement step is key towards producing high performance and reliable electrocatalyts since generally organic ligands strongly limit electronic transport and the ability of the NPs to interact with their surrounding media, i.e. with the scaffold and the electrolyte [32]. Furthermore, in the present case, the presence of organic ligands on the surface of the $CoFe_2O_4$ NPs impeded a homogeneous coating of the NF. Not mediating a ligand removal pretreatment, a porous two-dimensional organic film was deposited on the NF after dip coating it into a suspension of colloidal NPs (Fig. S2).

Two procedures were explored to support $CoFe_2O_4$ NPs on NFs: dip coating and drop casting. As depicted in Fig. 4a, the foam was either dipped into the dispersion of colloidal NPs and hold for 2 s or the suspension was dropped onto the foam (2 mg of solution) and let it dry. SEM characterization showed the dip coating process to result in a homogeneous distribution of NPs on the NF surface. On the other hand, drop-casted NFs displayed numerous NP agglomerates.

XPS survey spectrum of the $CoFe_2O_4$ NPs supported on the NF (3 dips) demonstrated the presence of Co, Fe, O, and Ni (Fig. S6). The Co 2p and Fe 2p spectra matched well with Co^{2+} and Fe^{3+} [33,34] and the O 1s spectrum displayed two peaks at about 531.1 and 532.4 eV which corresponded to oxygen in the metal-oxygen bond and hydroxyl groups, respectively [35]. Quantitatively, XPS analysis showed the atomic concentration of Fe on the surface to be a threefold of that of Co: Fe/Co = 3 (Table S1). Additionally XPS analysis showed a large surface Ni concentration, ca. 50 at% of the surface composition (Table S1). XRD and HRTEM analysis of the NPs after the annealing step, showed the $CoFe_2O_4$ crystal structure to be maintained (Figs. S8 and S9). SEM-EDX analysis showed a homogeneous distribution of the different elements on the NF (Fig. S10).

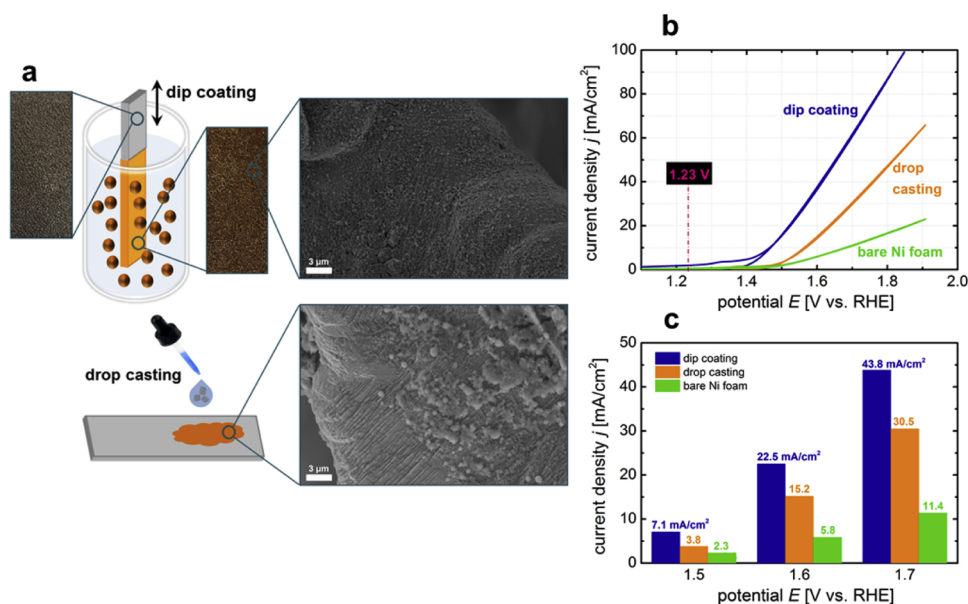The electrochemical performance toward OER of NFs loaded with

Fig. 4. a) Schematic illustration of the two tested coating techniques for the $CoFe_2O_4$ NPs on the NF (1 cm^2 geometric area): dip coating and drop-casting, including photographs of the NF before and after the coating processes, as well as SEM images showing the distribution of the deposited NPs on the NF. b) CV curves of the NF coated with $CoFe_2O_4$ NPs by dip coating and drop casting, respectively, compared with bare NF. Measurements were conducted in 1 M KOH at a scan rate of 10 mV/s. c) Current densities achieved at different applied potentials.

$CoFe_2O_4$ NPs (hereafter $CoFe_2O_4$@NF) is shown in Fig. 4b. In comparison with bare NF, used in industrial water splitting, $CoFe_2O_4$@NF electrodes displayed significantly enhanced OER catalytic activities. $CoFe_2O_4$@NF electrodes provided much higher current densities under the same applied potential than bare NF (Fig. 4c). In addition, $CoFe_2O_4$@NF electrodes prepared by dip coating provided higher performance over electrodes prepared by drop casting. This result was consistent with the usual assumption that thinly dispersed oxide nanoparticles favor electrochemical performance. A significant increase in the current density for potentials > 1.5 V was measured for samples prepared by dip coating, attaining 43.8 mA/cm^2 at 1.7 V_{RHE} (470 mV overpotential), which is 1.4 times higher than the current density obtained with the drop casted sample (Fig. 4b).

The dip coating technique was further optimized for large area electrodes (10 cm^2). Fig. 5 presents SEM images of the NF surfaces after 1, 3, 5, and 7 dips (each hold for 2 s) into the $CoFe_2O_4$ NP suspension. After 1 dip, major parts of the NF remained uncovered, whereas 3 dips resulted in a high coverage of the NF surface with highly dispersed NPs

(Fig. S4). Increasing the number of dips to 5 led to the formation of NP aggregates with sizes ranging from 50 to 200 nm (Fig. 5). This effect was even more pronounced after 7 dipping times, resulting in an almost complete coverage of the NF surface by $CoFe_2O_4$ NP agglomerates.

The electrochemical characteristics of the large-scale $CoFe_2O_4$@NF electrodes were assessed in a three-electrode configuration using 1 M KOH electrolyte solution (see Experimental Section). Fig. 6a shows the CV curves of the electrode samples investigated in Fig. 5. The number of dip coating steps had a significant influence on the OER performance. Best performances were achieved with $CoFe_2O_4$@NF electrodes produced using 3 dip coating steps, in good agreement with the observed homogeneous coverage of the NF surface with thinly dispersed NPs. OER overpotentials of the four tested samples for different current densities are shown in Fig. 6b. $CoFe_2O_4$@NF electrodes produced after 3 coating steps exhibited the lowest overpotentials, with 250 mV and 460 mV for 10 mA/cm^2 and 50 mA/cm^2, respectively. Higher $CoFe_2O_4$ NP loads containing NP agglomeration provided lower OER performance. This result is understandable as oxide structures generally suffer
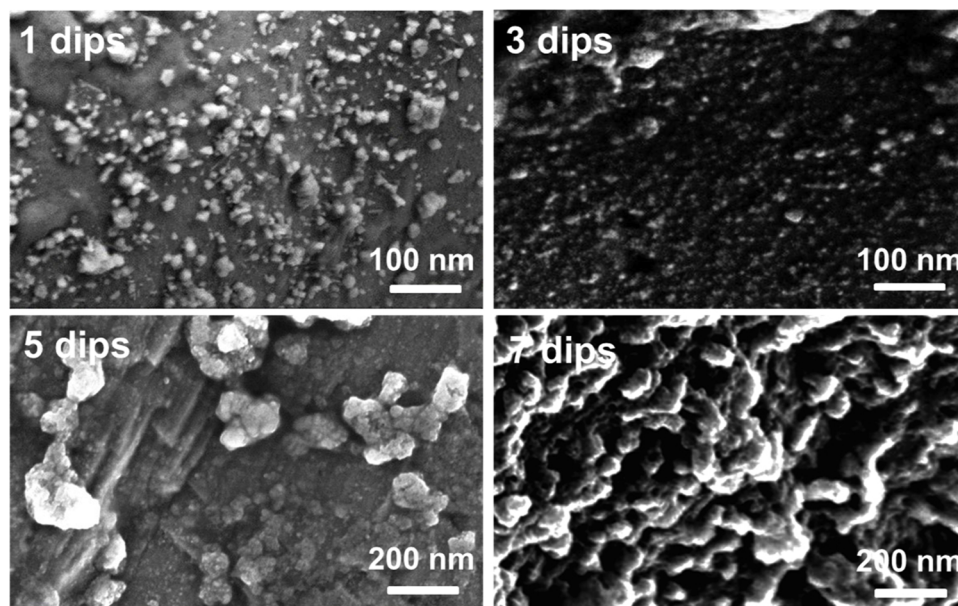

Fig. 5. SEM micrographs of $CoFe_2O_4$@NF electrodes (10 cm^2) produced using different dip coating steps: 1, 3, 5, and 7 as noted in each micrograph.
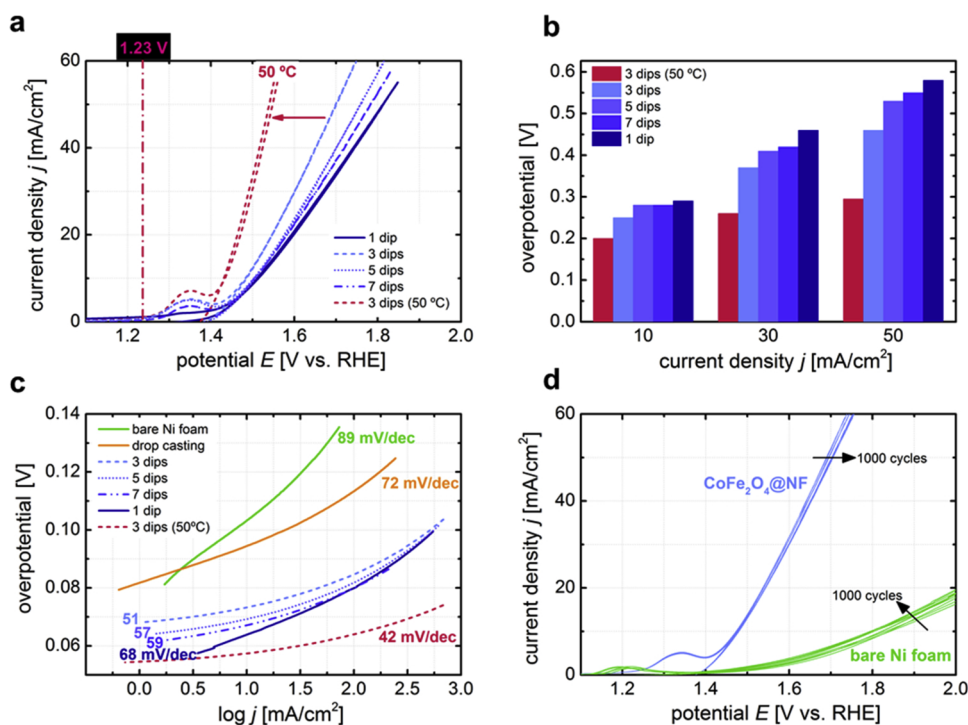
Fig. 6. a) CV curves of NF electrodes dipped into the CoFe$_2$O$_4$ NP solution, for 1 (solid), 3 (dashed), 5 (dotted), and 7 (dash-dotted) times. CV curves were measured in 1 M KOH at a scan rate of 10 mV/s. CoFe$_2$O$_4$@NF electrodes providing best OER catalytic performances (3 dips) were measured under elevated electrolyte temperature (50 °C, pink dashed line). The H$_2$O/O$_2$ oxidation potential is indicated by the straight dash-dotted line. b) Required overpotentials derived from CV curves at different current densities. c) Tafel plots of the tested samples. d) CV curves of the CoFe$_2$O$_4$@NF (3 dips) and bare NF electrodes, respectively, before and after 1000 cycles. Every 200th CV scan of each electrode is plotted.

from low electrical conductivities, which strongly limits the thickness of the oxide layer that can be practically used. The highest overpotential of 580 mV at 50 mA/cm^2 was measured for the 1 step coating CoFe$_2$O$_4$@NF electrode, presumably due to an insufficient coverage of the scaffold with CoFe$_2$O$_4$ NPs (Fig. 5).

Commercial alkaline electrolyzers work at operating temperature between 25 and 100 °C, which is why we tested the best performing electrode (3 dips) also under elevated electrolyte temperature. As observed in Fig. 6a and b, the OER performance was significantly enhanced by increasing the electrolyte temperature up to 50 °C. Extremely low overpotentials of 200 mV and 295 mV for 10 mA/cm^2 and 50 mA/cm^2, respectively, were obtained. Fig. S12 show results obtained for 4 additional samples in the same conditions, demonstrating the reproducibility of our procedure. Temperature has a strong influence on the thermodynamic and kinetic functions, including electronic, ionic and molecular diffusion. Increasing temperature can accelerate the reaction kinetics, improve diffusion, disturb the electrochemical double layer and increase the electrical conductivity of the electrolyte solution, among other, all of them having an important and beneficial influence on the OER performance [36–38].

We further compared the performance of the CoFe$_2$O$_4$@NF electrodes with that of other electrodes prepared from supporting the CoFe$_2$O$_4$ on other substrates, including Cu foam and carbon cloth (Fig. S13). The incorporation of the CoFe$_2$O$_4$ NPs on any of the substrates significantly reduced their overpotential. Among the different substrates, CoFe$_2$O$_4$@NF electrodes achieved the best performance, with an overpotential down to 250 mV at 10 mA/cm^2. Such value is below that of most of state-of-the-art OER electrodes in literature, evidencing the high potential for commercial applications of the herein developed large-scale CoFe$_2$O$_4$@NF OER electrodes. State-of-the-art electrocatalytic properties toward OER of previously reported Co-Fe and NF-based electrodes are summarized in Table S2 in the SI.

The electrocatalytic kinetics for OER of the CoFe$_2$O$_4$@NF electrodes were further investigated by Tafel plots (Fig. 6c). For comparison, the Tafel plots of the sample prepared by drop casting and the bare NF sample are also shown in Fig. 6c. In accordance with the results shown in Fig. 4b and c, the drop casted and the bare NF electrodes exhibited the worst kinetics among the analyzed electrodes, i.e. the highest Tafel

slopes, at 89 mV/dec and 72 mV/dec, respectively. For the CoFe$_2$O$_4$@NF electrodes prepared by dip coating, Tafel slopes were impressively low and ranged from 68 mV/dec for the 1 time dipped sample to 51 mV/dec for the 3 times dipped electrode. Hence, our CoFe$_2$O$_4$@NF electrodes showed comparable and even better electrocatalytic properties toward OER than related nonprecious metal-based OER electrocatalysts reported in literature (Table S1 of the SI). The CoFe$_2$O$_4$@NF electrode measured in a 50 °C alkaline solution provided the lowest Tafel slope, 42 mV/dec, as could be expected from the corresponding CV curve in Fig. 6a. In fact, such an outstanding kinetic behavior made it an ideal anode candidate for commercial electrolysis systems.

XPS analysis of the electrodes after long term cycling showed no significant difference in the chemical environment of Co and Fe with respect to the results obtained from electrodes after annealing (Fig. S7). However, quantitatively, after long term cycling the amount of Fe detected on the electrode surface was significantly lower from the initial Fe/Co = 3 to the final Fe/Co = 0.5 (Table S1). In parallel, the concentration of Ni significantly increased, from 50 at% to up to an 80 at% (Table S1). On the other hand, SEM-EDX analysis showed a similar Co and Fe concentration on top of the NF. We hypothesize that during cycling a significant amount of Ni from the NF is able to diffuse within the CoFe$_2$O$_4$ structure and to accumulate, together with Co, on the NP surface, partially displacing Fe ions. The presence of these Ni ions on the catalyst surface may contribute to the outstanding performance obtained from CoFe$_2$O$_4$@NF electrodes compared with other supports and literature results (Fig. S13 and Table S2)

Besides electrochemical performance, durability is another major parameter in the realization of industry-viable electrodes for electrolyzers. In this direction, we investigated the long-term stability for CoFe$_2$O$_4$@NF electrodes (3 dips) by cycling them 1000 times in 1 M KOH at ambient temperature (Fig. 6d). Again, bare NF was utilized for comparison. CoFe$_2$O$_4$@NF electrodes showed a negligible degradation after continuous 1000 CV cycles, indicating its superior operational stability under alkaline test condition. XPS and XRD analysis of the material after long term cycling (Figs. S7 and S8) also showed the chemical environment of Co and Fe and the crystal structure of the NPs to remain unmodified. The mechanical and structural stability was further confirmed by HRTEM analysis of the used catalyst, showing the

$CoFe_2O_4$ NPs to remain thinly dispersed onto the NF and maintaining their size after the long-term experiment (Fig. S9). No obvious NP aggregation/growth was observed, which was associated to the proper immobilization of the $CoFe_2O_4$ NP on the NF. Consistently with previous reports, bare NF slightly increased its activity towards OER with time (Fig. 6d). In alkaline solution, this activity enhancement has been associated to the contribution to the catalytic activity of metallic impurities (e.g. Fe) from the electrolyte that are deposited onto the Ni surface during long-term operation [40]. Because such a behavior was not observed with $CoFe_2O_4@NF$ electrodes, we assume that the Ni scaffold have a moderate catalytic role in this system.

We estimated the electrochemical active surface area (ECSA) of $CoFe_2O_4@NF$ (3 dips) and bare NF electrodes from the electrochemical double-layer capacitance (Cdl) at the solid/liquid interface [41]. Figs. S14a and S14b (SI) present the CV curves of the two electrodes recorded in a non-Faradic potential range under different scan rates. $CoFe_2O_4@$ NF cathodes exhibited a higher Cdl than bare NF, evidencing a higher active surface area, which was estimated as 80.5 cm^2 for $CoFe_2O_4@NF$ and 31.0 cm^2 for bare NF (Fig. 6c). This result probes the CoFe2O4@NF to provide a larger number of catalytically active sites and thus an improved OER activity, much higher than that of $CoFe_2O_4$ NPs on carbon nanofibers (20.6 cm^2) and commercial RuO_2 catalyst (14.5 cm^2) [15].

3.3. Prototype electrolysis reactor

The optimized large-scale $CoFe_2O_4@NF$ electrode was subsequently integrated in a prototype electrolysis reactor [41–44]. As illustrated in Fig. 7a, the reactor design allowed to work under flow conditions, where the anolyte and catholyte solutions are continuously recirculated through the respective compartments, i.e. a $CoFe_2O_4@NF$ anode compartment performing the OER and a Ti/Pt cathode compartment performing the hydrogen evolution reaction (HER). By this design, the flow dynamics of the electrolysis set-up could be significantly enhanced, fostering higher electrochemical activity. Both compartments were separated by a membrane and a gas chromatograph was employed for gaseous product identification. The configuration can even be adapted for the additional integration of photovoltaic devices, as shown in Fig. 7a with a thin-film silicon solar cell (see Experimental Section for details).

The characteristics of the complete reactor in two-electrode operation are shown in Fig. 7b for two different configurations. The first configuration consisted in using a cation-exchange membrane (Nafion ®117) and 1 M KOH electrolyte solution in both compartments. In the second configuration, we applied a bipolar membrane (BPM), enabling to operate the electrolysis reactor with two different electrolytes. In this configuration, we applied a 1 M KOH (pH = 13.7) for the anolyte to perform the OER and a 1 M H_2SO_4 (pH = 0) solution for the catholyte to perform the HER. As can be seen from the linear sweep voltammetry (LSV) curves in Fig. 7b, the configuration using the BPM exhibited a better overall electrolysis behavior than the reactor configuration containing the Nafion membrane. To provide 200 mA and 400 mA, respectively, the BPM configuration only required 1.51 V and 1.59 V, respectively, whereas in the Nafion configuration the complete electrolyser cell voltage augmented to 1.60 V and 1.76 V, respectively. The higher cell voltage was related with the reduced electrochemical performance of the Ti/Pt cathode in alkaline solution (Nafion configuration) compared to its performance in acid electrolytes (BPM configuration). In Fig. S15, the LSV curves of Ti/Pt in 1 M KOH and 1 M H_2SO_4 electrolyte solution are shown. LSV curves displayed overpotentials of 340 mV and 180 mV at 50 mA/cm^2 for basic and acidic catholytes, respectively, further demonstrating the superior cathode performance in acidic medium. To simulate real electrolyser conditions, the overall polarization of the reactor device was also measured at elevated electrolyte temperatures (50 °C) in the BPM configuration. As expected from the results shown in Figs. 6a and S15, the electrochemical performance increased with increasing electrolyte temperature, reaching complete electrolyzer cell voltages of 1.46 V and 1.51 V to produce 200 mA and 400 mA, respectively. From these values, electrochemical energy efficiency up to 75% and 81%, for ambient and elevated operation temperatures were calculated. Consequently, the herein proposed electrolyzer based on a $CoFe_2O_4@NF$ electrode presents an attractive alternative to commercial systems used for surplus electric power storage, such as pumped hydroelectric storage (70–80%
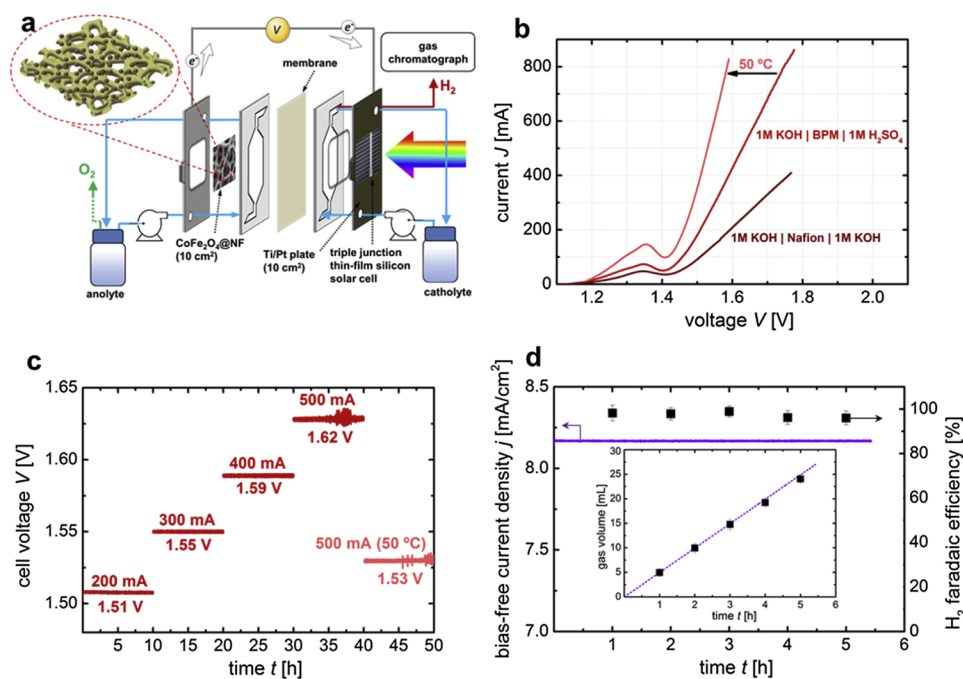

Fig. 7. a) Sketch of the experimental prototype reactor used to assess the overall electrolysis performance. The illustration shows the different components, including a schematic illustration of the 3D NF coated with $CoFe_2O_4$ NPs and the coupled triple junction thin-film silicon solar cell (a-Si:H/a-Si:H/μc-Si:H) for the bias-free operation test (see Fig. 7d). b) Linear sweep measurements of the $CoFe_2O_4@NF$ electrodes (10 cm^2 geometric area) combined with the Ti/Pt cathode (10 cm^2 geometric area) for a configuration containing Nafion and BPM membrane, respectively. The BPM configuration (best performing) was also measured at 50 °C electrolyte solution (1 M KOH). c) Long-term behavior of the electrolysis showing the required cell voltages of the reactor as a function of the applied current (each galvanostatic testing was conducted for ~10 h with the same electrodes and membrane). d) Bias-free solar water splitting using a triple junction a-Si:H/a-Si:H/μc-Si:H solar cell (as depicted in a)). Left y-axis shows the achieved bias-free current density over the operation time. Right y-axis represents the faradaic efficiency for H_2 production over the operation time. The error bars indicate standard deviations obtained from 3 experimental repeats. The inset shows the calculated gas volume obtained. The dotted purple line shows the theoretical (assuming 100% faradaic efficiency) gas evolution for the measured bias-free current density and the black squares show the experimental values. (For interpretation of the references to colour in this figure legend, the reader is referred to the web version of this article).

efficiency), power-to-gas based on alkaline and PEM electrolyzers (65–70% efficiency), or ion lithium batteries (92–95% efficiency) that have other severe limitation in terms of energy density, cost and life time.

The electrochemical durability of the prototype reactor was assessed by conducting chronoamperometry. Fig. 7c displays the electrolyzer cell voltages at successively increasing electrolysis currents of 200, 300, 400, and 500 mA applied for 10 h each, until a total of 50 h of continuous operation. The prototype electrolyzer showed no sign of decay when operated for 50 h, even when operated at higher temperature (50 °C).

Given its remarkable activity and high electrochemical energy efficiency, the prototype electrolysis reactor can be effectively powered by renewable energy sources, such as photovoltaics [25,42]. In this direction, the conversion of solar energy into chemical fuels energy is a promising route for future conversion and storage concepts. Solar-to-fuel conversion efficiencies using photovoltaics and electrolyzers depends on the efficiency of the two systems. Taking into account electrochemical conversion efficiency above 80% as reached for $CoFe_2O_4@$ NF electrodes, their combination with commercial high efficiency solar cells having 30% conversion efficiencies could result in 24% solar-to-fuel conversion efficiencies. However, in the present work, to achieve cost-effectiveness, we aimed at reducing the system cost using amorphous silicon solar cells. Thus, we electrically connected the prototype electrolyzer to a low-cost triple junction a-Si:H/a-Si:H/μc-Si:H solar cell with a photovoltaic conversion efficiency of around 13.4% (Fig. 7a.) [25]. In figure S16, the system current density-voltage (j-V) curve is overlaid with the polarization curve of the electrolyzer device. The crossing point of both j-V curves, which can serve to estimate the bias-free operation current density of the solar-driven electrolyzer, lied in the plateau region of the solar cell characteristics (near the maximum power point) at 1.45 V and 8.2 mA/cm^2. The bias-free measurement of the solar-driven electrolyzer is shown in Fig. 7d. This result demonstrates that the prototype electrolyzer can be powered only by sunlight energy, providing current densities up to 8.2 ± 0.2 mA/cm^2. The faradaic efficiency for H_2 production, measured by gas chromatography, was found to be close to 100% over the course of bias-free operation (> 5 h), as depicted on the right ordinate in Fig. 7d. The inset in Fig. 7d shows the theoretical and experimentally determined bias-free H_2 gas production over time, proving that H_2 was the only product formed during electrolysis (besides O_2). With these values, a solar-to-hydrogen conversion efficiency of 10.0 ± 0.2% was calculated, which is among the record bias-free water splitting efficiencies for thin-film silicon based devices [25,45,46]. Overall, this example demonstrates that electrolyzers based on $CoFe_2O_4@NF$ electrodes can match the stringent requirements for cost-effective renewable energy conversion and storage at large scale.

4. Discussion

The enhanced OER catalytic activity of the $CoFe_2O_4@NF$ electrodes here presented can be ascribed to the combination of nano-sized active $CoFe_2O_4$ particles with the 3D macroporous structure of the supporting NF, as illustrated in Fig. 7a. This marriage resulted in a significantly increased contact area between catalysts and electrolytes and provided a greater amount of active sites where OER could take place (see ECSA estimation in the SI, Figures S14c). The dip coating procedure eventually led to an optimum distribution of thinly dispersed $CoFe_2O_4$ NPs (Fig. 5), which allowed to circumvent the intrinsically inferior electrical conductivity of oxide particles (see low Tafel slopes in Fig. 6c), while ensuring an impressive stability of the $CoFe_2O_4@NF$ electrode (Figs. 6d and 7 c).

The large-scale electrode used, the high stability demonstrated and the low electrolyser cell voltages at industrial relevant currents and at ambient and elevated temperature probed the technology relevance of the present system. Values reported here are among the record

performance indices for overall water splitting using inexpensive and earth-abundant catalysts. Additionally, the present study assessed their performance on large-scale electrodes in a prototype electrolyzer. While the aspect of process scalability is vital in view of a real-world application, it has neither been experimentally evidenced, nor sufficiently discussed in previous related studies on OER materials (exemplarily see electrode areas in Table S1 in the SI). These previous studies focused on laboratory scale electrodes, neglecting critical issues, which have been addressed in the present study, such as homogeneous coverage of active electrocatalyst on large-scale scaffolds, higher chemical resistivity or low-cost and high throughput and yield processing techniques.

In general, the coupling of pure academic with engineered systems is urgently needed to mature renewable fuel production processes and open the pathway towards commercial application. This aspect is successfully addressed by the herein proposed system. In addition, the scalable process of the developed $CoFe_2O_4@NF$ electrode paired with the adaptability of the presented prototype reactor bears great benefits and cross-fertilization for a number of related catalytic and photovoltaic technologies. Thus, our electrolyzer concept is not limited to small active electrode areas [47,48] or expensive small-scale photovoltaic structures [49] but can be adapted to large scale designs. Nevertheless, from a scientific point of view, further attention should be devoted to investigate earth-abundant and active HER electrodes. The herein applied Ti/Pt plate served as stable and reliable proof-of-concept electrode, but could be replaced by a cathode system, which does not contain rare materials such as Pt. From a more engineering point of view, the evaluation of different approaches to upscale the photovoltaic structures up to the geometric size of the electrochemical active surface areas could be alluring if integrated photoelectrochemical cell (PEC) systems are envisaged. In this "PEC-farm" approach, multiple medium-scaled electrolyzers, i.e. electrolyzers similar to the herein presented prototype (10-100 cm^2 active photovoltaic and electrochemical electrode areas), could operate independently, while the produced fuels of all the electrolyzers would be collected together [50]. The advantageous feature of this concept is that lower photocurrent densities would be required, which would be beneficial regarding lower overpotential losses and thus, eventually higher overall solar-to-fuel efficiencies. In this regard, it is projected by techno-economic models of large scale, centralized solar H_2 production facilities that overpotential losses at high operating current densities are one of the most important factors in reducing the STH efficiency and thus, increasing the cost of H_2 [51,52].

In total, all these examples manifest the high versatility and cross-fertilization of the herein presented scalable $CoFe_2O_4@NF$ electrode and electrolysis system, respectively.

5. Conclusion

In conclusion, we have presented a simple and scalable colloidal synthesis and coating strategy for the homogeneous anchoring of bimetallic $CoFe_2O_4$ NPs on large-scale NF. $CoFe_2O_4@NF$ electrodes were demonstrated to be an efficient earth-abundant OER electrocatalysts with ultralow overpotential, large current density, small Tafel slope, and long-term durability in alkaline solution. The improved catalytic performances are believed to originate from the unique synergy between the nano-scaled active $CoFe_2O_4$ NPs and the highly conductive and high area Ni scaffold. The interdiffusion of Ni ions from the Ni scaffold to the $CoFe_2O_4$ NPs may also contribute to improve catalytic performance. Considering cost-effectiveness, facile, as well as reliable fabrication processes, and the outstanding catalytic performance of $CoFe_2O_4@NFs$ may hold great potential in future energy conversion and storage devices. Moreover, the performance of the large-scale $CoFe_2O_4@NF$ (10 cm^2 geometric active area) was investigated in a prototype electrolysis reactor, where currents of 500 mA were achieved with electrolyzer cell voltages of 1.62 V and 1.53 V at ambient and elevated temperatures, respectively, over prolonged operation times. Overall, the presented electrochemical results paired with the versatile

synthetic and coating strategy may stimulate future lines of work, which will be needed to address efficiency improvements and techno-economical questions while assessing cost competitiveness of promising (photo)-electrochemical technologies.

Author contributions

F.U., J. R. M. and A.C. conceived the project and designed the experiments. F.U. carried out the (photo)-electrochemical experiments. R.D. conducted the synthesis and coating of the Ni foam. P.Y.T., R.D. and J.A. conducted the structural and compositional analyses. F.U., R.D. and P.Y.T. interpreted data. F.U. wrote the manuscript. V.S. and F.F. performed and supervised the deposition of the multijunction thin-film silicon solar cells. J.R.M. T.A. and A.C. supervised the proposed and executed research program. All the authors participated in discussions and contributed to editing of the manuscript.

Declaration of Competing Interest

The authors declare no conflict of interest.

Acknowledgments

Appendix A. Supplementary data

Supplementary material related to this article can be found, in the online version, at doi:https://doi.org/10.1016/j.apcatb.2019.118055.

References

[1] S.B. Walker, U. Mukherjee, M. Fowler, A. Elkamel, Benchmarking and selection of Power-to-Gas utilizing electrolytic hydrogen as an energy storage alternative, Int. J. Hydrogen Energy 41 (2016) 7717–7731, https://doi.org/10.1016/J.IJHYDENE. 2015.09.008.

[2] N.-T. Suen, S.-F. Hung, Q. Quan, N. Zhang, Y.-J. Xu, H.M. Chen, Electrocatalysis for the oxygen evolution reaction: recent development and future perspectives, Chem. Soc. Rev. 46 (2017) 337–365, https://doi.org/10.1039/C6CS00328A.

[3] C.C.L. McCrory, S. Jung, I.M. Ferrer, S.M. Chatman, J.C. Peters, T.F. Jaramillo, Benchmarking hydrogen evolving reaction and oxygen evolving reaction electrocatalysts for solar water splitting devices, J. Am. Chem. Soc. 137 (2015) 4347–4357, https://doi.org/10.1021/ja510442p.

[4] S. Ardo, D.F. Rivas, M.A. Modestino, V.S. Greiving, F.F. Abdi, E.A. Llado, V. Artero, K. Ayers, C. Battaglia, J.-P. Becker, Pathways to electrochemical solar-hydrogen technologies, Energy Environ. Sci. 11 (2018) 2768–2783, https://doi.org/10.1039/ C7EE03639F.

[5] M. Ball, M. Weeda, The hydrogen economy–vision or reality? Int. J. Hydrogen Energy 40 (2015) 7903–7919, https://doi.org/10.1016/j.ijhydene.2015.04.032.

[6] T. Rostrup-Nielsen, Manufacture of hydrogen, Catal. Today 106 (2005) 293–296, https://doi.org/10.1016/j.cattod.2005.07.149.

[7] K. Chakrapani, G. Bendt, H. Hajiyani, I. Schwarzrock, T. Lunkenbein, S. Salamon, J. Landers, H. Wende, R. Schlögl, R. Pentcheva, Role of composition and size of cobalt ferrite nanocrystals in the oxygen evolution reaction, ChemCatChem. 9

[8] H. Zhou, F. Yu, Q. Zhu, J. Sun, F. Qin, L. Yu, J. Bao, Y. Yu, S. Chen, Z. Ren, Water splitting by electrolysis at high current densities under 1.6 volts, Energy Environ. Sci. 11 (2018) 2858–2864, https://doi.org/10.1039/C8EE00927A.

[9] T. Maiyalagan, K.A. Jarvis, S. Therese, P.J. Ferreira, A. Manthiram, Spinel-type lithium cobalt oxide as a bifunctional electrocatalyst for the oxygen evolution and oxygen reduction reactions, Nat. Commun. 5 (2014) (2014) 3949, https://doi.org/ 10.1038/ncomms4949.

[10] M. Tahir, L. Pan, F. Idrees, X. Zhang, L. Wang, J.-J. Zou, Z.L. Wang, Electrocatalytic oxygen evolution reaction for energy conversion and storage: a comprehensive review, Nano Energy 37 (2017) 136–157, https://doi.org/10.1016/j.nanoen.2017. 05.022.

[11] M. Li, Y. Xiong, X. Liu, X. Bo, Y. Zhang, C. Han, L. Guo, Facile synthesis of electrospun MFe $_2$O$_4$ (M= Co, Ni, Cu, Mn) spinel nanofibers with excellent electrocatalytic properties for oxygen evolution and hydrogen peroxide reduction, Nanoscale 7 (2015) 8920–8930, https://doi.org/10.1039/C4NR07243J.

[12] A. Kargar, S. Yavuz, T.K. Kim, C.-H. Liu, C. Kuru, C.S. Rustomji, S. Jin, P.R. Bandaru, Solution-processed CoFe$_2$O$_4$ nanoparticles on 3D carbon fiber papers for durable oxygen evolution reaction, ACS Appl. Mater. Interfaces 7 (2015) 17851–17856, https://doi.org/10.1021/acsami.5b04270.

[13] Y. Xu, W. Bian, J. Wu, J.-H. Tian, R. Yang, Preparation and electrocatalytic activity of 3D hierarchical porous spinel CoFe$_2$O$_4$ hollow nanospheres as efficient catalyst for oxygen reduction reaction and oxygen evolution reaction, Electrochim. Acta 151 (2015) 276–283, https://doi.org/10.1016/j.electacta.2014.11.042.

[14] L. Han, P. Tang, A. Reyes-Carmona, B. Rodríguez-García, M. Torréns, J.R. Morante, J. Arbiol, J.R. Galan-Mascaros, Enhanced activity and acid pH stability of prussian blue-type oxygen evolution electrocatalysts processed by chemical etching, J. Am. Chem. Soc. 138 (2016) 16037–16045, https://doi.org/10.1021/jacs.6b09778.

[15] T. Li, Y. Lv, J. Su, Y. Wang, Q. Yang, Y. Zhang, J. Zhou, L. Xu, D. Sun, Y. Tang, Anchoring CoFe$_2$O$_4$ nanoparticles on N-doped carbon nanofibers for high-performance oxygen evolution reaction, Adv. Sci. 4 (2017) 1700226, , https://doi.org/10. 1002/advs.201700226.

[16] X. Lu, L. Gu, J. Wang, J. Wu, P. Liao, G. Li, Bimetal-organic framework derived CoFe$_2$O$_4$/C porous hybrid nanorod arrays as high-performance electrocatalysts for oxygen evolution reaction, Adv. Mater. 29 (2017) 1604437, , https://doi.org/10. 1002/adma.201604437.

[17] W. Bian, Z. Yang, P. Strasser, R. Yang, A CoFe$_2$O$_4$/graphene nanohybrid as an efficient bi-functional electrocatalyst for oxygen reduction and oxygen evolution, J. Power Sources 250 (2014) 196–203, https://doi.org/10.1016/j.jpowsour.2013.11. 024.

[18] X. Ji, S. Hao, F. Qu, J. Liu, G. Du, A.M. Asiri, L. Chen, X. Sun, Core–shell CoFe $_2$O$_4$@ Co–Fe–Bi nanoarray: a surface-amorphization water oxidation catalyst operating at near-neutral pH, Nanoscale 9 (2017) 7714–7718, https://doi.org/10.1039/ C7NR02929B.

[19] Y. Xu, X. Wang, H. Chen, D. Kuang, C. Su, Toward high performance photoelectrochemical water oxidation: combined effects of ultrafine cobalt iron oxide nanoparticle, Adv. Funct. Mater. 26 (2016) 4414–4421, https://doi.org/10.1002/ adfm.201600232.

[20] C. Singh, A. Goyal, S. Singhal, Nickel-doped cobalt ferrite nanoparticles: efficient catalysts for the reduction of nitroaromatic compounds and photo-oxidative degradation of toxic dyes, Nanoscale 6 (2014) 7959–7970, https://doi.org/10.1039/ C4NR01730G.

[21] A.J. Martín, G.O. Larrazábal, J. Pérez-Ramírez, Towards sustainable fuels and chemicals through the electrochemical reduction of CO$_2$: lessons from water electrolysis, Green Chem. 17 (2015) 5114–5130, https://doi.org/10.1039/ C5GC01893E.

[22] P.K. Shen, C. Xu, Alcohol oxidation on nanocrystalline oxide Pd/C promoted electrocatalysts, Electrochem. Commun. 8 (2006) 184–188, https://doi.org/10.1016/j. elecom.2005.11.013.

[23] G. Chen, Electrochemical technologies in wastewater treatment, Sep. Purif. Technol. 38 (2004) 11–41, https://doi.org/10.1016/j.seppur.2003.10.006.

[24] K. Bouzek, M. Paidar, A. Sadilkova, H. Bergmann, Electrochemical reduction of nitrate in weakly alkaline solutions, J. Appl. Electrochem. 31 (2001) 1185–1193, https://doi.org/10.1023/A:1012755222981.

[25] F. Urbain, V. Smirnov, J.-P. Becker, A. Lambertz, F. Yang, J. Ziegler, B. Kaiser, W. Jaegermann, U. Rau, F. Finger, Multijunction Si photocathodes with tunable photovoltages from 2.0 V to 2.8 V for light induced water splitting, Energy Environ. Sci. 9 (2016) 145–154, https://doi.org/10.1039/C5EE02393A.

[26] A. Lambertz, F. Finger, R.E.I. Schropp, U. Rau, V. Smirnov, Preparation and measurement of highly efficient a-Si: H single junction solar cells and the advantages of μc-SiO$_x$: H n-layers, Prog. Photovoltaics Res. Appl. 23 (2015) 939–948, https://doi. org/10.1002/pip.2629.

[27] A. Cabot, V.F. Puntes, E. Shevchenko, Y. Yin, L. Balcells, M.A. Marcus, S.M. Hughes, A.P. Alivisatos, Vacancy coalescence during oxidation of iron nanoparticles, J. Am. Chem. Soc. 129 (2007) 10358–10360, https://doi.org/10.1021/ja072574a.

[28] A. Cabot, M. Ibáñez, P. Guardia, A.P. Alivisatos, Reaction regimes on the synthesis of hollow particles by the Kirkendall effect, J. Am. Chem. Soc. 131 (2009) 11326–11328, https://doi.org/10.1021/ja903751p.

[29] M. Ibáñez, J. Fan, W. Li, D. Cadavid, R. Nafria, A. Carrete, A. Cabot, Means and limits of control of the shell parameters in hollow nanoparticles obtained by the Kirkendall effect, Chem. Mater. 23 (2011) 3095–3104, https://doi.org/10.1021/ cm2006633.

[30] T. Berestok, P. Guardia, J.B. Portals, S. Estradé, J. Llorca, F. Peiró, A. Cabot, S.L. Brock, Surface chemistry and nano-/microstructure engineering on photocatalytic In$_2$S$_3$ nanocrystals, Langmuir. 34 (2018) 6470–6479, https://doi.org/10. 1021/acs.langmuir.8b00406.

[31] T. Berestok, P. Guardia, M. Ibáñez, M. Meyns, M. Colombo, M.V. Kovalenko, F. Peiró, A. Cabot, Electrostatic-driven gelation of colloidal nanocrystals, Langmuir 34 (2018) 9167–9174, https://doi.org/10.1021/acs.langmuir.8b01111.

[32] T. Berestok, P. Guardia, R. Du, J.B. Portals, M. Colombo, S. Estradé, F. Peiró, S.L. Brock, A. Cabot, Metal oxide aerogels with controlled crystallinity and faceting from the epoxide-driven cross-linking of colloidal nanocrystals, ACS Appl. Mater. Interfaces 10 (2018) 16041–16048, https://doi.org/10.1021/acsami.8b03754.

[33] Q.Q. Xiong, J.P. Tu, S.J. Shi, X.Y. Liu, X.L. Wang, C.D. Gu, Ascorbic acid-assisted synthesis of cobalt ferrite ($CoFe_2O_4$) hierarchical flower-like microspheres with enhanced lithium storage properties, J. Power Sources 256 (2014) 153–159, https://doi.org/10.1016/j.jpowsour.2014.01.038.

[34] J. Liu, R. Meng, J. Li, P. Jian, L. Wang, R. Jian, Achieving high-performance for catalytic epoxidation of styrene with uniform magnetically separable $CoFe_2O_4$ nanoparticles, Appl. Catal. B Environ. 254 (2019) 214–222, https://doi.org/10.1016/j.apcatb.2019.04.083.

[35] M. Zhang, X. Yang, X. Kan, X. Wang, L. Ma, M. Jia, Carbon-encapsulated $CoFe_2O_4$/graphene nanocomposite as high performance anode for lithium ion batteries, Electrochim. Acta 112 (2013) 727–734, https://doi.org/10.1016/j.electacta.2013.09.034.

[36] P. Gründler, A. Kirbs, L. Dunsch, Modern thermoelectrochemistry, ChemPhysChem 10 (2009) 1722–1746, https://doi.org/10.1002/cphc.200900254.

[37] G.G. Wildgoose, D. Giovanelli, N.S. Lawrence, R.G. Compton, High-Temperature Electrochemistry: A Review, Electroanal. Int. J. Devoted Fundam. Pract. Asp. Electroanal. 16 (2004) 421–433, https://doi.org/10.1002/elan.200302875.

[38] F. Urbain, J.-P. Becker, V. Smirnov, J. Ziegler, F. Yang, B. Kaiser, W. Jaegermann, S. Hoch, A. Maljusch, U. Rau, F. Finger, Influence of the operating temperature on the performance of silicon based photoelectrochemical devices for water splitting, Mater. Sci. Semicond. Process. 42 (2016) 142–146, https://doi.org/10.1016/j.mssp.2015.08.045.

[40] S. Klaus, Y. Cai, M.W. Louie, L. Trotochaud, A.T. Bell, Effects of Fe electrolyte impurities on $Ni(OH)_2$/NiOOH structure and oxygen evolution activity, J. Phys. Chem. C 119 (2015) 7243–7254, https://doi.org/10.1021/acs.jpcc.5b00105.

[41] F. Urbain, P. Tang, N.M. Carretero, T. Andreu, J. Arbiol, J.R. Morante, Tailoring copper foam with silver dendrite catalysts for highly selective carbon dioxide conversion into carbon monoxide, ACS Appl. Mater. Interfaces 10 (2018) 43650–43660, https://doi.org/10.1021/acsami.8b15379.

[42] F. Urbain, P. Tang, N.M. Carretero, T. Andreu, L.G. Gerling, C. Voz, J. Arbiol, J.R. Morante, A prototype reactor for highly selective solar-driven CO_2 reduction to synthesis gas using nanosized earth-abundant catalysts and silicon photovoltaics, Energy Environ. Sci. 10 (2017) 2256–2266, https://doi.org/10.1039/C7EE01747B.

[43] E. Irtem, T. Andreu, A. Parra, M.D. Hernández-Alonso, S. García-Rodríguez, J.M. Riesco-García, G. Penelas-Pérez, J.R. Morante, Low-energy formate production from CO_2 electroreduction using electrodeposited tin on GDE, J. Mater. Chem. A 4

(2016) 13582–13588, https://doi.org/10.1039/C6TA04432H.

[44] M.D.H. ALONSO, G.P. PÉREZ, T. Andreu, E. Irtem, A. Parra, C. Fábrega, J.R. Morante, Filter-press Photoelectrochemical Water Oxidation and CO_2 Reduction Cell, (2018).

[45] Q. Ma, M. Li, L. Pang, X. Ren, C. Li, X. Xu, S. Liu, Solar-to-hydrogen efficiency of 9.5% by using a thin-layer platinum catalyst and commercial amorphous silicon solar cells, ChemCatChem 8 (2016) 1713–1717, https://doi.org/10.1002/cctc.201600170.

[46] C. Trompoukis, A. Abass, J.-W. Schüttauf, T. Bosserez, J. Rongé, J. Lauwaert, J.A. Martens, R. Baets, Porous multi-junction thin-film silicon solar cells for scalable solar water splitting, Sol. Energy Mater. Sol. Cells 182 (2018) 196–203, https://doi.org/10.1016/j.solmat.2018.03.041.

[47] Y. Tan, H. Wang, P. Liu, Y. Shen, C. Cheng, A. Hirata, T. Fujita, Z. Tang, M. Chen, Versatile nanoporous bimetallic phosphides towards electrochemical water splitting, Energy Environ. Sci. 9 (2016) 2257–2261, https://doi.org/10.1039/C6EE01109H.

[48] N. Jiang, B. You, M. Sheng, Y. Sun, Electrodeposited cobalt-phosphorous-derived films as competent bifunctional catalysts for overall water splitting, Angew. Chem. Int. Ed. 54 (2015) 6251–6254, https://doi.org/10.1002/anie.201501616.

[49] J. Jia, L.C. Seitz, J.D. Benck, Y. Huo, Y. Chen, J.W.D. Ng, T. Bilir, J.S. Harris, T.F. Jaramillo, Solar water splitting by photovoltaic-electrolysis with a solar-to-hydrogen efficiency over 30%, Nat. Commun. 7 (2016) 13237, https://doi.org/10.1038/ncomms13237.

[50] F. Urbain, P. Tang, V. Smirnov, K. Welter, T. Andreu, F. Finger, J. Arbiol, J.R. Morante, Multilayered hematite nanowires with thin-film silicon photovoltaics in an all-earth-abundant hybrid tandem device for solar water splitting, ChemSusChem 12 (2019) 1428–1436, https://doi.org/10.1002/cssc.201802845.

[51] B.M. Klahr, D. Peterson, K. Randolph, E.L. Miller, Innovative approaches to addressing the fundamental materials challenges in advanced water splitting technologies for renewable hydrogen production, ECS Trans. 75 (2017) 3–11, https://doi.org/10.1149/07550.0003ecst.

[52] J.H. Montoya, L.C. Seitz, P. Chakthranont, A. Vojvodic, T.F. Jaramillo, J.K. Nørskov, Materials for solar fuels and chemicals, Nat. Mater. 16 (2017) 70, https://doi.org/10.1038/nmat4778.

Further reading

S.H. Joo , S.J. Choi , I. Oh , J. Kwak , Z. Liu , O. Terasaki , R. Ryoo . Ordered nanoporous arrays of carbon supporting high dispersions of platinum nanoparticles Nature 2001; 412: 169-172 . doi:10.1038/35084046.

Review

Controlled oxygen doping in highly dispersed Ni-loaded g-C$_3$N$_4$ nanotubes for efficient photocatalytic H$_2$O$_2$ production

Ruifeng Du [a,b], Ke Xiao [a,b], Baoying Li [c,*], Xu Han [d], Chaoqi Zhang [a,b], Xiang Wang [a,b], Yong Zuo [a,e], Pablo Guardia [a], Junshan Li [f], Jianbin Chen [c,*], Jordi Arbiol [d,g], Andreu Cabot [a,g,*]

[a] Catalonia Energy Research Institute - IREC, Sant Adrià de Besòs, 08930 Barcelona, Spain
[b] Departament d'Enginyeria Electrònica i Biomèdica, Universitat de Barcelona, 08028 Barcelona, Spain
[c] Shandong Provincial Key Laboratory of Molecular Engineering, State Key Laboratory of Biobased Material and Green Papermaking, School of Chemistry and Chemical Engineering, Qilu University of Technology, Shandong Academy of Sciences, Jinan 250353, PR China
[d] Catalan Institute of Nanoscience and Nanotechnology (ICN2), CSIC and BIST, Campus UAB, Bellaterra, 08193, Barcelona, Catalonia, Spain
[e] Istituto Italiano di Tecnologia, Via Morego 30, Genova 16163, Italy
[f] Institute of Advanced Study, Chengdu University, Chengdu 610106, China
[g] ICREA, Pg. Lluis Companys 23, 08010 Barcelona, Catalonia, Spain

ARTICLE INFO

ABSTRACT

Hydrogen peroxide (H$_2$O$_2$) is both a key component in several industrial processes and a promising liquid fuel. The production of H$_2$O$_2$ by solar photocatalysis is a suitable strategy to convert and store solar energy into chemical energy. Here we report an oxygen-doped tubular g-C$_3$N$_4$ with uniformly dispersed nickel nanoparticles for efficient photocatalytic H$_2$O$_2$ generation. The hollow structure of the tubular g-C$_3$N$_4$ provides a large surface with a high density of reactive sites and efficient visible light absorption during the photocatalytic reaction. The oxygen doping and Ni loading enable a fast separation of photogenerated charge carriers and a high selectivity toward the two-electron process during the oxygen reduction reaction (ORR). The optimized composition, Ni$_{4\%}$/O$_{0.2}$tCN, displays an H$_2$O$_2$ production rate of 2464 μmol g^{-1}·h^{-1}, which is eightfold higher than that of bulk g-C$_3$N$_4$ under visible light irradiation ($\lambda > 420$ nm), and achieves an apparent quantum yield (AQY) of 28.2% at 380 nm and 14.9% at 420 nm.

1. Introduction

Hydrogen peroxide is an important industrial raw material used among others as an eco-friendly oxidant for industrial synthesis, pulp bleaching and wastewater treatment, with a global annual demand of over 4 million tons.[1–4] Besides, H$_2$O$_2$ is also a promising liquid fuel that is safer and easier to store than compressed hydrogen.[5,6] At present, H$_2$O$_2$ is industrially produced mainly through the anthraquinone method, which is an energy-intensive process requiring large amounts of organic solvent.[7] Therefore, the development of cost-effective and environmentally friendly strategies for the large scale production of H$_2$O$_2$ is a worthwhile endeavour. In this scenario, the production of H$_2$O$_2$ using solar photocatalysis has received increased attention in recent years.[8,9].

Several photocatalysts have been applied for H$_2$O$_2$ generation, including titanium dioxide[10,11], graphitic carbon nitride (g-C$_3$N$_4$)

[12,13] and bismuth vanadate[14], to cite a few. Among them, g-C$_3$N$_4$ is particularly interesting as a metal-free, non-toxic and chemically stable material that has shown excellent potential not only for H$_2$O$_2$ generation but also for hydrogen generation and wastewater treatment, among others. However, the low surface area, moderate light absorption, rapid recombination of the photogenerated electron-hole pairs and low photocatalytic reaction selectivity towards H$_2$O$_2$ generation limits the cost-effective use of g-C$_3$N$_4$ for photocatalytic H$_2$O$_2$ production. To overcome these limitations, several strategies have been developed, including tuning the g-C$_3$N$_4$ morphology, extrinsic doping, and heterojunction formation through co-catalyst loading. [15–19].

It is well known that the morphology and nanostructure of g-C$_3$N$_4$ largely affect its photocatalytic performance. To date, several g-C$_3$N$_4$ morphologies, such as nanosheets,[20] nanospheres,[21] nanorods,[22] nanofibers[23] and nanotubes[24] have been prepared. Among them, nanotubes with a one-dimensional hollow structure offer particularly

---

large surface areas, high light absorption and fast electron transport to optimize photocatalytic performance.

Beyond controlling its morphology, the proper doping of g-C$_3$N$_4$ is critical to adjust its band structure and charge carrier concentration towards enhancing light absorption and promoting charge injection. [25,26] Dopants such as oxygen and phosphorus can not only adjust the valence band structure of the catalyst and improve the separation efficiency of photogenerated electrons and holes, but also improve the OER selectivity toward the two-electron pathway.[27,28].

The introduction of a co-catalyst on the surface of g-C$_3$N$_4$ is an effective strategy to improve photocatalytic performance by increasing the charge separation ability. Various noble metal co-catalyst, such as Pt, Pd, and Au, have been demonstrated to promote hydrogen evolution performance.[29–33] Nevertheless, the high cost of noble metals and the moderate H$_2$O$_2$ production rates reached limit the cost-effectiveness of the process. Thus, the development of co-catalysts based on abundant and low-cost elements, such as MoS$_2$, Ni, NiP or CoP, [34–37] that provide an efficient and high rate photocatalytic H$_2$O$_2$ production is highly desirable.

In this study, we detail the synthesis of hollow tubular g-C$_3$N$_4$ (tCN), demonstrate its controlled oxygen doping (OtCN), and describe its surface modification with highly dispersed nickel nanoparticles (Ni/OtCN) through a photoreduction process. Nitrogen adsorption–desorption isotherms, UV–vis absorption and photoluminescence spectroscopies, and photochemical tests are used to investigate the charge separation and transfer abilities of these materials. Besides, rotating ring disk electrode analysis, active species capture experiments and DFT calculations are used to analyze the mechanism of H$_2$O$_2$ generation. Owing to its unique 1-D hollow structure, high charge separation efficiency and excellent reaction selectivity, Ni/OtCN achieved outstanding H$_2$O$_2$ photocatalytic generation performance.

2. Experimental

2.1. Preparation of tubular g-C$_3$N$_4$ precursor (C-M)

g-C$_3$N$_4$ nanotubes were prepared by a self-assembly method using melamine (99%, Acros Organics) and cyanuric acid (99%, Acros Organics). Typically, 1 g melamine and 1 g cyanuric acid were separately added into 300 ml deionized water under stirring at 80 °C for about 10 min until completely dissolved. Then the melamine solution was slowly added to the cyanuric acid solution under homogeneous stirring, and let it self-assemble at 80 °C for 1.5 h. The product was centrifuged and washed twice with 80 °C deionized water to remove the unassembled melamine and cyanuric acid. The filtered product was re-dispersed in deionized water and then settled at room temperature for 12 h. Then the supernatant was removed to obtain a flocculent precipitate. The precipitate was then freeze-dried for 48 h to obtain the g-C$_3$N$_4$ precursor that we will refer to as C-M.

2.2. Preparation of O-doped tubular g-C$_3$N$_4$ (OtCN) and bulk g-C$_3$N$_4$ (bCN)

The OtCN was prepared by a two-step heating process. In detail, 2 g C-M was introduced into a lidded porcelain crucible and calcined at 520 °C for 2 h with a temperature increase rate of 2 °C·min^{-1} under Ar atmosphere. Then the product was mixed with the proper amount (0 g, 200 mg, 400 mg, 600 mg, or 800 mg) of ammonium persulfate (98%, Sigma) and calcined again at 520 °C for 2 h with a temperature ramp of 5 °C·min^{-1}. The products were named O$_x$tCN, with x = 0, 0.1, 0.2, 0.3, or 0.4 for the different amounts of ammonium persulfate introduced. The bulk g-C$_3$N$_4$ (bCN) was prepared through a similar method but replacing the C-M with melamine and adding no ammonium persulfate.

2.3. Preparation of Ni/OtCN, Au/OtCN and Pt/OtCN

100 mg of OtCN was added into 100 ml deionized water containing 10 ml triethanolamine (99%, Acros Organics), 8.5 mg nickel acetate tetrahydrate (99%, Acros Organics), and 500 mg sodium hypophosphite (99%, Sigma), and the solution was sonicated for 30 min. Afterwards, argon was bubbled into the solution for 30 min to displace the oxygen. Then the solution was irradiated with UV–vis light (300 W Xe lamp) under continuous stirring and argon bubbling for 30 min. The product was centrifuged and washed 3 times with water and ethanol (90%, Acros Organics) and finally dried under vacuum for 6 h. The sample was named Ni$_{2\%}$/OtCN. Samples with higher Ni concentration, Ni$_x$/OtCN (x = 4%, 6% and 8%), were prepared using the same procedure but adding the proper higher amount of nickel acetate. Au/OtCN and Pt/OtCN samples were also prepared by this photo-deposition method using H$_2$PtCl$_6$·6H$_2$O (99%, Acros Organics) and HAuCl$_4$·4H$_2$O (99%, Acros Organics) precursors and irradiating the samples with UV light for 1 h.

3. Results and discussions

3.1. Structural and chemical properties of oxygen-doped tubular g-C$_3$N$_4$ and the Ni-loaded composite

Oxygen-doped tubular carbon nitride samples loaded with Ni nanocrystals (Ni/OtCN) were obtained through a 4-step process involving the synthesis of the carbon nitride precursor from the combination of melamine and cyanuric acid in water, annealing under argon at 520 °C, oxygen doping using ammonium persulfate, and photo-deposition of Ni (Fig. 1).

Because the water solubility of melamine and cyanuric acid is very low at room temperature, the two components were dissolved at 80 °C to ensure their full and uniform dispersion before self-assembly. The assembly is driven by the hydrogen bond formation between the amino group on melamine and the hydroxyl group on cyanuric acid. To determine the optimum precursor composition, materials with different melamine and cyanuric acid molar ratios (1:2, 1:1 and 2:1) were prepared for comparison. SEM analysis of the obtained precursors (Fig. 2a and S1) showed the 1:1 ratio to provide the best-defined nanorod structures, with a diameter in the range 300–600 nm and lengths of 15–30 μm. This result is consistent with the equal number of functional groups of both molecules, thus assembling at a 1:1 M ratio. While the 1:2 and 2:1 ratios also resulted in nanorod-like structures, they showed poor uniformity and presented a large amount of unassembled precursor on their surfaces.

Once the self-assembly process was completed, the material was washed with hot water to remove the residual not-assembled precursors. To prevent agglomerating during the drying process, samples were freeze-dried, which yielded dried materials with high porosity, as observed in Figure S2. The freeze-drying step was demonstrated as particularly important because an extensive agglomeration of the nanorods results in a high sintering and very notable loss of porosity during the posterior annealing step at 520 °C.

To minimize the damage to the nanostructure during the thermal polymerization of the C-M precursor, the annealing and oxygen doping of the material was divided into two steps. The first annealing step at 520 °C used a relatively low heating rate of 2 °C·min^{-1}. After this step, samples were combined with a proper amount of ammonium persulfate and the mixture was annealed again at 520 °C for two additional hours using a temperature ramp of 5 °C·min^{-1}. This second annealing step completed the polymerization process. Besides, during the annealing process, the ammonium persulfate releases ammonia, sulfur dioxide, and oxygen gases creating a porous fluffy structure and inhibiting the agglomeration of nanotubes. At the same time, in this oxygen-enriched atmosphere, part of the generated oxygen gas reacts with the polymerizing carbon nitride incorporating oxygen into the structure. After the two-step thermal polymerization at 520 °C, the nanorod precursor was
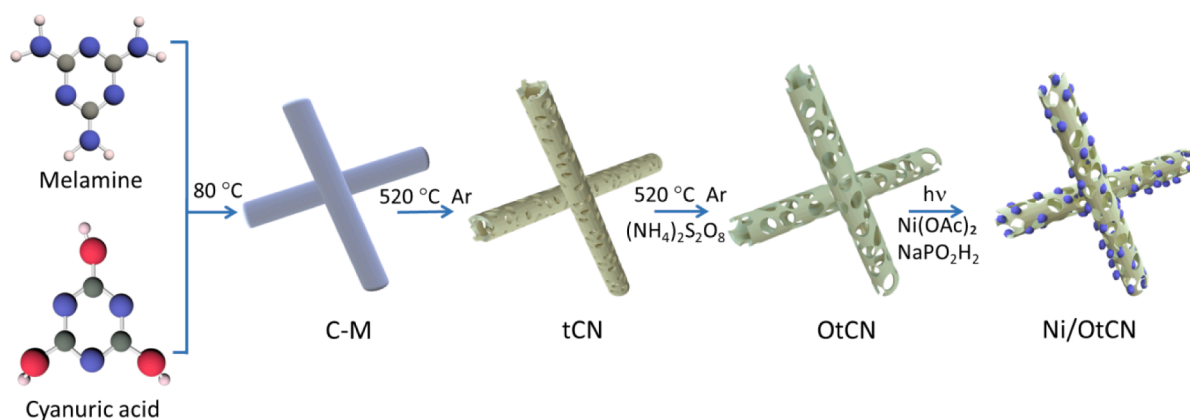
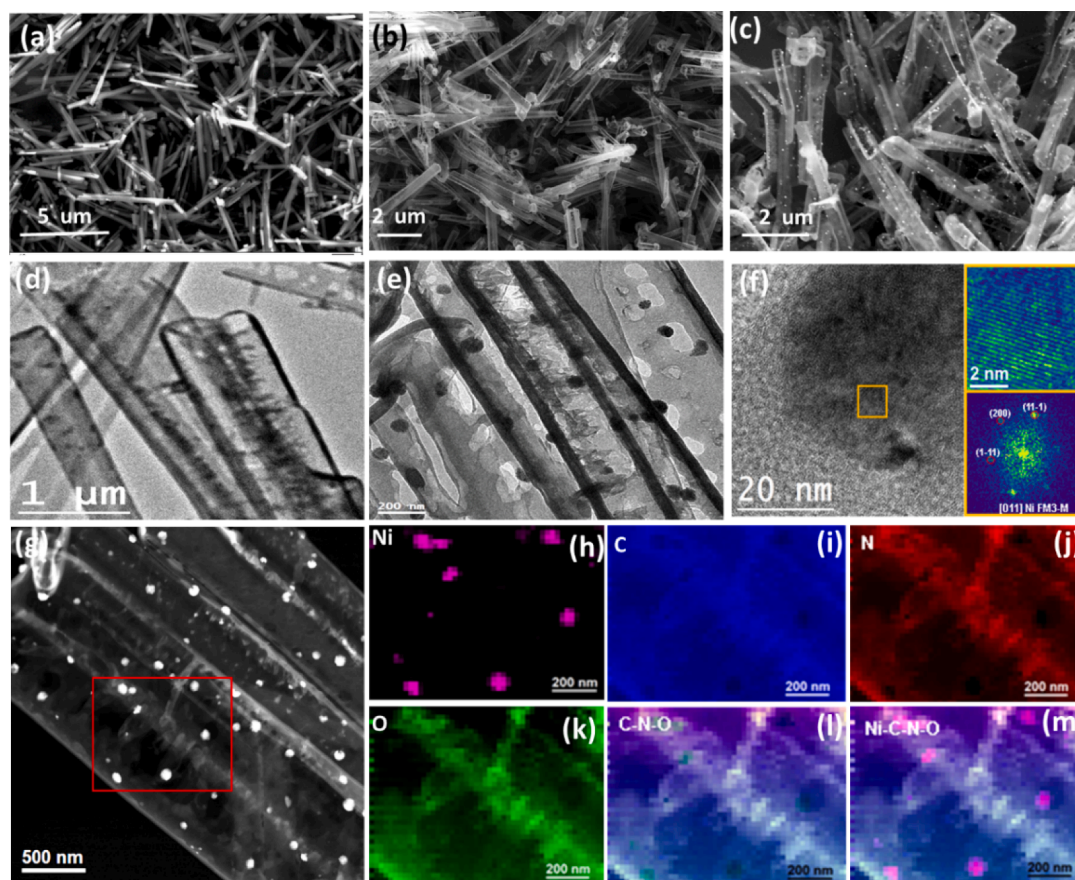**Fig. 1.** Schematic illustration on the synthesis of Ni/OtCN samples.

Fig. 2. (a) SEM image of the C-M precursor. (b) SEM image of OtCN. (c) SEM image of Ni/OtCN. (d) TEM image of OtCN. (e) TEM image of Ni/OtCN. (f) HRTEM micrograph obtained on a representative region of the Ni/OtCN nanostructures. On the top right, we show a magnified detail (top right) of the orange squared region in the HRTEM image and its corresponding indexed power spectrum (bottom right) which reveals that this nanoparticle has a crystal phase in agreement with the Ni cubic phase (space group = FM3-M) with a = b = c = 3.5241 Å, visualized along its [0 1 1] zone axis. (g) HAADF STEM general detail of the Ni/OtCN catalyst, showing the presence of Ni nanoparticles as bright spots. EELS chemical composition maps were obtained on the red squared area of the STEM micrograph. Individual composition maps were obtained by using: (h) Individual Ni $L_{2,3}$-edges at 855 eV (pink), (i) C K-edges at 284 eV (blue), (j) N K-edges at 401 eV (red) and (k) O K-edges at 532 eV (green), as well as their composites for C-N-O and Ni-C-N-O.

turned into g-C_3N_4 nanotubes that maintained approximately the same size as the precursor nanorods (Fig. 2b).

The annealed and oxygen-doped samples, OtCN, were dispersed in a solution containing nickel acetate tetrahydrate to be loaded with nickel nanoparticles through a photodeposition process. As a result, as observed in Fig. 2c, uniformly and highly dispersed Ni nanoparticles were grown on the surface of the OtCN. Figure S3 provides results from the EDX analysis of $Ni_{4\%}/O_{0.2}tCN$ showing the weight percentage of O and Ni to be 2.1 % and 3.2 %, respectively.

TEM analysis of OtCN samples confirmed the tubular structure of the products and further showed the nanotube walls have a porous structure (Fig. 2d). The tubular structure of OtCN was thus significantly different from that of bulk g-C_3N_4 (bCN) produced from the direct annealing of melamine (Figure S7a). TEM images of the Ni/OtCN samples also

confirmed the homogeneous distribution of Ni nanoparticles and showed their size to be in the range of 20–60 nm (Fig. 2e). HRTEM micrographs revealed that the selected nanoparticles had a crystal phase matching the Ni cubic phase (space group = FM3-M) with a = b = c = 3.5241 Å (Fig. 2f). EELS chemical composition maps obtained on the Ni/ OtCN nanotubes displayed a uniform distribution of O, N and C and the presence of Ni-rich regions corresponding to the Ni nanoparticles.

Fig. 3a displays the XRD patterns of $O_{0.2}tCN$, $Ni_x/O_{0.2}tCN$ and a reference bCN. The main diffraction peaks at about 13.1° and 27.4° observed from all the samples are assigned to the (100) and (002) family planes of g-C_3N_4, respectively. Compared with bCN, the (002) peak of OtCN samples shows a slight shift from 27.4° to 27.2° which is a signature of an increase of the interplanar distance associated with the presence of oxygen.[38,39] Besides, the (002) diffraction peak of OtCN is broader and weaker than that of bCN, which is attributed to the tubular structure of OtCN. The samples containing Ni show no alteration of the g-C_3N_4 diffraction peaks compared with OtCN, which indicates that the loading of Ni does not affect the OtCN structure. Meanwhile, Ni/ OtCN samples display two additional XRD peaks at 44.3° and 51.5° that are assigned to the (111) and (200) family planes of cubic nickel. The intensity of these peaks correlates with the amount of Ni introduced, proving the successful loading of controlled amounts of nickel.

FTIR spectroscopy was used to gain further insight into the structure of the material. As shown in Fig. 3b, all OtCN materials displayed the fingerprints of g-C_3N_4, including the absorption peak at 812 cm^{-1} that corresponds to the out-of-plane bending of the triazine units, and the range of peak at 1200–1600 cm^{-1} that are related to the stretching modes of C-N in the aromatic heterocyclic rings. Besides, OtCN samples displayed FTIR peaks at 1235 and 1075 cm^{-1}, which intensity increased with the amount of ammonium persulfate used during the synthesis. These peaks are associated with the stretching mode of C-O-C group. [27,40].

Fig. 3c displays the UV–vis diffuse reflectance spectra of the different samples. The absorption edge of OtCN samples presented an obvious red-shift compared with that of bCN. This redshift was accentuated with the increase in the oxygen content. As shown in Fig. 3d, the band gaps of bCN and OtCN samples, calculated according to Kubelk-Munk function, shifted from 2.73 eV for bCN, to 2.56 eV for $O_{0.4}tCN$. Besides, the

presence of oxygen resulted in a notable enhancement of the Urbach tail, which is associated with the presence of defects as a result of oxygen doping.[27,39] As expected from the metallic character of the introduced Ni nanoparticles, the Ni/OtCN composites presented a strong absorption in the visible range of the spectra, which was enhanced with the increasing contents of Ni, from 2% to 8%. On the other hand, the presence of Ni did not result in a shift of the OtCN absorption edge.

Fig. 3f displays the nitrogen adsorption–desorption isotherms of bCN and $O_{0.2}tCN$ nanotubes. Both samples exhibit type IV isotherms with H3 hysteresis loops, indicating the presence of a mesoporous structure. As shown in Table S2, the specific surface area (SSA) of $O_{0.2}tCN$ nanotubes was 124 $m^2 \cdot g^{-1}$, which is over six-fold larger than that of bCN (18.7 $m^2 \cdot g^{-1}$). The calculated pore size distribution of the two samples is shown in Figure S7b. As expected from SEM images, the pore volume of OtCN, 0.97 $cm^3 \cdot g^{-1}$, was significantly larger than that of bCN, 0.19 $cm^3 \cdot g^{-1}$.

Mott-Schottky analysis was used to further investigate the band structure of the samples (Figure S6). The flat band potentials of bCN and OtCN were obtained from the fitting of the Mott-Schottky plots and were used to estimate the position of the conduction band minimum (assuming it is ca. 0.1 eV above the flat band)[41,42] and valence band maximum (considering $E_g = E_{vb} - E_{cb}$).[43] Fig. 3e displays the schematized band structure experimentally determined from bCN and OtCN samples.

Fig. 4 displays the XPS spectra of bCN, $O_{0.2}tCN$, and $Ni_{4\%}/O_{0.2}tCN$ samples. The high-resolution C 1 s XPS spectra showed three main contributions at 288.2 eV, 286.5 eV, and 284.8 eV, which were assigned to C-(N_3), C–NH_X and C–C/C = C, respectively.[40] Besides, the OtCN samples displayed a fourth C 1 s peak 288.5 eV corresponding to C-O obtained from the replacement of N atoms by O in the CN heterocycles. All samples displayed the presence of oxygen at their surface, including the bCN. The high-resolution O 1 s XPS spectrum of bCN was fitted with two peaks at 531.7 eV and 533.1 eV, which were associated with adsorbed oxygen-containing species such as water, O_2, OH^- groups and even CO_2. [38] Besides, samples OtCN and Ni/OtCN displayed an additional contribution at 530.7 eV which is assigned to the C-O bond. Additionally, a peak at 529.7 eV was identified in the XPS spectrum of Ni/OtCN, and it was assigned to oxygen within a nickel oxide chemical
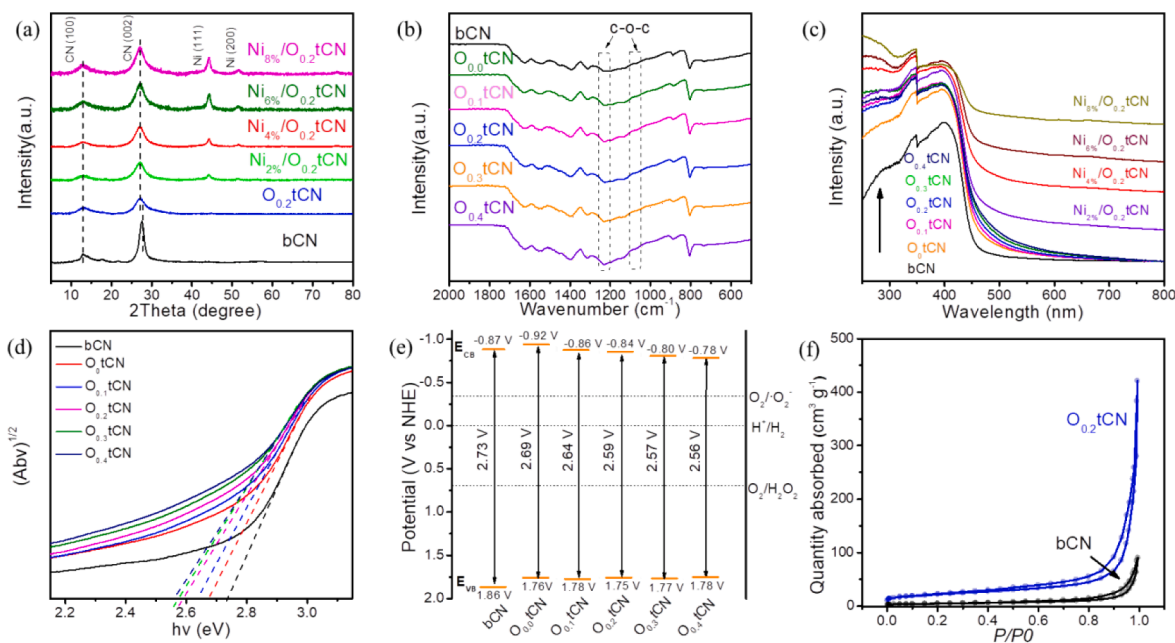

Fig. 3. (a) XRD pattern of bCN, $O_{0.2}tCN$ and $Ni_x/O_{0.2}tCN$ (x = 2%, 4%, 6% and 8%). (b) FTIR spectra of bCN and O_XtCN. (c) UV–Vis absorption spectra of bCN, O_XtCN and $Ni_x/O_{0.2}tCN$. (d) plot of the band energy spectra and (e) band structure alignments for bCN and OtCN. (f) N_2 adsorption–desorption isotherms of bCN and $O_{0.2}tCN$.
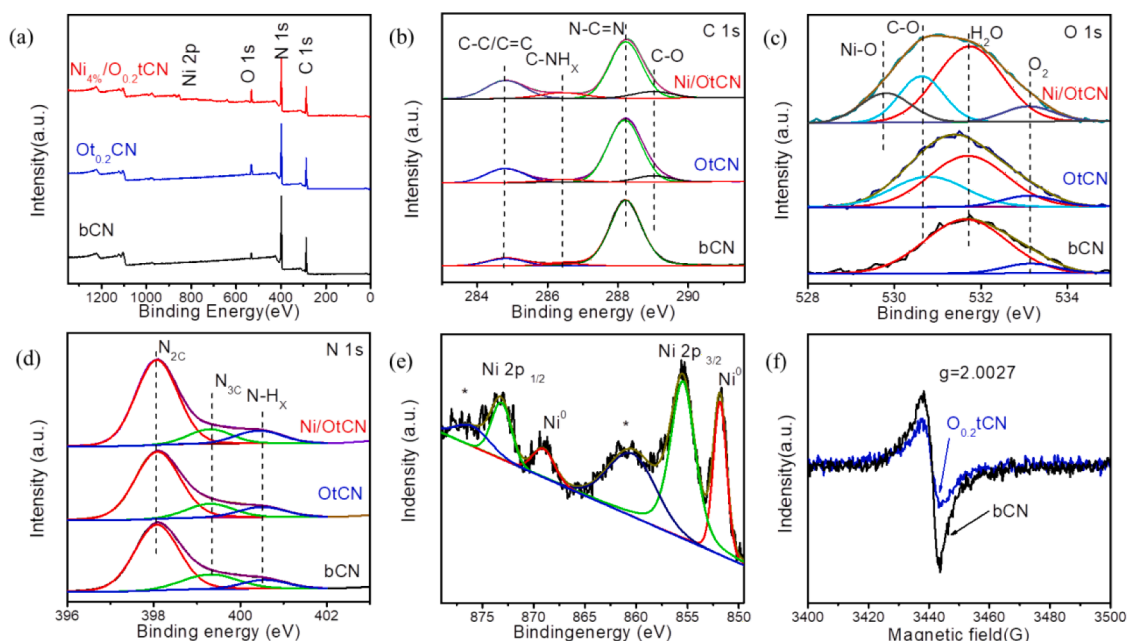
Fig. 4. (a) XPS survey spectra. (b-d) High-resolution XPS spectra of (b) C 1 s, (c) O 1 s and (d) N 1 s obtained from bCN, $O_{0.2}tCN$ and $Ni_{4\%}/O_{0.2}tCN$. (e) Ni 2p XPS spectrum of $Ni_{4\%}/O_{0.2}tCN$. (f) EPR spectra of bCN and $O_{0.2}tCN$.

environment created by the surface oxidation of the Ni nanoparticles. The high-resolution N 1 s XPS spectra of bCN, $O_{0.2}tCN$ and $Ni_{4\%}/O_{0.2}tCN$ were fitted with three peaks at binding energies of 398.1 eV, 499.4 eV, and 400.5 eV, which were assigned to N-(C_2), N-(C_3) and N-H_x groups of the heptazine framework, respectively. Finally, the high-resolution Ni 2p XPS spectrum of Ni/OtCN was fitted with three doublets, corresponding to metallic Ni ($2p_{3/2}$ at 851.6 eV), Ni $^{2+}$ ($2p_{3/2}$ at 855.8 eV) and a Ni $^{2+}$ shake-up satellite ($2p_{3/2}$ at 860.4 eV).[44] While $(NH_4)_2S_2O_8$,

added as the oxygen source, decomposes to NH_3 (g), SO_2 (g) and O_2 (g) during the second annealing step, no sulfur was detected by XPS and EDX analyses due to the low reactivity of sulfur within sulfur dioxide in the temperature range used (Figures S4 and S5).

The EPR spectra of bCN and OtCN samples are displayed in Fig. 4f. The Lorentzian absorption line at g = 2.0027 is a fingerprint of the unpaired electrons of the sp^2 hybridized C atoms in the aromatic rings. [27,38] The EPR signal of the OtCN sample is significantly less intense
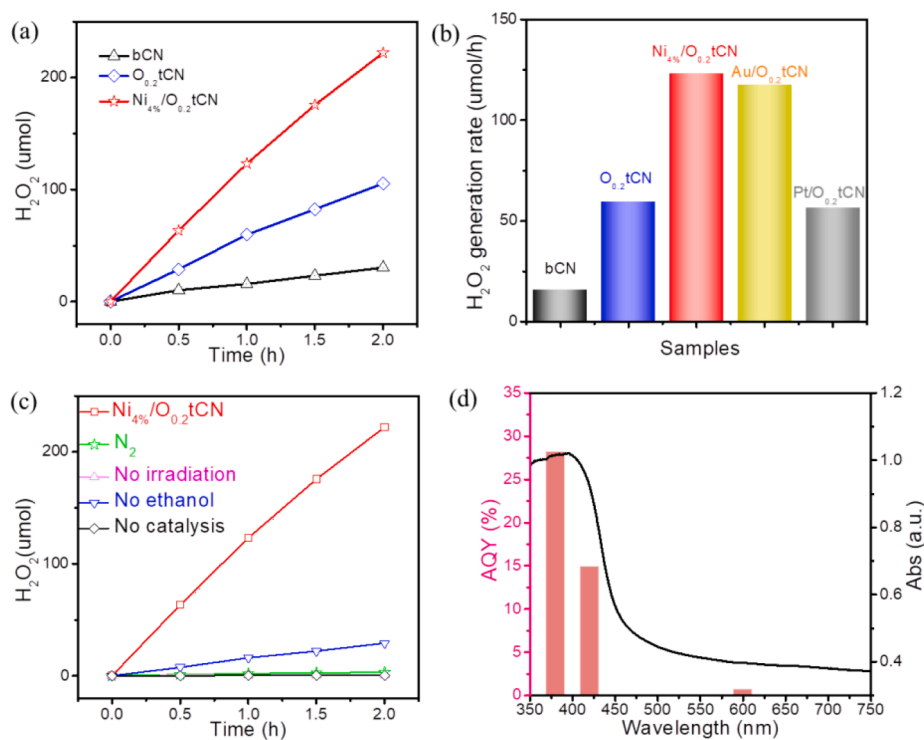

Fig. 5. (a) Photocatalytic H_2O_2 generation on bCN, $O_{0.2}tCN$ and $Ni_{4\%}/O_{0.2}tCN$ during 2 h under visible light (λ > 420 nm). (b) Photocatalytic H_2O_2 generation rate of bCN, $O_{0.2}tCN$, $Ni_{4\%}/O_{0.2}tCN$, $Au_{4\%}/O_{0.2}tCN$ and $Pt_{4\%}/O_{0.2}tCN$ (c) H_2O_2 production on $Ni_{4\%}/O_{0.2}tCN$ under different conditions: N_2 instead of O_2, no irradiation, no ethanol and no photocatalyst. (d) AQY of $Ni_{4\%}/O_{0.2}tCN$ at three different wavelengths, superimposed to the UV–vis spectrum.

than that of bCN, which is consistent with the partial replacement N by O atoms, thus decreasing the number of lone pair electrons. According to XPS data (Table S1), the N/C ratio of OtCN (1.13) is significantly lower than that of bCN (1.21), and the O/C ratio of OtCN (0.08) is higher than that of bCN (0.04), which is consistent with the hypothesis that O replaces N within the carbon nitride structure. Overall, the above experimental results confirmed the presence of O within OtCN replacing N atoms.

3.2. Photocatalytic H_2O_2 evolution

Fig. 5a displays the photocatalytic H_2O_2 generation from bCN, $O_{0.2}tCN$, and $Ni_{4\%}/O_{0.2}tCN$ irradiated during 2 h with visible light ($\lambda >$ 420 nm). The H_2O_2 production rate of $O_{0.2}tCN$ was fourfold higher than that of bCN (Fig. 5b). Besides, when loading the $O_{0.2}tCN$ with Ni, the H_2O_2 evolution rate further increased to reach nearly an order of magnitude higher values than bCN. Besides the Ni/OtCN sample displayed higher H_2O_2 evolution rates than noble metal co-catalyst: Au/OtCN and Pt/OtCN. The presence of Au showed an obvious improvement over OtCN, but the presence of Pt had no positive impact on the H_2O_2 generation, which is associated with a low two-electron reaction selectivity and a high H_2O_2 decomposition rate during the oxygen reduction reaction.

To find the optimal amount of oxygen doping, O_XtCN samples produced using different amounts of ammonium persulfate were tested (Figure S9a-b). O_XtCN samples containing relatively small amounts of oxygen ($0 < x < 0.4$) exhibited a significant enhancement of the H_2O_2 generation rate over tCN, but too high oxygen substitutions resulted in a lower H_2O_2 evolution rate. Among all the O_xtCN samples, $O_{0.2}tCN$ displayed the best H_2O_2 generation performance, 58.1 $\mu mol \cdot h^{-1}$.

The amount of Ni was optimized by measuring the photocatalytic hydrogen peroxide generation on $Ni_x/O_{0.2}tCN$ containing different Ni concentrations (Figure S9c-d). The loading of $O_{0.2}tCN$ with a moderate amount of Ni nanoparticles largely enhanced the photocatalytic performance toward H_2O_2 generation. At a Ni loading of 2% and 4%, the H_2O_2 generation rate was improved to 88.2 $\mu mol \cdot h^{-1}$ and 123.2 $\mu mol \cdot h^{-1}$, which is 1.5 and 2.1 times higher than that of $O_{0.2}tCN$, respectively. When further increasing the Ni loading to 6% and 8% the H_2O_2 production rate decreased to 101 $\mu mol \cdot h^{-1}$ and 75 $\mu mol \cdot h^{-1}$, respectively. This decrease of the H_2O_2 production rate at high Ni loads may be related to the aggregation of small Ni particles and the blocking of the visible light absorption of the C_3N_4 caused by an excess of Ni.

To further evidence the advantages of OtCN over bCN, we also prepared a Ni-loaded oxygen-doped bulk g-C_3N_4 (Ni/ObCN) to be used as a reference. As observed in Figure S10a, the $Ni_{4\%}/O_{0.2}bCN$ sample displayed a slightly improved H_2O_2 production rate over bCN, but still well below the rates obtained from OtCN samples. This moderate production rate is in part related to the small surface area of bCN and the uneven deposition of nickel nanoparticles (Figure S10b) caused by the insufficient active sites on the bCN surface.

As displayed in Fig. 5c, control experiments demonstrated that the presence of O_2 and light irradiation were required for the H_2O_2 generation, proving the production of H_2O_2 to take place by the ORR pathway instead of the water oxidation. Besides ethanol, other sacrificial agents, such as lactic acid and triethanolamine, also enabled a high H_2O_2 generation rate (Figure S11). But even in the absence of ethanol or another sacrificial agent, the $Ni_{4\%}/O_{0.2}tCN$ sample was able to achieve a notable photocatalytic H_2O_2 generation (Fig. 5c). Besides, as shown in Fig. S12, $Ni_{4\%}/O_{0.2}tCN$ also shows a prominent photocatalytic hydrogen peroxide generation performance of about 5012 $\mu mol \cdot g^{-1} \cdot h^{-1}$ under simulated solar light, using an AM1.5 filter.

The apparent quantum yield (AQY) of the process was evaluated under 380 nm (0.53 mW·cm^{-2}), 420 nm (9.91 mW·cm^{-2}) and 600 nm (17.66 mW·cm^{-2}) irradiation (Fig. 5d and S13, and Table S3, see details in the SI). For $Ni_{4\%}/O_{0.2}tCN$, the AQY at 380 nm and 420 nm was estimated at 28.2% and 14.9%, respectively. Even under 600 nm light

irradiation, an AQY of 0.7% was achieved for $Ni_{0.4}/O_{0.2}tCN$, which is consistent with UV–vis spectroscopy results (Fig. 5d).[45].

3.3. Charge carrier dynamics

The electrochemical characterization of the samples allowed the further study of their charge transfer and transport properties. As observed in Fig. 6a, bCN, $O_{0.2}tCN$ and $Ni_{4\%}/O_{0.2}tCN$ electrodes showed positive photocurrents under visible-light irradiation. Among them, $O_{0.2}tCN$ showed a slightly higher photocurrent density than bCN, but the highest photocurrents were obtained with the $Ni_{4\%}/O_{0.2}tCN$ electrode, reaching about 7.2 and 4 times higher current densities than with bCN and $O_{0.2}tCN$, respectively. These results demonstrate that $O_{0.2}tCN$ and especially the presence of Ni nanoparticles significantly increase the charge separation and transfer efficiency, which is in good agreement with the photocatalysis results. [46].

Charge transfer and transport properties were further evaluated by electrochemical impedance spectroscopy (EIS). Fig. 6b displays the Nyquist plot of the impedance spectra for the different materials. The larger arc associated with the transfer resistance of photo-generated charges[37] has a significantly smaller diameter for $O_{0.2}tCN$ than bCN, indicating a faster charge transfer efficiency in the former. Besides, the sample containing Ni, $Ni_{4\%}/O_{0.2}tCN$, presents a much smaller arc radius than the other two samples, confirming the much lower charge transfer resistance in the presence of Ni.

The photoluminescence (PL) spectra of the different samples under 300 nm light excitation is displayed in Fig. 6c. The bCN sample displayed a broad and intense PL band at ca. 455 nm, which is associated with the radiative band-to-band recombination of photogenerated charge carriers within C_3N_4. With oxygen doping, the PL intensity significantly decreases owing to the presence of oxygen-related nonradiative recombination centers. Besides, the presence of Ni introduces additional recombination sites which further quenches the C_3N_4 PL. As obtained from time-resolved PL (TRPL) spectroscopy (Fig. 6d) and consistently with previous results, $O_{0.2}tCN$ and $Ni_{4\%}/O_{0.2}tCN$ samples exhibited much shorter average PL lifetimes (4.06 ns and 3.39 ns) than bCN (6.22 ns), demonstrating the strong electronic effect of the substitutional oxygen and nickel nanoparticles.[3647].

3.4. Reaction mechanism

The generation of H_2O_2 from the coupling of the oxygen reduction reaction (ORR) with the oxidation of an alcohol takes place through two main pathways. Both paths share the alcohol dehydrogenation reaction and the oxygen adsorption as the initial ORR step:

$$RCH_2OH + 2\,h^+ \rightarrow RCHO + 2H^+ \tag{1}$$

$$O_2 + {}^* \text{-}\rightarrow {}^*O_2 \tag{2}$$

In one possible path, the reduction of the adsorbed oxygen molecule (*O_2) can take place through a direct two-electron route:

$$^*O_2 + 2H^+ + 2e^- \rightarrow H_2O_2 \tag{3}$$

The second possible ORR pathway is a two-step single-electron process, that can be broken down into the following steps:

$$^*O_2 + e^- \rightarrow {}^*O_2^- \tag{3}$$

$$^*O_2^- + H^+ \rightarrow {}^*HOO \tag{4}$$

$$^*HOO + e^- \rightarrow HOO^- \tag{5}$$

$$HOO^- + H^+ \rightarrow H_2O_2 \tag{6}$$

Besides, the H_2O_2 evolution reaction competes with the oxygen reduction to H_2O, which overall involves a total of 4e$^-$ (see details in the SI):
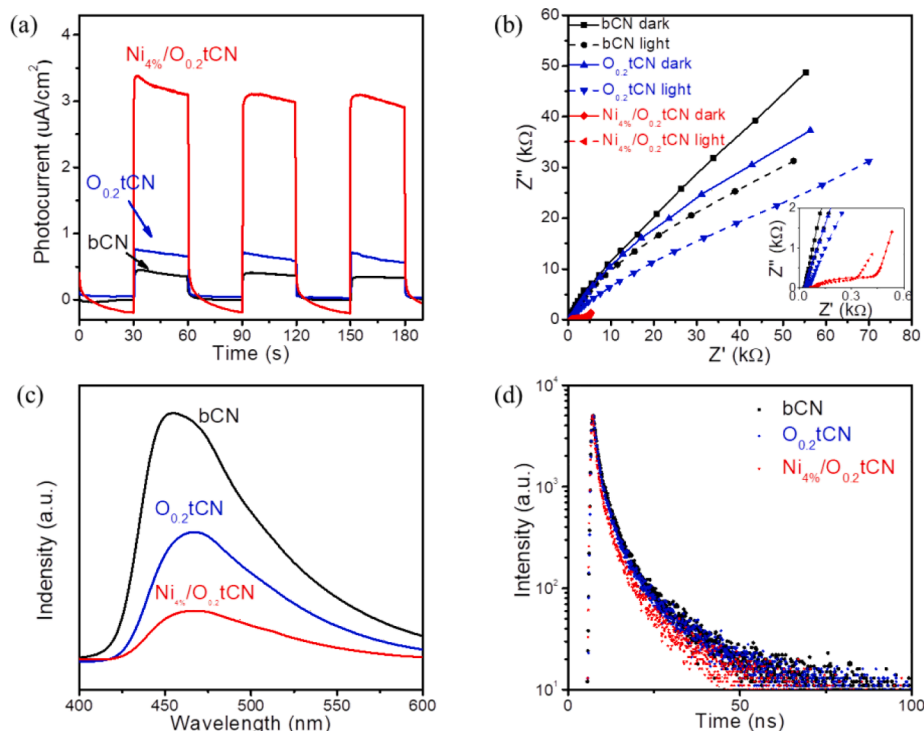
Fig. 6. (a) Photocurrent response curves of bCN, $O_{0.2}$tCN and $Ni_{4\%}/O_{0.2}$tCN; (b) Electrochemical impedance spectroscopy (EIS) Nyquist plots of bCN,$O_{0.2}$tCN and $Ni_{4\%}/O_{0.2}$tCN; (c,d) PL spectra and TRPL decay of bCN,$O_{0.2}$tCN and $Ni_{4\%}/O_{0.2}$tCN.

$$O_2 + 4H^+ + 4e^- \rightarrow 2H_2O \tag{7}$$

A rotating ring-disk electrode (RRDE) was used to determine the selectivity of the catalyst toward the production of H_2O_2 instead of H_2O. [48] The disk electrode was scanned cathodically at a scan rate of 10 $mV \cdot s^{-1}$, while the ring potential was set at 0.5 V vs. Ag/AgCl (Fig. 7). The linear sweep voltammetry (LSV) curves of bCN achieved $I_r = 0.40$ $mA \cdot cm^{-2}$ and $I_d = -1.91$ $mA \cdot cm^{-2}$ at -1.0 V vs. Ag/AgCl. From these values, a transfer number n = 2.71 and an H_2O_2 selectivity of 60.8% was determined.[49] Similarly, a transfer number n = 2.32 and an H_2O_2 selectivity of 81.2% was obtained for $O_{0.2}$tCN, and n = 2.24 and an H_2O_2 selectivity of 88.9% for $Ni_{4\%}/O_{0.2}$tCN. Overall, the RRDE measurements indicated that the oxygen doping and the presence of Ni significantly promoted the two-electron pathway for oxygen reduction to H_2O_2 over the four-electron H_2O generation.

To differentiate between the one-step two-electron direct ORR ($O_2 \rightarrow H_2O_2$) and the sequential two-step single-electron indirect reduction ($O_2 \rightarrow *O_2^- \rightarrow H_2O_2$) routes,[18,19] LSV curves were analyzed in more detail (Figures 7, S14 and S15). Notice that the bCN and $O_{0.2}$tCN samples exhibit two reduction plateaus at around -0.2 V and -0.5 V, suggesting

a two-step pathway for H_2O_2 generation.[19,50] As observed in Fig. 7b,c, no obvious H_2O_2 current is detected in the ring electrode during the first plateau, in the potential range -0.2 V to -0.4 V. Only when reaching the second plateau a ring current is measured, which indicates the successive two single-electron reduction pathway. On the other hand, after loading the Ni nanoparticles, the first plateau almost disappears and the onset potential of the H_2O_2 current at the ring electrode approximately matches that of the disk electrode, pointing at a one-step two-electron direct reduction pathway in $Ni_{4\%}/O_{0.2}$tCN. Overall, these results indicate that the introduction of nickel transforms the reaction from a two-step single-electron process to a direct two-electron process.

DFT calculations were carried out to further understand the selectivity of the ORR process on CN, OCN and Ni/OCN.(Fig. 8) The top view of the intermediates adsorption and the free energy diagram of ORR on the three materials are shown in Figure S16 and Table S5. The bCN sample is characterized by the strongest adsorption strength of ORR intermediates, which may hamper the product formation. The reduction of *OOH and *OH to form the final products, H_2O_2 or H_2O, are generally considered as the limiting ORR steps determining the reaction rate and pathway, either $2e^-$ or $4e^-$. [17] The change of Gibbs free energy (ΔG) for the reduction of *OOH and *OH on CN was calculated to be 1.42 eV and
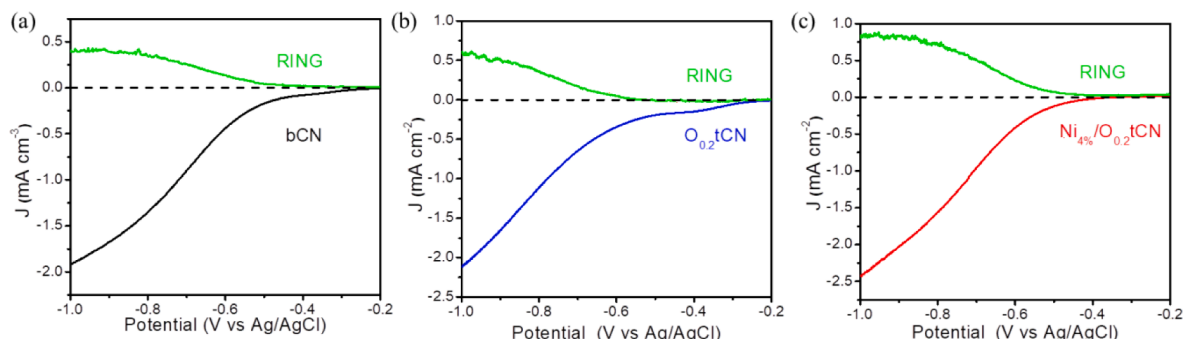

Fig. 7. LSV curves of (a) bCN, (b) $O_{0.2}$tCN and (c) $Ni_{4\%}/O_{0.2}$tCN obtained using an RRDE with a rotating speed of 1600 rpm and a ring biased at 0.5 V.
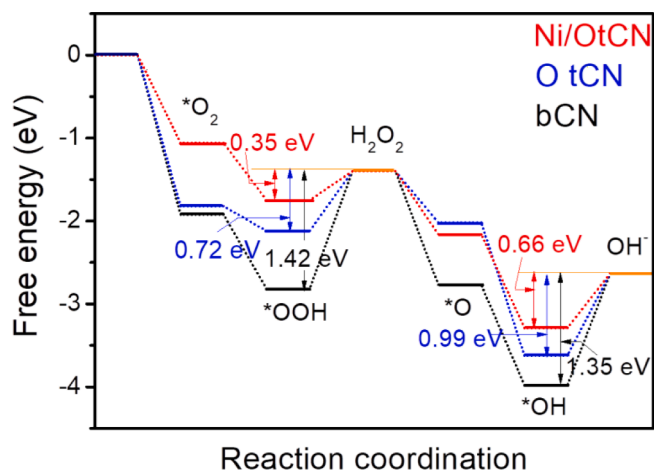
Fig. 8. Free energy diagrams of oxygen reduction reaction steps on bCN, $O_{0.2}tCN$ and $Ni_{4\%}/O_{0.2}tCN$.

1.35 eV, respectively (Fig. 7d). The similar ΔG for *OOH and *OH reduction on CN points toward the simultaneous occurrence of the two-electron and four-electron pathways. With the oxygen doping, ΔG for the reduction of *OOH and *OH on OCN decreased to 0.72 eV and 0.99 eV, respectively. Besides, with the introduction of Ni, ΔG values further decreased down to 0.35 eV and 0.66 eV, respectively. The lower ΔG values obtained for OCN and particularly for Ni/OCN are consistent with experimental data obtained for OtCN and Ni/OtCN. Besides, notice that the ΔG of the reduction of *OOH is significantly lower than that of *OH reduction in OCN and Ni/OCN samples, involving a higher probability of the $2e^-$ ORR pathway than the $4e^-$. These DFT calculation results are consistent with the experimental data obtained from the RRDE test, further demonstrating that the oxygen doping and the Ni loading incline the catalyst toward two-electron reactions, which can significantly improve the H_2O_2 generation efficiency.

Additional experimentally of the ORR pathway were obtained by introducing a $*O^{2-}$ trapping agent in the solution, PBQ (1 mM). As shown in Figure S17a-c, after introducing the PBQ, the H_2O_2 generation rate strongly decreased for bCN and $O_{0.2}tCN$, by an 88% and 84%, respectively, demonstrating the important role played by $*O^{2-}$ as an intermediate during H_2O_2 generation process, i.e. pointing at the two-step single-electron process as the main pathway for H_2O_2 generation process in bCN and $O_{0.2}tCN$. On the contrary, the $Ni_{4\%}/O_{0.2}tCN$ sample showed just a 35% decrease of H_2O_2 generation in the presence of PBQ, indicating the predominance of the two-electron process over the two single-electron processes.

To further explore the reaction mechanism and determine the role of superoxide radicals in the reaction process, DMPO spin-trapping EPR spectroscopy was used to determine the presence of $*O_2^-$ in the surface of the photocatalyst. As shown in Figure S17d, after irradiating bCN with visible light for 3 min with DMPO and methanol, four characteristic EPR features were observed. These DMPO-$*O_2^-$ characteristic EPR peaks were much more intense for the $Ot_{0.2}CN$ sample under the same conditions, indicating that $O_{0.2}tCN$ can generate larger amounts of $*O_2^-$ during the H_2O_2 evolution process, which is consistent with its higher H_2O_2 generation rate. On the other hand, while $Ni_{4\%}/O_{0.2}tCN$ provided much higher H_2O_2 generation rates than $O_{0.2}tCN$, the $*O_2^-$ characteristic EPR signal was less intense, involving significant participation of an alternative path for H_2O_2 generation, i.e. the direct two-electron process. This result further confirms that the direct two-electron process has a fundamental role in the large H_2O_2 generation rates obtained in the presence of Ni.

Stability cycles of the $Ni_{4\%}/O_{0.2}tCN$ for H_2O_2 evolution under visible-light irradiation are displayed Figure S18a. After 20 h of reaction, with five four-hour cycles, the catalyst maintained over 81 %

photocatalytic H_2O_2 generation activities, i.e. about 99.3 $\mu mol \cdot h^{-1}$, demonstrating excellent stability and reusability. Besides, SEM and XRD analysis of the catalyst after 20 h photocatalytic H_2O_2 reaction demonstrated the morphology and crystallographic structure of the material to be stable under photocatalytic reaction conditions (Figure S18b,c).

4. Conclusion

In summary, we detailed the synthesis of hollow tubular g-C_3N_4 (tCN), and demonstrated their controlled oxygen doping (OtCN), and their surface modification with highly dispersed nickel nanoparticles (Ni/OtCN) through a photoreduction process. OtCN samples displayed a hollow tubular structure with a large specific surface area (124 $m^2 \cdot g^{-1}$). With larger SSA and more porous structure, OtCN can provide more reactive sites, improve the light absorption by the multiple diffusion and accelerate the diffusion of reactants and products on the surface. Based on the DFT and RRDE results, the doping with oxygen and the presence of Ni nanoparticles greatly reduced the energy barrier for H_2O_2 generation, and improved the H_2O_2 selectivity from 60.8% to 88.9%, which enabled a more effective and efficient ORR towards H_2O_2 evolution. After loading the Ni nanoparticles, the electrons on the conduction band of OtCN are transferred to the surface of Ni which has a lower Femi level and then reducing the oxygen through a one-step two-electron direct reduction ($O_2 \rightarrow H_2O_2$) route, which is more efficient for H_2O_2 generation. Efficient charge separation and high selective formation of H_2O_2 during ORR process allow $Ni_{4\%}/O_{0.2}tCN$ to achieve an outstanding production rate up to 2464 μmol $g^{-1} \cdot h^{-1}$ under visible light and 5021 μmol $g^{-1} \cdot h^{-1}$ under simulated solar light and AQY of 28.2% at 380 nm and 14.9% at 420 nm.

Declaration of Competing Interest

The authors declare that they have no known competing financial interests or personal relationships that could have appeared to influence the work reported in this paper.

Appendix A. Supplementary data

Supplementary data to this article can be found online at https://doi.org/10.1016/j.cej.2022.135999.

References

[1] Y. Kofuji, Y. Isobe, Y. Shiraishi, H. Sakamoto, S. Tanaka, S. Ichikawa, T. Hirai, Carbon nitride-aromatic diimide–graphene nanohybrids: metal-free photocatalysts for solar-to-hydrogen peroxide energy conversion with 0.2% Efficiency, J. Am. Chem. Soc. 138 (2016) 10019–10025, https://doi.org/10.1021/jacs.6b05806.

[2] M. Melchionna, P. Fornasiero, M. Prato, The rise of hydrogen peroxide as the main product by metal-free catalysis in oxygen reductions, Adv. Mater. 31 (2019) 1802920, https://doi.org/10.1002/adma.201802920.

[3] S. Yang, A. Verdaguer-Casadevall, L. Arnarson, L. Silvioli, V. Čolić, R. Frydendal, J. Rossmeisl, I. Chorkendorff, I.E.L. Stephens, Toward the decentralized electrochemical production of H2O2: a focus on the catalysis, ACS Catal. 8 (2018) 4064–4081, https://doi.org/10.1021/acscatal.8b00217.

[4] S. Kato, J. Jung, T. Suenobu, S. Fukuzumi, Production of hydrogen peroxide as a sustainable solar fuel from water and dioxygen, Energy Environ. Sci. 6 (2013) 3756–3764.

[5] S.A. Mousavi Shaegh, N.-T. Nguyen, S.M. Mousavi Ehteshami, S.H. Chan, A membraneless hydrogen peroxide fuel cell using prussian blue as cathode material, Energy Environ. Sci. 5 (2012) 8225–8228, https://doi.org/10.1039/C2EE21806B.

[6] G.H. Miley, N. Luo, J. Mather, R. Burton, G. Hawkins, L. Gu, E. Byrd, R. Gimlin, P. J. Shrestha, G. Benavides, J. Laystrom, D. Carroll, Direct NaBH4/H2O2 fuel cells, J. Power Sources. 165 (2007) 509–516, https://doi.org/10.1016/j.jpowsour.2006.10.062.

[7] S. Fukuzumi, Production of liquid solar fuels and their use in fuel cells, Joule. 1 (4) (2017) 689–738.

[8] H. Hou, X. Zeng, X. Zhang, Production of hydrogen peroxide by photocatalytic processes, Angew. Chemie Int. Ed. 59 (40) (2020) 17356–17376.

[9] Y. Shiraishi, T. Takii, T. Hagi, S. Mori, Y. Kofuji, Y. Kitagawa, S. Tanaka, S. Ichikawa, T. Hirai, Resorcinol–formaldehyde resins as metal-free semiconductor photocatalysts for solar-to-hydrogen peroxide energy conversion, Nat. Mater. 18 (9) (2019) 985–993.

[10] D. Tsukamoto, A. Shiro, Y. Shiraishi, Y. Sugano, S. Ichikawa, S. Tanaka, T. Hirai, Photocatalytic H2O2 production from ethanol/O2 system using TiO2 loaded with Au–Ag bimetallic alloy nanoparticles, ACS Catal. 2 (2012) 599–603, https://doi.org/10.1021/cs2006873.

[11] M. Teranishi, S.-I. Naya, H. Tada, In situ liquid phase synthesis of hydrogen peroxide from molecular oxygen using gold nanoparticle-loaded titanium (IV) dioxide photocatalyst, J. Am. Chem. Soc. 132 (23) (2010) 7850–7851.

[12] H. Ou, C. Tang, X. Chen, M. Zhou, X. Wang, Solvated electrons for photochemistry syntheses using conjugated carbon nitride polymers, ACS Catal. 9 (4) (2019) 2949–2955.

[13] S. Zhao, T. Guo, X. Li, T. Xu, B. Yang, X. Zhao, Carbon nanotubes covalent combined with graphitic carbon nitride for photocatalytic hydrogen peroxide production under visible light, Appl. Catal. B Environ. 224 (2018) 725–732.

[14] H. Hirakawa, S. Shiota, Y. Shiraishi, H. Sakamoto, S. Ichikawa, T. Hirai, Au nanoparticles supported on BiVO4: effective inorganic photocatalysts for H2O2 production from water and O2 under visible light, ACS Catal. 6 (2016) 4976–4982.

[15] J. Luo, Y. Liu, C. Fan, L. Tang, S. Yang, M. Liu, M. Wang, C. Feng, X. Ouyang, L. Wang, L. Xu, J. Wang, M. Yan, Direct attack and indirect transfer mechanisms dominated by reactive oxygen species for photocatalytic H2O2 Production on g-C3N4 possessing nitrogen vacancies, ACS Catal. 11 (2021) 11440–11450, https://doi.org/10.1021/acscatal.1c03103.

[16] Q. He, B. Viengkeo, X. Zhao, Z. Qin, J. Zhang, X. Yu, Y. Hu, W. Huang, Y. Li, Multiscale structural engineering of carbon nitride for enhanced photocatalytic H2O2 production, Nano Res. (2021), https://doi.org/10.1007/s12274-021-3882-1.

[17] Y. Zhao, P. Zhang, Z. Yang, L. Li, J. Gao, S. Chen, T. Xie, C. Diao, S. Xi, B. Xiao, Mechanistic analysis of multiple processes controlling solar-driven H2O2 synthesis using engineered polymeric carbon nitride, Nat. Commun. 12 (2021) 1–11.

[18] L. Zhou, J. Feng, B. Qiu, Y. Zhou, J. Lei, M. Xing, L. Wang, Y. Zhou, Y. Liu, J. Zhang, Ultrathin g-C3N4 nanosheet with hierarchical pores and desirable energy band for highly efficient H2O2 production, Appl. Catal. B Environ. 267 (2020) 118396.

[19] S. Li, G. Dong, R. Hailili, L. Yang, Y. Li, F. Wang, Y. Zeng, C. Wang, Effective photocatalytic H2O2 production under visible light irradiation at g-C3N4 modulated by carbon vacancies, Appl. Catal. B Environ. 190 (2016) 26–35.

[20] Y. Zuo, X. Xu, C. Zhang, J. Li, R. Du, X. Wang, X. Han, J. Arbiol, J. Llorca, J. Liu, A. Cabot, SnS2/g-C3N4/graphite nanocomposites as durable lithium-ion battery anode with high pseudocapacitance contribution, Electrochim. Acta. 349 (2020), 136369, https://doi.org/10.1016/j.electacta.2020.136369.

[21] X. Dang, R. Yang, Z. Wang, S. Wu, H. Zhao, Efficient visible-light activation of molecular oxygen to produce hydrogen peroxide using P doped gC 3 N 4 hollow spheres, J. Mater. Chem. A. 8 (43) (2020) 22720–22727.

[22] X. Bai, L. Wang, R. Zong, Y. Zhu, Photocatalytic activity enhanced via g-C3N4 nanoplates to nanorods, J. Phys. Chem. C. 117 (2013) 9952–9961, https://doi.org/10.1021/jp402062d.

[23] M. Tahir, C. Cao, N. Mahmood, F.K. Butt, A. Mahmood, F. Idrees, S. Hussain, M. Tanveer, Z. Ali, I. Aslam, Multifunctional g-C3N4 nanofibers: a template-free fabrication and enhanced optical, electrochemical, and photocatalyst properties, ACS Appl. Mater. Interfaces. 6 (2014) 1258–1265, https://doi.org/10.1021/am405076b.

[24] C. Zhang, R. Du, J.J. Biendicho, M. Yi, K. Xiao, D. Yang, T. Zhang, X. Wang, J. Arbiol, J. Llorca, Y. Zhou, J.R. Morante, A. Cabot, Tubular CoFeP@CN as a mott-schottky catalyst with multiple adsorption sites for robust lithium−sulfur batteries, Adv. Energy Mater. 11 (2021) 2100432, https://doi.org/10.1002/aenm.202100432.

[25] S. Guo, Z. Deng, M. Li, B. Jiang, C. Tian, Q. Pan, H. Fu, Phosphorus-doped carbon nitride tubes with a layered micro-nanostructure for enhanced visible-light photocatalytic hydrogen evolution, Angew Chemie. 128 (5) (2016) 1862–1866.

[26] G. Liu, P. Niu, C. Sun, S.C. Smith, Z. Chen, G.Q. Lu, H.-M. Cheng, Unique electronic structure induced high photoreactivity of sulfur-doped graphitic C3N4, J. Am. Chem. Soc. 132 (33) (2010) 11642–11648.

[27] Z. Wei, M. Liu, Z. Zhang, W. Yao, H. Tan, Y. Zhu, Efficient visible-light-driven selective oxygen reduction to hydrogen peroxide by oxygen-enriched graphitic carbon nitride polymers, Energy Environ. Sci. 11 (9) (2018) 2581–2589.

[28] J. Cao, H. Wang, Y. Zhao, Y. Liu, Q. Wu, H. Huang, M. Shao, Y. Liu, Z. Kang, Phosphorus-doped porous carbon nitride for efficient sole production of hydrogen peroxide via photocatalytic water splitting with a two-channel pathway, J. Mater. Chem. A. 8 (7) (2020) 3701–3707.

[29] Y. Zhu, T. Wang, T. Xu, Y. Li, C. Wang, Size effect of Pt co-catalyst on photocatalytic efficiency of g-C3N4 for hydrogen evolution, Appl. Surf. Sci. 464 (2019) 36–42.

[30] Y. Zuo, Y. Liu, J. Li, R. Du, X. Yu, C. Xing, T. Zhang, L. Yao, J. Arbiol, J. Llorca, K. Sivula, N. Guijarro, A. Cabot, Solution-processed ultrathin SnS2–Pt nanoplates for photoelectrochemical water oxidation, ACS Appl. Mater. Interfaces. 11 (7) (2019) 6918–6926.

[31] B. Li, Y. Zhang, R. Du, L. Gan, X. Yu, Synthesis of Bi2S3–Au dumbbell heteronanostructures with enhanced photocatalytic and photoresponse properties, Langmuir. 32 (44) (2016) 11639–11645.

[32] X. Chang, J. Yang, D. Han, B. Zhang, X. Xiang, J. He, Enhancing light-driven production of hydrogen peroxide by anchoring Au onto C3N4 catalysts, Catalysts. 8 (2018) 147.

[33] G. Zuo, S. Liu, L. Wang, H. Song, P. Zong, W. Hou, B. Li, Z. Guo, X. Meng, Y.i. Du, T. Wang, V.A.L. Roy, Finely dispersed Au nanoparticles on graphitic carbon nitride as highly active photocatalyst for hydrogen peroxide production, Catal. Commun. 123 (2019) 69–72.

[34] H. Zhang, P. Zhang, M. Qiu, J. Dong, Y. Zhang, X.W. David Lou, Ultrasmall MoOx clusters as a novel cocatalyst for photocatalytic hydrogen evolution, Adv. Mater. 31 (2019) 1804883, https://doi.org/10.1002/adma.201804883.

[35] A. Indra, P.W. Menezes, K. Kailasam, D. Hollmann, M. Schröder, A. Thomas, A. Brückner, M. Driess, Nickel as a co-catalyst for photocatalytic hydrogen evolution on graphitic-carbon nitride (sg-CN): what is the nature of the active species? Chem. Commun. 52 (2016) 104–107.

[36] X. Yu, R. Du, B. Li, Y. Zhang, H. Liu, J. Qu, X. An, Biomolecule-assisted self-assembly of CdS/MoS2/graphene hollow spheres as high-efficiency photocatalysts for hydrogen evolution without noble metals, Appl. Catal. B Environ. 182 (2016) 504–512.

[37] R. Du, Y. Zhang, B. Li, X. Yu, H. Liu, X. An, J. Qu, Biomolecule-assisted synthesis of defect-mediated Cd 1–x Zn x S/MoS 2/graphene hollow spheres for highly efficient hydrogen evolution, Phys. Chem. Chem. Phys. 18 (24) (2016) 16208–16215.

[38] Y. Jiang, Z. Sun, C. Tang, Y. Zhou, L. Zeng, L. Huang, Enhancement of photocatalytic hydrogen evolution activity of porous oxygen doped g-C3N4 with nitrogen defects induced by changing electron transition, Appl. Catal. B Environ. 240 (2019) 30–38.

[39] P. Niu, L. Zhang, G. Liu, H.-M. Cheng, Graphene-like carbon nitride nanosheets for improved photocatalytic activities, Adv. Funct. Mater. 22 (22) (2012) 4763–4770.

[40] Y. Zhang, Z. Chen, J. Li, Z. Lu, X. Wang, Self-assembled synthesis of oxygen-doped g-C3N4 nanotubes in enhancement of visible-light photocatalytic hydrogen, J. Energy Chem. 54 (2021) 36–44.

[41] S. Zhao, X. Zhao, H. Zhang, J. Li, Y. Zhu, Covalent combination of polyoxometalate and graphitic carbon nitride for light-driven hydrogen peroxide production, Nano Energy. 35 (2017) 405–414.

[42] A. Ishikawa, T. Takata, J.N. Kondo, M. Hara, H. Kobayashi, K. Domen, Oxysulfide Sm2Ti2S2O5 as a stable photocatalyst for water oxidation and reduction under visible light irradiation (λ≤ 650 nm), J. Am. Chem. Soc. 124 (45) (2002) 13547–13553.

[43] C. Xing, Y. Liu, Y.U. Zhang, J. Liu, T. Zhang, P. Tang, J. Arbiol, L. Soler, K. Sivula, N. Guijarro, X. Wang, J. Li, R. Du, Y. Zuo, A. Cabot, J. Llorca, Porous NiTiO 3/TiO 2 nanostructures for photocatalytic hydrogen evolution, J. Mater. Chem. A. 7 (28) (2019) 17053–17059.

[44] X. Xie, L.u. Shang, R. Shi, G.I.N. Waterhouse, J. Zhao, T. Zhang, Tubular assemblies of N-doped carbon nanotubes loaded with NiFe alloy nanoparticles as efficient bifunctional catalysts for rechargeable zinc-air batteries, Nanoscale. 12 (24) (2020) 13129–13136.

[45] Y. Zhao, Y. Liu, J. Cao, H. Wang, M. Shao, H. Huang, Y. Liu, Z. Kang, Efficient production of H2O2 via two-channel pathway over ZIF-8/C3N4 composite photocatalyst without any sacrificial agent, Appl. Catal. B Environ. 278 (2020), 119289.

[46] C. Liu, Y. Fu, J. Zhao, H. Wang, H. Huang, Y. Liu, Y. Dou, M. Shao, Z. Kang, All-solid-state Z-scheme system of NiO/CDs/BiVO4 for visible light-driven efficient overall water splitting, Chem. Eng. J. 358 (2019) 134–142.

[47] Y. Li, H. Xu, S. Ouyang, D.a. Lu, X. Wang, D. Wang, J. Ye, In situ surface alkalinized gC 3 N 4 toward enhancement of photocatalytic H 2 evolution under visible-light irradiation, J. Mater. Chem. A. 4 (8) (2016) 2943–2950.

[48] R. Liu, H. Liu, Y. Li, Y. Yi, X. Shang, S. Zhang, X. Yu, S. Zhang, H. Cao, G. Zhang, Nitrogen-doped graphdiyne as a metal-free catalyst for high-performance oxygen reduction reactions, Nanoscale. 6 (2014) 11336–11343, https://doi.org/10.1039/C4NR03185G.

[49] L. Hao, S. Zhang, R. Liu, J. Ning, G. Zhang, L. Zhi, Bottom-up construction of triazine-based frameworks as metal-free electrocatalysts for oxygen reduction reaction, Adv. Mater. 27 (2015) 3190–3195, https://doi.org/10.1002/adma.201500863.

[50] H.-i. Kim, O.S. Kwon, S. Kim, W. Choi, J.-H. Kim, Harnessing low energy photons (635 nm) for the production of H 2 O 2 using upconversion nanohybrid photocatalysts, Energy Environ. Sci. 9 (3) (2016) 1063–1073.

RESEARCH ARTICLE

Tubular CoFeP@CN as a Mott–Schottky Catalyst with Multiple Adsorption Sites for Robust Lithium–Sulfur Batteries

Chaoqi Zhang, Ruifeng Du, Jordi Jacas Biendicho, Mingjie Yi, Ke Xiao, Dawei Yang, Ting Zhang, Xiang Wang, Jordi Arbiol, Jordi Llorca, Yingtang Zhou,* Joan Ramon Morante, and Andreu Cabot*

The shuttle effect and the sluggish reaction kinetics of lithium polysulfide (LiPS) seriously compromise the performance of lithium–sulfur batteries (LSBs). To overcome these limitations and enable the fabrication of robust LSBs, here the use of a Mott–Schottky catalyst based on bimetallic phosphide CoFeP nanocrystals supported on carbon nitride tubular nanostructures as sulfur hosts is proposed. Theoretical calculations and experimental data confirm that CoFeP@CN composites are characterized by a suitable electronic structure and charge rearrangement that allows them to act as a Mott–Schottky catalyst to accelerate LiPS conversion. In addition, the tubular geometry of CoFeP@CN composites facilitates the diffusion of Li ions, accommodates volume change during the reaction, and offers abundant lithiophilic/sulfiphilic sites to effectively trap soluble LiPS. Therefore, S@CoFeP@CN electrodes deliver a superior rate performance of 630 mAh g^{-1} at 5 C, and remarkable cycling stability with 90.44% capacity retention over 700 cycles. Coin cells with high sulfur loading, 4.1 mg cm^{-2}, and pouch cells with 0.1 Ah capacities are further produced to validate their superior cycling stability. In addition, it is demonstrated here that CoFeP@CN hosts greatly alleviate the often overlooked issues of low energy efficiency and serious self-discharging in LSBs.

1. Introduction

Lithium–sulfur batteries (LSBs) are regarded as the most promising candidate to replace lithium–ion batteries (LIBs) in next-generation energy storage systems. Compared with LIBs, LSBs are characterized by a sixfold higher theoretical energy density, 2600 W h kg^{-1}, and a potentially lower cost and environmental impact if properly selecting the cathode materials.[1–3] Despite these attractive advantages, the electrically insulating character of sulfur and the shuttle effect of intermediate lithium polysulfides (LiPS) greatly limit the practical application of LSBs.[4] Additionally, the serious volume changes and slow redox kinetics during the charging/discharging process also reduce the cycling life and power density.[5]

Several sulfur host materials have been proposed to overcome the aforementioned limitations.[2,6] Carbon-based hosts with high electrical conductivity

C. Q. Zhang, R. F. Du, Dr. J. J. Biendicho, K. Xiao, D. W. Yang,
X. Wang, Prof. J. R. Morante, Prof. A. Cabot
Catalonia Institute for Energy Research—IREC
Sant Adrià de Besòs, Barcelona 08930, Spain
E-mail: acabot@irec.cat

C. Q. Zhang, R. F. Du, K. Xiao, D. W. Yang, X. Wang, Prof. J. R. Morante
Department of Electronic and Biomedical Engineering
Universitat de Barcelona
Barcelona 08028, Spain

M. J. Yi
State Key Laboratory of Advanced Welding and Joining
Harbin Institute of Technology
Shenzhen 518055, China

T. Zhang, Prof. J. Arbiol
Catalan Institute of Nanoscience and Nanotechnology (ICN2)
CSIC and BIST
Campus UAB, Bellaterra, Barcelona 08193, Spain

Prof. J. Arbiol, Prof. A. Cabot
ICREA
Pg. Lluís Companys 23, Barcelona 08010, Spain

Prof. J. Llorca
Institute of Energy Technologies
Department of Chemical Engineering and Barcelona
Research Center in Multiscale Science and Engineering
Universitat Politècnica de Catalunya
EEBE, Barcelona 08019, Spain

Prof. Y. T. Zhou
National Engineering Research Center for Marine Aquaculture
Marine Science and Technology College
Zhejiang Ocean University
Zhoushan, Zhejiang Province 316004, China
E-mail: zhouyingtang@zjou.edu.cn

ADVANCED
SCIENCE NEWS
www.advancedsciencenews.com

ADVANCED
ENERGY
MATERIALS
www.advenergymat.de

and large specific surface area (SSA), like graphene,[7] carbon nanotubes,[8] and hollow carbon spheres,[9] have been employed to disperse sulfur species and confine the volume expansion. However, the weak physical interaction between LiPS and the non-polar surfaces of these materials makes them ineffective to capture soluble LiPS, which results in a serious shuttle effect and a reduced cyclability.[10] Previous work has demonstrated that LiPS can be confined through strong chemical binding and rapid catalytic conversion at polar surfaces.[11] In this direction, the use of transition metal oxides (TMO) and sulfides (TMS) remarkably improve cycling performance. But unfortunately, polar TMO/TMS usually suffer from unsatisfying electrical conductivities that greatly limit the rate performance.

Alternatively, transition metal phosphides (TMP) with metallic character may simultaneously provide the required high electrical conductivity and polar surfaces.[12,13] Besides, TMP also show exceptional catalytic activity towards Li–S redox reactions. As an example, the Qian group showed cobalt phosphide to exhibit the best catalytic performance among several Co-based compounds and associated this experimental evidence with an appropriate p-band position.[14] Among phosphides, bimetallic compositions provide an additional degree of freedom to tune the electronic structure and optimize electrocatalytic activity in several reactions, including hydrogen and oxygen evolution,[15,16] and CO_2 reduction,[17] among others. To maximize the amount of LiPS adsorption sites and catalytic activity, the TMP should be nanostructured. In this direction, TMP nanocrystals (NCs) can provide relatively high SSAs and abundant unsaturated sites and defects to effectively reduce the reaction energy barrier.[18] To prevent their aggregation caused by the surface energy, and also compensate for the relatively high volumetric density of TMP, TMP NCs can be combined with lightweight support, which should be characterized by a large SSA to support a high dispersion of the TMP phase and high porosity to allow an effective diffusion of lithium ions.

As a proper support material, graphite C_3N_4 is based on abundant elements and it can be obtained with high SSA.[19] Besides, in contrast to graphene and carbon nanotubes, the presence of Lewis-base pyridine nitrogen in C_3N_4 can effectively interact with the strong Lewis-acid of terminal Li atoms in LiPS, thus contributing to prolonging the lifespan of LSBs.[20–22] In terms of geometric structure, graphite C_3N_4 nanosheets (s-CN) prepared by the traditional liquid-phase exfoliation method usually suffer from low SSA due to re-aggregation by van der Waals forces.[23] On the other hand, template methods to produce high-SSA C_3N_4 are cumbersome and wasteful, inappropriate for a technology with a huge potential market and thus potentially requiring enormous amounts of materials.[19]

Besides, the catalytic activity of C_3N_4-based catalysts can be significantly augmented by altering their electronic structures through tuning the surface/interface atom environment.[24,25] When combining metallic TMP NCs with n-type semiconductive C_3N_4, the charge is rearranged at the created Mott–Schottky junction and a built-in electric field appears at the TMP/C_3N_4 interphase.[25–27] This electric field with altered electron cloud density potentially promotes catalytic activity, suppress the shuttle effect, and boost lithium ion diffusion, subsequently improved Li–S performance.[28,29] Despite the great promise on regulating Li–S reaction, there is little research on

Mott–Schottky catalyst up to date. And to the best of our knowledge, there is no report investigating the electronic structure of TMP/C_3N_4 heterojunction attempt to apply for LSBs.

In the present study, we first engineer and characterize a novel porous graphite C_3N_4 tubular structure (t-CN). Subsequently, we use an electrostatic self-assembly method to blend this novel t-CN with colloidal CoFeP NCs, which we selected taking into account the catalytic activity toward Li–S reaction of single-metal cobalt/iron phosphides and its proper band alignment with CN.[30,31] The obtained tubular CoFeP@CN Mott–Schottky catalysts are then analyzed both experimentally and through theoretical calculations. Afterwards, the performance of S@CoFeP@CN cathodes is thoroughly tested and their superior cycling stability and rate capability are demonstrated. Finally, lithium–sulfur pouch cells are manufactured and their potential toward practical applications is validated.

2. Results and Discussions

t-CN was synthesized by annealing a mixture of urea and melamine that had been previously pressed at 10 MPa. The mixture was annealed at 550 °C during 4 h in air and resulted in a yellow powder (see details in the Experiment Section). No post-exfoliation or etching treatment was carried out. Scanning electron microscopy (SEM) characterization of the yellow powder displayed a hollow tubular structure with 300–500 nm outer diameter and several micrometer long tubes (**Figure 1**a). Transmission electron microscopy (TEM) confirmed the tubular morphology of the product and further displayed the tube walls to be highly porous (Figure 1b; Figure S1a, Supporting Information). Powder X-ray diffraction (XRD) patterns revealed the obtained powder to display the graphite C_3N_4 crystal structure (Figure S1b, Supporting Information). The uniform distribution of C and N in t-CN was confirmed by scanning transmission electron microscopy-electron energy loss spectroscopy (STEM-EELS) and X-ray photoelectron spectroscopy (XPS) (Figure S1a,c, Supporting Information). Meanwhile, the high-resolution XPS N1s spectrum (Figure S1d, Supporting Information) proved a high 68.3% content of pyridinic nitrogen, which could be beneficial to capture LiPS by forming Li−N bonds through its extra pair of electrons.[20]

As a reference material, s-CN was produced through the conventional liquid-phase exfoliation method. XRD and SEM analysis showed s-CN to have a similar crystallinity as t-CN, but an obviously different geometry (Figure S2a,b, Supporting Information). The Barrett–Joyner–Halenda SSA of t-CN was 186 m^2 g^{-1} and its pore volume 0.85 cm^3 g^{-1}, with a relatively narrow microporous distribution and a fraction of mesopores (Figure S2c,d, Supporting Information). This contrasted with the sevenfold lower SSA and sixfold lower pore volume obtained for s-CN, related to the different geometry. s-CN suffers from strong van der Waals interaction that drives their re-stacking and thus results in moderate surface areas. On the contrary, the folding of C_3N_4 sheets into tubular structures can effectively avoid stacking, thus providing much larger SSAs and pore volumes. A comparison of the SSA and pore volume of previously reported graphite C_3N_4 can be found in Table S1, Supporting Information. Besides a simple preparation, the t-CN reported

ADVANCED
SCIENCE NEWS
www.advancedsciencenews.com

ADVANCED
ENERGY
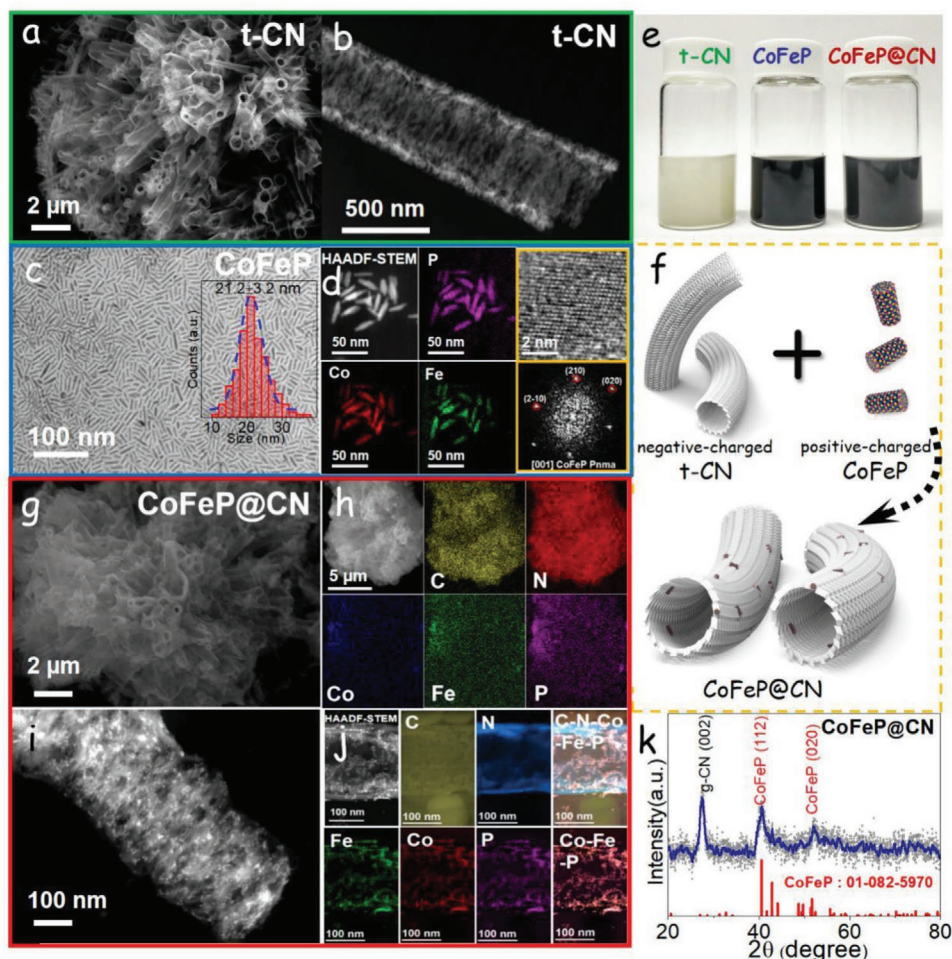MATERIALS
www.advenergymat.de

Figure 1. a) FESEM and b) TEM images of t-CN. c) TEM image of CoFeP nanocrystals and their size distribution histogram. d) (Left and middle) HAADF STEM image and EELS chemical composition maps of CoFeP nanocrystals. (Right) HRTEM image and corresponding indexed power spectrum e) Optical image of t-CN, CoFeP, and CoFeP@CN particles dispersed in solution. f) Schematic illustration of the process used to produce CoFeP@CN composites from the assembly of the two types of differently-charged particles. g) FESEM image and h) EDX compositional mapping of CoFeP@CN. i) TEM image of a CoFeP@CN composite. j) HAADF STEM image and EELS chemical composition maps of CoFeP@CN. k) XRD pattern of CoFeP@CN.

here exhibited significant advantages in terms of SSA and pore volume compared with previously reported materials.

CoFeP NCs with an elongated geometry and an average size of 21.2 ± 3.2 nm were produced using our previously reported colloidal synthesis method (Figure 1c).[32] A uniform distribution of Co, Fe, and P elements within each particle was revealed by STEM-EELS elemental composition maps (Figure 1d). High-resolution TEM (HRTEM) and XRD characterization proved the CoFeP NCs to have an orthorhombic crystal phase belonging to the *pnma* space group (JCPDS 01-082-5970, Figure 1d; Figure S3, Supporting Information). SEM-energy dispersive X-ray spectroscopy (EDX) analysis revealed the ratio of the elements of Co:Fe:P to be close to 1:1:1.2 (Figure S3b, Supporting Information), with the small excess of phosphorous most probably located at the NC surface and playing a ligand role.[33]

Zeta potential measurements (Figure S4, Supporting Information) revealed the different signs of the charge at the surface of CoFeP NCs (positively charged) and t-CN (negatively charged). Taking advantage of this different charge, CoFeP@CN nanocomposites with a 1:1 mass ratio were

prepared by a simple solution-phase electrostatic self-assembly method (Figure 1e,f).[34] This process maintained the tubular morphology of t-CN intact (Figure 1g).[35] EDX elemental maps showed a homogeneous dispersion of CoFeP NCs throughout the t-CN surface (Figure 1h). High-angle annular dark-field (HAADF) images further confirmed the homogeneous distribution of CoFeP NCs on t-CN (Figure 1i). In HAADF images, CoFeP NCs with a higher atomic number possess a stronger ability to scatter electrons than t-CN, thus appear much brighter. XRD patterns of the composites displayed diffraction peaks corresponding to both crystallographic structures: the diffraction peak at 27.4° belonging to the (002) plane of graphite C_3N_4 and the diffraction peaks at 40.5° and 51.7° corresponding to the (112) and (020) planes of CoFeP (Figure 1k).

Graphite C_3N_4 is an n-type semiconductor. Its computed work function (WF) is around 4.4 eV and its band gap is ≈2.6 eV.[36] On the other hand, the WF of metallic CoFeP can be estimated at around 4.8 eV (Figure S5, Supporting Information).[27,37] When placed in contact, the difference in Fermi levels drives an injection of electrons from C_3N_4 to CoFeP, until
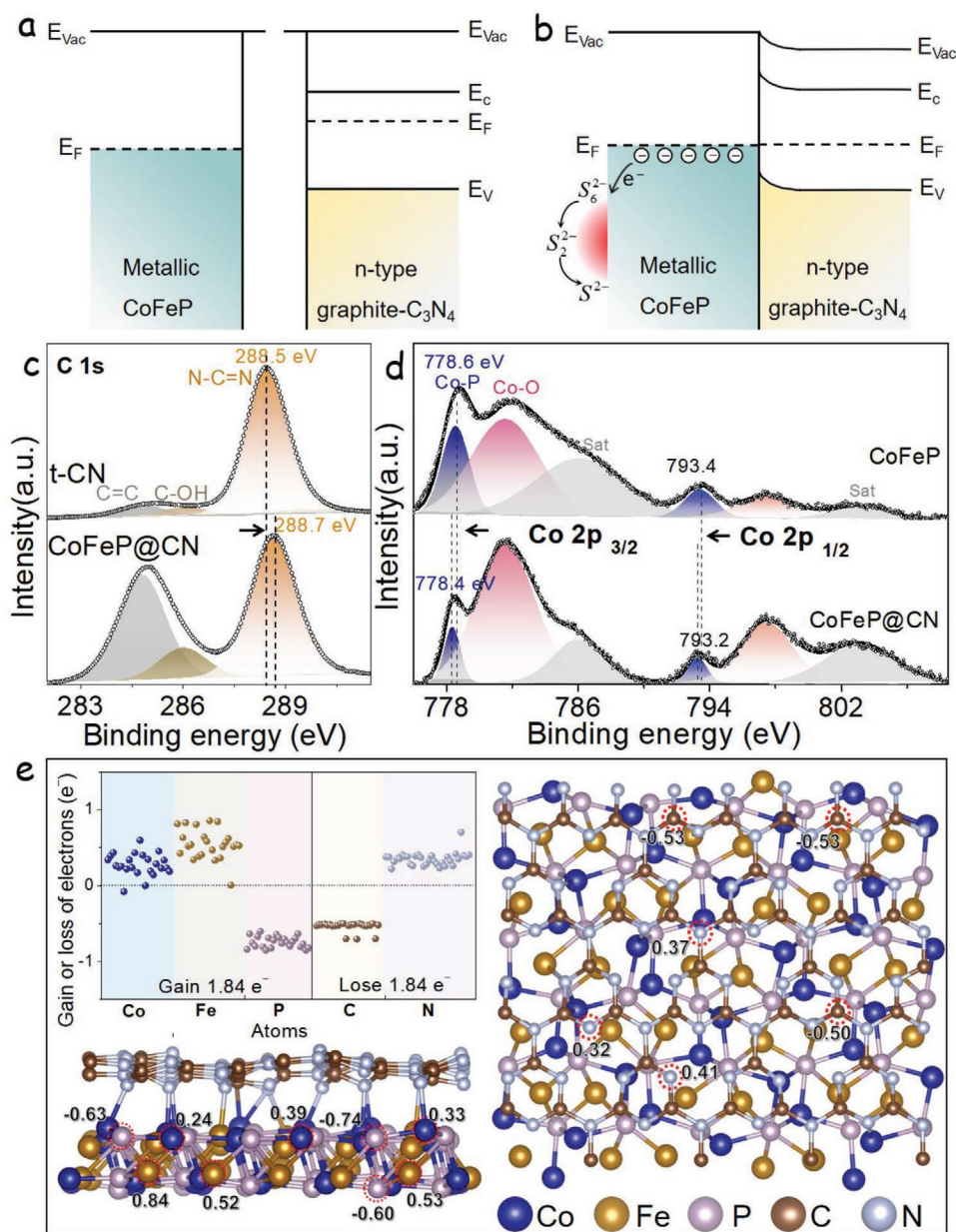
**ADVANCED
SCIENCE NEWS**

www.advancedsciencenews.com

**ADVANCED
ENERGY
MATERIALS**

www.advenergymat.de

Figure 2. a,b) Energy band diagrams of metallic CoFeP and n-type semiconducting graphite-C_3N_4 before (a) and after (b) Schottky contact formation. E_{vac} = vacuum level, E_c = conduction band minimum, E_v = valence band maximum, E_F = Fermi level. c) C 1s high-resolution XPS spectra from t-CN and CoFeP@CN. d) Co 2p high-resolution XPS spectra from CoFeP and CoFeP@CN. e) Gain/loss of electrons of the different atoms calculated by Bader charge analysis.

the WFs of the two materials at the interface are equilibrated. At equilibrium, an upward bending of the electron energy bands of C_3N_4 at the interface and an electric field pointing from C_3N_4 to CoFeP remain, forming a Mott–Schottky heterostructure (**Figure 2**a,b).[27,38]

High-resolution XPS valence band spectra confirmed the semiconducting and metallic character of t-CN and CoFeP, respectively (Figure S6b, Supporting Information). The XPS valence band spectrum of CoFeP@CN composite also showed the Fermi level to lie within a band of states, as in the case of CoFeP. The C 1s spectra of t-CN and CoFeP@CN showed

three bands (Figure 2c). The band at 284.8 eV corresponding to adventitious C—C was used as a reference. The main C 1s peak from t-CN was located at 288.5 eV and corresponded to the N—C=N chemical environment of carbon nitride.[15] In the composite material, a significant blue shift of the this N—C=N band, up to 288.7 eV, was obtained. This shift was related to the electron loss of t-CN when in contact with CoFeP NCs.[15,39]

The Co 2p spectrum of CoFeP displayed two bands at 778.6 eV ($2p_{3/2}$) and 793.4 eV ($2p_{1/2}$), associated with a Co—P chemical environment (Figure 2d). Two additional bands at 781.6 eV ($2p_{3/2}$) and 797.5 eV ($2p_{1/2}$) were assigned to oxidized

**ADVANCED
SCIENCE NEWS**

www.advancedsciencenews.com

**ADVANCED
ENERGY
MATERIALS**

www.advenergymat.de

cobalt species arising from the exposure of the sample to air during handling and transportation.[26,40] Additional shake-up satellite peaks located at 786.1 and 803.2 eV were also discerned. A slight shift of the Co 2p bands toward lower binding energies was observed when supporting the CoFeP NCs on t-CN, consistent with a charge arrangement at the interface and an increased electron density in Co atoms.[26,40]

Similar results were obtained when analyzing the Fe 2p spectra, displaying bands associated with a Fe-P environment at 707.6 eV ($2p_{3/2}$) and 720.0 eV ($2p_{1/2}$), and bands associated to an oxidized environment at 710.7 eV ($2p_{3/2}$) and 724.2 eV ($2p_{1/2}$).[41] A similar band shift was observed for Fe and Co when contacting CoFeP with t-CN (Figure S6c, Supporting Information).

A larger degree of surface oxidation was observed in the CoFeP NCs supported on t-CN than in the unsupported NCs. However, XRD patterns in Figure 1k confirmed the presence of the CoFeP phase in both samples, indicating an overall low content of $CoPO_x$ or $FePO_x$ in CoFeP@CN samples. Notice in any case that recent reports have demonstrated that TMPs with an oxidized surface can still effectively promote LiPS capture through the metal oxide and phosphate sites, which can form strong metal-S and oxide P-Li bonds, respectively.[42]

Density functional theory (DFT) calculations further demonstrated a charge redistribution at the atomic scale when placing the two materials in contact. According to XRD results of CoFeP, we constructed a slab model based on the exposed CoFeP (112) facet and a graphite C_3N_4 monolayer to evaluate the charge transfer at the interface. Bader charge analysis calculated charge redistribution at the CoFeP/C_3N_4 interface and quantified that the bottom CoFeP unit cell gains 1.84 electrons from the CN layer. The gain/loss of electrons of the different atoms is displayed in Figure 2e.

Sulfur was introduced within the CoFeP@CN by a melt-diffusion process (see the Experimental Section for details). SEM characterization of the obtained S@CoFeP@CN composites revealed the tubular structure of CoFeP@CN to be conserved after S addition (Figure S7a, Supporting Information). XRD patterns confirmed the presence of crystalline sulfur (JCPDS No. 08-0247) within S@CoFeP@CN composites (Figure S7b, Supporting Information)[43] and a homogenous distribution of the different elements was proven by EDS mapping (Figure S7c, Supporting Information). With the introduction of sulfur, the SSA value sharply decreased from 86.8 m^2 g^{-1} (CoFeP@CN) to 1.8 m^2 g^{-1} (S@CoFeP@CN), as shown in Figure S7d, Supporting Information. Thermogravimetric analysis allowed quantifying the sulfur content in the S@CoFeP@CN composite at about 70 wt%, consistent with the nominal amount introduced (Figure S7e, Supporting Information). The same preparation process was employed to load equivalent amounts of sulfur into other hosts, CoFeP, t-CN, and Super P, which were used as reference materials when testing CoFeP@CN performance (Figure S8, Supporting Information).

The LiPS adsorption ability of the host material plays a key role in suppressing the shuttle effect in LSBs, thus it is the first property analyzed when screening different materials toward finding a good sulfur host. To evaluate LiPS affinity, the same amount of the different hosts was immersed into a 10 mM LiPS (≈Li_2S_6) solution. After 12 h, clear differences in the color of the solution containing the different materials were observed,

indicating a different degree of LiPS adsorption (**Figure 3**a; Figure S9, Supporting Information). Adsorption results were also confirmed by analyzing the UV–vis spectra of the solutions in the range of 400–500 cm^{-1} (Figure 3b).[31,44,45]

Comparing the t-CN developed here with s-CN obtained by conventional exfoliation methods, we observed how the t-CN exhibited a much higher LiPS adsorption ability as qualitatively observed by the much lighter color of its final solution (Figure S9, Supporting Information). This result is consistent with the larger SSA and pore volume of t-CN compared with s-CN. Subsequently, we compared the LiPS adsorption ability of CofeP@CN, CoFeP, t-CN, and Super P. We noticed that the color of the solutions containing t-CN and/or CoFeP was much lighter than that of the solution containing Super P, inferring a stronger interaction of t-CN and CoFeP with LiPS. The clearest solution was obtained with the presence of CoFeP@CN, demonstrating that the composite was characterized by an additional LiPS adsorption capability when compared with the same amount of each of the components.

Additional XPS analyses were conducted to understand the chemical interaction between CoFeP@CN and LiPS during the Li_2S_6 adsorption experiment. From the comparison of the N 1s spectra of the composite before and after Li_2S_6 adsorption (Figure 3c), a distinct shift could be observed in the pyridinic-N band from 399.1 to 399.3 eV.[46] The small additional band in the CoFeP@CN-LiPS sample at 397.8 eV is attributed to N-Li bond formation during the adsorption process.[47,48] These results were consistent with previous reports demonstrating that LiPS could anchor on active nitrogen sites through dipole–dipole interactions. This Li-N chemical interaction certainly contributes to inhibiting the shuttling effect.[49]

Meanwhile, the Co $2p_{3/2}$ and Fe $2p_{3/2}$ XPS spectra displayed in Figure 3d,e show that after interaction with Li_2S_6, bands corresponding to Co-P or Fe-P environments suffered an obvious shift to higher binding energy, indicating the formation of Co-P/S and Fe-P/S bonds.[30,44] Additionally, the relative intensity of the oxide Co and Fe bands decreased in the CoFeP@CN-LiPS sample, which was also consistent with the formation of strong Co-S and Fe-S bonds during the Li_2S_6 adsorption process which partially prevented the surface oxidation.[42,44] In Figure 3f, a band shift can be also found in the P 2p spectrum, which might be attributed to the accumulation of electrons at P sites related to the interaction with terminal Li atoms in Li_2S_6 species.[50,51]

DFT calculations were conducted to determine the affinity between chained LiPS species and CoFeP and t-CN. The binding energies and atomic structures between LiPS (Li_2S_2, Li_2S_4, Li_2S_6, and Li_2S_8) and CoFeP (001) and graphite C_3N_4 (001) surfaces were calculated (Figure S10, Supporting Information). Compared with previous reports on graphitic carbon,[52,53] the more negative LiPS binding energies on the surface of CoFeP and graphite C_3N_4 (Figure 3i) indicated stronger adsorption of soluble LiPS on the latter two. The chemical adsorption of LiPS with CoFeP@CN is mainly originated from the treble interactions: i) Lewis-base pyridine N in t-CN with extra pair of electrons interact with Lewis acid of terminal $Li^{\delta+}$ atoms in LiPS; ii) chemical bonding between the terminal $S^{\delta-}$ atoms and $Co^{\delta+}$/$Fe^{\delta+}$ atoms in CoFeP NCs; and iii) chemical bonding between $Li^{\delta+}$ atoms and $P^{\delta-}$ atoms. Taking Li_2S_6-adsorbed structures as

**ADVANCED
SCIENCE NEWS**

www.advancedsciencenews.com

**ADVANCED
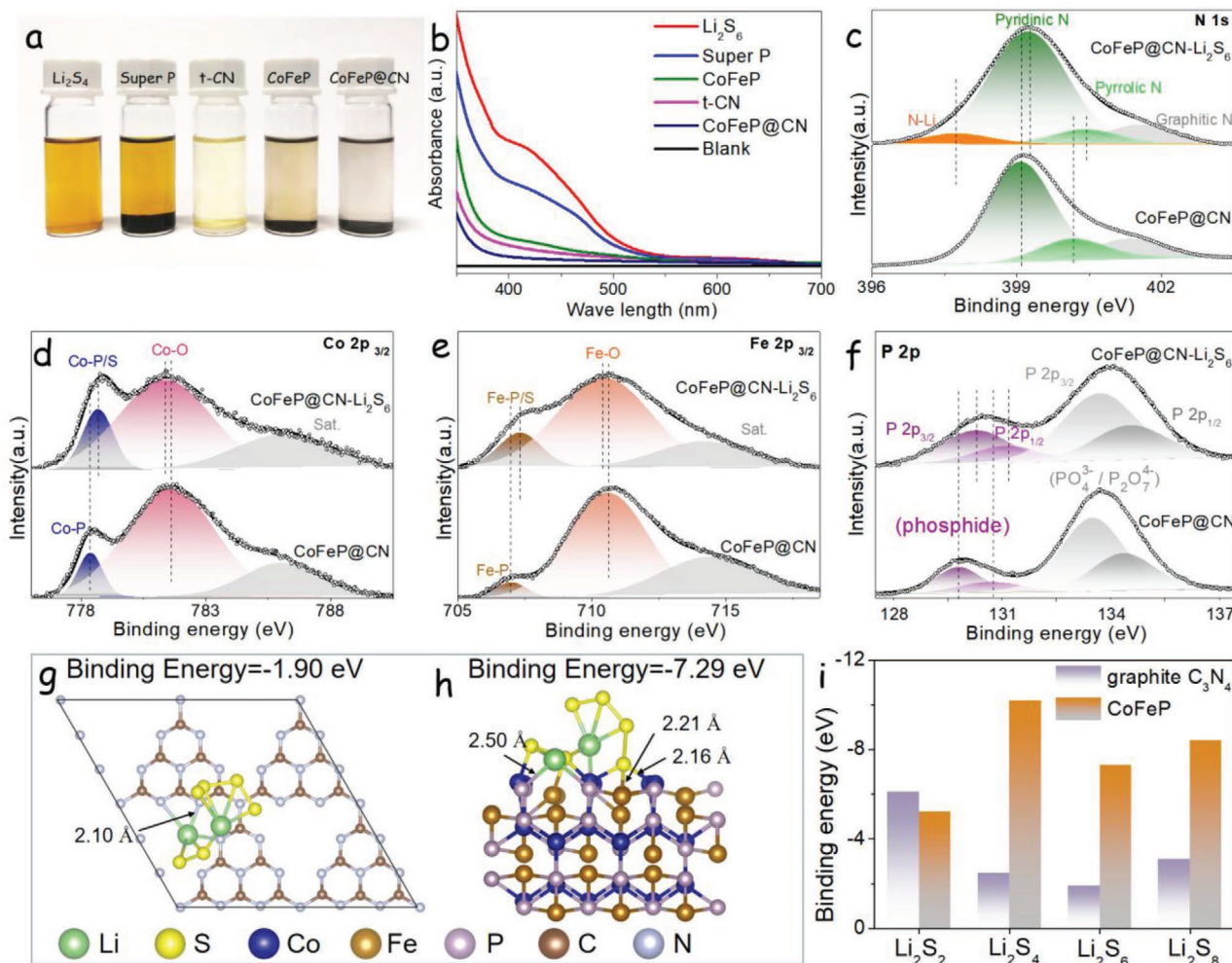ENERGY
MATERIALS**

www.advenergymat.de

Figure 3. LiPS adsorption ability. a) Optical image and b) UV–vis spectra of the polysulfide solution containing the different adsorbers overnight. High-resolution XPS spectrum of c) N 1s, d) Co 2p$_{3/2}$, e) Fe 2p$_{3/2}$, and f) P 2p before and after CoFeP@CN interaction with Li$_2$S$_6$. g,h) Relaxed Li$_2$S$_6$-adsorbed structures on the surface of g) graphite-C$_3$N$_4$ and h) CoFeP calculated with DFT. i) The calculated binding energy between LiPSs (Li$_2$S$_2$, Li$_2$S$_4$, Li$_2$S$_6$, and Li$_2$S$_8$) and graphite-C$_3$N$_4$ and CoFeP surfaces.

an example (Figure 3g,h), Li atoms preferentially bind to N sites in C$_3$N$_4$, with a Li–N bond distance in the C$_3$N$_4$/Li$_2$S$_6$ model of only 2.10 Å. S atoms tend to bind with Co and Fe atoms into a small 2.16 Å Co–S and 2.21 Å Fe–S bond distance. Besides, the calculated Li–P bond distance was 2.50 Å. Overall, the coexistence of multiple adsorption sites to strongly capture the LiPS by Li–N, Fe/Co–S and Li–P bonds endow the great potential of CoFeP@CN composite as S host in LSBs.

To evaluate the ability of host materials to catalytically accelerate the kinetics of polysulfide conversion, cyclic voltammetry (CV) tests of Li$_2$S$_6$ symmetrical cells were conducted in the voltage window −1 to 1 V. As shown in **Figure 4**a, t-CN, CoFeP, and CoFeP@CN electrodes showed significantly different CV curves. The symmetric curves of CoFeP@CN electrodes exhibited higher peak current densities than t-CN and CoFeP electrodes, demonstrating the combination of both materials within a heterostructured composite to boost the electrochemical activity of polysulfide conversion.[54] When similar experiments were carried out on CoFeP@CN electrodes without Li$_2$S$_6$

addition in the electrolyte (Figure S11, Supporting Information), the approximately rectangular-shaped CV curves obtained demonstrated a pure capacitive behavior rather than a chemical reaction. This result implies that Li$_2$S$_6$ was the unique electrochemically active species in the system.[43]

The electrochemical performance of the electrodes was evaluated using LSBs assembled in coin cells. Figure 4b and Figure S13, Supporting Information display the CV curves obtained from S@t-CN, S@CoFeP, S@CoFeP@CN, and S@Super P cells, respectively. All curves showed two reduction peaks (peak I and II), which corresponded to a two-step S reduction process upon cathodic scanning: peak I was attributed to the transformation from S$_8$ to soluble long-chain LiPSs (Li$_2$S$_x$, 4 ≤ x ≤ 8), followed by a further reduction to insoluble Li$_2$S$_2$/Li$_2$S in peak II.[53,55] The anodic peak (peak III) was ascribed to the reverse multistep oxidation process of short-chain sulfides to LiPS and eventually to sulfur. S@CoFeP@CN electrodes exhibited the most intense peak currents and the cathodic/anodic peaks located at the most positive/negative potentials
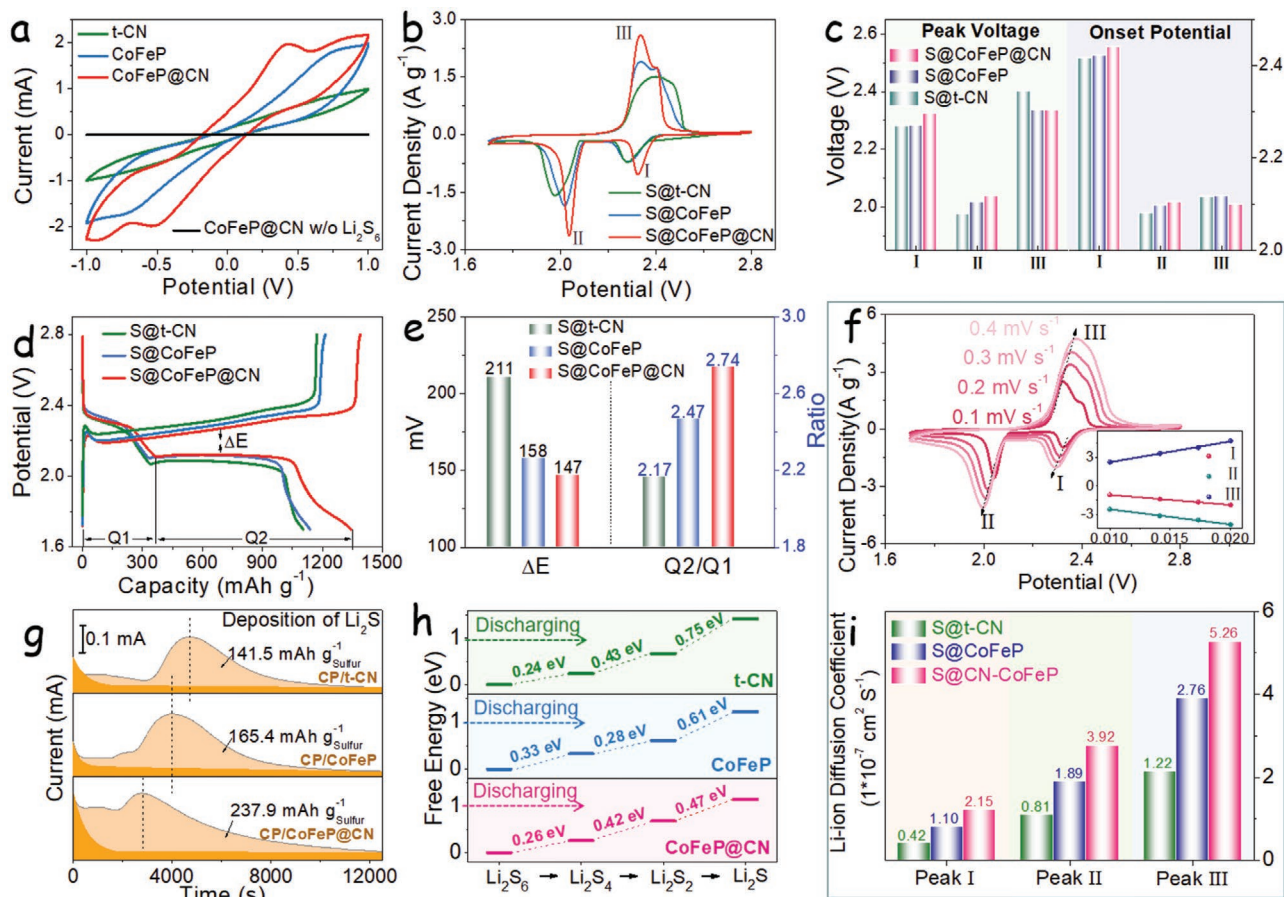
Figure 4. Polysulfide redox activity. a) CV profiles of symmetrical cells with three different host materials using an electrolyte containing 0.5 mol L^{-1} Li$_2$S$_6$ and 1 mol L^{-1} LiTFSI dissolved in DOL/DME (v/v = 1/1). b) CV profiles of lithium–sulfur coin cells. c) Peak voltages and onset potentials obtained from CV curves with different electrodes. d) Charging/discharging curves of different electrodes at the current rate of 0.1 C. e) DE and Q2/Q1 values obtained from charging/discharging curves. f) CV curves of S@CoFeP@CN electrode at various scan rates. Inset shows the CV peak current for peaks I, II, and III versus the square root of the scan rates. g) Potentiostatic discharge profile of Li$_2$S nucleation at 2.05 V on different electrodes with Li$_2$S$_8$ catholyte. h) DFT-calculated Gibbs free energy changes of reduction of LiPS (Li$_2$S$_6$, Li$_2$S$_4$, Li$_2$S$_2$, and Li$_2$S) in the presence of three hosts. i) Li-ion diffusion coefficient value at peaks I, II, and III.

(Figure 4c). This result indicated that among the tested materials, CoFeP@CN was the most effective catalyst in promoting the polysulfides redox reaction kinetics. Catalytic activities were further quantified through the onset potentials at 10 μA cm^{-2} current density beyond the baseline current (Figure S12, Supporting Information).[43,53] Among the three kinds of electrode tested, the onset potentials of S@CoFeP@CN were the highest/lowest in reduction/oxidation peaks (Figure 4c), demonstrating an effective decrease of the overpotential in LiPS conversion reaction.

Charging/discharging tests at different current rates were conducted for the three types of electrodes. At the current rate of 0.1 C, all electrodes showed one charging and two discharging plateaus, consistently with the measured CV peaks (Figure 4d). A voltage gap ΔE found between the oxidation and the second reduction plateaus introduced polarization potential in the redox reaction, which was taken as the voltage gap at 50% discharged capacity.[43,56] S@CoFeP@CN electrodes displayed a lower polarization potential (ΔE = 147 mV) than S@CoFeP (ΔE = 158 mV), S@t-CN electrodes (ΔE = 211 mV), and

S@Super P electrodes (ΔE = 223 mV, Figure S13b, Supporting Information), demonstrating the synergism between the two components within CoFeP@CN to accelerate the LiPS conversion kinetics. S@CoFeP electrodes exhibited a much better polarization than S@CN because of the intrinsic metallic and semiconductor nature of CoFeP and t-CN, respectively. S@CoFeP@CN electrodes also exhibited the lowest overpotentials in the phase conversion between soluble Li$_2$S$_4$ and insoluble Li$_2$S$_2$/Li$_2$S (Figure S14, Supporting Information).[57]

The catalytic activity of the host materials toward the LiPS conversion reaction can be quantified by the ratio Q2/Q1, where Q1 and Q2 denote the capacity of the two discharge plateaus (Figure 4d). Q1 corresponds to the reduction of sulfur to soluble LiPS (S$_8$ + 4Li$^+$ + 4e$^-$ → 2Li$_2$S$_4$) and Q2 to the subsequent transfer to insoluble sulfide (2Li$_2$S$_4$ + 12Li$^+$ + 12e$^-$ → 8Li$_2$S), respectively.[43] During the second plateau (Q2), the final product Li$_2$S generally accompanied by the presence of Li$_2$S$_2$ due to sluggish reaction kinetics, which inhibits the release of capacity during the Q2 stages. Thus, while the capacity ratio should be Q2/Q1 = 3, taking into account the electrons involved

**ADVANCED
SCIENCE NEWS**
www.advancedsciencenews.com

**ADVANCED
ENERGY
MATERIALS**
www.advenergymat.de

in each process (4 for Q1 and 12 for Q2), generally ratios lower than 3 are obtained. Additionally, the LiPS shuttle effect is also reflected in a capacity loss. In all cases, the higher Q2/Q1, the better the catalytic ability. As displayed in Figure 4e, S@CoFeP@CN exhibited the highest $Q2/Q1$ ratio at 2.74, close to the theoretical value and well above that of S@CoFeP (2.47), S@t-CN (2.17), and S@Super P (1.88, Figure S13b, Supporting Information), which further evidenced the synergistic effect towards LiPS redox reaction obtained when combining both materials in the CoFeP@CN Mott–Schottky heterostructure.

The efficiency of LSBs is limited by the high charging/discharging overpotentials that are in large part related to the sluggish kinetics of deposition/dissolution of insulating solid Li_2S.[58,59] Thus, we performed Li_2S nucleation and dissolution experiments to further assess the performance of the materials developed here. For this experiment, electrode materials were supported on carbon paper (CP, see details in the Supporting Information) which is able to soak the catholyte. From the potentiostatic discharge profiles in Figure 4g, CP/CoFeP@CN exhibited the sharpest nucleation peak and the fastest responsivity toward Li_2S nucleation, when compared with CP/t-CN and CP/CoFeP electrodes. According to Faraday's law, the conversion capacity was obtained by integrating the area below the current curves. The Li_2S deposition capacity of CP/CoFeP@CN (237.9 mAh g^{-1}) was larger than that of CP/t-CN and CP/CoFeP electrodes (141.5 and 165.4 mAh g^{-1}, respectively), demonstrating that CoFeP@CN could effectively decrease the overpotential and promote the Li_2S nucleation reaction.[43,59] We investigated the kinetics of the Li_2S dissolution experiment using a similar protocol (Figure S15, Supporting Information). In the potentiostatic charge curves, the highest peak current densities and shortest peak current time were obtained for the CP/CoFeP@CN electrode, indicating a faster Li_2S dissolution. Moreover, CP/CoFeP@CN electrodes revealed a 532 mAh g^{-1} dissolution capacity, much higher than that measured for the other electrodes (406 mAh g^{-1} for CP/t-CN and 466 mAh g^{-1} for CP/CoFeP).

To further verify the catalytic activity of catalysts on the LiPS conversion, the Gibbs free energy changes during the LiPS reduction on t-CN, CoFeP, and CoFeP@CN were calculated (Figure 4h). For the liquid-to-solid (Li_2S_6 to Li_2S) nucleation reaction, all LiPS reduction steps were endothermic with relatively large positive Gibbs energy barriers, especially for the Li_2S_2 to Li_2S conversion, which was the rate-limiting step.[60] However, CoFeP@CN exhibited the lowest Gibbs free energy changes (0.47 eV) than CoFeP and t-CN (0.61 and 0.75 eV, respectively), and this value is much lower than previously reported graphene or N-doped graphene (above 1 eV), which suggested that the composite CoFeP@CN was a relatively excellent catalyst to promote the LiPS conversion kinetics.[57,61,62] The lowest Gibbs free energy change in the reduction of Li_2S_2 measured for CoFeP@CN was consisted of Li_2S nucleation test and overall, these results demonstrated that CoFeP@CN Mott–Schottky heterostructure catalyst plays a catalytic role to accelerate the Li_2S formation.

To obtain further insight into the role of CoFeP@CN in accelerating the LiPS reaction, electrode kinetics were further analyzed by measuring CV at different scan rates, from 0.1 to 0.4 mV s^{-1} (Figure 4f). When increasing the scan rate, the two

cathodic peaks shifted to more negative potentials and the anodic peak shifted to a positive potential, overall increasing the polarization voltage. The linear relationship between the anodic/cathodic peak current and the square root of the scanning rates pointed at a diffusion-limited reaction (inset in Figure 4f). Thus, the classical Randles–Sevcik equation was used to calculate the Li$^+$ diffusivity in the process:[63,64]

$$I_p = (2.69 \cdot 10^5) n^{1.5} A D_{Li^+}^{0.5} C_{Li^+} v^{0.5} \tag{1}$$

where I_p is the peak current, n is the number of charge transfer, A is the geometric electrode area, D_{Li+} is the Li$^+$ diffusion coefficient, C_{Li+} is the concentration of Li$^+$ in the electrolyte, and v is the scan rate. At a given n, A, and C_{Li+}, sharper $I_p/v^{0.5}$ slopes denote faster Li$^+$ diffusion. As displayed in Figure 4f,i and Figure S16, Supporting Information, S@CoFeP@CN electrodes exhibited the sharpest slopes for the 3 peaks, thus the highest Li$^+$ diffusivity during the redox reactions. In peak I, II, and III, the Li$^+$ diffusion coefficients of S@CoFeP@CN were 2.15, 3.92, and 5.26 $\times 10^{-7}$ cm^2 S^{-1}, respectively. Li$^+$ diffusivity strongly depends on the viscosity of the electrolyte containing LiPS and the accumulation of insulating Li_2S/Li_2S_2 on the electrode.[43,64] The highest diffusivities obtained for the CoFeP@CN host reflected that the improved reaction kinetics by the Mott–Schottky catalyst was in part related to a confined shuttle effect and an improved catalytic activity towards LiPS conversion, consistently with the above results.

To further demonstrate the influence of the Mott–Schottky heterostructure on the catalytic activity of CoFeP@CN electrodes toward the Li–S reaction, we compared the catalytic performance of CoFeP@CN electrodes with that of two additional electrode architectures that minimized or reduced the interaction between the two materials, CoFeP and t-CN. In one first design, we divided the electrode area into 4 parts, and loaded two of them with CoFeP and two of them with t-CN, so the physical, chemical and electronic interaction between the two materials was minimized (CoFeP⊗CN, Figure S17a, Supporting Information). In a second design, we physically mixed CoFeP particles with t-CN (CoFeP+CN, Figure S17b, Supporting Information), thus reducing but still maintaining some interaction between the two materials. When comparing the CV curves of the three electrodes (S@CoFeP@CN; S@CoFeP⊗CN; and S@CoFeP+CN, Figure S17c, Supporting Information), we observed that the S@CoFeP@CN electrode exhibited the highest peak current and the most positive peak potential in the reduction process. On the other hand, the worst performance was obtained for the electrode having no interaction between the two materials, S@CoFeP⊗CN. Similar results were obtained in the Li_2S nucleation test (Figure S17d, Supporting Information), with CP/CoFeP@CN electrodes showing the fastest peak time and the highest Li_2S nucleation capacity, and CP/CoFeP⊗CN showing the worse performance as a consequence of the lack of heterostructure formation. CoFeP+CN electrodes showed an intermediate behavior as they contained a non-optimized mixture of the two compounds with a partial heterostructure formation. Both CV measurements and Li_2S nucleation test further pointed toward the association of the improved catalytic effect with the formation of CoFeP/CN Mott–Schottky heterojunctions.
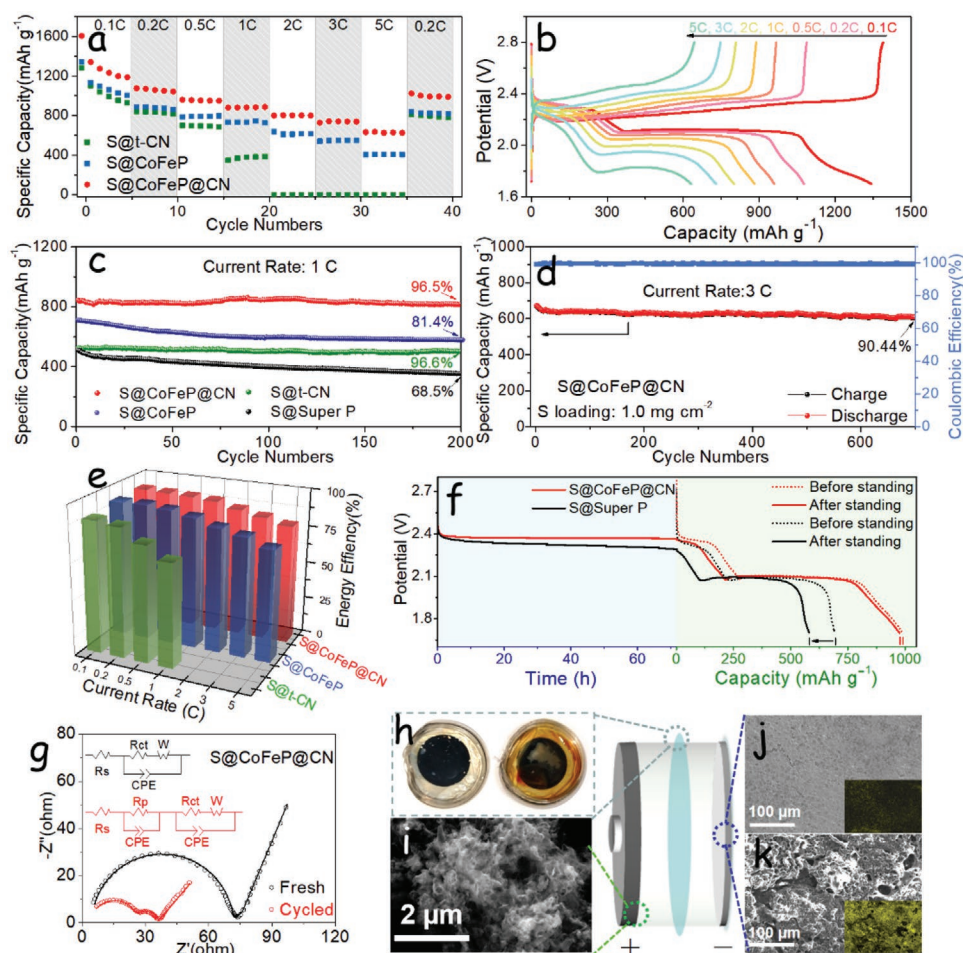
Figure 5. Electrochemical performance of lithium–sulfur coin cells. a) Rate performances of S@CoFeP@CN, S@CN, and S@CoFeP electrodes. b) Charging/discharging curves of S@CoFeP@CN electrode at current rates from 0.1 to 5 C. c) Capacity retention of different electrodes at 1 C over 200 cycles. d) Cycling stability of S@CoFeP@CN electrode at 3 C over 700 cycles. e) The energy efficiency of three different electrodes at various current rates. f) Change of open-circuit voltage at 72 h self-discharge test and comparison of discharge curves before and after standing of S@Super P and S@CoFeP@CN electrodes. g) EIS plot of S@CoFeP@CN electrode before and after 200 cycles at 1 C. The Nyquist curves were fitted considering the equivalent circuits shown as inset, where R_s, R_p, R_{ct}, and W stand for the resistance of the electrolyte, insoluble Li_2S_2/Li_2S precipitation layer, interfacial charge-transportation, and semi-infinite Warburg diffusion, respectively; and CPE stands for the corresponding capacitance. After cycling at 1 C for 200 cycles: h) optical images of membranes recovered from coin cells based on S@CoFeP@CN electrode (left) and S@Super P electrode (right); i) SEM image of S@CoFeP@CN electrode; j,k) SEM image of lithium foil recovered from a coin cell based on S@CoFeP@CN (j) and S@Super P (k). Inset images in (j,k) show the map of the sulfur signal detected by EDX.

Figure 5a shows the rate performances of the three types of electrodes tested, at current rates from 0.1 to 5 C. S@CoFeP@CN electrodes systematically exhibited the highest discharge capacity at any current rate among the different electrodes tested. A high initial discharge capacity at 1607 mAh g^{-1} was measured, demonstrating a very high sulfur activity and utilization. Even at high current rates of 5 C, the average capacity stabilized at 630 mAh g^{-1}, well above the capacity obtained for S@CoFeP and S@CN electrodes, 406 and 0.23 mAh g^{-1}, respectively. When the current rate was returned to 0.2 C, the average capacity of the cells with S@CoFeP@CN electrodes returned to ≈1010 mAh g^{-1}, demonstrating remarkable reversibility and stability. It is worth mentioning that a negligible capacity was obtained from pure CoFeP@CN electrodes, that is, without sulfur, under the same measuring conditions (Figure S18, Supporting Information). The galvanostatic charging/discharging

profiles of S@CoFeP@CN at different current rates are displayed in Figure 5b. All discharge curves exhibited two well-defined discharge plateaus, even at a current density of 5 C. In contrast, S@CoFeP electrodes displayed a similar shape but much lower capacity (Figure S19a, Supporting Information), and S@CN electrodes showed a high polarization potential and no capacity response above 2 C (Figure S19b, Supporting Information), due to the huge potential barrier and the limited redox kinetics of the electrode material. And change of the $Q2/Q1$ ratio with the current rate can be found in Figure S20, Supporting Information.

To evaluate the long-term cycling stability of the different host materials, cells were continuously cycled at 1 C (Figure 5c). The initial discharge capacity of S@CoFeP@CN electrodes at 1 C was about 844 mAh g^{-1}, and retained about 96.5% capacity after 200 cycles, 814 mAh g^{-1}. Significantly lower capacity

**ADVANCED
SCIENCE NEWS**

www.advancedsciencenews.com

**ADVANCED
ENERGY
MATERIALS**

www.advenergymat.de

retention was obtained for S@CoFeP electrodes (81.4%), which suffered a notable capacity decay during the first 100 cycles. This result might be attributed to the relatively low SSA of the CN-free CoFeP host (38 $m^2\,g^{-1}$ experiment result, that is, a 50% of the theoretical SSAs of geometric model, Figure S21, Supporting Information), associated with the high atomic mass of its constituents. The partially aggregated CoFeP NCs had insufficient active sites to anchor the initial excess of sulfur species, but as the S content decreased, its stability improved owing to its sulfiphilic surface. Capacity retention differences can be clearly observed comparing the charging/discharging profiles at various cycles (Figure S22a,c, Supporting Information). Surprisingly, even though S@t-CN electrodes exhibited a relatively low initial capacity, they were characterized by remarkable stabilities, with retention of about 96.6% after 200 cycles. This superior stability can be explained by the t-CN with tubular structure here presented that provides a very high SSA to trap LiPS species by the lithiophilic sites and a high pore volume to accommodate the volume change during cycles, although a poor conductivity resulted in a large voltage gap (Figure S21b, Supporting Information). Additional cycling was carried out on the S@CoFeP@CN electrodes at a higher current rate of 3 C (Figure 5d; Figure S23, Supporting Information). After 700 stable cycles at 3 C, S@CoFeP@CN electrodes still provided a discharge capacity of 606 mAh g^{-1}, showing an average 0.014% decay per cycle and a stable and high Columbic efficiency above 99.6%.

The compositional ratio of the host material certainly affected its catalytic performance. To determine the optimum composition, three samples with different CoFeP:t-CN weight ratio (one above and one below the 50% CoFeP:t-CN ratio analyzed in the rest of this work) were prepared and characterized. The weight ratios studied were 25%CoFeP:75%t-CN, 50%CoFeP:50%t-CN, and 75%CoFeP:25%t-CN, and the samples were named as 25%CoFeP@CN, 50%CoFeP@CN, and 75%CoFeP@CN, respectively. S@50%CoFeP@CN electrodes exhibited better rate performance and higher capacity than S@25%CoFeP@CN (Figure S24, Supporting Information), which can be attributed to a larger Mott–Schottky interface and catalytic sites. On the other hand, S@75%CoFeP@CN electrodes provided the worse performances, which is explained by a reduced amount of catalytic sites and thus of catalytic activity related to the aggregation of the CoFeP NCs on the surface of t-CN, as observed by TEM characterization (Figure S25, Supporting Information).

The LSB energy conversion efficiency in the charging/discharging process, different from the above Columbic efficiency, was calculated by the ratio of energy output/input ($E = \int UIdt$).[53,65] At 0.1 C current rate, the three types of electrode tested exhibited a high energy efficiency of around 90% (Figure 5e). When increasing the current rate, S@CoFeP@CN displayed the highest and most stable energy efficiency, retaining 89.91% efficiency at 1 C and 79.89% at 5 C, well above the 69.37% for S@CN at 1 C and 74.61% for S@CoFeP at 5 C. We associate this higher energy efficiency to the lower polarization potential of CoFeP@CN electrodes, which was in turn related to its excellent catalytic properties, as discussed above.

Self-discharging is another main drawback of LSBs. The self-discharge profiles of S@CoFeP@CN and S@Super P electrodes are presented in Figure 5f. The open-circuit voltage

(OCV) of the cells was measured during 72 consecutive hours after 30 stabilization cycles. During this time, S@Super P electrodes showed a significant OCV decrease to 2.288 V, denoting a notable self-discharging. On the other hand, the S@CoFeP@CN electrode maintained a much more stable OCV, with a final voltage of 2.367 V, suggesting superior stability against self-discharge. Self-discharging may be more clearly seen in the right side of Figure 5f, where the dash/solid curves present the discharge curves before/after 72 h of rest under a current rate of 0.2 C. After the 72 h rest period, an obvious capacity decay, from 691 to 580 mAh g^{-1}, was obtained from the S@Super P electrode, consistently with the OCV change. On the other hand, just a slight capacity loss was measured from the S@CoFeP@CN electrode, from 989.2 to 975.5 mAh g^{-1}. Under shelf storage conditions, the capacity of batteries shows exponential decay with storage time t_S, so the self-discharge behavior can be quantitatively analyzed using the following equation:[66]

$$Q_D = Q_D^0 e^{-K_S t_S} \tag{2}$$

Q_D^0 and Q_D are discharge capacities before and after storage for a period of time t_S, so the self-discharge constant K_S can be easily obtained from:

$$K_S = \ln\frac{Q_D^0}{Q_D} \cdot \frac{1}{t_S} \tag{3}$$

While S@Super P electrodes were characterized by a K_S value of $2.40 \times 10^{-3}\,h^{-1}$, an order of magnitude lower self-discharge constant was obtained for S@CoFeP@CN, $K_S = 1.96 \times 10^{-4}\,h^{-1}$, S@CoFeP, $K_S = 5.9 \times 10^{-4}\,h^{-1}$, and S@t-CN, $K_S = 6.5 \times 10^{-4}\,h^{-1}$, electrodes in (Figure S26, Supporting Information). The lower self-discharge constant of S@CoFeP@CN batteries was related to the lower loss of active material and a stronger LiPS anchoring.

Electrochemical impedance spectroscopy (EIS) was used to further understand the parameters behind the enhanced redox kinetics of S@CoFeP@CN electrodes. Figure 5g and Figure S27, Supporting Information display the Nyquist plot obtained from S@CoFeP@CN, S@CoFeP, and S@CN coin cells before and after cycling at 1 C. The fresh electrodes displayed a semicircle in the high-frequency region associated with the charge-transfer resistance (R_{ct}), followed by a linear dependence in the low-frequency region that is related to the diffusion of lithium ions.[43,67] Data were fitted considering the equivalent circuit displayed as an inset in Figure 5g. A moderate R_{ct} was obtained for the S@CoFeP@CN electrode (62.99 Ω), when compared with that of S@CoFeP (80.36 Ω) and S@CN (125.5 Ω). This low R_{ct} denoted an enhanced charge transferability of the CoFeP@CN composite when compared with electrodes based on each of the composite components. After charging/discharging loops, an additional semicircle in the high-frequency range was evidenced. This newly appearing loop was associated with the resistance of an insoluble Li_2S_2/Li_2S passivation layer (R_p in the equivalent circuit) grown during cycling.[60,67] After cycling, R_{ct} notably decreased for the three types of electrode tested due to the activation process. After cycling, S@CoFeP@CN electrodes were characterized by smaller R_{ct} (9.56 Ω) and R_p
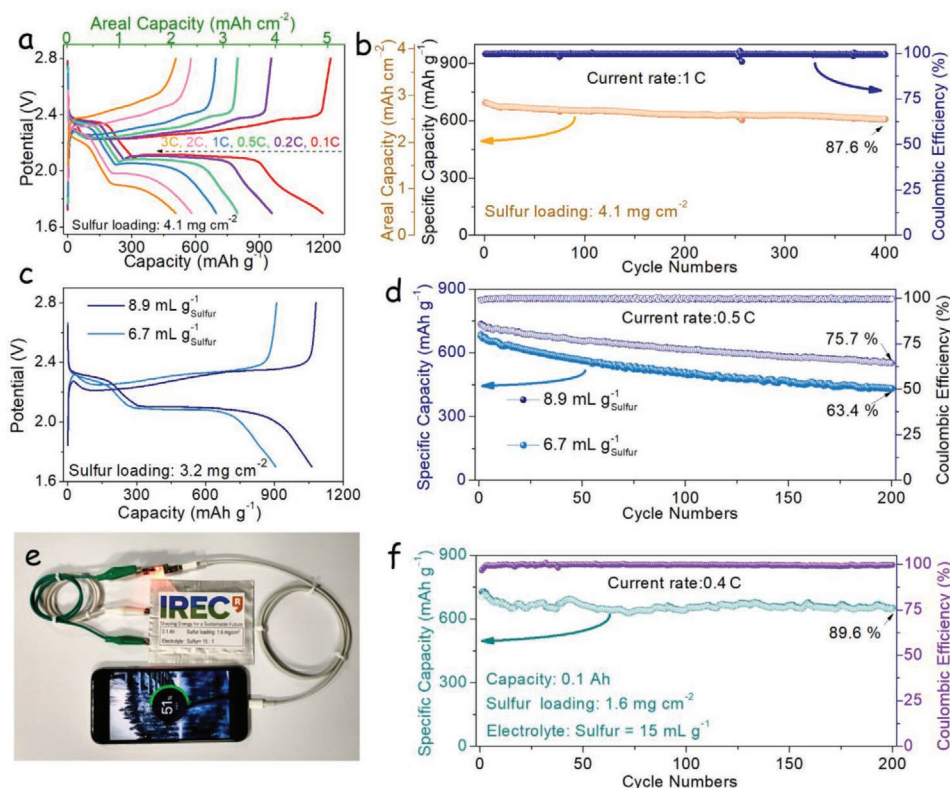
**ADVANCED
SCIENCE NEWS**

www.advancedsciencenews.com

**ADVANCED
ENERGY
MATERIALS**

www.advenergymat.de

Figure 6. a) Charging/discharging curves and b) cycling performance of S@CoFeP@CN electrodes with a 4.1 mg cm^{-2} sulfur loading. c) Charging/discharging curves of S@CoFeP@CN electrodes at 0.1 C with lean electrolyte. d) Cycling performance of S@CoFeP@CN electrodes with lean electrolyte. e) Optical photograph of a mobile phone being charged by a pouch cell based on a S@CoFeP@CN electrode. f) Cycling performances at 0.4 C of a pouch cell based on a S@CoFeP@CN cathode.

(20.14 Ω), when compared with S@CoFeP (R_{ct} = 29.39 Ω and R_p = 23.36 Ω) and S@CN electrodes (R_{ct} = 52.67 Ω and R_p = 120.91 Ω). The small R_p value obtained for CoFeP and especially CoFeP@CN hosts indicated a reduction of the deposition of insulting Li$_2$S/Li$_2$S$_2$ on the surface, associated with an accelerated LiPS conversion.[67]

To thoroughly demonstrate that CoFeP@CN host could effectively capture soluble LiPS to confine the shuttle effect in the charging/discharging process, cycled coin cells were disassembled and analyzed after 200 cycles at 1 C. A striking contrast in the color of separators of the different cells can be observed in Figure 5h. The membrane disassembled from a S@CoFeP@CN cell (left one) showed a much lighter color than the dark brown membrane recovered from a S@Super P (right one). This simple visual inspection demonstrated that the CoFeP@CN host could trap polysulfide much more effectively than Super P, and thus suppressed self-discharging and overall improved the cell efficiency and stability. Another strong evidence in support of the inhibited LiPS dissolution of CoFeP@CN was found from the surface morphology of the cycled Li anode. Different from the large cracks and severe corrosion phenomenon observed in the surface of the Li anodes recovered from S@Super P coin cells, Li foils recovered from cycled S@CoFeP@CN coin cells showed a smooth surface and lower sulfur signal at their surface, as detected by SEM and EDS analysis (Figure 5j,k). Finally, Figure 5i displays the morphology of cycled S@CoFeP@CN. Due to the inevitable

grinding and shearing treatment during the slurry preparation, partial crushing happened on the S@CoFeP@CN composite, but the original tubular nanostructure was still recognizable after cycling, indicating good mechanical stability of the material towards lithiation/delithiation cycles.

Increasing the sulfur loading and decreasing the electrolyte addition are mandatory to achieve the high energy density LSBs required in practical applications. Hence, a series of electrochemical tests of S@CoFeP@CN electrodes were conducted with high sulfur loading and a lean electrolyte. The results of the rate performance of cells produced with 4.1 mg cm^{-2} high S loading can be found in **Figure 6**a and Figure S28, Supporting Information. S@CoFeP@CN electrodes displayed high initial discharge capacities at 1255 mAh g^{-1}, which corresponded to an areal capacity of 5.15 mAh cm^{-2}, notably above that of commercial LIBs (4 mAh cm^{-2}). Even at high current rates of 3 C, a stable discharge capacity at 508 mAh g^{-1} was obtained. Besides, when the current rate was returned to 0.2 C, the initial capacity was recovered (Figure S28, Supporting Information). All the galvanostatic charging/discharging profiles at different current rates clearly exhibited one charge plateau and two discharge plateaus, indicating that CoFeP@CN hosts could effectively reduce the polarization of LiPS conversion even under high sulfur-loading (Figure 6a). And the change of the $Q2/Q1$ ratio with the current rate for a S@CoFeP@CN electrode with a high sulfur loading can be found in Figure S29, Supporting Information. A high $Q2/Q1$ value at a low rate was delivered, but

the increased resistance and thickness of the electrode strongly limited the $Q2$ capacity at a high current rate. Figure 6b shows the long-term cycling performance of high sulfur loading S@CoFeP@CN electrode at 1 C. After 400 cycles, the discharge capacity was maintained at 608 mAh g^{-1}, which involved an 87.6% capacity retention, that is, a 0.031% average capacity loss per cycle. Figure S30, Supporting Information displays the charging/discharging profiles at various cycles, exhibiting excellent stability. S@CoFeP@CN electrodes were also characterized by a high and stable Columbic efficiency at 99.3%. Lean electrolyte tests were conducted with a low electrolyte usage of 8.9 and 6.7 mL g^{-1}$_{Sulfur}$ (Figure 6c,d; Figure S31, Supporting Information). The corresponding galvanostatic charge/discharge profiles (Figure 6c) clearly exhibit the enlarged voltage gap with the decreased electrolyte volume, which is attributed to deteriorative polarization caused by weakened ion transportation in the higher viscosity electrolyte.[68] In spite of this, the S@CoFeP@CN cathode with 8.9 mL g^{-1}$_{Sulfur}$ electrolyte still showed superior cycling stability with a capacity retention of 75.7% after 200 cycles. When the electrolyte amount decreased to 6.7 mL g^{-1}$_{Sulfur}$, the capacity rapidly decreased to some extent but still maintained a stable cycling performance demonstrating that the CoFeP@CN catalysts could effectively promote the Li–S reaction even under lean electrolyte conditions. Table S2, Supporting Information displays a comparison of several parameters of state-of-the-art TMP-based and C$_3$N$_4$-based materials as cathode hosts for LSBs. Notice that the CoFeP@CN host presented here is characterized by the highest capacities and stabilities. Besides, to illustrate the practical applicability of LSBs based on S@CoFeP@CN cathodes, pouch cells were also fabricated according to the schematic diagram shown in Figure S32, Supporting Information. S@CoFeP@CN-based pouch batteries revealed a stable operation at 0.4 C during 200 cycles, remarkable capacity retention of 89.6% was obtained and accompanied by a high Columbic efficiency at 99.5% (Figure 6d; Figure S33, Supporting Information), and the charged mobile phone clearly demonstrate their potential (Figure 6c; Video S1, Supporting Information). All these results indicate that S@CoFeP@CN electrodes can definitively help LSBs to reach practical applications.

3. Conclusion

In summary, we reported a highly efficient sulfur host for robust LSBs, enabled by orthorhombic phased bimetallic phosphide CoFeP NCs decorated on novel nanotubular t-CN by a facile self-assembly process that took advantage of the different sign of the particles surface charge. While each of the materials provided advantages in terms of adsorption sites and available SSA, the combination of the two materials within CoFeP@CN heterostructures awoke a clear synergism between them that significantly contributed to improving LiPS adsorption and catalytic activity. Besides t-CN allowing a high distribution of CoFeP NCs, experimental results and DFT calculations displayed a charge redistribution within the formed Mott–Schottky heterostructures. Additionally, experimental and theoretical work also confirmed the superior LiPS adsorbability realized by abundant sulfiphilic/lithiophilic sites in CoFeP and t-CN.

Besides, the modified electron distribution within heterostructures allowed reducing the potential barriers and improved the redox kinetics during the charging/discharging processes, including LiPS phase change and Li$_2$S deposition/dissolution. Moreover, the porous CoFeP@CN host provides sufficient space to accommodate the volume change and efficient channels for Li$^+$ diffusion in reaction. As a result, S@CoFeP@CN electrodes delivered a high sulfur utilization, superior rate performance (630 mAh g^{-1} at 5 C), and remarkable cycling stability with 90.44% capacity retention over 700 cycles at 3 C. Even with 4.1 mg cm^{-2} high-loading sulfur electrode coin cells and the 0.1 Ah capacity pouch cells test, the robust electrochemical performance results were obtained. In addition, S@CoFeP@CN electrodes exhibit high energy efficiency and low self-discharge property, which are two frequently neglected issues in material research of LSBs. This work not only demonstrated a new and highly suitable form of t-CN and further probed the suitability of metal phosphides in the field of LSBs, but also provided valuable insights into the design of heterostructural electrocatalyst to regulate LiPS.

4. Experimental Section

Preparing of CoFeP Nanoparticles: In a typical synthesis, 2.4 g (10 mmol) of 1-hexadecylamine (HDA, 90%, Acros Organics) were combined with 10.0 mL of 1-octadecene (ODE, 90%, ACROS Organics) and 2.6 mL (10 mmol) of triphenyl phosphite (99%, ACROS Organics) in a 50 mL flask. The system was degassed and heated to 150 °C and maintained at this temperature for 1 h to remove low boiling point impurities, moisture, and oxygen. After 4 mL ODE contain 384 mg (1 mmol) Co$_2$(CO)$_8$ (95%, ACROS Organics) and 390 mg (2 mmol) Fe(CO)$_5$ (Sigma Aldrich) was added into the system the temperature was then increased to 290 °C in 20 min and kept there for 1 h. Afterward, the mixture was allowed to cool down to 200 °C by removing the heating mantle and then cooled rapidly down to room temperature with a water bath. The black product was isolated by precipitation with acetone. To remove as many organics as possible, two redispersion and precipitation cycles using chloroform and acetone were additionally carried out. To further remove the organic ligands, 10 mL of CoFeP NCs dispersion (10 mg mL^{-1}) in hexane (99.0%, Honeywell) was combined with 10 mL acetonitrile (99%, ACROS Organics) to form a two-phase mixture and then 1 mL HBF$_4$ solution (48%) was added in it. The resulting solution was sonicated until the NCs transferred from the upper to the bottom layer. The surface-modified NCs were washed with ethanol three times and dispersed in 10 mL ethanol with a little amount of *N,N*-dimethylformamide (DMF, 99.8%, Alfa Aesa) for further use.

Preparing Tubular t-CN and s-CN: The t-CN was prepared by an annealing method using a mixture of urea and melamine as the precursor. Typically, 100 mg urea (99.5%, ACROS Organics) and 10 mg melamine (99%, ACROS Organics) was put in a mortar and grinded for 10 min. The mixture powder was loaded into a graphite die and compacted into cylinders (Ø 10 mm × 10 mm) under a pressure of 10 MPa. Then cylinders were put into a crucible covered loosely with a lid and then heated at 550 °C for 4 h in static air in a muffle furnace. The ramping rate was 5 °C min^{-1}. After cooled naturally to room temperature, the resultant yellow solid was collected and grounded into powder for further use. s-CN was prepared by the same annealing method using melamine as the precursor but without any pressure treatment. After cooling naturally to room temperature, the resultant yellow solid was collected and grounded into powder, then an ultrasonic treatment was conducted for 2 h to obtain the s-CN.

Synthesis of CoFeP@CN Composites: Typically, 50 mg of t-CN powder was dispersed in 15 mL ethanol and DMF mixed solution and then

sonicated for 1 h. Then 5 mL of a CoFeP ethanol dispersion (10 mg mL^{-1}) was added into the mixture solution and stirred for 24 h. The product CoFeP@CN (also named 50%CoFeP@CN) was washed with ethanol three times and dried under vacuum overnight. 25%CoFeP@CN and 75%CoFeP@CN were fabricated by the same methods with different weight ratio.

Synthesis of S@CN, S@CoFeP, S@CoFeP@CN, and S@Super P: Typically, CoFeP@CN and sulfur powder (99.98%, Sigma Aldrich) were well mixed with the weight ratio of 1:3, and then heated the mixture at 155 °C for 6 h in a sealed glass bottle under Ar protection. The redundant sulfur not incorporated into CoFeP@CN was removed by 10 mL CS$_2$ (99.9%, Alfa Aesa) and ethanol solution (1:4, volume ratio). S@CN, S@CoFeP, and S@Super P were prepared by the same method.

Supporting Information

Supporting Information is available from the Wiley Online Library or from the author.

Conflict of Interest

The authors declare no conflict of interest.

Data Availability Statement

Original measurement data are available upon reasonable request.

[1] P. G. Bruce, S. A. Freunberger, L. J. Hardwick, J.-M. Tarascon, *Nat. Mater.* **2012**, *11*, 19.

[2] L. Zhou, D. L. Danilov, R. Eichel, P. H. L. Notten, *Adv. Energy Mater.* **2020**, *11*, 2001304.

[3] Z. Liang, D. Yang, P. Tang, C. Zhang, J. J. Biendicho, Y. Zhang, J. Llorca, X. Wang, J. Li, M. Heggen, J. David, R. E. Dunin-Borkowski, Y. Zhou, J. R. Morante, A. Cabot, J. Arbiol, *Adv. Energy Mater.* **2021**, *11*, 2003507.

[4] M. Zhang, W. Chen, L. Xue, Y. Jiao, T. Lei, J. Chu, J. Huang, C. Gong, C. Yan, Y. Yan, Y. Hu, X. Wang, J. Xiong, *Adv. Energy Mater.* **2020**, *10*, 1903008.

[5] W. Lim, S. Kim, C. Jo, J. Lee, *Angew. Chem., Int. Ed.* **2019**, *58*, 18746.

[6] Z. Li, H. B. Wu, X. W. (David) Lou, *Energy Environ. Sci.* **2016**, *9*, 3061.

[7] C. Zu, A. Manthiram, *Adv. Energy Mater.* **2013**, *3*, 1008.

[8] J.-Q. Huang, Q. Zhang, S.-M. Zhang, X.-F. Liu, W. Zhu, W.-Z. Qian, F. Wei, *Carbon* **2013**, *58*, 99.

[9] B. Zhang, X. Qin, G. R. Li, X. P. Gao, *Energy Environ. Sci.* **2010**, *3*, 1531.

[10] H. Wang, W. Zhang, J. Xu, Z. Guo, *Adv. Funct. Mater.* **2018**, *28*, 1707520.

[11] X. Liu, J.-Q. Huang, Q. Zhang, L. Mai, *Adv. Mater.* **2017**, *29*, 1601759.

[12] S. Yu, W. Cai, L. Chen, L. Song, Y. Song, *J. Energy Chem.* **2021**, *55*, 533.

[13] H. Yuan, X. Chen, G. Zhou, W. Zhang, J. Luo, H. Huang, Y. Gan, C. Liang, Y. Xia, J. Zhang, J. Wang, X. Tao, *ACS Energy Lett.* **2017**, *2*, 1711.

[14] J. Zhou, X. Liu, L. Zhu, J. Zhou, Y. Guan, L. Chen, S. Niu, J. Cai, D. Sun, Y. Zhu, J. Du, G. Wang, Y. Qian, *Joule* **2018**, *2*, 2681.

[15] Q. Zhu, B. Qiu, H. Duan, Y. Gong, Z. Qin, B. Shen, M. Xing, J. Zhang, *Appl. Catal., B* **2019**, *259*, 118078.

[16] Y. Tan, H. Wang, P. Liu, Y. Shen, C. Cheng, A. Hirata, T. Fujita, Z. Tang, M. Chen, *Energy Environ. Sci.* **2016**, *9*, 2257.

[17] F. Geng, Y. Bonita, V. Jain, M. Magiera, N. Rai, J. C. Hicks, *Ind. Eng. Chem. Res.* **2020**, *59*, 6931.

[18] Y. Li, Z. Dong, L. Jiao, *Adv. Energy Mater.* **2020**, *10*, 1902104.

[19] W.-J. Ong, L.-L. Tan, Y. H. Ng, S.-T. Yong, S.-P. Chai, *Chem. Rev.* **2016**, *116*, 7159.

[20] T.-Z. Hou, X. Chen, H.-J. Peng, J.-Q. Huang, B.-Q. Li, Q. Zhang, B. Li, *Small* **2016**, *12*, 3283.

[21] Q. Pang, L. F. Nazar, *ACS Nano* **2016**, *10*, 4111.

[22] Z. Jia, H. Zhang, Y. Yu, Y. Chen, J. Yan, X. Li, H. Zhang, *J. Energy Chem.* **2020**, *43*, 71.

[23] P. Zhang, F. Wang, Y. Qin, N. Wang, *ACS Appl. Nano Mater.* **2020**, *3*, 7847.

[24] Y. Wang, R. Zhang, J. Chen, H. Wu, S. Lu, K. Wang, H. Li, C. J. Harris, K. Xi, R. V. Kumar, S. Ding, *Adv. Energy Mater.* **2019**, *9*, 1900953.

[25] X. Du, J. Huang, J. Zhang, Y. Yan, C. Wu, Y. Hu, C. Yan, T. Lei, W. Chen, C. Fan, J. Xiong, *Angew. Chem., Int. Ed.* **2019**, *58*, 4484.

[26] X. Wang, X. Tian, Y. Sun, J. Zhu, F. Li, H. Mu, J. Zhao, *Nanoscale* **2018**, *10*, 12315.

[27] Z. Zhuang, Y. Li, Z. Li, F. Lv, Z. Lang, K. Zhao, L. Zhou, L. Moskaleva, S. Guo, L. Mai, *Angew. Chem.* **2018**, *130*, 505.

[28] Y. Wang, R. Zhang, Z. Sun, H. Wu, S. Lu, J. Wang, W. Yu, J. Liu, G. Gao, S. Ding, *Adv. Mater. Interfaces* **2020**, *7*, 1902092.

[29] D. Sun, K. Liu, J. Hu, J. Zhou, *Small* **2020**, *17*, 2006374.

[30] X. Chen, X. Ding, C. Wang, Z. Feng, L. Xu, X. Gao, Y. Zhai, D. Wang, *Nanoscale* **2018**, *10*, 13694.

[31] Y. Zhang, Y. Wang, R. Luo, Y. Yang, Y. Lu, Y. Guo, X. Liu, S. Cao, J.-K. Kim, Y. Luo, *Nanoscale Horiz.* **2020**, *5*, 530.

[32] J. Liu, M. Meyns, T. Zhang, J. Arbiol, A. Cabot, A. Shavel, *Chem. Mater.* **2018**, *30*, 1799.

[33] J. Liu, X. Yu, R. Du, C. Zhang, T. Zhang, J. Llorca, J. Arbiol, Y. Wang, M. Meyns, A. Cabot, *Appl. Catal., B* **2019**, *256*, 117846.

[34] T. Berestok, P. Guardia, M. Ibáñez, M. Meyns, M. Colombo, M. V. Kovalenko, F. Peiró, A. Cabot, *Langmuir* **2018**, *34*, 9167.

[35] D. Zeng, W. Xu, W.-J. Ong, J. Xu, H. Ren, Y. Chen, H. Zheng, D.-L. Peng, *Appl. Catal., B* **2018**, *221*, 47.

[36] Y.-L. Wang, Y. Tian, Z.-L. Lang, W. Guan, L.-K. Yan, *J. Mater. Chem. A* **2018**, *6*, 21056.

[37] Q. Pang, X. Liang, C. Y. Kwok, J. Kulisch, L. F. Nazar, *Adv. Energy Mater.* **2017**, *7*, 1601630.

[38] Z. Chen, Y. Yu, X. She, K. Xia, Z. Mo, H. Chen, Y. Song, J. Huang, H. Li, H. Xu, *Appl. Surf. Sci.* **2019**, *495*, 143528.

[39] J. Wu, C. Li, W. Zhang, J. Han, L. Wang, S. Wang, Y. Wang, *Energy Technol.* **2019**, *7*, 1800927.

[40] J.-X. Feng, S.-Y. Tong, Y.-X. Tong, G.-R. Li, *J. Am. Chem. Soc.* **2018**, *140*, 5118.

[41] Z. Peng, X. Qiu, G. Cai, X. Zhang, Z. Dong, *J. Alloys Compd.* **2020**, *842*, 155784.

[42] Y. Zhong, L. Yin, P. He, W. Liu, Z. Wu, H. Wang, *J. Am. Chem. Soc.* **2018**, *140*, 1455.

[43] C. Zhang, J. J. Biendicho, T. Zhang, R. Du, J. Li, X. Yang, J. Arbiol, Y. Zhou, J. R. Morante, A. Cabot, *Adv. Funct. Mater.* **2019**, *29*, 1903842.

[44] Y. Chen, W. Zhang, D. Zhou, H. Tian, D. Su, C. Wang, D. Stockdale, F. Kang, B. Li, G. Wang, *ACS Nano* **2019**, *13*, 4731.

[45] X.-F. Yu, D.-X. Tian, W.-C. Li, B. He, Y. Zhang, Z.-Y. Chen, A.-H. Lu, *Nano Res.* **2019**, *12*, 1193.

[46] J. Zhang, J.-Y. Li, W.-P. Wang, X.-H. Zhang, X.-H. Tan, W.-G. Chu, Y.-G. Guo, *Adv. Energy Mater.* **2018**, *8*, 1702839.

[47] X. Hong, J. Jin, T. Wu, Y. Lu, S. Zhang, C. Chen, Z. Wen, *J. Mater. Chem. A* **2017**, *5*, 14775.

[48] N. Pavlin, S. Hribernik, G. Kapun, S. D. Talian, C. Njel, R. Dedryvère, R. Dominko, *J. Electrochem. Soc.* **2018**, *166*, A5237.

[49] X. Chen, H.-J. Peng, R. Zhang, T.-Z. Hou, J.-Q. Huang, B. Li, Q. Zhang, *ACS Energy Lett.* **2017**, *2*, 795.

[50] Y. Luo, N. Luo, W. Kong, H. Wu, K. Wang, S. Fan, W. Duan, J. Wang, *Small* **2018**, *14*, 1702853.

[51] S. Huang, Y. V. Lim, X. Zhang, Y. Wang, Y. Zheng, D. Kong, M. Ding, S. A. Yang, H. Y. Yang, *Nano Energy* **2018**, *51*, 340.

[52] Y. Qiu, W. Li, W. Zhao, G. Li, Y. Hou, M. Liu, L. Zhou, F. Ye, H. Li, Z. Wei, S. Yang, W. Duan, Y. Ye, J. Guo, Y. Zhang, *Nano Lett.* **2014**, *14*, 4821.

[53] Z. Yuan, H.-J. Peng, T.-Z. Hou, J.-Q. Huang, C.-M. Chen, D.-W. Wang, X.-B. Cheng, F. Wei, Q. Zhang, *Nano Lett.* **2016**, *16*, 519.

[54] S. Chen, J. Luo, N. Li, X. Han, J. Wang, Q. Deng, Z. Zeng, S. Deng, *Energy Storage Mater.* **2020**, *30*, 187.

[55] Y. Li, P. Xu, G. Chen, J. Mou, S. Xue, K. Li, F. Zheng, Q. Dong, J. Hu, C. Yang, M. Liu, *Chem. Eng. J.* **2020**, *380*, 122595.

[56] W. Tian, B. Xi, Z. Feng, H. Li, J. Feng, S. Xiong, *Adv. Energy Mater.* **2019**, *9*, 1901896.

[57] Z. Du, X. Chen, W. Hu, C. Chuang, S. Xie, A. Hu, W. Yan, X. Kong, X. Wu, H. Ji, L.-J. Wan, *J. Am. Chem. Soc.* **2019**, *141*, 3977.

[58] F. Y. Fan, W. C. Carter, Y.-M. Chiang, *Adv. Mater.* **2015**, *27*, 5203.

[59] H. Yuan, H.-J. Peng, B.-Q. Li, J. Xie, L. Kong, M. Zhao, X. Chen, J.-Q. Huang, Q. Zhang, *Adv. Energy Mater.* **2018**, *9*, 1802768.

[60] Y. Pan, X. Cheng, M. Gao, Y. Fu, J. Feng, H. Ahmed, L. Gong, H. Zhang, V. S. Battaglia, *ACS Appl. Mater. Interfaces* **2020**, *12*, 32726.

[61] R. Wang, C. Luo, T. Wang, G. Zhou, Y. Deng, Y. He, Q. Zhang, F. Kang, W. Lv, Q. Yang, *Adv. Mater.* **2020**, *32*, 2000315.

[62] Y. Yan, Z. Chen, J. Yang, L. Guan, H. Hu, Q. Zhao, H. Ren, Y. Lin, Z. Li, M. Wu, *Small* **2020**, *16*, 2004631.

[63] X. Zhu, W. Zhao, Y. Song, Q. Li, F. Ding, J. Sun, L. Zhang, Z. Liu, *Adv. Energy Mater.* **2018**, *8*, 1800201.

[64] G. Zhou, H. Tian, Y. Jin, X. Tao, B. Liu, R. Zhang, Z. W. Seh, D. Zhuo, Y. Liu, J. Sun, J. Zhao, C. Zu, D. S. Wu, Q. Zhang, Y. Cui, *Proc. Natl. Acad. Sci. U. S. A.* **2017**, *114*, 840.

[65] A. Eftekhari, *Sustainable Energy Fuels* **2017**, *1*, 2053.

[66] Y. V. Mikhaylik, J. R. Akridge, *J. Electrochem. Soc.* **2004**, *151*, A1969.

[67] A.-H. Shao, Z. Zhang, D.-G. Xiong, J. Yu, J.-X. Cai, Z.-Y. Yang, *ACS Appl. Mater. Interfaces* **2020**, *12*, 5968.

[68] S. Wang, S. Feng, J. Liang, Q. Su, F. Zhao, H. Song, M. Zheng, Q. Sun, Z. Song, X. Jia, J. Yang, Y. Li, J. Liao, R. Li, X. Sun, *Adv. Energy Mater.* **2021**, *11*, 2003314.

Article

2D/2D Heterojunction of TiO$_2$ Nanoparticles and Ultrathin G-C$_3$N$_4$ Nanosheets for Efficient Photocatalytic Hydrogen Evolution

Ruifeng Du [1,2], Baoying Li [3,*], Xu Han [4], Ke Xiao [1,2], Xiang Wang [1,2], Chaoqi Zhang [1,2], Jordi Arbiol [4,5] and Andreu Cabot [1,5,*]

[1] Catalonia Energy Research Institute—IREC, Sant Adrià de Besòs, 08930 Barcelona, Spain; ruifengdu@irec.cat (R.D.); kexiao@irec.cat (K.X.); xwang@irec.cat (X.W.); czhang@irec.cat (C.Z.)
[2] Departament d'Enginyeria Electrònica i Biomèdica, Universitat de Barcelona, 08028 Barcelona, Spain
[3] Shandong Provincial Key Laboratory of Molecular Engineering, State Key Laboratory of Biobased Material and Green Papermaking, School of Chemistry and Chemical Engineering, Qilu University of Technology, Shandong Academy of Sciences, Jinan 250353, China
[4] Catalan Institute of Nanoscience and Nanotechnology (ICN2), CSIC and BIST, Campus UAB, Bellaterra, 08193 Barcelona, Spain; xuhan@irec.cat (X.H.); arbiol@icrea.cat (J.A.)
[5] ICREA, Pg. Lluis Companys 23, 08010 Barcelona, Spain
* Correspondence: libaoying@qlu.edu.cn (B.L.); acabot@irec.cat (A.C.)

Abstract: Photocatalytic hydrogen evolution is considered one of the promising routes to solve the energy and environmental crises. However, developing efficient and low-cost photocatalysts remains an unsolved challenge. In this work, ultrathin 2D g-C$_3$N$_4$ nanosheets are coupled with flat TiO$_2$ nanoparticles as face-to-face 2D/2D heterojunction photocatalysts through a simple electrostatic self-assembly method. Compared with g-C$_3$N$_4$ and pure TiO$_2$ nanosheets, 2D/2D TiO$_2$/g-C$_3$N$_4$ heterojunctions exhibit effective charge separation and transport properties that translate into outstanding photocatalytic performances. With the optimized heterostructure composition, stable hydrogen evolution activities are threefold and fourfold higher than those of pure TiO$_2$, and g-C$_3$N$_4$ are consistently obtained. Benefiting from the favorable 2D/2D heterojunction structure, the TiO$_2$/g-C$_3$N$_4$ photocatalyst yields H$_2$ evolution rates up to 3875 µmol·g^{-1}·h^{-1} with an AQE of 7.16% at 380 nm.

Keywords: hydrogen evolution; 2D/2D heterojunction; charge separation

1. Introduction

Owing to the abundance of low-cost solar energy, the numerous uses of hydrogen and its advantages as an energy carrier, the photocatalytic generation of hydrogen is a highly appealing process [1,2]. However, the cost-effective photogeneration of hydrogen requires high activity and stable photocatalysts, development of which has been a long-standing goal. Over the past decades, numerous semiconductors have been tested as photocatalysts for hydrogen evolution. Among them, titanium dioxide (TiO$_2$) has received special attention owing to its stability, high abundance, low toxicity, being the earliest to be discovered and becoming the first to be industrialized [3]. Nevertheless, due to its wide bandgap and relatively fast charge recombination rate, its applicability has been strongly limited. Numerous strategies have been proposed to improve the photocatalytic performance of TiO$_2$, facilitating charge separation and promoting efficiency and activity, [4–7] including the control of its particle facets and morphology [8–11], its modification with cocatalysts [12–15] and its coupling with other semiconductors to form heterostructures [16–24].

Graphite carbonitride (g-C$_3$N$_4$) with a layered structure similar to graphite, high chemical stability and low cost has received increasing interest in recent years [25–27]. In particular, as a polymeric semiconductor, g-C$_3$N$_4$ has been recently reported as a promising candidate photocatalyst due to its unique structure and electronic characteristics, with a

2.7 eV bandgap that allows absorbing part of the visible spectrum [28,29]. Additionally, two-dimensional (2D) g-C$_3$N$_4$ nanosheets, benefiting from a huge specific surface area and a suitable band structure, have shown especially interesting properties and offer an excellent platform to produce heterojunctions with other semiconductors [30–33].

Recently, 2D/2D heterojunctions have been demonstrated to provide great advantages to improve charge separation [34,35]. 2D/2D heterojunctions simultaneously maximize the interface and surface areas, i.e., the charge transfer between the two materials and the interaction with the media, which can potentially improve photocatalytic activities.

In the present work, we target improving photocatalytic hydrogen production using 2D/2D heterojunctions. In this direction, we report the first synthesis of 2D/2D TiO$_2$/g-C$_3$N$_4$ heterostructures. Such composite materials are produced from the electrostatic assembly of 2D anatase TiO$_2$ flat nanoparticles synthesized through a simple colloidal method with 2D ultrathin g-C$_3$N$_4$. The produced heterostructures are tested as photocatalysts for hydrogen evolution under simulated solar light irradiation. The excellent hydrogen evolution performance obtained after optimizing the weight contents of TiO$_2$ and g-C$_3$N$_4$ within 2D/2D heterojunction are rationalized using photoluminescence, photocurrent and impedance spectroscopy analysis.

2. Experiment

Synthesis of bulk g-C$_3$N$_4$ (bCN) and ultrathin g-C$_3$N$_4$ (uCN): Bulk g-C$_3$N$_4$ powder was synthesized by thermal polymerization of urea. Briefly, 10 g of urea (99%, Acros Organics) was placed into a ceramic crucible. The crucible was covered and heated to 550 °C at a ramp rate of 2 °C min^{-1} for 4 h under air atmosphere. After cooling to room temperature, the resulting light-yellow solid was ground with the mortar to obtain the bulk g-C$_3$N$_4$ powder. To obtain ultrathin g-C$_3$N$_4$ (uCN), bulk g-C$_3$N$_4$ (2.0 g) was placed in a covered ceramic crucible, and it was heated to 520 °C with a ramp rate of 5 °C min^{-1} for 2 h under air atmosphere to obtain a light-yellow powder.

Synthesis of TiO$_2$ nanosheets: Titanium dioxide nanoparticles were prepared using a colloidal method. All the syntheses were performed using standard airless techniques [36,37]. Typically, 10 mL of oleylamine (OAm, 80–90%, Acros Organics, Geel, Belgium), 10 mL of octadecene (ODE, 90%, Sigma-Aldrich, Burlington, MA, USA) and 1 mL of oleic acid (OAc, 90%, Sigma-Aldrich, Burlington, MA, USA) were loaded in a three-neck flask and degassed under vacuum at 120 °C for 1 h while being strongly stirred using a magnetic bar. Then, 300 mg of TiF$_4$ (99%, Sigma, Burlington, MA, USA) was added in a mixed solution of 2 mL OAm, 3 mL OAc and 6 mL ODE and sonicated for 0.5 h to prepare a precursor solution. Subsequently, under nitrogen atmosphere, 10 mL of the precursor solution were slowly added to the reaction flask, which was then heated to 290 °C at a rate of 5 °C min^{-1} and maintained for 1 h. The solid product was centrifuged and washed with acetone and hexane three times. The particles were finally dispersed in hexane at a concentration of 10 mg/mL.

Ligand removal from TiO$_2$ nanoparticles: In a typical process, 10 mL of a TiO$_2$ dispersion in hexane (2 mg/mL) was combined with 10 mL acetonitrile to form a two-phase mixture. Then, 1 mL of a HBF$_4$ solution (48%, Sigma-Aldrich, Burlington, MA, USA) was added. The resulting solution was sonicated until the particles transferred from the upper to the bottom layer. The surface-modified particles were washed with ethanol and a 1 mol/L sodium hydroxide (85%, Sigma-Aldrich, Burlington, MA, USA) aqueous solution three times to remove the residual fluoride ions and ligands. The particles were then washed with water to adjust the PH close to neutral. Finally, the particles were dispersed in 10 mL of water with a small amount of DMF.

Synthesis of 2D/2D TiO$_2$/ultrathin g-C$_3$N$_4$ (TiO$_2$/uCN) composite: TiO$_2$/uCN heterojunctions were produced by an electrostatic self-assembly method. Briefly, 20 mg of as prepared ultrathin g-C$_3$N$_4$ was dissolved in 10 mL of ultrapure water and sonicated for 1 h. The solution was then mixed with an ethanol solution of ligand-removed TiO$_2$ nanoparticles with a weight ratio of 1:2, 1:1 and 2:1. The mixed solution was stirred for

24 h after 1 h of sonication. The obtained composite was collected by centrifuging, it was washed with ethanol 2 times, and it was finally dried at 60 °C for 12 h. The collected materials were named T_1/uCN_2, T_1/uCN_1 and T_2/uCN_1 based on the different TiO_2/ultrathin g-C_3N_4 weight ratios. TiO_2/bulk g-C_3N_4 (T/bCN) samples were prepared using the same procedure. For photocatalytic measurements, 1 wt% of Pt was loaded on the surface of the photocatalysts by a photoreduction method.

Photocatalytic Hydrogen Evolution Procedure

The photocatalytic hydrogen evolution experiments were carried out in a Perfect Light Labsolar-III (AG) photoreactor (Pyrex glass) connected to a closed-loop gas circulation system. In a typical experiment, 20 mg photocatalyst was dispersed in 100 mL aqueous solution containing 10 mL methanol and 1 wt% Pt cocatalyst (40 uL 25.625 mmol/L H_2PtCl_6 aqueous solution). The mixed solution was bubbled with N_2 for 30 min to ensure anaerobic state and illuminated 30 min with UV light before simulated solar light irradiation to ensure the complete loading of Pt. The incident light was provided by a 300 W Xe lamp with an AM 1.5 filter, and the reaction conditions were kept at room temperature. The resulting gas was analyzed by a Labsolar-III (AG) gas chromatograph equipped with a thermal conductivity detector, with high-purity argon as the carrier gas.

3. Result and Discussion

TiO_2/g-C_3N_4 heterostructures were obtained by the electrostatic assembly of TiO_2 nanoparticles and ultrathin g-C_3N_4 nanosheets (Figure 1, see Experimental section for details). Colloidal TiO_2 nanoparticles were produced in the presence of OAm and OAc using TiF_4 as the Ti precursor. As shown in Figure 2a, low-resolution TEM images exhibited the TiO_2 particles to have a flat square morphology with a side length of 30–50 nm and a thickness of about 5–10 nm. g-C_3N_4 nanosheets were produced by the thermal etching of bulk g-C_3N_4. As observed by scanning electron microscopy (SEM, Figure S1a,b) and transmission electron microscopy (TEM, Figure 2b) characterization, bCN and uCN displayed significantly different morphologies. The uCN showed a thin nanosheet-based structure pointing at the occurrence of a layer etching during the thermal process. Figure S1c displays the nitrogen adsorption–desorption isotherms of bCN and uCN, which further proved uCN (85.7 m^2/g) to be characterized by a larger specific surface area than bCN (46.3 m^2/g).
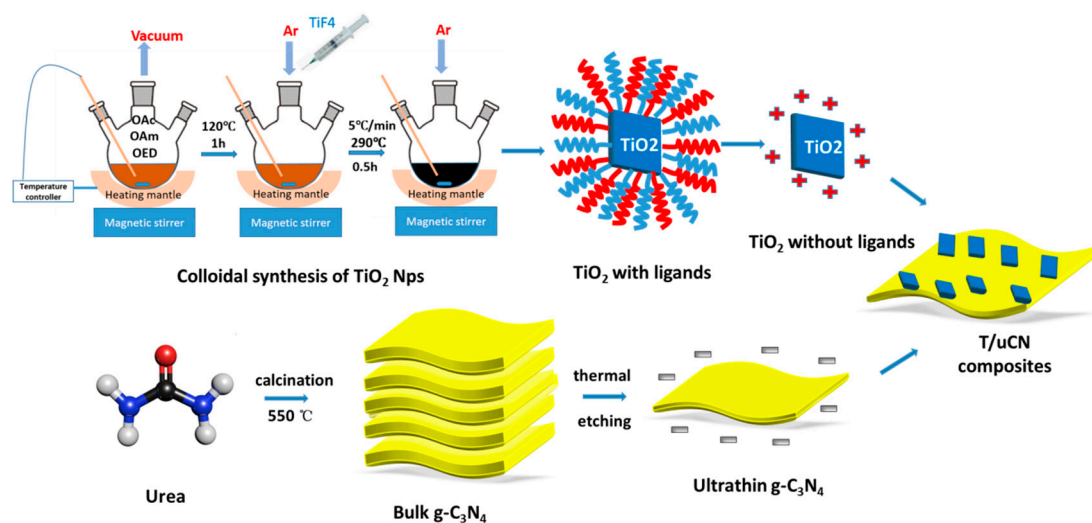
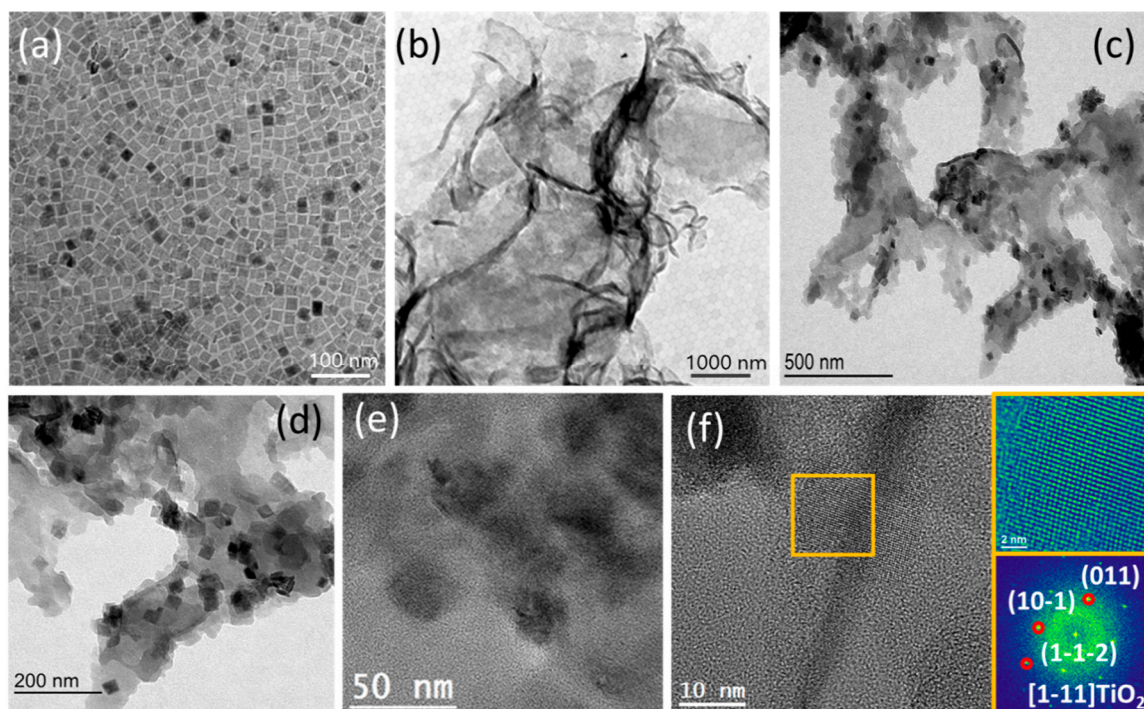**Figure 1.** Schematic illustration of the process used to produce 2D/2D TiO_2/uCN composite.

Figure 2. Representative TEM images of (**a**) TiO_2 nanoparticles; (**b**) g-C_3N_4 nanosheets and T_1/uCN_1 composite with representative (**c**) low and (**d**) high magnification. (**e**,**f**) HRTEM images of T_1/uCN_1. A magnified detail (**top right**) of the orange squared region in the HRTEM image and its corresponding indexed power spectrum (**bottom right**) is shown, revealing the TiO_2 anatase phase (space group = $I4_1$/amd) with a = b = 3.7840 Å, and c = 9.5000 Å. TiO_2 lattice fringe distances were measured to be 0.233 nm, 0.352 nm and 0.348 nm at 41.30° and 139.38°, which could be interpreted as the anatase TiO_2 phase, visualized along its [1–11] zone axis.

To positively charge the surface of the TiO_2 particles, enable their dispersion in an aqueous solution and promote charge transfer with the media; the organic ligands attached to the particle surface were removed using HBF_4 (Figure S2). As observed by zeta-potential analysis, while the g-C_3N_4 nanosheets were negatively charged (V = −33.8 mV), after ligands removal the TiO_2 particles were positively charged (V = +18.6 mV), which enabled the electrostatic self-assembly of the two components [38]. Indeed, when combining solutions of the two types of material, a light-yellow precipitate was formed. The precipitate was composed of large uCN nanosheets containing numerous nanoparticles attached to their surface. TEM analyses showed these nanoparticles lie flat on the surface of uCN, forming 2D/2D heterostructures (Figure 2c,d). High resolution TEM (HRTEM) further confirmed these nanoparticles are TiO_2 with good crystallinity (Figure 2e,f).

SEM-EDS elemental maps (Figure S4) displayed a homogeneous distribution of C, N, O and Ti, demonstrating a uniform distribution of TiO_2 particles on the uCN surface at the microscale. On the other hand, quantitative EDX analyses showed the TiO_2:CN weight ratio to be close to that of the nominal combination of each phase: TiO_2:CN = 0.47 for T_1/uCN_2; TiO_2:CN = 1.1 for T_1/uCN_1 and TiO_2:CN = 1.9 for T_2/uCN_1, obtained from mixing 1:2, 1:1 and 2:1 mass ratios of particles, respectively (Figures S5–S7).

Figure 3a displays the X-ray diffraction (XRD) patterns of bCN, uCN, TiO_2 and T/uCN samples. The XRD peaks at 25.2° (101), 38.0° (004), 47.7° (200) and 54.8° (211) are associated with the anatase TiO_2 phase (JCPDS No. 21-1272) [39]. Additonally, the characteristic diffraction peaks at 13.1° and 27.4° correspond to the (002) and (100) planes of g-C_3N_4 (JCPDS No. 87-1526) [40]. The characteristic diffraction peaks of both TiO_2 and g-C_3N_4 can be observed in all the composites samples, confirming the coexistence of anatase TiO_2 and g-C_3N_4.
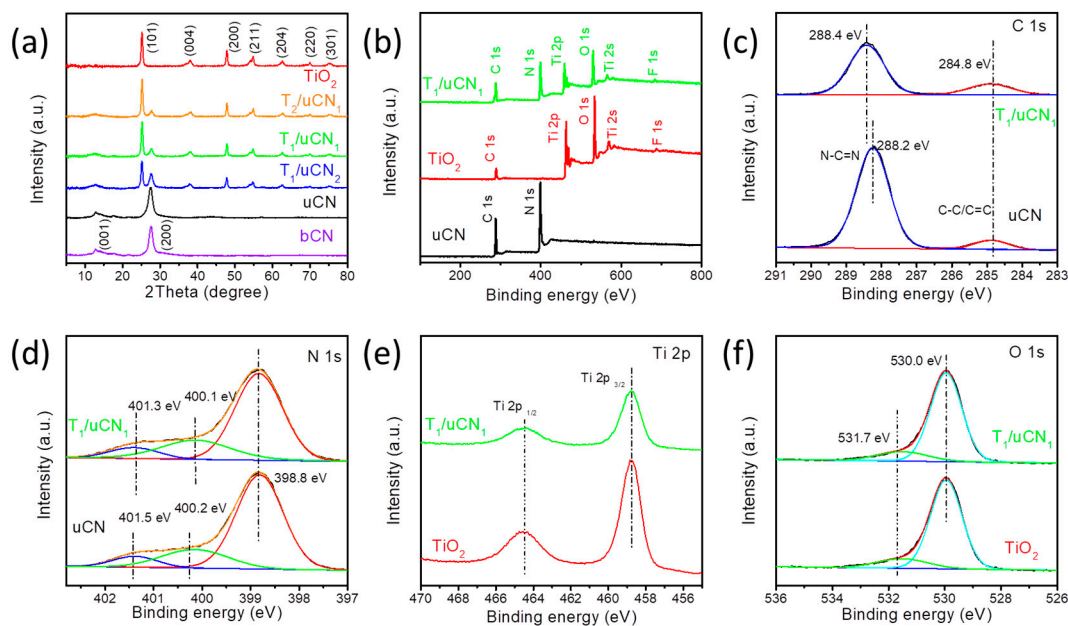
Figure 3. (**a**) XRD patterns of TiO_2, uCN and T/uCN. (**b**) XPS survey spectrum of TiO_2, uCN and T/uCN; high-resolution XPS spectra at the regions (**c**) C 1s, (**d**) N 1s, (**e**) Ti 2p and (**f**) O 1s.

The X-ray photoelectron spectroscopy spectra of TiO_2, uCN and T/uCN are displayed in Figure 3b–f. As observed from the survey XPS spectrum, besides Ti, C, O and N, a residual amount of F from the TiF_4 precursor used to prepare the TiO_2 particles was also present in the final material (Figure 3b). The high-resolution C 1s XPS spectrum of uCN showed two main contributions at 288.2 eV and 284.8 eV, which were assigned to C-(N3) and C–C/C=C, respectively (Figure 3c). Compared with pure uCN, the peak for C-(N3) of the T_1/uCN_1 sample was slightly shifted to 288.2 eV. The high-resolution N 1s XPS spectra were deconvoluted using three contributions at binding energies of 398.1 eV, 499.4 eV and 400.5 eV for uCN and 398.1 eV, 499.6 eV and 400.7 eV for T/uCN (Figure 3d). These three contributions were assigned to N-(C_2), N-(C_3) and N-H_x groups of the heptazine framework. The small shifts detected for C and some of the N components might be related to a certain degree of charge between the TiO_2 and the CN phases. Figure 3e displays the high-resolution Ti 2p XPS spectra of TiO_2 and T/uCN. Both samples show two strong peaks at approximately 458.7 and 464.5 eV, which are assigned to the Ti $2p_{3/2}$ and Ti $2p_{1/2}$ levels of Ti within a TiO_2 environment. The high-resolution O 1s XPS spectra of TiO_2 and T/uCN were fitted with two peaks at 530.4 eV and 531.8 eV, which were associated with oxygen within the TiO_2 lattice and oxygen-containing surface adsorption groups such as surface hydroxyl, respectively (Figure 3f).

The UV-vis spectra showed the UV absorption edge of TiO_2 particles and uCN nanosheets at about 390 nm and 445 nm, respectively (Figure 4a). T/uCN composites showed a similar onset absorption edge as uCN but an increased absorption below 400 nm related to the presence of the TiO_2 component. All TiO_2 and T/uCN samples presented a small absorption in the range 500–800 nm related to a small amount of F ion doping. According to the Kubelk–Munk function, the band gaps of TiO_2, uCN and T_1/Ucn_1 samples were calculated at about 3.02 eV, 2.62 eV and 2.65 eV, respectively (Figure 4b).

According to Mott–Schottky analyses (Figure 4c,d and Figure S3), the flat band potentials of TiO_2 and uCN were −0.36 V and −0.86 V vs. the normal hydrogen electrode (NHE). The valence band (VB) XPS spectra of TiO_2 and uCN showed the valence band maximum (VBM) to be located at 2.89 eV and 2.46 eV from the Fermi level, respectively. Since the flat band potentials are approximately equal to the Fermi level [41,42], the VBM was located at 2.53 eV and 1.60 eV with respect to the NHE for TiO_2 and uCN, respectively. Then, taking into account the calculated band gaps ($E_g = E_{vb} - E_{cb}$) [43], the conduction band minimum (CBM) was located at 0.49 and −1.02 for TiO_2 and uCN, respectively. Figure 4f displays

the energy-level diagram calculated for TiO_2 and uCN samples. According to this scheme, when combining uCN with TiO_2, a type II heterojunction is formed, involving electron transfer from the uCN to the TiO_2 particles. Besides, it is predicted that within such heterostructure, photogenerated electrons move toward the TiO_2 phase and photogenerated holes toward the uCN, respectively.
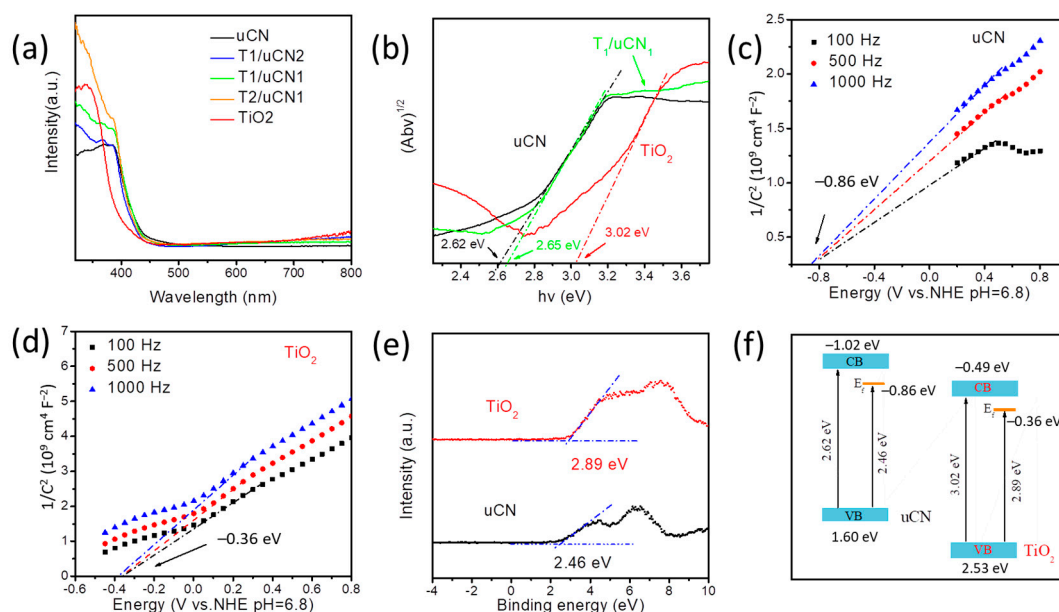

Figure 4. (**a**) UV-vis absorption spectra. (**b**) Kubelka–Munk-transformed function of TiO_2, uCN and T_1/uCN_1. (**c**,**d**) Mott–Schottky plots of uCN (**c**) and TiO_2 (**d**). (**e**) Valence band XPS spectrum of TiO_2 and uCN. (**f**) Diagram of the band structure of TiO_2 and uCN.

To analyze the photocatalytic activity towards hydrogen generation, all the samples were loaded with 1 wt% platinum as cocatalyst. Figure 5 displays the photocatalytic hydrogen generation from bCN, uCN, TiO_2 and TiO_2/uCN composites for 4 h under simulated solar light and using methanol as a sacrificial agent. Figures S8 and S9 and Table S2 show the chromatogram plots and the linear fitting of the standard hydrogen curve for gas chromatography, which show our measurement error is less than 0.2%.

For TiO_2, a high hydrogen evolution rate (HER) up to 1449 $\mu mol \cdot g^{-1} \cdot h^{-1}$ was obtained. Additionally, a notable HER was also obtained from uCN (801 $\mu mol \cdot g^{-1} \cdot h^{-1}$), well above that of bCN (599 $\mu mol \cdot g^{-1} \cdot h^{-1}$), which is consistent with the larger surface area provided by the thin-layered structure of uCN. All the TiO_2/uCN composites displayed a significant HER improvement with respect to pure TiO_2 or uCN. The highest HERs were obtained with the TiO_2/uCN composites having a 1:1 weight ratio of the two components, reaching a HER of 3875 $\mu mol \cdot g^{-1} \cdot h^{-1}$, which is 2.7 and 4.8 times higher than that of TiO_2 and uCN, respectively. The observed synergistic effect obtained when mixing both materials is related to the transfer and thus separation of photogenerated carriers at the 2D/2D heterojunctions, which prevents their recombination. Table S3 provides a comparison of the activity obtained here with those of previous published works, demonstrating the outstanding activity provided by the 2D/2D TiO_2/uCN heterojunction.

As a reference, we also measured the HER of TiO_2/bCN composites with the optimized weight ratio 1:1 (T_1/bCN_1). As observed in Figure 5c and Figure S7, the HER of T_1/bCN_1 also showed an obvious improvement with respect to that of pure TiO_2 and bCN, but the highest HER values were well below those of 2D/2D T/uCN heterojunctions having extended surface and interface areas.
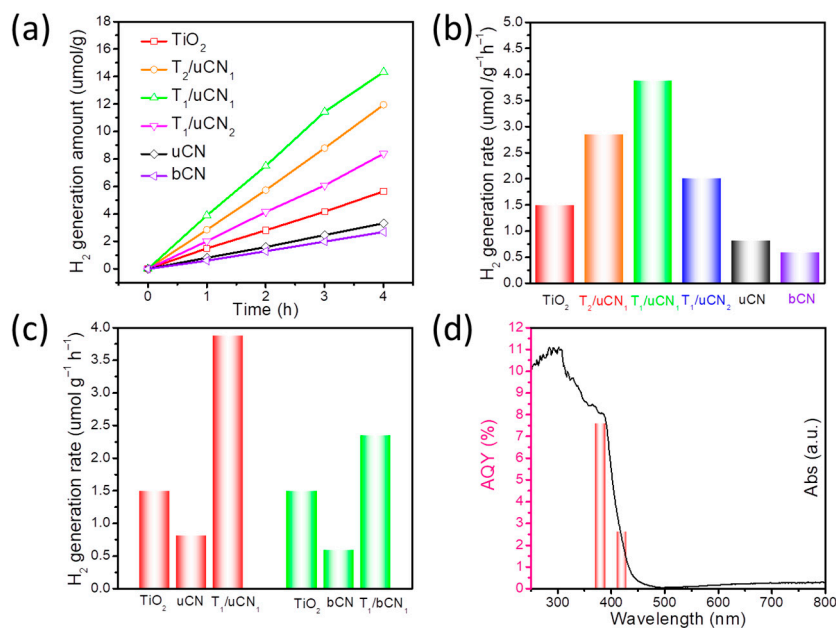
Figure 5. (**a**) Photocatalytic hydrogen generation on bCN, TiO_2 and T/uCN samples during four hours under simulated solar light illumination. (**b**) Photocatalytic hydrogen peroxide generation rate of bCN, TiO_2 and T/uCN samples. (**c**) H_2 production rate contrast between T_1/uCN_1 and T_1/bCN_1. (**d**) Wavelength-dependent AQY of T_1/uCN_1.

The apparent quantum yield (AQY) of the process was evaluated under 380 nm (4.51 mW·cm^{-2}) and 420 nm (12.14 mW·cm^{-2}) irradiation (Table S4, see details in the SI). For T_1/uCN_1, the AQY at 380 nm and 420 nm was estimated at 7.61% and 2.64%, respectively, which is consistent with UV-vis spectroscopy results (Figure 5d).

Figure 6a displays the positive photocurrents measured from uCN, TiO_2 and TiO_2/uCN samples under simulated solar irradiation. All the composite T/uCN, electrodes displayed significantly higher photocurrents than pure TiO_2 and uCN, especially the T_1/uCN_1 electrode that showed the highest photocurrents, fourfold higher than those of uCN and TiO_2. This result further confirms an improvement of the charge separation/transport with the formation of the 2D/2D heterojunction.
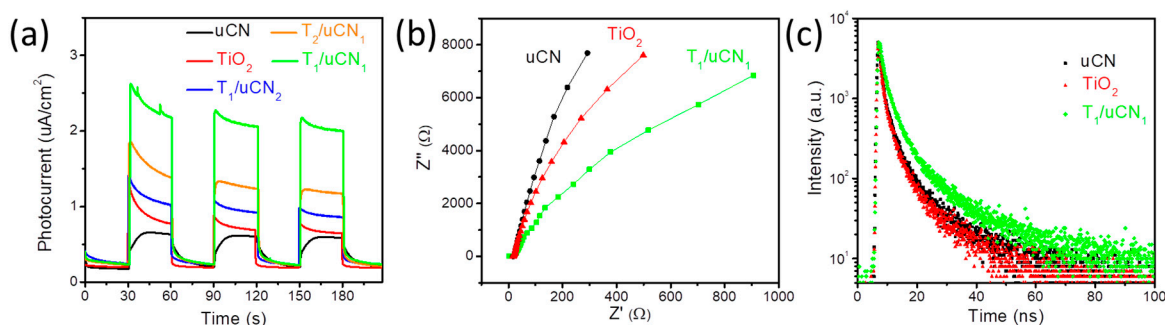
Figure 6. (**a**) Photocurrent response curves of bCN, TiO_2 and T/uCN samples; (**b**) electrochemical impedance spectroscopy (EIS) Nyquist plots of bCN, TiO_2 and T_1/uCN_1 sample; (**c**) TRPL decay of bCN, TiO_2 and T/uCN samples.

Electrochemical impedance spectroscopy (EIS) was further employed to identify the charge transport dynamics. Figure 6b displays the Nyquist plot of the impedance spectra of TiO_2, uCN and T_1/uCN_1. Consistent with previous results, the T_1/uCN_1 electrode presented a much smaller arc radius than the other two samples, confirming a much lower charge transfer resistance with the formation of the 2D/2D TiO_2/uCN heterojunction [44].

A strong photoluminescence (PL) peak was obtained under 370 nm light excitation from the uCN sample at about 455 nm, which is ascribed to the radiative band-to-band recombination of photogenerated charge carriers. When incorporating increasing amounts of TiO_2, the PL intensity of T/uCN was progressively quenched (Figure S10). Additional time-resolved PL (TRPL) spectra under 365 nm light excitation (Figure 6c) allowed calculating significantly longer PL lifetimes (4.72 ns) for T_1/uCN$_1$ samples than for TiO_2 (3.15 ns) and uCN (3.51 ns), which points at an effective separation of photogenerated charge carriers within the TiO_2/uCN heterostructures [45].

Based on the above results, the photocatalytic mechanism displayed in Figure 7 is proposed for hydrogen generation in T/uCN heterojunction photocatalysts. While both TiO_2 and uCN can generate electrons and holes under simulated solar light irradiation, the photogenerated electron–hole pairs in pure TiO_2 and uCN rapidly recombine, resulting in moderate HERs. Through the formation of a 2D/2D T/uCN heterostructure, the photogenerated electrons remain or are transferred to the TiO_2 CB because the TiO_2 CBM is located 0.53 eV below that of CN. Similarly, photogenerated holes remain or are driven to the uCN VB, which is located 0.93 eV above that of TiO_2. Electrons at the TiO_2 CB migrate to the platinum, which has a larger work function, thus a lower Fermi level, from where they are transferred to adsorbed H^+ to produce H_2. On the other hand, holes react with sacrificial methanol at the CN surface. Consequently, the photocatalytic hydrogen evolution process using sacrificial methanol can be described as follows:

$$uCN/TiO_2 \xrightarrow{h\nu} uCN/TiO_2\left(e^- + h^+\right) \tag{1}$$

$$uCN/TiO_2\left(e^- + h^+\right) \rightarrow uCN\left(h^+\right) + TiO_2\left(e^-\right) \tag{2}$$

$$TiO_2\left(e^-\right) + Pt \rightarrow TiO_2 + Pt\left(e^-\right) \tag{3}$$

$$2H^+ + e^- \rightarrow H_2 \tag{4}$$

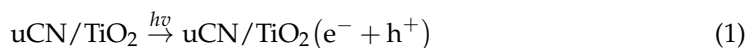$$2h^+ + CH_3OH \rightarrow CH_2O + 2H^+ \tag{5}$$

Figure 7. Schematic diagram of photocatalytic hydrogen production over T/uCN photocatalyst.

Finally, the stability of the T_1/uCN$_1$ photocatalyst in hydrogen evolution conditions under simulated solar light irradiation was measured through five four-hour cycles. As shown in Figure S11a, after this 20 h of reaction, the photocatalytic performance was hardly reduced, proving the excellent stability and reusability of the T_1/uCN$_1$ photocatalyst. Additionally, as displayed in Figure S11b,c, SEM and XRD analysis of the catalyst after 20 h

photocatalytic hydrogen generation reaction demonstrated the morphology and crystallographic structure of the material to be stable under photocatalytic reaction conditions.

4. Conclusions

In summary, we detailed the synthesis of 2D/2D T/uCN heterojunctions from ultrathin g-C$_3$N$_4$ (uCN) and colloidal TiO$_2$ nanosheets through an electrostatic self-assembly approach. The highest hydrogen generation rate was achieved from T/uCN composites with a 1:1 mass ratio of the two components. The photocatalytic performance for H$_2$ production was increased in the following order: bCN < uCN < TiO$_2$ < T$_1$/uCN$_2$ < T$_2$/uCN$_1$ < T$_1$/uCN$_1$. The enhanced performance was attributed to the unique 2D/2D type II heterojunction architecture that simultaneously maximized the surface area to interact with the media and the interface between the two materials. The face-to-face interfacial contact between ultrathin layers of g-C$_3$N$_4$ and the faceted TiO$_2$ provided fast separation of photogenerated charges inside the composites, reducing recombination and thus increasing the apparent quantum yield.

Author Contributions: In this work, R.D. designed the experiment and the nanocomposites, prepared all the materials and conducted XRD, SEM, ZEM-EDS, TEM characterization, photoelectrochemical measurements and wrote the first draft of the manuscript. B.L. conducted the photocatalytic hydrogen evolution test and TRPL test. K.X., C.Z. and X.W. significantly contributed to the result discussion. X.H. and J.A. participated in high-resolution TEM characterization. A.C. conceived and guided the project and supervised the work. The manuscript was corrected and improved by all authors. All authors have read and agreed to the published version of the manuscript.

Institutional Review Board Statement: Not applicable.

Informed Consent Statement: Not applicable.

Data Availability Statement: The data are available on reasonable request from the corresponding authors.

Conflicts of Interest: The authors declare no conflict of interest.

References

1. Campos-Martin, J.M.; Blanco-Brieva, G.; Fierro, J.L.G. Hydrogen peroxide synthesis: An outlook beyond the anthraquinone process. *Angew. Chem. Int. Ed.* **2006**, *45*, 6962–6984. [CrossRef] [PubMed]
2. Xiang, Q.; Cheng, B.; Yu, J. Hierarchical porous CdS nanosheet-assembled flowers with enhanced visible-light photocatalytic H2-production performance. *Appl. Catal. B Environ.* **2013**, *138*, 299–303. [CrossRef]
3. Fujishima, A.; Honda, K. Electrochemical photolysis of water at a semiconductor electrode. *Nature* **1972**, *238*, 37–38. [CrossRef] [PubMed]
4. Zhang, J.; Xu, Q.; Feng, Z.; Li, M.; Li, C. Importance of the relationship between surface phases and photocatalytic activity of TiO_2. *Angew. Chem.* **2008**, *120*, 1790–1793. [CrossRef]
5. Irie, H.; Watanabe, Y.; Hashimoto, K. Carbon-doped anatase TiO_2 powders as a visible-light sensitive photocatalyst. *Chem. Lett.* **2003**, *32*, 772–773. [CrossRef]
6. Zhang, Y.; Tang, Z.-R.; Fu, X.; Xu, Y.-J. TiO_2- graphene nanocomposites for gas-phase photocatalytic degradation of volatile aromatic pollutant: Is TiO_2- graphene truly different from other TiO_2- carbon composite materials? *ACS Nano* **2010**, *4*, 7303–7314. [CrossRef] [PubMed]
7. Thompson, T.L.; Yates, J.T. Surface science studies of the photoactivation of TiO_2 new photochemical processes. *Chem. Rev.* **2006**, *106*, 4428–4453. [CrossRef]
8. Hamad, S.; Catlow, C.R.A.; Woodley, S.M.; Lago, S.; Mejias, J.A. Structure and stability of small TiO_2 nanoparticles. *J. Phys. Chem. B* **2005**, *109*, 15741–15748. [CrossRef]
9. Sang, L.; Zhao, Y.; Burda, C. TiO_2 nanoparticles as functional building blocks. *Chem. Rev.* **2014**, *114*, 9283–9318. [CrossRef]
10. Chen, J.S.; Lou, X.W. Anatase TiO_2 nanosheet: An ideal host structure for fast and efficient lithium insertion/extraction. *Electrochem. Commun.* **2009**, *11*, 2332–2335. [CrossRef]
11. Zhang, Y.X.; Li, G.H.; Jin, Y.X.; Zhang, Y.; Zhang, J.; Zhang, L.D. Hydrothermal synthesis and photoluminescence of TiO_2 nanowires. *Chem. Phys. Lett.* **2002**, *365*, 300–304. [CrossRef]
12. Wang, P.; Wang, J.; Wang, X.; Yu, H.; Yu, J.; Lei, M.; Wang, Y. One-step synthesis of easy-recycling TiO_2-rGO nanocomposite photocatalysts with enhanced photocatalytic activity. *Appl. Catal. B Environ.* **2013**, *132*, 452–459. [CrossRef]
13. Zhou, W.; Yin, Z.; Du, Y.; Huang, X.; Zeng, Z.; Fan, Z.; Liu, H.; Wang, J.; Zhang, H. Synthesis of few-layer MoS_2 nanosheet-coated TiO_2 nanobelt heterostructures for enhanced photocatalytic activities. *Small* **2013**, *9*, 140–147. [CrossRef] [PubMed]
14. Ou, Y.; Lin, J.; Fang, S.; Liao, D. MWNT–TiO_2: Ni composite catalyst: A new class of catalyst for photocatalytic H_2 evolution from water under visible light illumination. *Chem. Phys. Lett.* **2006**, *429*, 199–203. [CrossRef]
15. Liu, Q.; Huang, J.; Tang, H.; Yu, X.; Shen, J. Construction 0D TiO_2 nanoparticles/2D CoP nanosheets heterojunctions for enhanced photocatalytic H_2 evolution activity. *J. Mater. Sci. Technol.* **2020**, *56*, 196–205. [CrossRef]
16. Meng, A.; Zhu, B.; Zhong, B.; Zhang, L.; Cheng, B. Direct Z-scheme TiO_2/CdS hierarchical photocatalyst for enhanced photocatalytic H_2-production activity. *Appl. Surf. Sci.* **2017**, *422*, 518–527. [CrossRef]
17. Cheng, C.; Amini, A.; Zhu, C.; Xu, Z.; Song, H.; Wang, N. Enhanced photocatalytic performance of TiO_2-ZnO hybrid nanostructures. *Sci. Rep.* **2014**, *4*, 4181. [CrossRef]
18. Yan, J.; Wu, H.; Chen, H.; Zhang, Y.; Zhang, F.; Liu, S.F. Fabrication of TiO_2/C_3N_4 heterostructure for enhanced photocatalytic Z-scheme overall water splitting. *Appl. Catal. B Environ.* **2016**, *191*, 130–137. [CrossRef]
19. Xie, M.; Fu, X.; Jing, L.; Luan, P.; Feng, Y.; Fu, H. Long-lived, visible-light-excited charge carriers of TiO_2/$BiVO_4$ nanocomposites and their unexpected photoactivity for water splitting. *Adv. Energy Mater.* **2014**, *4*, 1300995. [CrossRef]
20. Wang, Y.; Zhu, C.; Zuo, G.; Guo, Y.; Xiao, W.; Dai, Y.; Kong, J.; Xu, X.; Zhou, Y.; Xie, A. 0D/2D Co_3O_4/TiO_2 Z-Scheme heterojunction for boosted photocatalytic degradation and mechanism investigation. *Appl. Catal. B Environ.* **2020**, *278*, 119298. [CrossRef]
21. Yuan, L.; Weng, B.; Colmenares, J.C.; Sun, Y.; Xu, Y. Multichannel charge transfer and mechanistic insight in metal decorated 2D–2D Bi2WO6–TiO_2 cascade with enhanced photocatalytic performance. *Small* **2017**, *13*, 1702253. [CrossRef] [PubMed]
22. Zhang, Y.; Xu, J.; Mei, J.; Sarina, S.; Wu, Z.; Liao, T.; Yan, C.; Sun, Z. Strongly interfacial-coupled 2D-2D TiO_2/g-C_3N_4 heterostructure for enhanced visible-light induced synthesis and conversion. *J. Hazard. Mater.* **2020**, *394*, 122529. [CrossRef] [PubMed]
23. Liu, Q.; Lu, H.; Shi, Z.; Wu, F.; Guo, J.; Deng, K.; Li, L. 2D $ZnIn_2S_4$ nanosheet/1D TiO_2 nanorod heterostructure arrays for improved photoelectrochemical water splitting. *ACS Appl. Mater. Interfaces* **2014**, *6*, 17200–17207. [CrossRef] [PubMed]
24. Chava, R.K.; Son, N.; Kang, M. Surface engineering of CdS with ternary Bi/Bi_2MoO_6-MoS_2 heterojunctions for enhanced photoexcited charge separation in solar-driven hydrogen evolution reaction. *Appl. Surf. Sci.* **2021**, *565*, 150601. [CrossRef]
25. Fu, J.; Yu, J.; Jiang, C.; Cheng, B. g-C_3N_4-Based heterostructured photocatalysts. *Adv. Energy Mater.* **2018**, *8*, 1701503. [CrossRef]
26. Wen, J.; Xie, J.; Chen, X.; Li, X. A review on g-C_3N_4-based photocatalysts. *Appl. Surf. Sci.* **2017**, *391*, 72–123. [CrossRef]

27. Chava, R.K.; Do, J.; Kang, M. Strategy for improving the visible photocatalytic H$_2$ evolution activity of 2D graphitic carbon nitride nanosheets through the modification with metal and metal oxide nanocomponents. *Appl. Catal. B Environ.* **2019**, *248*, 538–551. [CrossRef]

28. Ran, Y.; Cui, Y.; Zhang, Y.; Fang, Y.; Zhang, W.; Yu, X.; Lan, H.; An, X. Assembly-synthesis of puff pastry-like g-C$_3$N$_4$/CdS heterostructure as S-junctions for efficient photocatalytic water splitting. *Chem. Eng. J.* **2022**, *431*, 133348. [CrossRef]

29. Cabot, A.; Du, R.; Xiao, K.; Li, B.; Han, X.; Zhang, C.; Wang, X.; Zuo, Y.; Pablo, G.; Li, J.; et al. Controlled Oxygen Doping in Highly Dispersed Ni-Loaded G-C$_3$N$_4$ Nanotubes for Efficient Photocatalytic H$_2$O$_2$ Production. *SSRN Electron. J.* **2022**, *441*, 135999. [CrossRef]

30. Zhang, X.; Yuan, X.; Jiang, L.; Zhang, J.; Yu, H.; Wang, H.; Zeng, G. Powerful combination of 2D g-C$_3$N$_4$ and 2D nanomaterials for photocatalysis: Recent advances. *Chem. Eng. J.* **2020**, *390*, 124475. [CrossRef]

31. Zuo, Y.; Xu, X.; Zhang, C.; Li, J.; Du, R.; Wang, X.; Han, X.; Arbiol, J.; Llorca, J.; Liu, J.; et al. SnS$_2$/g-C$_3$N$_4$/graphite nanocomposites as durable lithium-ion battery anode with high pseudocapacitance contribution. *Electrochim. Acta* **2020**, *349*, 136369. [CrossRef]

32. Fu, J.; Xu, Q.; Low, J.; Jiang, C.; Yu, J. Ultrathin 2D/2D WO$_3$/g-C$_3$N$_4$ step-scheme H$_2$-production photocatalyst. *Appl. Catal. B Environ.* **2019**, *243*, 556–565. [CrossRef]

33. Qin, Y.; Li, H.; Lu, J.; Feng, Y.; Meng, F.; Ma, C.; Yan, Y.; Meng, M. Synergy between van der waals heterojunction and vacancy in ZnIn$_2$S$_4$/g-C$_3$N$_4$ 2D/2D photocatalysts for enhanced photocatalytic hydrogen evolution. *Appl. Catal. B Environ.* **2020**, *277*, 119254. [CrossRef]

34. Cao, S.; Shen, B.; Tong, T.; Fu, J.; Yu, J. 2D/2D heterojunction of ultrathin MXene/Bi$_2$WO$_6$ nanosheets for improved photocatalytic CO$_2$ reduction. *Adv. Funct. Mater.* **2018**, *28*, 1800136. [CrossRef]

35. Su, J.; Li, G.; Li, X.; Chen, J. 2D/2D heterojunctions for catalysis. *Adv. Sci.* **2019**, *6*, 1801702. [CrossRef]

36. Urbain, F.; Du, R.; Tang, P.; Smirnov, V.; Andreu, T.; Finger, F.; Divins, N.J.; Llorca, J.; Arbiol, J.; Cabot, A. Upscaling high activity oxygen evolution catalysts based on CoFe$_2$O$_4$ nanoparticles supported on nickel foam for power-to-gas electrochemical conversion with energy efficiencies above 80%. *Appl. Catal. B Environ.* **2019**, *259*, 118055. [CrossRef]

37. Zuo, Y.; Liu, Y.; Li, J.; Du, R.; Yu, X.; Xing, C.; Zhang, T.; Yao, L.; Arbiol, J.; Llorca, J. Solution-processed ultrathin SnS$_2$–Pt nanoplates for photoelectrochemical water oxidation. *ACS Appl. Mater. Interfaces* **2019**, *11*, 6918–6926. [CrossRef]

38. Zhang, C.; Du, R.; Biendicho, J.J.; Yi, M.; Xiao, K.; Yang, D.; Zhang, T.; Wang, X.; Arbiol, J.; Llorca, J.; et al. Tubular CoFeP@CN as a Mott–Schottky Catalyst with Multiple Adsorption Sites for Robust Lithium−Sulfur Batteries. *Adv. Energy Mater.* **2021**, *11*, 2100432. [CrossRef]

39. Liu, M.; Piao, L.; Lu, W.; Ju, S.; Zhao, L.; Zhou, C.; Li, H.; Wang, W. Flower-like TiO$_2$ nanostructures with exposed {001} facets: Facile synthesis and enhanced photocatalysis. *Nanoscale* **2010**, *2*, 1115–1117. [CrossRef]

40. Li, Y.; Lv, K.; Ho, W.; Dong, F.; Wu, X.; Xia, Y. Hybridization of rutile TiO$_2$ (rTiO$_2$) with g-C$_3$N$_4$ quantum dots (CN QDs): An efficient visible-light-driven Z-scheme hybridized photocatalyst. *Appl. Catal. B Environ.* **2017**, *202*, 611–619. [CrossRef]

41. Tian, N.; Zhang, Y.; Li, X.; Xiao, K.; Du, X.; Dong, F.; Waterhouse, G.I.N.; Zhang, T.; Huang, H. Precursor-reforming protocol to 3D mesoporous g-C$_3$N$_4$ established by ultrathin self-doped nanosheets for superior hydrogen evolution. *Nano Energy* **2017**, *38*, 72–81. [CrossRef]

42. Tian, N.; Huang, H.; Wang, S.; Zhang, T.; Du, X.; Zhang, Y. Facet-charge-induced coupling dependent interfacial photocharge separation: A case of BiOI/g-C$_3$N$_4$ pn junction. *Appl. Catal. B Environ.* **2020**, *267*, 118697. [CrossRef]

43. Yu, X.; Du, R.; Li, B.; Zhang, Y.; Liu, H.; Qu, J.; An, X. Biomolecule-assisted self-assembly of CdS/MoS$_2$/graphene hollow spheres as high-efficiency photocatalysts for hydrogen evolution without noble metals. *Appl. Catal. B Environ.* **2016**, *182*, 504–512. [CrossRef]

44. Du, R.; Zhang, Y.; Li, B.; Yu, X.; Liu, H.; An, X.; Qu, J. Biomolecule-assisted synthesis of defect-mediated Cd$_{1-x}$ZnxS/MoS$_2$/graphene hollow spheres for highly efficient hydrogen evolution. *Phys. Chem. Chem. Phys.* **2016**, *18*, 16208–16215. [CrossRef] [PubMed]

45. Chen, Y.; Liu, X.; Hou, L.; Guo, X.; Fu, R.; Sun, J. Construction of covalent bonding oxygen-doped carbon nitride/graphitic carbon nitride Z-scheme heterojunction for enhanced visible-light-driven H$_2$ evolution. *Chem. Eng. J.* **2020**, *383*, 123132. [CrossRef]